1994

Numerical Simulation And Control Of Thermocapillary Convection In Cavities And Liquid Layers

Changhai Chen

NUMERICAL SIMULATION AND CONTROL OF THERMOCAPILLARY CONVECTION IN CAVITIES AND LIQUID LAYERS

by

Changhai Chen

Faculty of Engineering Science

Department of Mechanical Engineering

Submitted in partial fulfilment

of the requirements for the degree of

Doctor of Philosophy

Faculty of Graduate Studies

The University of Western Ontario

London, Ontario

October 1993

ISBN 0-315-90566-2

ABSTRACT

The problem of steady thermocapillary convection in cavities and liquid layers in the absence of gravity is studied. The flow is driven by a temperature gradient parallel to the interface.

An effective algorithm for analysis of the above problem has been developed. The algorithm is based on a coordinate transformation method, streamfunction vorticity formulation, and second-order finite-difference discretization. The unknown physical domain is mapped onto a rectangular computational domain, with the explicit form of the mapping function not being known. The field variables and the mapping function are determined simultaneously using Picard-type iteration. The numerical experiments indicate that the algorithm delivers the second-order accuracy even for very large interfacial distortion.

The question of existence of nonisothermal interfaces has been investigated. It is demonstrated that the external temperature has to satisfy constraint conditions in order for a nonisothermal interface to exist in a continuous form.

Extensive numerical parameter studies show that the dominant response of the flow system consists of a large interfacial distortion and not just a pure convection as commonly assumed. This is consistent with the analytical results describing conditions guaranteeing existence of a nonisothermal interface.

The nonunique steady solutions have been found to exist at very low Reynolds and capillary numbers. The primary bifurcation point appears to be supercritical. The response of the system is very sensitive with respect to the functional form of the external heating, variations of transport parameters, such as Reynolds and capillary numbers, and geometrical constraints, such as length of the cavity and the type of contact conditions.

Double liquid layer systems have been studied in order to assess potential of the encapsulation technique for control of the thermocapillary convection. A detailed analysis of the flow and temperature fields has been carried out. The results show that the thermocapillary convection can be controlled by properly selecting the properties of the encapsulating liquid.

ACKNOWLEDGEMENTS

I wish to express my sincere appreciation to Professor J.M. Floryan, my supervisor, for his guidance, encouragement and financial support during the course of the work.

I am very grateful to Professor T.E. Base, Professor D. Surry, and Professor D.J. Jeffrey, my advisory committee, for their helpful suggestions and guidance.

I wish to thank Professor E.S. Nowak, Professor J.D. Tarasuk, and Professor C.W.S. To for their assistance and help.

Special thanks should be given to Dr. J. Rokicki and Mr. J. Perwaiz with whom I have had many fruitful discussions.

Thanks are also due to Mr. D. Corrin, Mr. J. Sherk, Mrs. W.M. Shyr, and Mr. M. Cote for their computer supports.

To Mr. M. Jaworski, Mrs. L. Miles, Ms. A. Goncalves, and Ms. C. Seres, my thanks for their assistance when in need.

Financial assistance received by the author during this project from the Ministry of Colleges and Universities,

Province of Ontario, from the Faculty of Graduate Studies, the University of Western Ontario, and from the Faculty of Engineering Science, the University of Western Ontario is greatly acknowledged.

Lastly, I want to extend my special appreciation to my parents, my wife and my friends for their support, patience, and encouragement during these years of intensive work.

TABLE OF CONTENTS

LIST OF FIGURES

LIST OF TABLES

NOMENCLATURE

A	aspect ratio
Bi	Biot number, $Bi=Hh_s/k$
Br	Brinkman number, $Br=\mu u_*^2/(\Delta T\kappa)$
Ca	capillary number, $Ca=\mu u_*/\sigma_0$
C_p	specific heat per unit mass
G	ratio of thermal conductivities of two liquids; also a measure of asymmetry of the interface
h_0	interface shape under isothermal conditions
h_1	interface deviation caused by dynamic effects, or small deformation of the interface
h(x)	function describing location of the interface
H	thickness of the liquid layer
$\bar{H}$	thickness of the upper liquid layer, $\bar{H}=H-1$
h_s	heat transfer coefficient
H_L	location of contact point at the left wall
H_R	location of contact point at the right wall
i	unit vector in the x direction
j	unit vector in the y direction
k	unit vector in the z direction
k	thermal conductivity; also wavenumber
k_1	x-component of the wave vector
k_2	y-component of the wave vector

K	constant in pressure; also ratios of viscosities of two liquids
L	length of cavity; also ratio of interface temperature and wall temperature for a two-layer system
L_1	ratio of interface temperature and wall temperature for a single-layer system
m	ratio of the negative temperature derivative of surface tension
M	number of grid points in the ξ direction
Ma	Marangoni number, $Ma=u.H/\kappa$
Mc	ratio of capillary numbers
n	unit outward normal vector
N	number of grid points in the η direction
n_i	i-component of unit normal vector to the interface
p	pressure
p′	dimensionless pressure
p_s	static pressure
p_0	pressure in the leading-order approximation
Pr	Prandtl number, Pr=Ma/Re
Re	Reynolds number, $Re=u.H/\nu$
S_{ij}	stress tensor of the liquid
t	unit tangent vector to the interface
t_i^x	unit tangent vector to the interface in the (x,z) plane

t_y	unit tangent vector to the interface in the (y,z) plane
T	temperature
$T_g(x)$	temperature in the gas phase
T_m	amplitude of temperature at the interface
T_L	temperature at the left wall
T_{max}	a measure of the maximum of the interface temperature
T_{min}	a measure of the minimum of the interface temperature
T_0	temperature in the leading-order approximation
T_R	temperature at the right wall
$T_w(x,y)$	temperature along the bottom plate (Chapter 6)
T_∞	reference temperature
ΔT	temperature difference
$\hat{T}$	Fourier transform of temperature
T'	dimensionless temperature
u	x component of velocity vector
u_∞	reference velocity
v	y component of velocity vector
V	volume; also magnitude of the interface velocity vector
$\bar{V}$	dimensionless volume
w	z component of velocity vector
x	cartesian coordinate
y	cartesian coordinate

z	cartesian coordinate

Greek

α	order of grid-convergence
γ	negative of the derivative of the surface tension with respect to temperature
δ_{ij}	Kronecker delta
η	cartesian coordinate in the computational domain
$\Delta\eta$	grid size in η direction
θ_L	contact angle between the liquid and the left wall
θ_R	contact angle between the liquid and the right wall
κ	thermal diffusivity, $\kappa=k/\rho C_p$
λ	length of the wave vector
Λ	mean curvature
μ	dynamic viscosity
ν	kinematic viscosity
ξ	cartesian coordinate in the computational domain
$\Delta\xi$	grid size in the ξ direction
ρ	density
σ	surface tension
σ_0	surface tension at the reference temperature T.
τ_1	x-component of surface traction
τ_2	y-component of surface traction
ψ	streamfunction

ω	vorticity

Subscripts

0	leading-order approximation
A	belongs to liquid A
B	belongs to liquid B
i	grid indices in the ξ direction
j	grid indices in the η direction
x	derivative with respect to x
y	derivative with respect to y
z	derivative with respect to z
η	derivative with respect to η
ξ	derivative with respect to ξ

CHAPTER 1

INTRODUCTION

1.1 Introduction

Fluid and interfacial transport phenomena are central to a wide range of physical processes, many of which have technological importance in both earth and space based applications, such as material processing. This is because many materials are processed from or in a liquid state.

Consider the configuration shown in Figure 1.1 in which a solid passes through a heater, melts and re-solidifies into a single crystal of (it is to be hoped) high quality. Obviously, the qualities of the crystal, like purity, compositional uniformity, and crystallographic perfection, depend to a large extent on transport conditions in the fluid phase during processing. As a result, a quantitative understanding of the flow and temperature fields, and interfacial processes is of paramount importance.

In ground-based material studies, gravity often introduces complexities which severely limit the fundamental understanding of a large number of these phenomena.

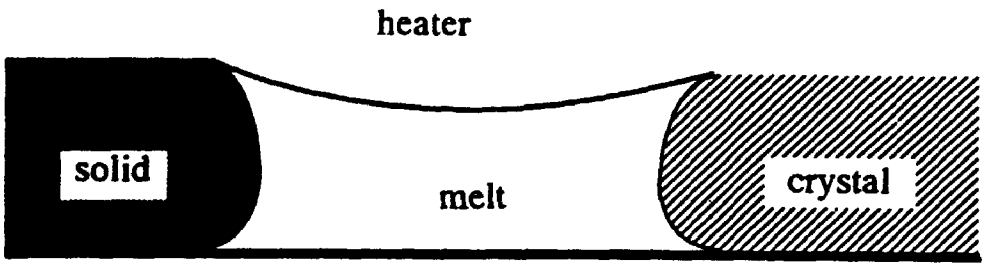

Figure 1.1 Schematic drawing of an open boat zoning configuration.

Interfacial phenomena are normally masked by gravitationally induced flows, hydrostatic pressure and sedimentation. Microgravity provides a unique environment in which to process materials. The effects of buoyancy-driven convection, sedimentation, and hydrostatic pressure are absent in the weightless environment of space. In a low-gravity environment, the surface energy effects become important in causing fluid flow. Appropriate investigation can help quantify and lead to a more complete understanding of these surface energy effects. It should also be emphasized that systematic studies inspired by microgravity-oriented material processing already has led to significant improvements of earth-based technology (Ostrach, 1983; Brown, 1988; Coriell, et al, 1985; Davis,

1987; Glicksman, et al, 1986; Henry & Roux, 1988; McFadden, et al, 1985; Ostrach, 1980; Ostrach, 1982; and Schwabe, 1988).

Material processing under a microgravity environment, although occurring under largely reduced natural convection, can still suffer from undesirable thermocapillary convection. An example of the adverse effects of thermocapillary convection is the formation of striations in the crystals, as shown in Figure 1.2 (Kim & Kou, 1989). The striations in the crystals are caused by thermal fluctuations induced by

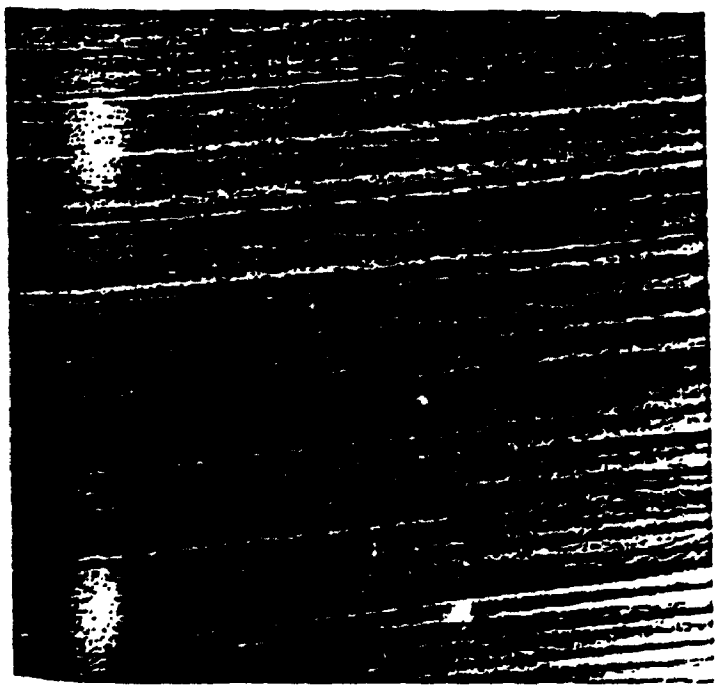

Figure 1.2 Striations in the resultant crystal.

thermocapillary convection in the melt zone. Therefore, control and optimization of those processes, particularly for zero gravity application, critically depend on the complete understanding of all phenomena that may be induced by the thermocapillary effect.

Consider a model problem shown in Figure 1.3. The upper surface, described by z=h(x), is a free surface bounded by a passive gas of negligible density and viscosity, therefore, the gas will not influence the flow and the temperature fields in the liquid. The temperature distribution in the gas is assumed to be known. The differential heating induces a temperature gradient along the interface which then generates a surface tension gradient along the interface. Variation of the surface tension produces tangential force along the interface, which in turn, causes motion in the adjacent phases. The final shape of the interface comes as result of interaction among the surface tension, the pressure and the normal viscous stresses generated by the convection field. The actual form of the surface tension variations depends on the energy transport in the adjacent phases. Analysis of the problem requires determination of the solutions of the free/moving boundary problems for the Navier-Stokes and energy equations. This free boundary, the shape of which is unknown a priori, introduces many extra difficulties (Floryan & Rasmussen, 1989).

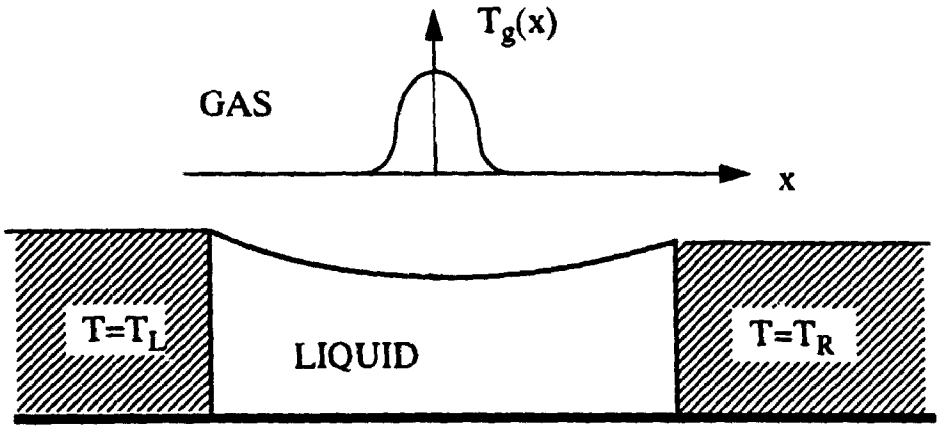

Figure 1.3 Sketch of the model problem.

1.2 Literature Review

The subject of thermocapillary convection has been an area of active research. For the problems of thermocapillary convection in connection with materials processing, the reviews by Rosenberger (1979), Pimputkar & Ostrach (1981), and Langlois (1985) give excellent account of the research.

Numerous studies have been devoted to the onset of Marangoni convection in long horizontal layers but subject to

a vertical temperature gradient. These studies include experimental, theoretical (stability) and numerical approaches. Among these are Pearson (1958), Perez-Garcia & Carneiro (1991), Guo & Yang (1989), Gouesbet et al. (1990), Winters et al. (1988), Smith & Davis (1983), Goussis & Kelly (1990), and Jimenez-Fernandez & Garcia-Sane (1989).

Thermocapillary convection in finite cavities subject to a temperature gradient parallel to the interface has also attracted a lot attention. Schwabe & Scharmann (1981) experimentally studied Marangoni convection in an open boat with an oxide melt. Marangoni convection was identified to be a significant flow phenomenon for heat and mass transport in melt growth of oxide.

Thermocapillary convection in a molten zone of $NaNO_3$ contained in a boat with a free horizontal surface, that was heated from above by a centrally located wire heater, was studied by Kim & Kou (1989) in order to simulate flow in zone-melting crystal growth.

Sen & Davis (1982) considered flow in a very long cavity driven by a linear temperature distribution with capillary number decreasing inversely proportionally to the cavity length. They used an asymptotic theory which was valid for $A \to 0$ to obtain the fluid and thermal fields as well as the

interfacial shapes. They presented results with the Reynolds number Re=O(A), the Marangoni number Ma=O(A), and the capillary number $Ca=O(A^4)$.

Sen (1986) reconsidered this problem and presented results which were valid for $Ca=O(A^3)$. His results show that the interface undergoes an O(1) deformation from its initially flat form and the flow inside the cavity becomes nonparallel everywhere.

A computational procedure was proposed by Strani & Piva (1982) to solve thermocapillary flow in a rectangular enclosure with a temperature gradient between the lateral walls. The numerical results showed the importance of considering the interface to be deformable for an accurate evaluation of the convective flow. Since they just used a coarse mesh (10*10) for their finite - difference computations, the accuracy of their results was not certain.

Strani et al. (1983) numerically computed thermocapillary motions in a rectangular cavity with A=0.2, 1, and 5 and with Prandtl number Pr=1 and Re=3000. Again, the accuracy of their results was uncertain.

Bergmann & Webb (1990) presented numerical results for the melting of a pure metal from an isothermal vertical wall.

The investigation focused on the influence of surface tension on the flow and heat transfer in the liquid phase as well as the resultant shape and motion of the solid - liquid interface. They calculated results for Ma as high as $4*10^3$.

A numerical study has been conducted by Keller & Bergman (1990) to examine the influence of free surface curvature, due to the presence of various contact angles, on thermocapillary convection within a cavity.

Hadid & Roux (1992, 1990) numerically simulated the influence of thermocapillary forces on buoyancy - driven convection for shallow open cavities with differentially heated endwalls and filled with low-Prandtl-number fluid. Calculations were carried out for three aspects ratios A=4, 12.5 and 25 and for Reynolds number up to $1.67*10^4$.

Zebib et al. (1985) and Carpenter & Homsy (1990) examined steady thermocapillary flow in a square two-dimensional cavity. Their numerical solutions were obtained for Ma up to 10^5 and Re as high as $5*10^4$.

Homsy & Meiburg (1984) considered the effect of insoluble surfactant on the steady thermocapillary flow in a differentially heated slot treated by Sen & Davis (1982).

Rivas & Ostrach (1989) studied steady thermocapillary flows of low-Prandtl-number fluids in shallow enclosures. They analyzed the influence of the thermal boundary conditions for Reynolds number up to 10^4 and A=0.2.

Laure et al. (1990) presented a theoretical study of motions of viscous fluids driven by a constant stress acting on an upper surface of a long rectangular cavity. They studied the stability of the Couette flow.

Steady thermocapillary flows of low-Prandtl-number fluids in shallow rectangular enclosures under an imposed-heat-flux configuration were studied by Rivas (1991). The field equation was solved numerically for Reynolds number up to 10^4.

The subject of thermocapillary convection in infinite layers has been considered before under a variety of simplifying assumptions. Levich (1962) and Birikh (1966) analyzed a two-dimensional layer with non-deformable interface and flow being parallel to the boundaries. The resulting solution did not satisfy the condition of constant pressure along the interface. Yih (1968) reconsidered this problem in the context of chemico-capillary flows with gravity present and with allowance for small interface deformation. Sanochkin (1983) considered the interface to be flat and included transverse velocity components with simplifying assumptions

analogous to those used in the boundary-layer theory. Lai & Chai (1986) carried out an assessment of convective heat transport effects under similar assumptions. Sanochkin (1984) evaluated inertial effects and Vybornov & Sanochkin (1985) analyzed small interface distortions. Pshenichnikov & Tokmenina (1983) demonstrated experimentally that an appreciable curving of the interface occurs when the thickness of the layer is sufficiently small. Adler & Sowerby (1970) extended Yih's (1968) analysis into three dimensions. Pimputkar & Ostrach (1980) considered transient flow induced by a fixed interface temperature with the flow being, in effect, parallel to the interface and inertial effects being negligible. Kopbosynov & Pukhnachev (1986) extended this approach to three-dimensional situations.

1.3 Outline of the Present Work

The above literature review shows that there has been a tremendous amount of research into thermocapillary convection in liquid layers and cavities from different viewpoints. However, by far the majority of papers are concerned with the asymptotic limit in which the shape of the interface, while unknown, deviates only slightly from some predefined configurations. They solved fixed boundary problems for a regular physical domain in order to avoid the complexity caused by the existence of the unknown free interface shape.

The studies are only valid for small interfacial deformation cases. But very large deformations of the free surface may actually occur in technological applications and it is important to study thermocapillary convection with large interfacial deformation.

The main objective of the present work is, therefore, to carry out a complete numerical analysis on the thermocapillary convection in liquid layers and cavities. The motion is induced by imposing a known temperature distribution in the bounding gas phase. The governing equations are the two-dimensional steady Navier-Stokes, energy, continuity and interfacial equations. There will be no simplifying assumptions involving interfacial deformation in the analysis in order to maintain the generality of our analysis. More specifically, this study will consist of the following elements:

i) Development of an accurate and reliable algorithm which can handle thermocapillary convection in cavities with very large interfacial deformation. The algorithm will be based on a mapping method. The unknown physical domain is mapped onto a rectangular computational domain, with the explicit form of the mapping function not being known. The governing equations are expressed in terms of the streamfunction and vorticity. A finite-difference discretization procedure is used. The

discretized field equations are solved by the standard Gauss-Seidel iteration procedure. The Picard-type iteration is used to determine the shape of the interface.

ii) Confirmation of the accuracy and reliability of the algorithm, especially for large deformation cases. It will be shown the algorithm has a second-order accuracy and that it can reproduce existing results in the case of small interfacial deformation.

iii) Study of conditions guaranteeing existence of only small interfacial deformations. It will show that the temperature field has to satisfy restrictive conditions in order to get small interfacial deformations. The dominant response of the system to an external heating consists of large interfacial distortions.

iv) Extensive parameter studies of thermocapillary convection. The parameters studied include Reynolds, Marangoni, and capillary numbers, types of temperature distribution, types of geometry, and contact conditions.

v) Investigation of the possible appearance of non-unique steady solutions. It will demonstrate that the solutions become non-unique even at $Re \sim 10$. The dependence of steady

solutions on various parameters, such as Re, Ma and L, will be studied.

vi) Investigation of the potential for control of thermocapillary convection in a liquid layer by covering the layer with a blanket made of another liquid. It will be shown that the thermocapillary convection in the lower layer can be effectively controlled by selecting appropriate properties of the upper liquid.

CHAPTER 2

FORMULATION

2.1 Governing Equations and Boundary Conditions

Consider a two-dimensional, open, rectangular cavity, Figure 2.1, of height H and length L, having two differentially - heated side walls kept at temperature T_L and T_R , and filled with a liquid of density ρ, thermal conductivity k, specific heat per unit mass c_p, thermal diffusivity $\kappa=k/\rho c_p$,
kinematic viscosity ν and dynamic viscosity μ. The free surface, described by $z=h(x)$, is bounded by a passive gas of negligible viscosity and density, therefore, the gas will not influence the flow and the temperature fields in the liquid. As mentioned in Chapter 1, one usually considers the temperature distribution in the gas $T=T_g(x)$ to be known.

The problem appears to be a standard cavity flow problem, except that the upper boundary is replaced by a free surface. In order to compare with the existing results, we follow the standard assumptions for the problem except the deformation of the interface. We will not make any assumption about the deformation. The assumptions are given as follows:

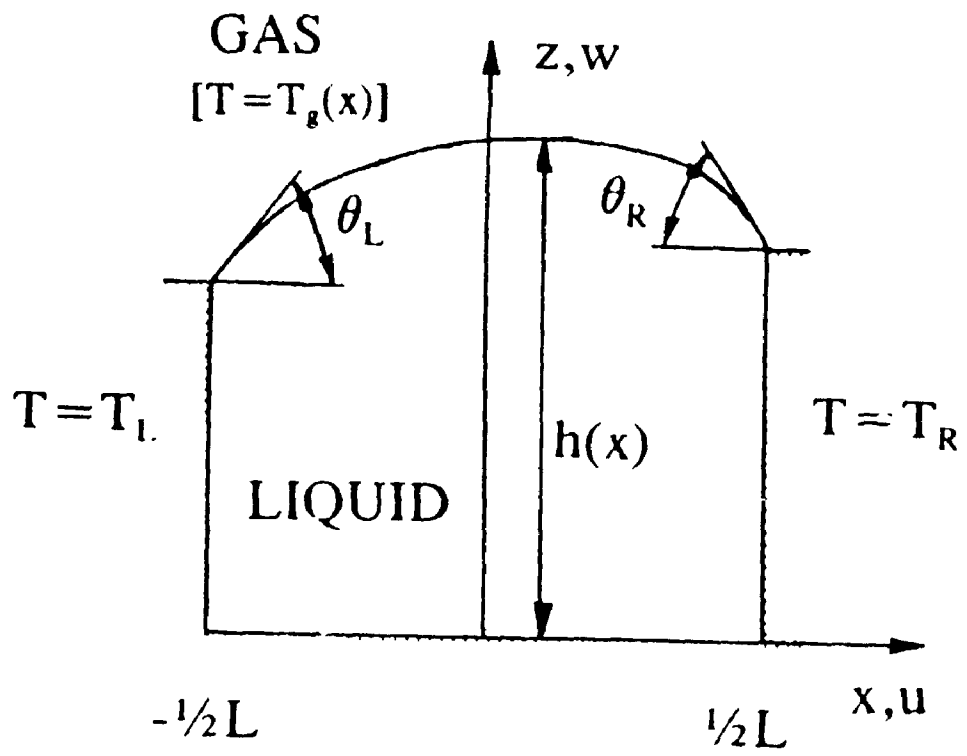

Figure 2.1 Schematic diagram of liquid in a cavity.

(i) that the flow is steady;

(ii) that the liquid has constant properties (except for surface tension);

(iii) that the liquid is Newtonian;

(iv) that there is no body force; and

(v) that the flow is laminar.

The motion of the liquid in the cavity is governed by the equations:

$$u_x+w_z=0, \tag{2.1}$$

$$uu_x+wu_z=-\rho^{-1}p_x+\nu(u_{xx}+u_{zz}), \tag{2.2}$$

$$uw_x+ww_z=-\rho^{-1}p_z+\nu(w_{xx}+w_{zz}), \tag{2.3}$$

$$uT_x+wT_z=\kappa(T_{xx}+T_{zz}), \tag{2.4}$$

where u and w are components of the velocity vector in the x and z directions, respectively, p is the pressure of the liquid, T is the temperature of the liquid, and subscripts x and z denote partial derivatives $\partial/\partial x$ and $\partial/\partial z$, respectively.

These equations are subject to the following boundary conditions:

$$x=-\frac{1}{2}L, \qquad u=w=0, \qquad T=T_L, \tag{2.5}$$

$$x=\frac{1}{2}L, \qquad u=w=0, \qquad T=T_R, \tag{2.6}$$

$$z=0, \qquad u=w=0, \qquad T_z=0, \tag{2.7}$$

$$z=h(x), \qquad w=uh_x, \tag{2.8}$$

$$s_{ij}n_jn_i=2\sigma\Lambda, \tag{2.9}$$

$$S_{ij}n_jt_i=\sigma_{sx}, \tag{2.10}$$

$$kT_n+h_g[T-T_g(x)]=0. \tag{2.11}$$

In the above, the subscripts n and sx denote normal and tangential derivatives at the interface, respectively.

Equation (2.8) is the kinematic condition at the liquid-gas interface. The stress balances at the interface in the normal direction and tangential in the x-direction are given by equations (2.9) and (2.10). The jump in the normal stress across the interface is balanced by the surface tension times the mean curvature, the jump in the x-component of the shear stress at the interface is balanced by the x-component of the surface tension gradient. In these equations, the s_{ij} are the components of the stress tensor of the liquid defined by

$$s_{ij}=-p\delta_{ij}+2\mu\epsilon_{ij}\ , \quad \epsilon_{ij}=\frac{1}{2}(u_{i,j}+u_{j,i}) \quad i,j=1,2, \tag{2.12}$$

where δ_{ij} is the Kronecker delta and $\mathbf{u}=u\mathbf{i}+w\mathbf{k}$ is the velocity vector, with $\mathbf{i}$ and $\mathbf{k}$ being unit vectors in the x and z direction, respectively. The unit outward normal vector $\mathbf{n}$, and the unit tangent vector $\mathbf{t}$ are defined as follows:

$$n=(-h_x\mathbf{i}+\mathbf{k})/N, \tag{2.13}$$

$$t=(\mathbf{i}+h_x\mathbf{k})/N, \tag{2.14}$$

with

$$N=(1+h_x^2)^{1/2}. \tag{2.15}$$

The mean curvature Λ of the interface in equation (2.9) has the definition

$$\Lambda=\frac{1}{2}\frac{h_{xx}}{N^3}. \tag{2.16}$$

The thermal boundary condition at the interface is given by equation (2.11) in which k is the thermal conductivity of the liquid, h_g is the heat transfer coefficient in the gas and $T_g(x)$ is the temperature in the gas phase. The thermal boundary condition presumes that the gas temperature $T_g(x)$ is known and that the heat transport at the liquid-gas interface can be described by using a heat transfer coefficient h_g.

Apart from boundary conditions (2.5)-(2.11), the liquid must also satisfy the mass conservation constraint. Since the liquid is assumed to be incompressible, its total volume V must remain constant, i.e.,

$$V=\int_{-\frac{L}{2}}^{\frac{L}{2}} h(x)\,dx=const. \tag{2.17}$$

A linear equation of state will be used for the surface tension. Specifically, the linear equation takes the form of:

$$\sigma(T)=\sigma_0-\gamma(T-T_*), \tag{2.18}$$

where σ_0 is the surface tension of the liquid at the reference temperature T_*, and the constant γ is the negative of the derivative of the surface tension with respect to temperature.

Finally, to close the problem, the type of contact between the free surface and the end walls has to be specified. There are several possible contact conditions describing either moving or fixed contact lines. Modelling of motion of a fluid in the neighbourhood of a contact line leads to a stress discontinuity at the contact point. The following two cases will be considered:

Case I. Fixed contact points which describes the case of static (fixed) contact lines. The liquid sticks to a sharp edge at the end walls with

$$h(-\frac{L}{2})=H_L, \tag{2.19}$$

$$h(\frac{L}{2})=H_R. \tag{2.20}$$

Case II. Fixed contact angles which describes the case of moving contact lines. A contact angle θ is prescribed at the contact point between the interface and the side wall, i.e.,

$$h_x(-\frac{L}{2}) = \tan\theta_L , \tag{2.21}$$

$$h_x(\frac{L}{2}) = -\tan\theta_R . \tag{2.22}$$

2.2 Scaling

It is convenient to convert the above governing equations (2.1)-(2.4) to non-dimensional forms. The problem is scaled in terms of lubrication-type variables by introducing the following primed quantities:

$$\begin{aligned} &x=Hx', \quad z=Hz', \quad h=Hh', \quad u=u_*u', \quad w=u_*w', \\ &p=(\mu u_* L/H^2)p', \quad T-T_*=\Delta T T', \quad \sigma=\sigma_0\sigma', \end{aligned} \tag{2.23}$$

$$u_* = \gamma \Delta T/\mu , \tag{2.24}$$

$$T_* = \frac{1}{2}(T_{max}+T_{min}) , \tag{2.25}$$

$$\Delta T = T_{max} - T_{min} , \tag{2.26}$$

$$A = \frac{H}{L} , \tag{2.27}$$

$$\sigma' = 1 - \frac{\gamma(T-T_*)}{\sigma_0} . \tag{2.28}$$

Here, T_{max} and T_{min} denote a measure of the maximum and minimum of the interface temperature, respectively.

With the above scales, the dimensionless governing equations (with the primes dropped) can be written in the form:

$$u_x+w_z=0, \tag{2.29}$$

$$-p_x+u_{xx}+u_{yy}=Re(uu_x+wu_z), \tag{2.30}$$

$$-p_z+w_{xx}+w_{zz}=Re(uw_x+ww_z), \tag{2.31}$$

$$T_{xx}+T_{zz}=Ma(uT_x+wT_z). \tag{2.32}$$

The Reynolds number Re and the Marangoni number Ma appearing in the above equations have the following definitions

$$Re=\frac{u_* H}{\nu}, \tag{2.33}$$

$$Ma=\frac{u_* H}{\kappa}, \tag{2.34}$$

The Prandtl number

$$Pr=\frac{\nu}{\kappa} \tag{2.35}$$

may be recounted from

$$Pr=\frac{Ma}{Re}. \tag{2.36}$$

The boundary conditions (2.5)-(2.11) become

$$x=-\frac{L}{2}, \qquad u=w=0, \quad T=T_L, \tag{2.37}$$

$$x=\frac{L}{2}, \qquad u=w=0, \quad T=T_R, \tag{2.38}$$

$$z=0, \qquad u=w=0, \quad T_z=0, \tag{2.39}$$

$$z=h(x), \qquad w=uh_x, \tag{2.40}$$

$$-p+\frac{2}{1+h_x^2}\left[w_z-h_xu_z+h_x(h_xu_x-w_x)\right]=\frac{h_{xx}}{Ca\,(1+h_x^2)^{3/2}}(1-CaT), \tag{2.41}$$

$$(1-h_x^2)\,(u_z+w_x)+2h_x(w_z-u_x)=-(1+h_x^2)^{1/2}(T_x+h_xT_z), \tag{2.42}$$

$$\frac{T_z-h_xT_x}{(1+h_x^2)^{1/2}}+Bi\left[T-T_g(x)\right]=0. \tag{2.43}$$

In equation (2.41), Ca is the capillary number, and is defined as

$$Ca=\frac{\mu u_*}{\sigma_0}. \tag{2.44}$$

The capillary number can be interpreted as a measure of the degree of deformation of the free surface induced by thermocapillary effects; the limit of the capillary number approaching zero implies that deformation becomes asymptotically small.

In equation (2.43), Bi stands for the Biot number which is defined as

$$Bi=\frac{Hh_g}{k} \tag{2.45}$$

and measures the heat transport between the gas and liquid phases.

The dimensionless forms of (2.17) is as follows:

$$\int_{-\frac{1}{2}L}^{\frac{1}{2}L} h(x)\,dx=\overline{V}. \tag{2.46}$$

$$\overline{V}=\frac{V}{HL}. \tag{2.47}$$

The contact conditions are as follows:

Case I.

$$h(-\frac{L}{2})=1, \tag{2.48}$$

$$h(\frac{L}{2})=1. \tag{2.49}$$

Case II.

$$h_x(-\frac{L}{2})=\tan\theta_L. \tag{2.50}$$

$$h_x(\frac{L}{2})=-\tan\theta_R. \tag{2.51}$$

Equations (2.29)-(2.51) constitute a so-called free-boundary problem, where the location of the interface has to be determined as part of the solution. Any form of this solution

valid for arbitrary values of parameters can be found only numerically. One of main difficulties associated with the numerical solution of the above equations is the lack of boundary conditions for pressure. Since a streamfunction - vorticity formulation can avoid this difficulty, it was chosen in this study.

2.3 Formulation in Terms of Streamfunction and Vorticity

The streamfunction, ψ, and vorticity, ω, are defined as:

$$u=\psi_z\ , \quad w=-\psi_x, \tag{2.52}$$

$$\omega=-\psi_{zz}-\psi_{xx}. \tag{2.53}$$

Substitution of (2.52)-(2.53) into (2.32) leads to the following form of the governing equations:

$$\omega=-\psi_{zz}-\psi_{xx}, \tag{2.54}$$

$$\omega_{zz}+\omega_{xx}=Re\,(\psi_z\omega_x-\psi_x\omega_z)\ , \tag{2.55}$$

$$T_{xx}+T_{zz}=Ma\,(\psi_z T_x-\psi_x\ _z)\ . \tag{2.56}$$

The boundary conditions become

$$x=-\frac{L}{2}, \qquad \psi=\psi_x=0, \quad T=T_L, \tag{2.57}$$

$$x=\frac{L}{2}, \qquad \psi=\psi_x=0, \quad T=T_R. \tag{2.58}$$

$$z=0, \qquad \psi=\psi_z=0, \quad T_z=0, \tag{2.59}$$

$z=h(x)$:

$$\psi_x=-h_x\psi_z, \tag{2.60}$$

$$-p+\frac{2}{1+h_x^2}\left[(h_x^2-1)\psi_{xz}+h_x(\psi_{xx}-\psi_{zz})\right]=\frac{h_{xx}}{Ca(1+h_x^2)^{3/2}}(1-CaT), \tag{2.61}$$

$$(1-h_x^2)(\psi_{zz}-\psi_{xx})-4h_x\psi_{xz}=-(1+h_x^2)^{1/2}(T_x+T_zh_x), \tag{2.62}$$

$$\frac{T_z-h_xT_x}{(1+h_x^2)^{1/2}}+Bi[T-T_g(x)]=0. \tag{2.63}$$

The numerical algorithm developed for the solution of the above problem will be discussed in the next chapter.

CHAPTER 3

NUMERICAL METHODS

3.1 Introduction

The existing literature on free boundary problems as applied to the thermocapillary problem in fluid mechanics is quite extensive. By far, the majority of papers are concerned with asymptotic or limiting cases in which the shape of the interface, while unknown, deviates only slightly from some predefined configurations. In the case of the cavity problem, for example, a number of authors have used the so-called "domain perturbation" method to solve for the first (infinitesimal) deviations from a flat interface in a variety of flows (Sen & Davis, 1982; Sen, 1986; Rivas & Ostrach, 1989; Hadid & Roux, 1992; Laure et. al., 1990; Hadid & Roux, 1990; Carpenter & Homsy, 1990; Rivas, 1990; Zebib et.al., 1985; Cowley & Davis, 1983). These so-called domain perturbation or small deformation theories will be discussed in Section 3.5.1 When the deformation is not expected to be small, the solution can rarely be obtained analytically. The problems require a fully numerical method of solution. The difficulties in the problem are as follows:

(i) The interfacial boundary conditions are nonlinear and of a mixed type, and they involve pressure which has to be evaluated accurately at the boundary;

(ii) The field equations are nonlinear;

(iii) The solution domain has an irregular, constantly changing geometry. Its connectivity may change, e.g., the breakup of a liquid layer;

(iv) The interface may undergo large distortions;

(v) Tracking the shape of the interface, i.e., its curvature, demands high accuracy to account properly for the surface tension effects; and

(vi) Presence of singularities at the contact points poses serious difficulties for accurate determination of the location of the boundary.

Most of the difficulties described above can be attributed to the presence of a free boundary, the type of boundary conditions, and the physical processes taking place at the interface. The numerical implementation of the interfacial boundary conditions on a free interface is therefore quite challenging.

An "ideal" method for the free boundary problems would be a method that is capable of accurate representation of an arbitrarily large deformation of the interface. Several

approaches have been tried with a mixed degree of success. A detailed review of different numerical methods can be found in Floryan and Rasmussen (1989).

The available algorithms can be categorized in general as Eulerian, Lagrangian, and Mixed, i.e., Eulerian-Lagrangian. Lagrangian methods are characterized by a coordinate system that moves with the fluid. Accordingly, each computational cell always contains the same fluid element. The two main problems with the Lagrangian methods are mesh tangling and numerical inaccuracy due to highly irregular meshes. In contrast, Eulerian methods employ a coordinate system that either is stationary in the laboratory reference frame or is moving in a certain prescribed manner in order to accommodate the continually changing shape of the solution domain. The fluid travels between different computational cells even when the grid moves, because the grid movements are not related to the motion of the fluid. The main advantage of this approach is that the fluid can undergo arbitrarily large distortions without loss of accuracy, in contrast to the Lagrangian methods. The Eulerian algorithms are believed to be the most mature and are most widely used. While many new concepts have been proposed in the context of Lagrangian algorithms, their usefulness remains to be demonstrated for viscous flows. Therefore, only Eulerian methods are described here.

The Eulerian method can be divided into four main types:

(i) fixed grid methods;

(ii) adaptive grid methods;

(iii) mapping methods; and

(iv) special methods.

(i) Fixed grid methods

In the fixed grid method, the grid is fixed in the physical domain. Since in general the moving interface does not coincide with a grid line, some special procedures must be included to handle such situations. The main advantages of the fixed grid methods are: (i) the interfaces may undergo large deformation without loss of accuracy; (ii) it is relatively straightforward to handle multiple interfaces. The main disadvantage is the difficulty in calculating the position of the interface accurately. More detailed discussions can be found in references such as those by Hyman (1984a) and Laskey et al. (1987) and Hirt and Nichols (1981a).

(ii) Adaptive grid methods

Adaptive (moving) grid methods alter the computational grid so that the interface always coincides with one of the grid lines. The interface is then a well-defined continuous

curve and information regarding its location, orientation, and curvature is readily available. Techniques for the construction of boundary conforming coordinates are described by Thompson et al. (1985).

(iii) Mapping methods

In the mapping methods, a mapping of the independent variables is used to transform the irregularly shaped flow domain onto a regularly shaped computational domain before discretization of the governing equations and boundary conditions. The problem is then a fixed domain problem. The mapping function appears explicitly as one of the unknown functions in the system of governing equations and has to be determined together with the field variables. Some of the adaptive grid methods can be interpreted as mapping methods since numerical grid generation is similar to determination of the mapping function. The method maintains sharp resolution of the interface; however, its applicability is limited to a class of geometries that do not lead to a singular mapping. Shokoohi and Elrod (1987, 1990) used a coordinate mapping technique in analysis of capillary break-up of a cylindrical jet, in which a special discretization technique was used which resulted in high usage of computing resources. Christon and Volkov (1985) investigated the steady viscous axisymmetric flow passing a stationary deformable bubble with surface

tension using a streamfunction-vorticity formulation. Loh and Rasmussen (1987) presented a finite-difference procedure for two-dimensional unsteady viscous free surface flows with surface tension. They used a primitive variable formulation and transformed the flow domain onto a fixed rectangular computational domain. The procedure consisted of predicting a new shape of the interface using explicit time discretization of the kinematic condition and iterative determination of the actual flow field and the shape of the interface through a Picard iteration on an implicit form of the kinematic condition.

The choice of a particular method depends to a large extent on the flow problem at hand. In the fixed grid methods, the interface travels through a fixed grid which leads to difficulties in accurate determination of the location between the grid points. However, the location of the interface is crucial in the present problem because it affects modelling of normal viscous stress and surface tension effects at the interface. The adaptive grid methods can accurately model interfacial effects, but the cost of calculations may be very high due to repetitive numerical coordinate generations. It is also difficult to estimate the overall error due to combination of errors originating from the numerically generated grid and from the discretized field equations. Since the mapping method is more computationally efficient and

accurate, it has been selected as the basis for the present study.

The above methods can effectively handle free boundary problems where deformations are small. For problems with large deformations, the above methods can produce results that are reasonable from a physical viewpoint, but their accuracy is uncertain. For example, Strani and Piva (1982) used a mapping method in the analysis of thermocapillary convection in which primitive variable formulations were used. It is difficult to assess the accuracy of their solution, especially for large deformations, since only results for grids 10x10 were given. Chen et al. (1990) considered the same problem, but used numerically generated boundary fitted coordinates. Yet the issue of the effective accuracy of the algorithm was not discussed.

The main goal of this chapter is to provide an accurate and reliable algorithm for simulation of free capillary surfaces with large interfacial deformation. Stream-function-vorticity formulation is used in the actual calculations. The governing equations are discretized with the standard second-order finite-difference techniques. Geometry of the solution domain is regularized using coordinate transformation method.

3.2 Coordinate Transformation Method

The flow problem equations (2.54) to (2.63) were developed on an irregular solution domain. Introduction of the following coordinate transformation

$$\xi = x, \quad \eta = \frac{z}{h(x)}, \tag{3.1}$$

transforms the originally irregular solution domain (x,z) into a rectangular domain in the (ξ,η) plane, as shown in Figure. 3.1.

This mapping results in the following transformation of the variables and their derivatives:

$$\frac{\partial f}{\partial x} = \frac{\partial f}{\partial \xi} - \frac{\eta}{h}\frac{\partial h}{\partial \xi}\frac{\partial f}{\partial \eta}, \tag{3.2}$$

$$\frac{\partial f}{\partial z} = \frac{1}{h}\frac{\partial f}{\partial \eta}, \tag{3.3}$$

$$\frac{\partial^2 f}{\partial x^2} = \frac{\partial^2 f}{\partial \xi^2} - \frac{2h_\xi \eta}{h}\frac{\partial^2 f}{\partial \xi \partial \eta} + \frac{h_\xi^2 \eta^2}{h^2}\frac{\partial^2 f}{\partial \eta^2} + \frac{(2h_\xi^2 - h_{\xi\xi}h)\eta}{h^2}\frac{\partial f}{\partial \eta}, \tag{3.4}$$

$$\frac{\partial^2 f}{\partial z^2} = \frac{1}{h^2}\frac{\partial^2 f}{\partial \eta^2}. \tag{3.5}$$

In the above, f stands for T, ψ, and ω. Thus, the governing equations (2.54) to (2.56) are transferred to the following forms:

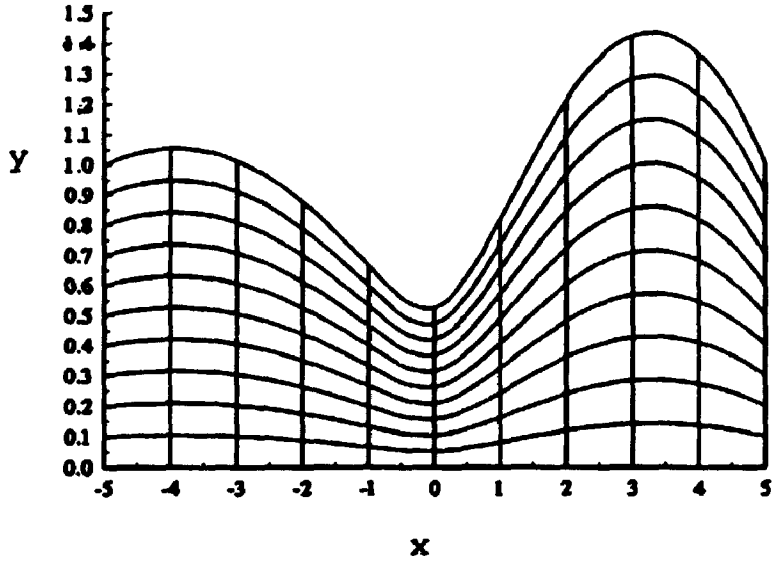

Physical Plane

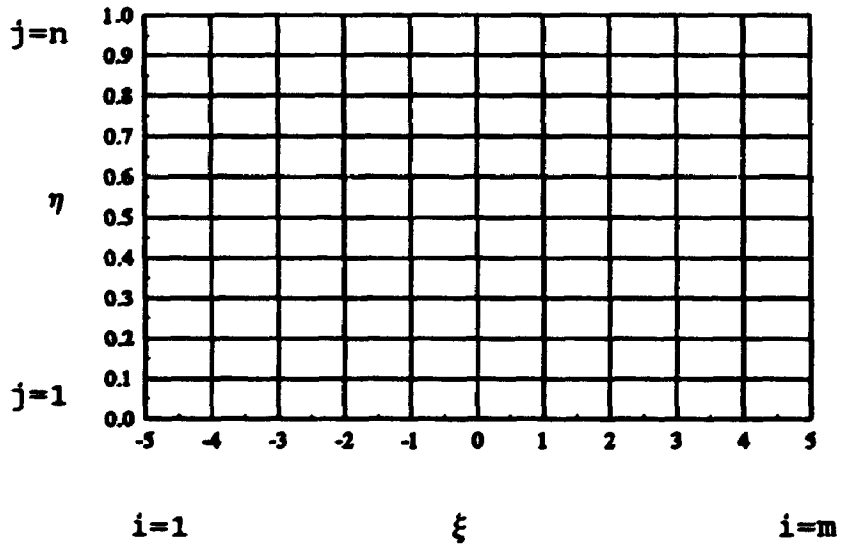

Computational Plane

Figure 3.1 Ideogram of coordinate transformation.

$$\nabla^2\psi=-\omega, \tag{3.6}$$

$$\nabla^2\omega=\frac{Re}{h}(\psi_\eta\omega_\xi-\psi_\xi\omega_\eta), \tag{3.7}$$

$$\nabla^2T=\frac{Ma}{h}(\psi_\eta T_\xi-\psi_\xi T_\eta), \tag{3.8}$$

where

$$\nabla^2 f=\frac{\partial^2 f}{\partial\xi^2}-\frac{2h_\xi\eta}{h}\frac{\partial^2 f}{\partial\xi\partial\eta}+\frac{h_\xi^2\eta^2}{h^2}\frac{\partial^2 f}{\partial\eta^2}+\frac{(2h_\xi^2-h_{\xi\xi}h)\eta}{h^2}\frac{\partial f}{\partial\eta}+\frac{1}{h^2}\frac{\partial^2 f}{\partial\eta^2}. \tag{3.9}$$

The transformed boundary conditions are:

$\xi=-1/2L$: $\psi=\psi_\xi=0, \quad T=T_L,$ (3.10)

$\xi=1/2L$: $\psi=\psi_\xi=0, \quad T=T_R,$ (3.11)

$\eta=0$: $\psi=\psi_\eta=0, \quad T_\eta=0,$ (3.12)

$\eta=1$: $\psi=0,$ (3.13)

$$\frac{(1+h_\xi^2)^2}{h^2}\psi_{\eta\eta}-\frac{2h_\xi}{h}(1+h_\xi^2)\psi_{\xi\eta}+[(1-h_\xi^2)hh_{\xi\xi}+(1+h_\xi^2)2h_\xi]^2\frac{\psi_\eta}{h^2} \tag{3.14}$$
$$=-(1+h_\xi^2)^{1/2}T_\xi,$$

$$\frac{(1+h_\xi)^{1/2}}{h}T_\eta-\frac{h_\xi}{(1+h_\xi^2)^{1/2}}T_\xi+Bi(T-T_g)=0, \tag{3.15}$$

$$-p+\frac{2}{1+h_\xi^2}[-\frac{1+h_\xi^2}{h}\psi_{\xi\eta}+\frac{h_\xi}{h^2}(h_\xi^2-h_{\xi\xi}h+1)\psi_\eta]=\frac{h_{\xi\xi}(1-CaT)}{Ca(1+h_\xi^2)^{3/2}}. \tag{3.16}$$

It is possible to devise other mappings of a similar form to deal with the problem at hand, for example mapping onto a unit circle, or mapping of only a part of the solution domain. These mappings are not general. Consequently, they cannot deal with completely arbitrary geometries. However, they can handle a sufficiently large class of problems. The advantages of such mappings can be summarized as follows:

(i) They are given analytically.

(ii) They avoid numerical coordinate generation.

(iii) They lead to a simpler form of the governing equations when compared to the form appropriate for the general curvilinear systems.

(iv) They can deal with almost arbitrary geometries.

Nevertheless, they have the following limitations:

(i) They are limited to a single valued function h(x) describing the location of the interface.

(ii) They become singular when the slope of the interface becomes vertical.

3.3 Finite-Difference Discretization

3.3.1 Finite-Difference Discretization

After the mapping (3.1), the computational domain has the form of a rectangular domain, therefore the standard second-order finite-difference discretizations can be used. A rectangular computational grid of uniform size $\Delta\xi$, $\Delta\eta$ in the ξ, η directions is considered, with grid lines being parallel to the ξ and η axes such that the grid fits exactly the geometry of the computational domain, in which the side and bottom walls and the interface become certain grid lines. The finite-difference formulas for an interior point are (Figure. 3.2):

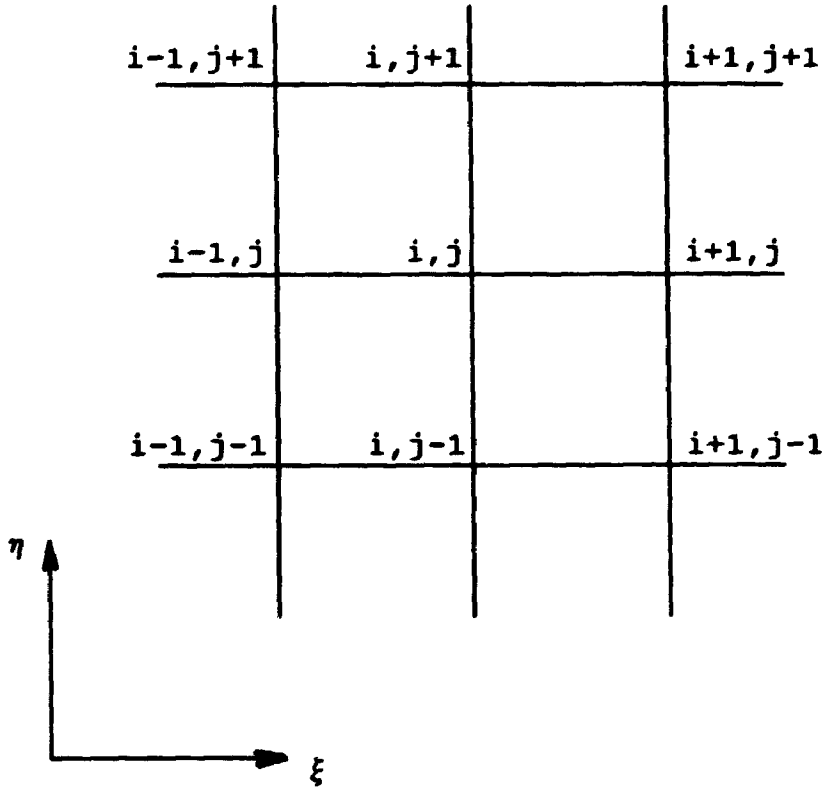

Figure 3.2 Sketch of a typical computational molecule.

$$\frac{\partial f}{\partial \xi}\Big|_{i,j} = \frac{f_{i+1,j} - f_{i-1,j}}{2\Delta\xi} + O(\Delta\xi^2), \tag{3.17}$$

$$\frac{\partial^2 f}{\partial \xi^2}\Big|_{i,j} = \frac{f_{i+1,j} - 2f_{i,j} + f_{i-1,j}}{\Delta\xi^2} + O(\Delta\xi^2), \tag{3.18}$$

$$\frac{\partial f}{\partial \eta}\Big|_{i,j} = \frac{f_{i+1,j} - f_{i-1,j}}{2\Delta\eta} + O(\Delta\eta^2), \tag{3.19}$$

$$\frac{\partial^2 f}{\partial \eta^2}\Big|_{i,j} = \frac{f_{i+1,j} - 2f_{i,j} + f_{i-1,j}}{\Delta\eta^2} + O(\Delta\eta^2), \tag{3.20}$$

$$\frac{\partial^2 f}{\partial \xi \partial \eta}\Big|_{i,j} = \frac{f_{i+1,j+1} - f_{i+1,j-1} - f_{i-1,j+1} + f_{i-1,j-1}}{4\Delta\xi\Delta\eta} + O(\Delta\xi^2) + O(\Delta\eta^2), \tag{3.21}$$

where $f_{i,j}$ denotes the value of function f at grid point (i,j).

At the boundary points, one-sided derivative approximations were employed. For instance, the first-order derivatives of f, with respect to η at η=0 and η=1, are:

$$\frac{\partial f}{\partial \eta}\Big|_{\eta=0} = \frac{-3f_{i,1} + 4f_{i,2} - f_{i,3}}{2\Delta\eta} + O(\Delta\eta^2), \tag{3.22}$$

$$\frac{\partial f}{\partial \eta}\Big|_{\eta=1} = \frac{3f_{i,N} - 4f_{i,N-1} + f_{i,N-2}}{2\Delta\eta} + O(\Delta\eta^2), \tag{3.23}$$

where N stands for the total number of grid points in the η direction. The first-order derivative of f with respect to ξ can be constructed similarly. The mixed derivative approximation has the form:

$$\frac{\partial^2 f}{\partial \xi \partial \eta}\Big|_{\eta=1} = \frac{3[f_{i+1,N}-f_{i-1,N}]-4[f_{i+1,N-1}-f_{i-1,N-1}]+f_{i+1,N-2}-f_{i-1,N-2}}{4\Delta\xi\Delta\eta} \qquad (3.24)$$
$$+O(\Delta\xi^2)+O(\Delta\eta^2).$$

In the above, equations (3.17) to (3.23) are standard second-order finite-difference discretizations. Equation (3.24) needs special attention. The details of the derivation of (3.24) are given in Appendix A.

Equations (3.6) to (3.8) can be written after discretization in the following difference equations:

$$\begin{aligned} &-2(A_1+A_2)\psi_{i,j}+A_1\psi_{i+1,j}-A_3\psi_{i+1,j+1}+(A_2+A_4)\psi_{i,j+1}+A_3\psi_{i-1,j+1} \\ &+A_1\psi_{i-1,j}-A_3\psi_{i-1,j-1}+(A_2-A_4)\psi_{i,j-1}+A_3\psi_{i+1,j-1}+\omega_{i,j}=0, \end{aligned} \qquad (3.25)$$

$$\begin{aligned} &-2(A_1+A_2)\omega_{i,j}+[A_1-ReA_5(\psi_{i,j+1}-\psi_{i,j-1})]\omega_{i+1,j}-A_3\omega_{i+1,j+1}+ \\ &[A_2+A_4+ReA_5(\psi_{i+1,j}-\psi_{i-1,j})]\omega_{i,j+1}+A_3\omega_{i-1,j+1}+ \\ &[A_1+ReA_5(\psi_{i,j+1}-\psi_{i,j-1})]\omega_{i-1,j}-A_3\omega_{i-1,j-1}+ \\ &[A_2-A_4-ReA_5(\psi_{i+1,j}-\psi_{i-1,j})]\omega_{i,j-1}+A_3\omega_{i+1,j-1}=0, \end{aligned} \qquad (3.26)$$

$$\begin{aligned} &-2(A_1+A_2)T_{i,j}+[A_1-MaA_5(\psi_{i,j+1}-\psi_{i,j-1})]T_{i+1,j}-A_3T_{i+1,j+1}+ \\ &[A_2+A_4+MaA_5(\psi_{i+1,j}-\psi_{i-1,j})]T_{i,j+1}+A_3T_{i-1,j+1}+ \\ &[A_1+MaA_5(\psi_{i,j+1}-\psi_{i,j-1})]T_{i-1,j}-A_3T_{i-1,j-1}+ \\ &[A_2-A_4-MaA_5(\psi_{i+1,j}-\psi_{i-1,j})]T_{i,j-1}+A_3T_{i+1,j-1}=0, \end{aligned} \qquad (3.27)$$

where

$$A_1=\frac{1}{\Delta\xi^2}, \quad A_2=\frac{(1+\eta^2 h_\xi^2)}{h^2\Delta\eta^2}, \quad A_3=\frac{\eta h_\xi}{2h\Delta\xi\Delta\eta},$$

$$A_4=\frac{\eta(2h_\xi^2-hh_{\xi\xi})}{2h^2\Delta\eta}, \qquad A_5=\frac{1}{4h\Delta\psi\Delta\eta}.$$

3.3.2 Boundary Conditions

The boundary conditions for equations (3.25) to (3.27) are given by equations (3.10) to (3.16). For equation (3.25), the values of ψ are known at all grid points on the solid walls and along the interface. For equation (3.26), a boundary condition for ω is required at grid points on the solid walls. Here, a second-order approximation is used

$$\omega_{1,j}=-\frac{8\psi_{2,j}-\psi_{3,j}}{2\Delta\xi^2}, \tag{3.28}$$

$$\omega_{M,j}=-\frac{1}{2\Delta\xi^2}(8\psi_{M-1,j}-\psi_{M-2,j}), \tag{3.29}$$

$$\omega_{i,1}=-\frac{1}{h^2}\frac{8\psi_{i,2}-\psi_{i,3}}{2\Delta\eta^2}. \tag{3.30}$$

The boundary condition at the interface is obtained by substituting equation (3.14) into equation (3.6) resulting in

$$\omega=\frac{(1+h_\xi^2)^{1/2}T_\xi h+2h_{\xi\xi}\psi_\eta}{h(1+h_\xi^2)} \tag{3.31}$$

where T_ξ is evaluated using the standard central difference approximation, and ψ_η is determined using one-sided difference

approximation. Both T_ξ and ψ_η have to be updated during the iteration process. For the energy equation (3.8), values of T are known at the side walls. At the remaining two boundaries, T is determined from the discretized boundary conditions (3.10) and (3.15). All discretization formulas are second-order accurate.

3.3.3 Pressure Solution

One of the advantages of working with the stream-function-vorticity formulation is that the number of variables is reduced. Pressure is eliminated from the momentum equations. Since the deformation problem involves the pressure at the interface, it is necessary to extract the pressure from the values of ψ and ω.

The common method to obtain pressure is to solve the Poisson equation for pressure obtained from the Navier-Stokes equations. The Poisson equation for pressure is identical to the equation for stream-function. Since the pressure at the interface is of primary interest, the following simpler approach is adopted.

From equations (2.30) and (2.31), after introducing the stream-function, ψ, and vorticity, ω, and mapping, it is easy to write

$$p_\xi = h_\xi \omega_\xi - \frac{1+h_\xi^2}{h}\omega_\eta - \frac{Re}{h^2}\psi_\eta\left[(1+h_\xi^2)\psi_{\xi\eta} + \frac{h_\xi}{h}(h_{\xi\xi}h - h_\xi^2 - 1)\psi_\eta\right] \quad (3.32)$$

at the interface. The pressure distribution at the interface can be obtained by starting at an arbitrary point with an arbitrary pressure level (constant of integration) and numerically integrating equation (3.32). In the present study, the integration is done by using the trapezoidal rule in the $\pm\xi$ directions beginning at $\xi=0$. The mixed derivative of the stream-function at the interface is evaluated according to formula (3.24). Other flow quantities are evaluated using standard one sided or central second-order finite-difference approximations.

3.3.4 Deformation Problem

For flows with fixed boundaries, three boundary conditions are given at each boundary (stream-function, vorticity, and temperature). For flows with a free interface an extra boundary condition should be given at the interface and it is used to determine the location of the interface. The procedure used in the present study is to use a trial location of the interface, and solve the field equations using only three of the four boundary conditions. The fourth condition is then used to adjust the location of the interface. The procedure is repeated until convergence is achieved. This

raises the question of which of the four conditions should be used for the determination of the interface. The choice of the boundary conditions that are used to adjust the interface depends strongly on the relative strength of the surface tension as measured by the capillary number Ca. Experience shows that when the surface tension dominates (Ca is less than unity), iteration using the normal stress condition converges while iteration using the kinematic condition eventually diverges. As the capillary number Ca is increased, the performances are reversed (Silliman and Scriven, 1980). In the present case, the surface tension dominates, therefore, the normal stress condition is chosen to adjust the interface.

The normal stress boundary condition is re-written as

$$p-2(1+h_\xi^2)^{-1}\left[-\frac{1+h_\xi^2}{h}\psi_{\xi\eta}+\frac{h_\xi}{h^2}(h_\xi^2-h_{\xi\xi}h+1)\psi_\eta\right]+\frac{h_{\xi\xi}}{(1+h_\xi^2)^{3/2}Ca}(1-CaT)=0. \tag{3.33}$$

Pressure and shape of the interface are represented by

$$p=p_sCa^{-1}+p_0+K, \tag{3.34}$$

$$h=h_0+h_1, \tag{3.35}$$

$$p_0=-\frac{h_{0\xi\xi}}{(1+h_{0\xi}^2)^{3/2}}, \tag{3.36}$$

where h_0 denotes the known shape of the isothermal interface corresponding to the known volume of the liquid (2.46), P_s the known pressure of the isothermal liquid, h_1 denotes the change of the shape of the interface due to non-isothermal effects, p_0 stands for the pressure associated with the thermocapillary convection and determined numerically from the solution of the field equations, and K is an arbitrary constant that can be present in the pressure field.

Equation (3.33) can be written for any grid point along the interface in the form

$$F_i(h_i, h_{\xi i}, h_{\xi\xi i}, K) = 0, \tag{3.37}$$

where h_i, $h_{\xi i}$, $h_{\xi\xi i}$, i=1,...M, denote values of h_1, $h_{1\xi}$, $h_{1\xi\xi}$ at the grid points i, with i=1 corresponding to the left contact point, and all the remaining quantities being known. Derivatives in equation (3.37) are approximated using the standard central-difference approximations leading to an equation of the form

$$F_i(h_{i-1}, h_i, h_{i+1}, K) = 0, \tag{3.38}$$

which is then linearized as follows

$$\begin{aligned} F_i(\hat{h}_{i-1}^{(k+1)}, \hat{h}_i^{(k+1)}, \hat{h}_{i+1}^{(k+1)}, K^{(k+1)}) = & F_i(\hat{h}_{i-1}^{(k)}, \hat{h}_i^{(k)}, \hat{h}_{i+1}^{(k)}, K^{(k)}) \\ & + \frac{\partial F_i}{\partial \hat{h}_{i-1}} (\hat{h}_{i-1}^{(k+1)} - \hat{h}_{i-1}^{(k)}) + \frac{\partial F_i}{\partial \hat{h}_i} (\hat{h}_i^{(k+1)} - \hat{h}_i^{(k)}) \\ & + \frac{\partial F_i}{\partial \hat{h}_{i+1}} (\hat{h}_{i+1}^{(k+1)} - \hat{h}_{i+1}^{(k)}) + (K^{(k+1)} - K^{(k)}) = 0. \end{aligned} \tag{3.39}$$

In the above equation, superscripts denote iteration count and derivatives are evaluated analytically at $\hat{h}_{i-1}^{(k)}$, $\hat{h}_i^{(k)}$, $\hat{h}_{i+1}^{(k)}$.

Hence, equation (3.39) can be rewritten as

$$A_i\hat{h}_{i-1}^{(k+1)}+B_i\hat{h}_i^{(k+1)}+C_i\hat{h}_{i+1}^{(k+1)}+K^{(k+1)}=M_i^{(k)}, \qquad (3.40)$$

where

$$A_i=\frac{\partial F_i}{\partial \hat{h}_{i-1}}, \qquad B_i=\frac{\partial F_i}{\partial \hat{h}_i}, \qquad C_i=\frac{\partial F_i}{\partial \hat{h}_{i+1}},$$

$$M_i^{(k)}=\frac{\partial F_i}{\partial \hat{h}_{i-1}}\hat{h}_{i-1}^{(k)}+\frac{\partial F_i}{\partial \hat{h}_i}\hat{h}_i^{(k)}+\frac{\partial F_i}{\partial \hat{h}_{i+1}}\hat{h}_{i+1}^{(k)}+K^{(k)}-F_i^{(k)}.$$

The actual derivation of equation (3.40) is done by using Maple, a symbolic language software developed by the University of Waterloo. Note that such an equation can be written for each grid point along the interface. The above system of the linear algebraic equations is then closed by using the volume constraint (2.46) and contact conditions (2.48) to (2.51). Equation (2.46) takes the form

$$\int_{-\frac{L}{2}}^{\frac{L}{2}} h_1 d\xi = 0 \qquad (3.41)$$

and is discretized using the trapezoidal rule. The matrix of coefficients for the complete system, in the case of fixed contact point conditions, has the form:

$$\begin{bmatrix} B_2 & C_2 & . & . & & & & & & N_2 \\ A_3 & B_3 & C_3 & . & & & & & & N_3 \\ . & A_4 & B_4 & C_4 & & & & & & N_4 \\ & & & & & & & & & . \\ & & & & & & & & & . \\ & & & & A_{M-3} & B_{M-3} & C_{M-3} & & & N_{M-3} \\ & & & & . & A_{M-2} & B_{M-2} & C_{M-2} & & N_{M-2} \\ & & & & . & . & A_{M-1} & B_{M-1} & & N_{M-1} \\ D_2 & D_3 & D_4 & D_5 & . & D_{M-4} & D_{M-3} & D_{M-2} & D_{M-1} & . \end{bmatrix} \begin{bmatrix} \hat{h}_2 \\ \hat{h}_3 \\ \hat{h}_4 \\ \\ \\ \hat{h}_{M-3} \\ \hat{h}_{M-2} \\ \hat{h}_{M-1} \\ K \end{bmatrix} = \begin{bmatrix} M_2 \\ M_3 \\ M_4 \\ . \\ . \\ M_{M-3} \\ M_{M-2} \\ M_{M-1} \\ W \end{bmatrix} \quad (3.42)$$

where only the non-zero elements are shown, and

$$D_i=\Delta\xi, \qquad D_2=D_{M-1}=\frac{1}{2}\Delta\xi, \qquad W=V-\frac{1}{2}\Delta\xi(\hat{h}_1+\hat{h}_M), \quad N_i=1$$

where volumetric constraint V and locations of the end points, $\hat{h}_1$, $\hat{h}_M$ are kept non-zero, for generality purposes. A very efficient algorithm for the direct solution of equation (3.42) is described in Appendix B.

Change of the fixed contact point conditions to the fixed contact angle conditions leads to the approximation of the slope of the interface at the contact points in the form

$$h_{1\xi}=(-3\hat{h}_1+4\hat{h}_2-\hat{h}_3)/2\Delta\xi+O(\Delta\xi^2)=M_1 \qquad \xi=-\frac{1}{2}L \qquad (3.43)$$

$$h_{1\xi}=(3\hat{h}_M-4\hat{h}_{M-1}+\hat{h}_{M-2})/2\Delta\xi+O(\Delta\xi^2)=M_M \qquad \xi=\frac{1}{2}L \qquad (3.44)$$

and results in a matrix equation of the following structure

$$\begin{bmatrix} B_1 & C_1 & G_1 & . & & & & & N_1 \\ A_2 & B_2 & C_2 & . & & & & & N_2 \\ . & A_3 & B_3 & C_3 & & & & & N_3 \\ & & & & & & & & . \\ & & & & & & & & . \\ & & & & A_{M-2} & B_{M-2} & C_{M-2} & . & N_{M-2} \\ & & & & . & A_{M-1} & B_{M-1} & C_{M-1} & N_{M-1} \\ & & & & . & G_M & A_M & B_M & N_M \\ D_1 & D_2 & D_3 & D_4 & \ldots & D_{M-3} & D_{M-2} & D_{M-1} & D_M \end{bmatrix} \begin{bmatrix} \hat{h}_1 \\ \hat{h}_2 \\ \hat{h}_3 \\ \\ \\ \hat{h}_{M-2} \\ \hat{h}_{M-1} \\ \hat{h}_M \\ K \end{bmatrix} = \begin{bmatrix} M_1 \\ M_2 \\ M_3 \\ . \\ . \\ M_{M-2} \\ M_{M-1} \\ M_M \\ V \end{bmatrix} \qquad (3.45)$$

In the above matrix, A_i, B_i, C_i, D_i, N_i, M_i have the same meaning as before, with the exception of $M_2=M(\hat{h}_2)$, $M_{M-1}=M(\hat{h}_{M-1})$ and M_1, M_M are defined by equations (3.43) and (3.44) and $G_1=G_M=-1/2\Delta\xi^{-1}$. A very efficient algorithm for the direct solution of equation (3.45) is described in Appendix B.

3.4 The Numerical Iterative Procedure

The problem, from a numerical point of view, is to solve the equations (3.25), (3.26), (3.27), and (3.42) or (3.45) for the stream-function, vorticity, temperature fields and the mapping function subject to the conditions (3.10) to (3.16) and (3.28) to (3.31).

A simple approach which has been found to be efficient for solution of this coupled fluid-dynamics-mapping problem involves an iterative procedure that can be summarized as follows:

1. Choose an initial shape of the interface (usually taken as flat);
2. Take initial guesses for the stream-function, vorticity, and temperature (which are usually zero);
3. Obtain an approximation to the stream-function, vorticity, and temperature fields by carrying out a few iterations on equations (3.25), (3.26), and (3.27), subject to the boundary conditions (3.10) to (3.16) and (3.28) to (3.31);
4. Solve for pressure from equation (3.32);
5. Obtain an approximation to the interface by carrying out a few iterations on equation (3.42) or equation (3.45);
6. Check if: (i) the absolute values of the difference between two successive iterations for the stream-function, vorticity, temperature, and the interface at all grid points are less than a specified convergence criterion; and (ii) the absolute values of residual of the field equations at all grid points are less than a specified convergence criterion. In the present work, both convergence criteria were set to be 10^{-6}. Certain cases were additionally checked by reducing the criteria to $\varepsilon=10^{-8}$;

7. Return to step 3 and repeat until all equations and boundary conditions are satisfied.

The efficiency of the algorithm strongly depends on the specific values of the parameters present in the problem, such as Re, Ma, and Ca. The most efficient solution is obtained by carrying out one iteration on the flow field followed by one iteration of the interface. In all cases strong under-relaxation (0.01-0.1) is used when adjusting the shape of the interface. This under-relaxation parameter is usually decreased with an increasing value of Ca.

3.5. Testing of the Algorithm

In the previous sections, the algorithm for the solution of free boundary problems in which the interface takes an arbitrary shape and undergoes large deformations has been developed. It is of primary importance to determine the effective accuracy of the algorithm. In this section, the algorithm verification procedures will be described. First, a domain perturbation solution is developed to provide a test for the general algorithm; second, comparisons with other asymptotic solutions are made; third, the order of the grid convergence is checked; and lastly, the accuracy of the numerical results is discussed.

3.5.1. Domain Perturbation Solution

The domain perturbation solution is based on the assumption that the shape of the interface can be accurately estimated without solving the whole problem. Then, the actual location of the interface is described as a small deviation from the initial estimate. The complete moving boundary problem (2.29) to (2.32) splits into a convection problem with the known location of the interface (fixed boundary problem) followed by the evaluation of the (small) deformation of the interface.

Consider a solution of problem (2.29) to (2.32) in the asymptotic limit of Ca→0, which corresponds to the case of small surface tension variations as compared to mean surface tension. The interface is dominated by capillary forces with a thermocapillary effect producing only small distortions (Rybicki & Floryan, 1987).

The flow quantities are represented as

$$q=q_0+Caq_1+O(Ca^2), \tag{3.46}$$

$$p=Ca^{-1}p_s+p_0+Cap_1+O(Ca^2), \tag{3.47}$$

where q stands for u,w,T or h. Substitution of equations (3.46) and (3.47) into equations (2.29) to (2.32) results in: problem $O(Ca^{-1})$:

$$p_{sx}=0, \quad p_{sy}=0, \tag{3.48}$$

$$-p_s=\frac{h_{0xx}}{(1+h_{0x}^2)^{3/2}}, \tag{3.49}$$

$$\int_{-\frac{1}{2}L}^{\frac{1}{2}L} h_0 dx=V, \tag{3.50}$$

$$h_0(-\frac{1}{2}L)=H_L \text{ or } h_{0x}(-\frac{1}{2}L)=\tan\theta_L, \tag{3.51}$$

$$h_0(\frac{1}{2}L)=H_R \text{ or } h_{0x}(\frac{1}{2}L)=-\tan\theta_R. \tag{3.52}$$

problem $O(Ca^0)$:

flow problem:

$$u_{0x}+w_{0z}=0, \tag{3.53}$$

$$Re(u_0u_{0x}+w_0u_{0z})=-p_{0x}+u_{0xx}+u_{0zz}, \tag{3.54}$$

$$Re(u_0w_{0x}+w_0w_{0z})=-p_{0z}+w_{0xx}+w_{0zz}, \tag{3.55}$$

$$Ma(u_0T_{0x}+v_0T_{0z})=T_{0xx}+T_{0zz}, \tag{3.56}$$

$x=-L/2$: $$u_0=w_0=0, \quad T_0=T_L, \tag{3.57}$$

$x=L/2$: $$u_0=w_0=0, \quad T_0=T_R, \tag{3.58}$$

$y=h_0(x)$: $$w_0=u_0h_{0x}, \tag{3.59}$$

$$\frac{T_{0x}-h_{0x}T_{0z}}{(1+h_{0x}^2)^{1/2}}+Bi\,(T_0-T_g)=0, \tag{3.60}$$

$$(1-h_{0x}^2)\,(u_{0z}+w_{0x})+2h_{0x}(w_{0z}-u_{0x})=-(1+h_{0x}^2)^{1/2}(T_{0x}+h_{0x}T_{0z})\,. \tag{3.61}$$

deformation problem:

$$z=h_0(x):\qquad -p_0+\frac{2}{(1+h_{0x})^2}\,[h_{0x}^2u_{0x}+w_{0z}-h_{0x}(w_{0x}+u_{0z})\,]= \{h_{1xx}-h_{0xx}[\,T_0+\frac{3h_{0x}h_{1x}}{1+h_{0x}^2}\,]\}\frac{1}{(1+h_{0x}^2)^{3/2}}, \tag{3.62}$$

$$\int_{-\frac{1}{2}L}^{\frac{1}{2}L}h_1dx=0, \tag{3.63}$$

$$h_1(-\tfrac{1}{2}L)=0\quad or\quad h_{1x}(-\tfrac{1}{2}L)=0, \tag{3.64}$$

$$h_1(\tfrac{1}{2}L)=0\quad or\quad h_{1x}(\tfrac{1}{2}L)=0. \tag{3.65}$$

The leading-order problem (3.48) to (3.52) describes the initial approximation to the shape of the interface. It consists of the Young-Laplace equation (3.49) (describing isothermal capillary surfaces) whose solutions are given by a straight line or by an arc of a circle. The form of the straight line, and the radius of curvature and the location of the centre of curvature for a particular element of a circle are determined by the mass constraint (3.50) and the contact conditions (3.51) and (3.52). It is noted that equations

(3.50) and (3.52) have to satisfy consistency conditions for a solution to exist.

Equations (3.53) to (3.61) describe a flow problem for the known location $h_0(x)$ of the interface. The problem is closed without including the normal stress boundary condition at the interface. Equations (3.62) to (3.65) describe deformation $h_1(x)$ of the interface on the basis of the normal stress boundary condition (3.62) subject to volumetric constraint (3.63) and contact conditions (3.64) and (3.65).

(i) Flow Problem

Flow problem equations (3.53) to (3.61) are to be solved numerically on an irregular solution domain (as defined by $h_0(x)$). After application of the transformation

$$\xi = x, \quad \eta = \frac{y}{h_0(x)}, \tag{3.66}$$

the domain assumes a rectangular shape in the (ξ, η) plane and this permits application of the standard finite difference discretizations. Field equations (3.53) to (3.61) are expressed in terms of the stream-function (ψ_0) and vorticity (ω_0) in the form

$$\nabla^2 \psi_0 = -\omega_0, \tag{3.67}$$

$$\nabla^2\omega_0=\frac{Re}{h_0}(\psi_{0\eta}\omega_{0\xi}-\psi_{0\xi}\omega_{0\eta}), \tag{3.68}$$

$$\nabla^2 T_0=\frac{Ma}{h_0}(\psi_{0\eta}T_{0\xi}-\psi_{0\xi}T_{0\eta}), \tag{3.69}$$

where

$$u_0=\psi_{0z}, \quad w_0=-\psi_{0x}, \quad \omega_0=-u_{0z}+w_{0x},$$

$$\nabla^2=\frac{\partial^2}{\partial\xi^2}-2\eta\frac{h_{0\xi}}{h_0}\frac{\partial^2}{\partial\xi\partial\eta}+\frac{\eta^2h_{0\xi}^2+1}{h_0^2}\frac{\partial^2}{\partial\eta^2}+\frac{(2h_{0\xi}^2-h_0h_{0\xi\xi})\eta}{h_0^2}\frac{\partial}{\partial\eta}. \tag{3.70}$$

The boundary conditions are, at the same time, transformed to

$$\xi=-\frac{1}{2}L: \qquad \psi_0=\psi_{0\xi}=0, \quad T_0=T_L, \tag{3.71}$$

$$\xi=\frac{1}{2}L: \qquad \psi_0=\psi_{0\xi}=0, \quad T_0=T_R, \tag{3.72}$$

$$\eta=0: \qquad \psi_0=\psi_{0\eta}=0, \quad T_{0\eta}=0, \tag{3.73}$$

$$\eta=1: \qquad \psi_0=0, \tag{3.74}$$

$$\frac{(1+h_{0\xi}^2)^2}{h_0^2}\psi_{0\eta\eta}-\frac{2h_{0\xi}(1+h_{0\xi}^2)}{h_0}\psi_{0\xi\eta}+\frac{[(1-h_{0\xi}^2)h_0h_{0\xi\xi}+(1+h_{0\xi}^2)2h_{0\xi}^2]}{h_0^2}\psi_{0\eta} \tag{3.75}$$

$$=-(1+h_{0\xi}^2)^{1/2}T_{0\xi},$$

$$\frac{(1+h_{0\xi}^2)^{1/2}}{h_0}T_{0\eta}-\frac{h_{0\xi}}{(1+h_{0\xi}^2)^{1/2}}T_{0\xi}+Bi(T_0-T_g)=0. \tag{3.76}$$

The algorithm developed here to solve the flow problem is similar to the one developed in Section 3.3. The only difference is in the treatment of the normal stress boundary condition.

(ii) Deformation Problem

Deformation equation (3.62) is rewritten, with the help of equations (3.66) and (3.70), as

$$h_{1\xi\xi}+H(\xi)h_{1\xi}=M(\xi)+KN(\xi), \tag{3.77}$$

$$H(\xi)=-\frac{3h_{0\xi}h_{0\xi\xi}}{(1+h_{0\xi})^2}, \tag{3.78}$$

$$\begin{aligned} M(\xi)=&-p_0(1+h_{0\xi}^2)^{3/2}+h_{0\xi\xi}T_0 \\ &+2(1+h_{0\xi}^2)^{1/2}\left[-\frac{1+h_{0\xi}^2}{h_0}\psi_{0\xi\eta}+\frac{h_{0\xi}}{h_0^2}(h_{0\xi}^2-h_{0\xi\xi}h_0+1)\psi_{0\eta}\right], \end{aligned} \tag{3.79}$$

$$N(\xi)=-(1+h_{0\xi}^2)^{3/2}, \tag{3.80}$$

with p_0, T_0, $\psi_{0\xi\eta}$, $\psi_{0\eta}$ being evaluated at $\eta=1$. Here, p_0 stands for the normalized pressure satisfying condition $p_0(0,1)=0$ and K denotes an unknown additive constant that can be present in the pressure field.

The deformation equation (3.77) is linear, thus its solution consists of a superposition of two linearly independent solutions of the homogeneous problem and a particular solution of the inhomogeneous problem. Two boundary conditions (3.64) and (3.65) and the volumetric constraint condition (3.63) provide the three required conditions for the determination of the two constants of superposition and the pressure constant K.

The numerical solution of equation (3.77) subject to volumetric constraint (3.63) and boundary conditions (3.64) and (3.65) begins with the discretization of equation (3.77) using standard central-difference formulas and the approximation of equation (3.63) using the trapezoidal rule. The matrix of coefficients for the complete system has the same form as given by equation (3.42) for the fixed contact points case, and by equation (3.45) for the fixed contact angles case. This system can be solved directly using algorithms described in Appendixes A and B.

3.5.2 Grid Convergence Check

The proposed algorithm is formally second-order accurate, i.e., the discretization error is $O(\Delta\xi^2, \Delta\eta^2)$. The actual accuracy is determined on the basis of calculations with

different grid sizes, and observing the tendency of results as $\Delta\xi=\Delta\eta=\Delta$ is decreased. The discretization error can be assumed to vary as $C_e\Delta^\alpha$, where C_e is a constant, and α is the order of grid-convergence. Then the exponent α can be evaluated from (Kania, 1987)

$$\frac{\varepsilon_{\Delta_1/\Delta_2}}{\varepsilon_{\Delta_2/\Delta_3}}=\frac{\Delta_2^\alpha-\Delta_3^\alpha}{\Delta_1^\alpha-\Delta_2^\alpha} \tag{3.81}$$

where

$$\varepsilon_{\Delta_1/\Delta_2}=\frac{1}{N}\left[\sum_{i=1}^{N}(S^i_{\Delta_1}-S^i_{\Delta_2})^2\right]^{1/2}, \tag{3.82}$$

$$\varepsilon_{\Delta_2/\Delta_3}=\frac{1}{N}\left[\sum_{i=1}^{N}(S^i_{\Delta_2}-S^i_{\Delta_3})^2\right]^{1/2}. \tag{3.83}$$

In the above, S stands for any solution quantity; subscripts Δ_1, Δ_2, Δ_3 refer to solutions obtained on grids Δ_1, Δ_2, Δ_3, respectively, and the summation extends over all grid points that overlap on all grids employed. In the following testing grid sizes are set to $\Delta_1=1/20$, $\Delta_2=1/40$, $\Delta_3=1/80$.

(i) Testing for Accuracy of the Coordinate Transformation

The purpose of this test is to determine how the coordinate transformation (3.6) affects the accuracy of the

algorithm, especially for cases corresponding to large distortions of the interface.

Table 3.1 presents tests performed on a square cavity with Re=Ma=30. The first test deals with a reference case of an isothermal flow with a flat interface and shear stress condition (3.75) replaced by a known velocity distribution $u=16*(x-L/2)^2(x+L/2)^2$. This particular velocity distribution

Table 3.1

Results of grid convergence tests of the algorithm solving field equations with various degree of boundary deformation (for Re=Ma=30)

Test	ψ_0	ω_0	T_0
1	2.18	1.76	not calculated
2	1.84	2.08	1.99
3	1.57	2.44	1.86
4	1.33	1.67	1.69
5	1.62	1.39	1.56
6	1.48	0.82	1.44
7	1.12	0.81	1.28

has been selected in order to reduce singularities at the upper corners. The second test returns to the original boundary conditions and specifies Bi=∞ in the heat transfer boundary condition (3.76), thus decoupling the energy transport equation from Navier-Stokes equations. Shear stress at the interface is specified by assuming that $T_{0x}=T_{0\xi}=(x-L/2)^2(x+L/2)^2$ in equation (3.75). The third test is a repetition of the second one with Bi = 1 and $T_{gx}=T_{g\xi}=(x-L/2)^2(x+L/2)^2$. In the following tests, the shape of the interface is changed to the form $h_0(x)=1+A_0\cos(2\pi x)$ with A_0 being 0.3, 0.5, 0.6, and 0.7, respectively, for the fourth to seventh test. Topology of the flow field for $A_0=0.6$ is shown in Figure 3.3.

The first test shows that the algorithm under standard conditions reproduces the expected accuracy. The same accuracy can be maintained with the shear stress boundary condition (test 2). The third test shows reduction in the accuracy due to singularity in the temperature field at the upper corners. The fourth and fifth test show that the same accuracy is maintained by deforming the interface by up to 50%. Tests six and seven show a decrease of the accuracy associated with high deformations of the interface. While tests 2-7 should be viewed only as qualitative (they are somewhat contaminated by the presence of a singularity in the temperature field), they nevertheless demonstrate that the algorithm maintains fairly

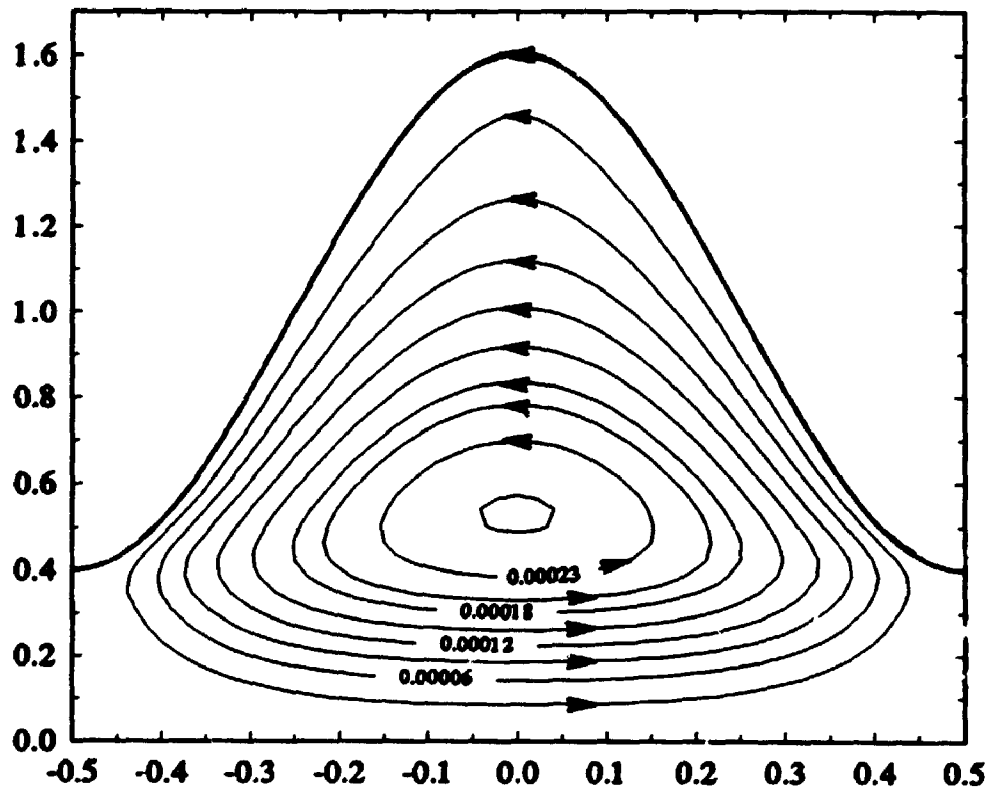

Figure 3.3 Flow patterns for interface described by equation $h_0=1+0.6\cos(2\pi x)$.

high accuracy even for deformations reaching 50% of the depth of the cavity. Further increase of the deformation reduces the accuracy of the algorithm to first-order.

(ii) Testing for different initial interface shapes

Three initial approximations of the shape $h_0(x)$ of the interface are used for the testing purpose, (i) $h_0(x)=1$ (flat interface), (ii) $h_0(x)=1.1-L^2/1.6+[(L_2/1.6+0.1)_2-x^2]^{1/2}$ (interface bulging out, $h_{0max}=1.2$), (iii) $h_0=0.9+L_2/1.6-[L^2/1.6+0.1)^2-x^2]^{1/2}$ (interface bulging in, $h_{0min}=0.8$). Note that all these shapes

Table 3.2

Results of grid convergence tests of the algorithm solving (small) deformation equation

($T_{gx}=(x-L/2)^2(x+L/2)^2$, Re=Ma=30, L=1)

Test	$\psi_{0\eta}$	$\psi_{0\xi\eta}$	p_0	T_0	h_1 fixed contact points	h_1 fixed contact angles
1 (Bi=10^4)	1.85	1.84	1.70	1.99	1.73	1.94
2 (Bi=10^4)	1.77	2.10	1.80	1.83	2.80	2.50
3 (Bi=10^4)	1.83	1.73	2.14	1.96	1.93	1.71
4 (Bi=1)	1.53	2.72	1.48	1.86	2.23	0.71

correspond to solutions of the isothermal capillary problem (3.48) to (3.52). Calculations are carried out with Re=Ma=30, Bi=1, $T_{gx}=T_{g\xi}=(x+L/2)^2(x-L/2)^2$, and variations of errors as a function of the grid size are estimated according to the formulas (3.81) to (3.83). Table 3.2 gives values of the exponent α for all flow quantities entering the deformation equation (e.g., $\psi_{0\eta}$, $\psi_{0\xi\eta}$, p_0, T_0) evaluated at the interface and for the deformation $h_1(x)$ itself. Results show that the algorithm maintains approximately second-order accuracy.

The case of the initially flat interface, $h_0(x)=1$, provides an opportunity for another test. Equation (3.77) is reduced to the form

$$h_{1\xi\xi}=-W(\xi)-K, \quad W(\xi)=p_0+2\psi_{\xi\eta}. \tag{3.84}$$

The solution for the above equation corresponding to the fixed contact point condition is

$$h_1(\xi)=-\int_{-\frac{1}{2}L}^{\xi}\int_{-\frac{1}{2}L}^{\xi} W d\xi d\xi + \frac{1}{2}K\left(\frac{L^2}{4}-\xi^2\right)+\left(\frac{\xi}{L}+\frac{1}{2}\right)\int_{-\frac{1}{2}L}^{\frac{1}{2}L}\int_{-\frac{1}{2}L}^{\xi} W d\xi d\xi, \tag{3.85}$$

where

$$K=\frac{24}{L^3}\int_{-\frac{1}{2}L}^{\frac{1}{2}L}\int_{-\frac{1}{2}L}^{\xi}\int_{-\frac{1}{2}L}^{\xi} W d\xi d\xi d\xi - \frac{12}{L^2}\int_{-\frac{1}{2}L}^{\frac{1}{2}L}\int_{-\frac{1}{2}L}^{\xi} W d\xi d\xi. \tag{3.86}$$

Solution for the fixed contact angles case is

$$h_1(\xi) = -\int_{-\frac{1}{2}L}^{\xi}\int_{-\frac{1}{2}L}^{\xi} W d\xi d\xi + \left(\frac{\xi^2}{2L} + \frac{\xi}{2} - \frac{L}{24}\right)\int_{-\frac{1}{2}L}^{\frac{1}{2}L} W d\xi + \frac{1}{L}\int_{-\frac{1}{2}L}^{\frac{1}{2}L}\int_{-\frac{1}{2}L}^{\xi}\int_{-\frac{1}{2}L}^{\xi} W d\xi d\xi . \tag{3.87}$$

The above integrals were evaluated by repetitive application of the trapezoidal rule. Calculations show the maximum difference between deformations evaluated using both methods (equations (3.77) and (3.85) or equations (3.77) and (3.87)). The maximum difference is in order of 10^{-7} in the fixed contact point case and 10^{-5} in the fixed contact angle case.

(iii) Testing of the Algorithm for Direct Solution

All discretization formulas used in the direct algorithm are formally of second-order accuracy. To determine the actual performance of the algorithm, calculations were carried out on grids, $\Delta\xi=\Delta\eta=\Delta=1/20$, $1/40$, $1/80$. The tendency of the results as Δ decreased was observed. The effective accuracy is then determined on the basis of equations (3.81) to (3.83). Results presented in Table 3.3 demonstrate that the algorithm does deliver the second-order accuracy. Figures. 3.4 and 3.5 show flow patterns corresponding to the above test conditions.

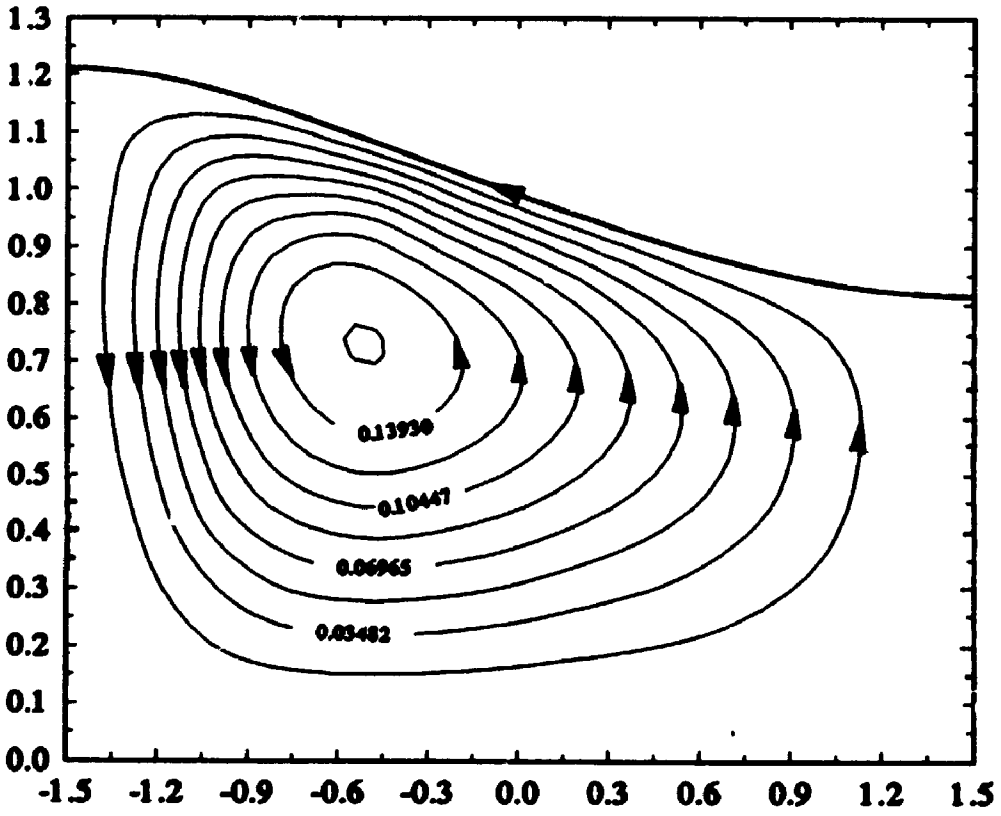

Figure 3.4 Flow patterns corresponding to the Table 3.3. Fixed contact angle cases.

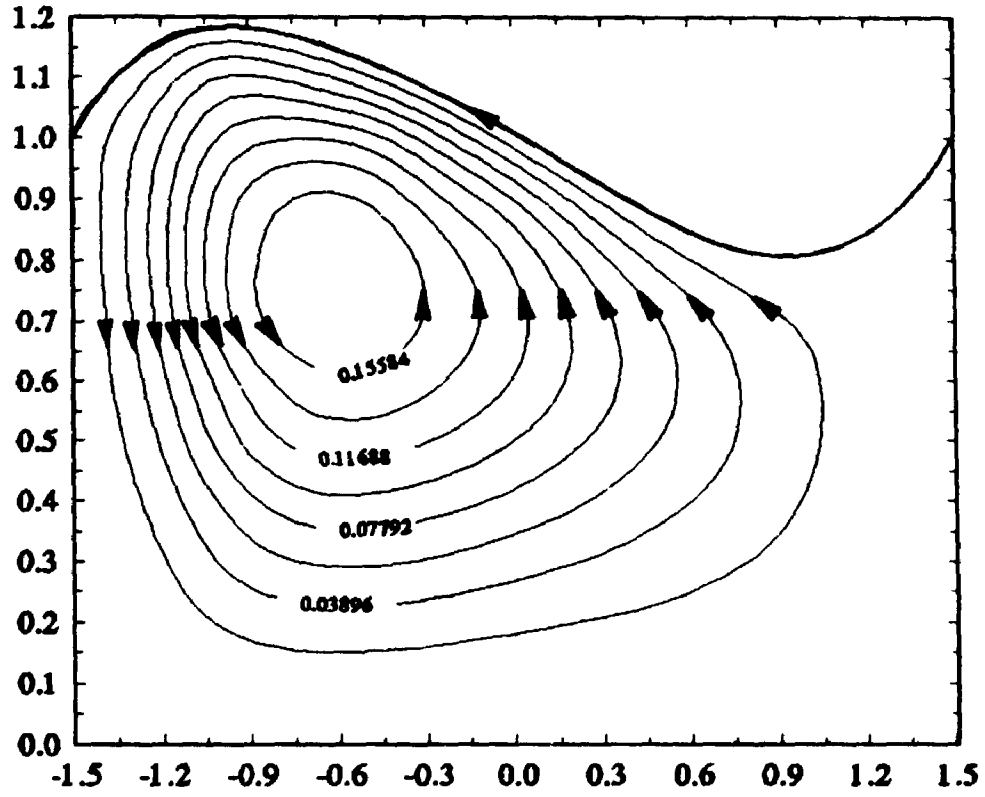

Figure 3.5 Flow patterns corresponding to the Table 3.3. Fixed contact point cases.

Table 3.3

Results of grid convergence tests of the direct algorithm (for $T_{ex}=(x-L/2)^2(x+L/2)^2$, Re=Ma=20, Bi=$10^4$, L=3)

Test	ψ	ω	T	p	h_l
Fixed contact points ($D_L=D_R=1$, Ca=0.075)	1.58	1.58	1.69	1.56	1.61
Fixed contact angles ($\theta_L=\theta_R=0$, Ca=0.020)	1.70	1.76	1.68	1.49	1.54

3.5.3. Comparison with Asymptotic Solutions

The first test involves comparison with the asymptotic solution given in Sen & Davis (1982), which is valid for elongated cavities, with initially flat interface. The other pertinent parameters are Re=Ma=0, Bi=∞, linear temperature distribution at the interface and capillary number sufficiently small so that Ca=O(A^4), where A<<1 is the cavity aspect ratio (A=height/length). The solution is constructed formally in the limit A→0. Results illustrated in Figure 3.6 are for the fixed contact point case and are obtained using the present algorithms for L=5 (A=0.2), Ca=0.024, and $\Delta\xi=\Delta\eta=1/20$. They match the asymptotic results (Sen & Davis, 1982) with the expected accuracy. For the fixed angle case, the solution given in Sen & Davis (1982) assumes that

$h_{1x}(-1/2L)=h_{1x}(1/2L)=A$. Calculations are conducted with parameters Ca=0.008, L=5 (A=0.2) and $\Delta\xi=\Delta\eta=1/20$, and the results shown in Figure 3.7 which again demonstrates agreement with the asymptotic solution.

The second test involves comparison with the solution obtained by the domain perturbation method. Results shown in Figures 3.6 and 3.7 demonstrate a good agreement between the two results.

Therefore, it can be concluded that the present algorithm reproduces results obtained by other methods.

3.5.4. The Accuracy of the Numerical Results

The accuracy of the numerical results is assessed by comparing the converged solutions of a function, e.g., the interface, for different grid sizes. The influence of the grid sizes on the solution at Re=Ma=30, $Bi=10^4$, Ca=0.024, L=3 is shown in Tables 3.4 to 3.7, which tabulate the solutions obtained on four grids. Figures 3.8 and 3.9 illustrate the interfaces obtained on four grids.

Tables 3.4 and 3.6 show that the results generally have two digits accuracy, which is within the expected accuracy.

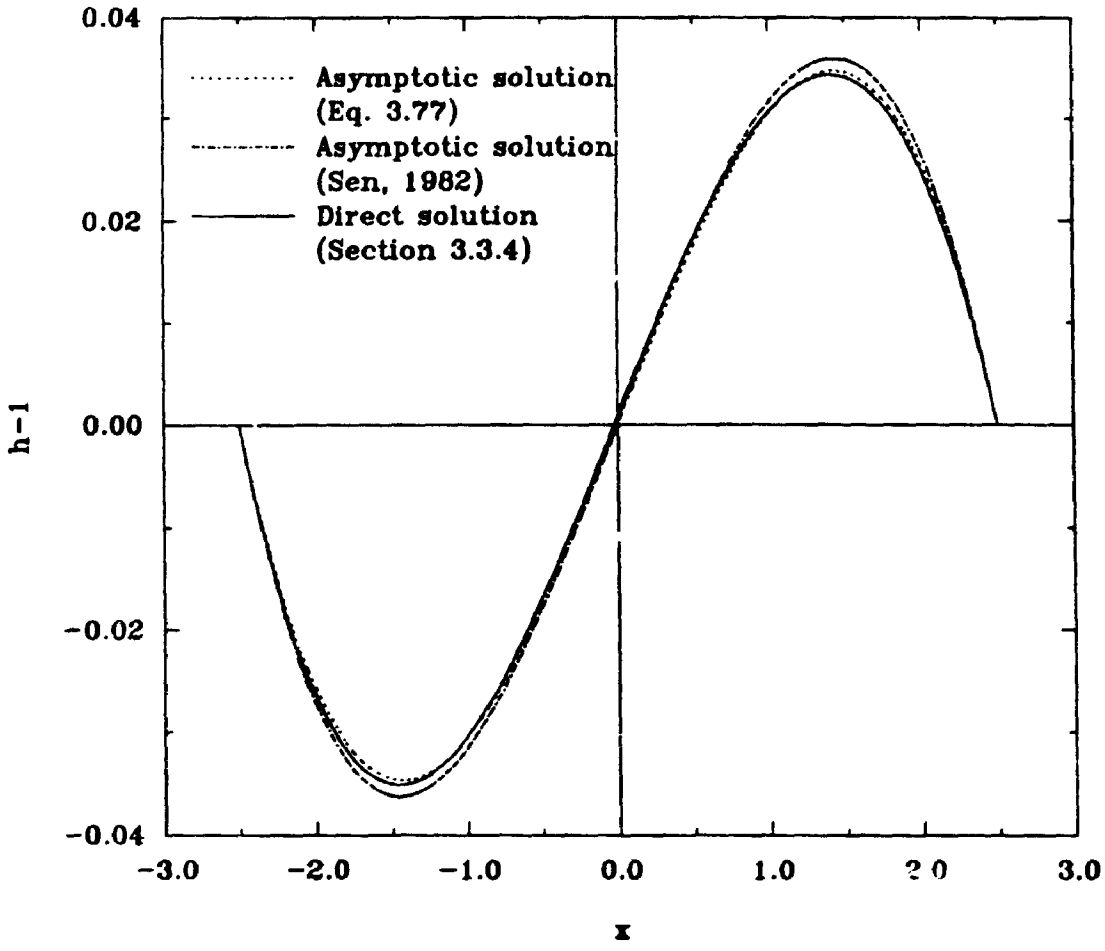

Figure 3.6 Interface deformation $h_1(x)$ obtained by different methods for fixed contact point cases and initially flat interface ($h(-\frac{1}{2}L)=h(\frac{1}{2}L)=1$, $Re=Ma=0$, $Bi=\infty$, $T_{gx}=-1$, $L=5$, $Ca=0.024$).

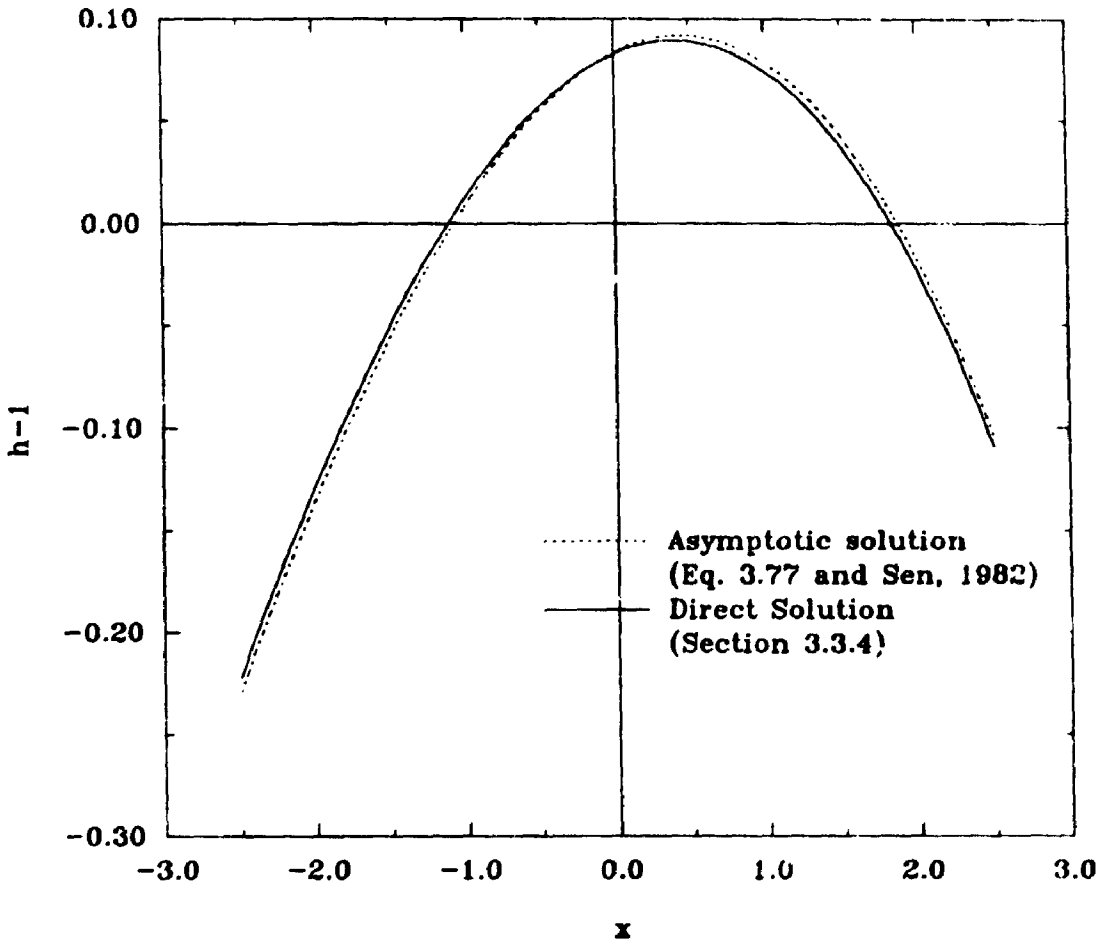

Figure 3.7 Interface deformation $h_1(x)$ obtained by different methods for fixed contact angle cases and initially flat interface ($\tan\theta_L$=0.2, $\tan\theta_R$=−0.2, Re=Ma=0, Bi=∞, T_{gs}=−1, L=5, Ca=0.008).

Tables 3.5 and 3.7 show the difference between the results obtained for different grid sizes and the result obtained with $\Delta\xi=\Delta\eta=1/80$. From Tables 3.5 and Table 3.7, it can be seen that the variations of computational variables (stream-function, vorticity, temperature, pressure, and interface) relative to the maximum magnitudes of these variables are generally less than one percent, and in no case are greater than five percent.

It may also be noted, from Tables 3.4 to 3.7 and Figures 3.7 and 3.8, that the results obtained on $\Delta\xi=1/20$ and $\Delta\eta=1/40$ have almost the same accuracy as those obtained on $\Delta\xi=1/40$ and $\Delta\eta=1/40$. It can be expected the computing time for $\Delta\xi=1/20$ and $\Delta\eta=1/40$ grid to be much less than for $\Delta\xi=1/40$ and $\Delta\eta=1/40$ grid. Therefore, from the viewpoint of both accuracy and computational cost, it may be decided to adopt $\Delta\xi=1/20$ and $\Delta\eta=1/20$ grid for usual computations and $\Delta\xi=1/20$ and $\Delta\eta=1/40$, rather than $\Delta\xi=1/40$ and $\Delta\eta=1/40$ grid for cases in which a higher accuracy is required.

3.6. Limits of Applicability of the Domain Perturbation Solution

Figures 3.10 and 3.11 illustrate the evolution of the maximum of the interface deformation as a function of the

Table 3.4

Results obtained from different grid sizes

(Re=Ma=30, Ca=0.024, Bi=10^4, fixed contact points)

Grid size		$\lvert\psi\rvert_{max}$	$\lvert\omega\rvert_{max}$	T_{max}	$\lvert p\rvert_{max}$	$\lvert h\rvert_{max}$
$\Delta\xi$	$\Delta\eta$					
1/20	1/20	0.1759	5.1314	8.0922	26.9696	1.1844
1/40	1/40	0.1761	5.1360	8.0990	27.3803	1.1796
1/80	1/80	0.1760	5.1371	8.0999	28.1969	1.1780
1/20	1/40	0.1760	5.1319	8.0965	27.1119	1.1793

Table 3.5

Relative differences between the results

(Re=Ma=30, Ca=0.024, Bi=10^4, fixed contact points)

Grid size		$\frac{\lvert\Delta\psi_{max}\rvert}{\lvert\psi\rvert_{max}}$	$\frac{\lvert\Delta\omega_{max}\rvert}{\lvert\omega\rvert_{max}}$	$\frac{\lvert\Delta T_{max}\rvert}{T_{max}}$	$\frac{\lvert\Delta p_{max}\rvert}{\lvert p\rvert_{max}}$	$\frac{\lvert\Delta h_{1max}\rvert}{\lvert h_1\rvert_{max}}$
$\Delta\xi$	$\Delta\eta$					
		%	%	%	%	%
1/20	1/20	0.06	0.10	0.09	4.35	0.54
1/40	1/40	0.06	0.02	0.01	2.89	0.14
1/20	1/40	0.00	0.10	0.04	3.85	0.11

Table 3.6

Results obtained from different grid sizes

(Re=Ma=30, Ca=0.024, Bi=10^4, fixed contact angles)

Grid size		$\lvert\psi\rvert_{max}$	$\lvert\omega\rvert_{max}$	T_{max}	$\lvert p\rvert_{max}$	$\lvert h\rvert_{max}$
$\Delta\xi$	$\Delta\eta$					
1/20	1/20	0.1571	4.9211	8.0706	20.9161	1.2108
1/40	1/40	0.1580	4.9284	8.0925	20.4290	1.2059
1/80	1/80	0.1580	4.9312	8.0981	20.2533	1.2042
1/20	1/40	0.1579	4.9261	8.0847	20.4214	1.2052

Table 3.7

Relative differences between the results

(Re=Ma=30, Ca=0.024, Bi=10^4, fixed contact angles)

Grid size		$\frac{\lvert\Delta\psi_{max}\rvert}{\lvert\psi\rvert_{max}}$	$\frac{\lvert\Delta\omega_{max}\rvert}{\lvert\omega\rvert_{max}}$	$\frac{\lvert\Delta T_{max}\rvert}{T_{max}}$	$\frac{\lvert\Delta p_{max}\rvert}{\lvert p\rvert_{max}}$	$\frac{\lvert\Delta h_{1max}\rvert}{\lvert h_1\rvert_{max}}$
$\Delta\xi$	$\Delta\eta$					
		%	%	%	%	%
1/20	1/20	0.56	0.20	0.33	3.27	0.55
1/40	1/40	0.0	0.06	0.07	0.87	0.14
1/20	1/40	0.05	0.10	0.16	0.83	0.08

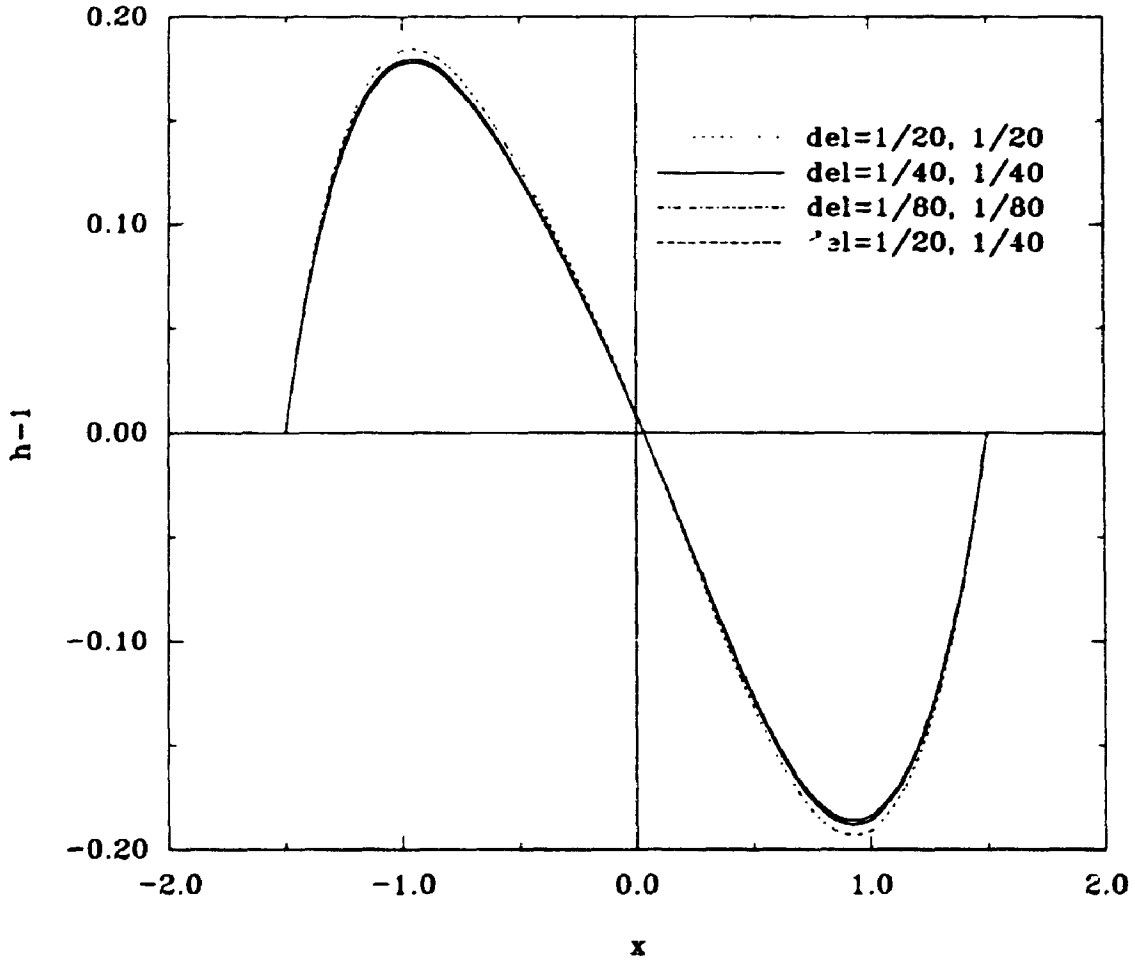

Figure 3.8 Interface deformation $h_1(x)$ obtained with different grid sizes for fixed contact point cases ($h(-\frac{1}{2}L)=h(\frac{1}{2}L)=1$, Re=Ma=20, Bi=$10^4$, $T_{gx}=(1.5-x)^2(1.5+x)^2$, L=3, Ca=0.075).

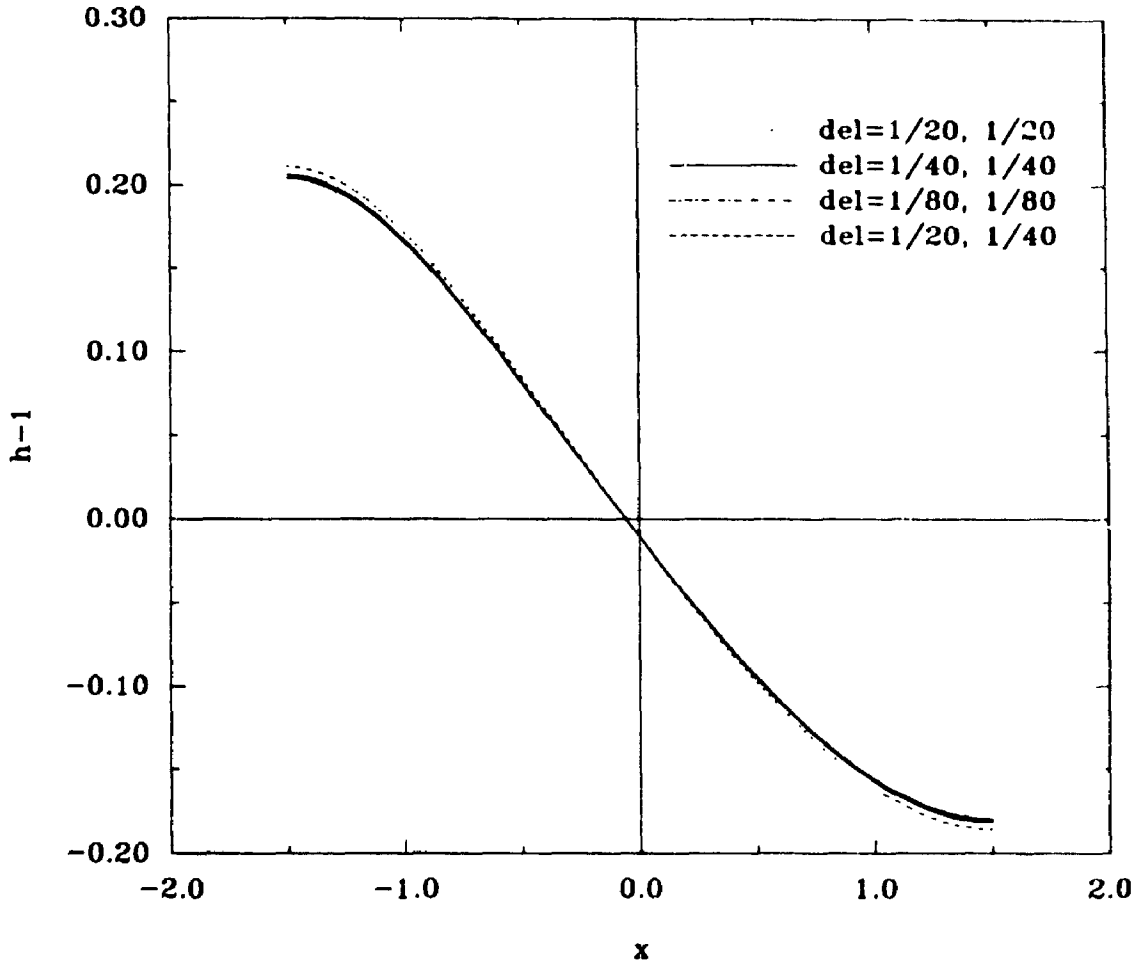

Figure 3.9 Interface deformation $h_1(x)$ obtained with different grid sizes for fixed contact angle cases (θ_L=0, θ_R=0, Re=Ma=20, Bi=10^4, $T_{gx}=(1.5-x)^2(1.5+x)^2$, L=3, Ca=0.02).

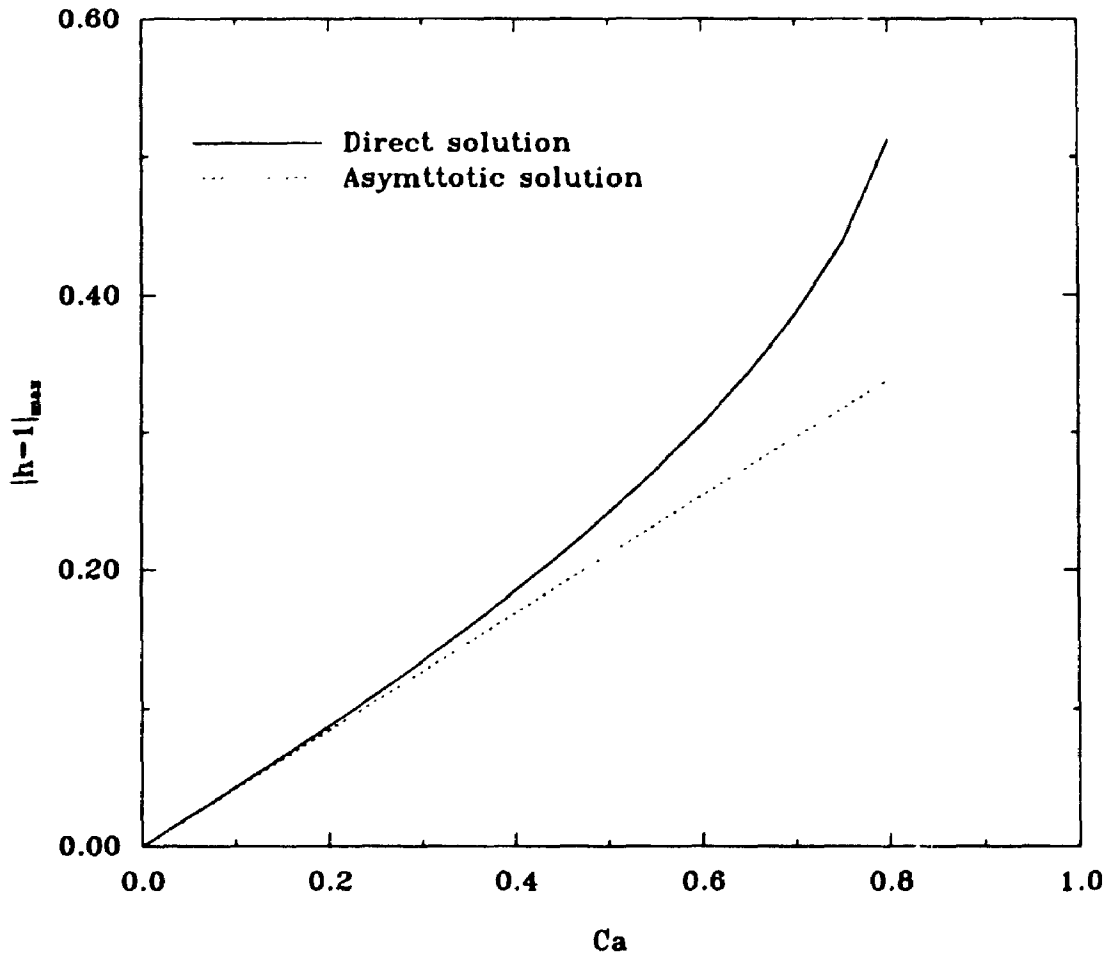

Figure 3.10 Comparison between direct and domain perturbation solutions for fixed contact point cases and initial flat interface (Re=Ma=0, Bi=∞, $h(-\frac{1}{2}L)=h(\frac{1}{2}L)=1$, $T_g(x)=-x/L$, L=6).

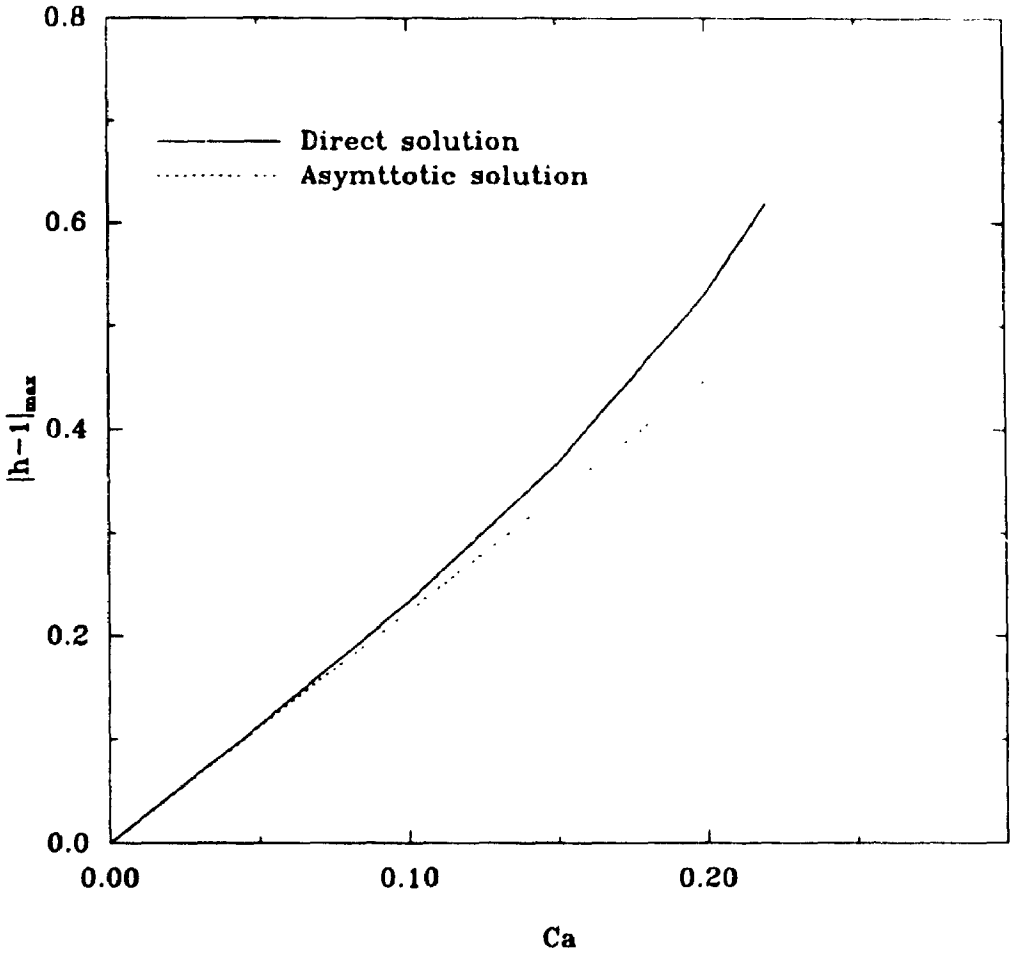

Figure 3.11 Comparison between direct and domain perturbation solutions for fixed contact angle cases and initial flat interface (θ_L=0, θ_R=0, Re=Ma=0, Bi=∞, $T_g(x)=-x/L$, L=6).

capillary number Ca determined using asymptotic and direct methods of solution. The displayed results have been obtained for the external heating of T=-x/L and cavity length L=6. These results demonstrate that for a cavity of fixed length the error of the asymptotic solution increases approximately proportionally to Ca^2, thus confirming the regular character of the expansions (3.46) and (3.47). Figures 3.12 and 3.13 show evolution of the pattern of the interface deformation. One may note that in the limiting case of Ca→0 (asymptotic solution), the deformation is antisymmetric while the flow pattern is symmetric. Small but finite values of Ca eliminate anti-symmetry of the deformation and produce an asymmetric flow field. The upper bound on the capillary number under which the domain perturbation method produces solution within a specified accuracy may be estimated from curves given in Figures 3.10 and 3.11.

3.7 Concluding Remarks

An effective algorithm for numerical simulation of the thermocapillary convection problem has been developed. Different methods were employed to check the algorithm. The numerical results are shown to be in good agreement with previous asymptotic results in the small deformation cases. The algorithm delivers the second-order accuracy even for very large interfacial distortion. The results obtained on $\Delta\xi=1/20$

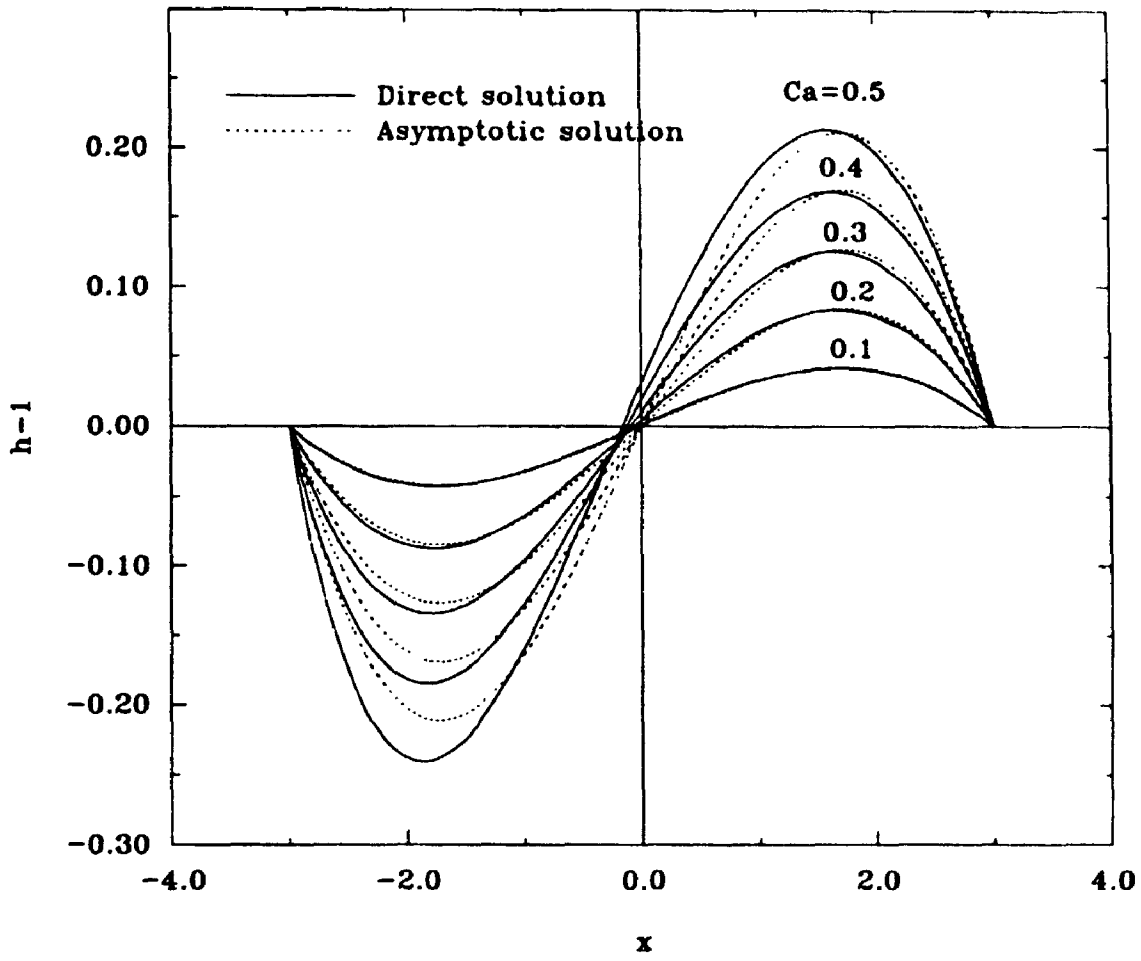

Figure 3.12 Interface deformation as a function of capillary number Ca for fixed contact point cases (Re=Ma=0, $h(-\frac{1}{2}L)=h(\frac{1}{2}L)=1$, Bi=∞, L=6, $T_g(x)=-x/L$).

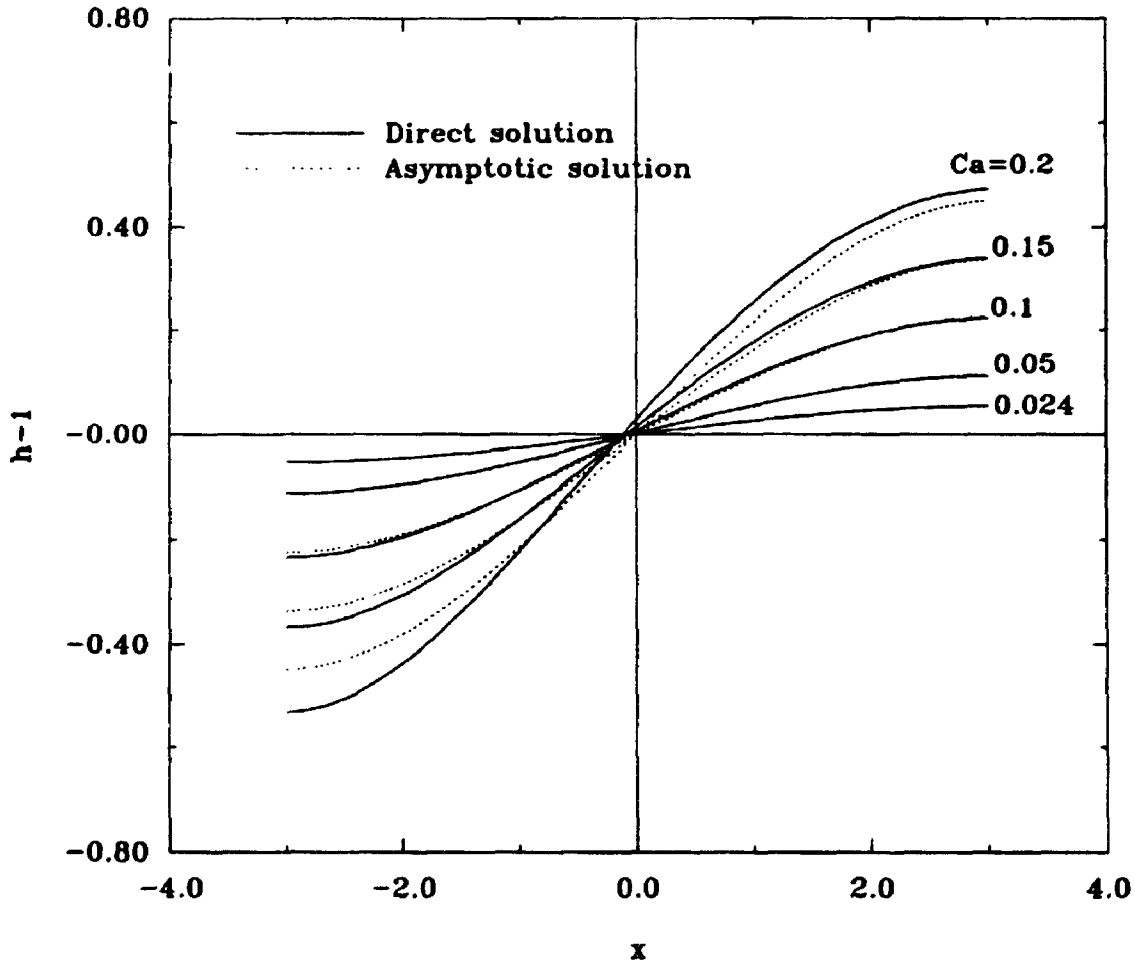

Figure 3.13 Interface deformation as a function of capillary number Ca for fixed contact angle cases. ($\tan\theta_L$=0, $\tan\theta_R$=0, $T_s(x)$=-x/L, Re=Ma=0, Bi=∞, L=6).

and $\Delta\eta=1/20$ provide accuracy no worse than 5%. The grid size $\Delta\xi=1/20$ and $\Delta\eta=1/40$ is preferred to the grid size $\Delta\xi=1/40$ and $\Delta\eta=1/40$ in cases where a higher accuracy is needed.

CHAPTER 4

Existence of Liquid Layers and Numerical Results for Zero Reynolds Number Situations

4.1 Introduction

The objective of this chapter is to use the algorithm developed in Chapter 3 to study phenomena induced by thermocapillarity in a liquid layer in the absence of gravity. This configuration has been selected due to its simple geometrical form. The layer is resting on a solid plate and its upper free surface is subject to an arbitrary external heating (Figure 4.1). Since the temperature gradient vector is parallel to the interface, the thermocapillary effect always generates some motion, regardless of the magnitude of the temperature gradient.

Two types of layers, i.e., infinite (Figure 4.1) and finite (cavity, Figure 1.3), have been selected for the analysis. Their comparison allows us to estimate the importance of geometrical constraints (end walls, contact conditions) on the convection inside the layer and on the deformation of the interface.

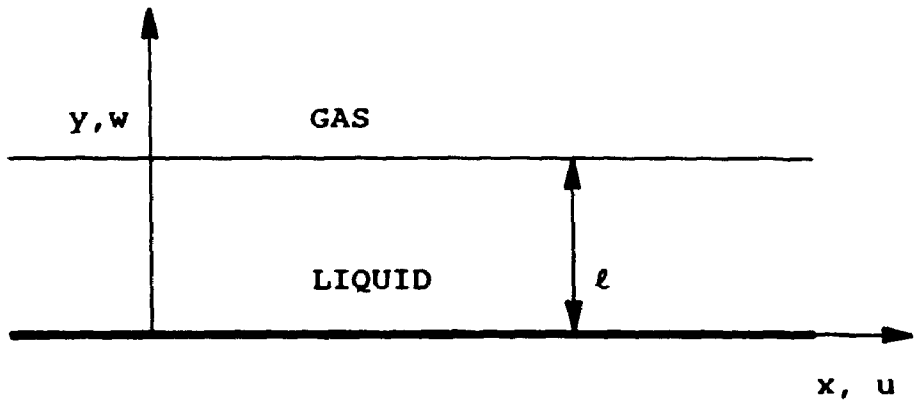

Figure 4.1 Schematic diagram of liquid layer.

A complete analysis of the response of a liquid layer to external heating will be carried out. It will be demonstrated that the dominant part of this response consists of large interfacial distortions (and possible break-up), and not just convection, as commonly assumed. Small deformations may occur only if the external temperature field satisfies a set of existence conditions. The form of these conditions shows that it may not be possible to satisfy them in most practical applications. The analysis will be carried out without simplifying assumptions in order to demonstrate the generality of the existence conditions. A set of carefully selected examples will be used to illustrate the response of the layer

to various types of external heating and to show that the layer, if sufficiently long, will break-up when exposed to heating that violates the existence conditions.

4.2 The Necessary Conditions for Existence of Small Deformation of Interface

In this section, an initially flat liquid layer will be discussed. From the domain perturbation solution (Section 3.5.1), the deformation equations (3.62) and constraint conditions (3.63) to (3.65) reduce in the case of a plane layer to the following form

$$h_{1xx}=W(x), \tag{4.1}$$

$$\int_{-\infty}^{\infty} h_1(x)dx=0, \tag{4.2}$$

$$h_1(x)<M, \quad as \quad x\to\pm\infty, \quad or \tag{4.3}$$

$$h_{1x}(x)\to 0 \quad as \quad x\to\pm\infty, \tag{4.4}$$

where

$$W(x)=-p_0(x,1)+2w_{0y}(x,1)-B \tag{4.5}$$

is referred to as the loading function, p_0 denotes pressure normalized in an arbitrary way and B stands for the corresponding normalization constant. Equations (4.1) to (4.5)

remain valid for arbitrary values of Re and Ma, as long as the interface distortion remains small.

The following discussion will focus on the case of an interface being flat as $x \to \pm\infty$. The existence and character of solutions of (4.1) to (4.5) depend on the behaviour of the loading function $W(x)$ in the limit $x \to \pm\infty$. Simple integration of (4.1) and application of boundary conditions (4.3) and (4.4) gives that

$$I_1 = \int_{-\infty}^{A} W(x)dx \quad and \tag{4.6}$$

$$I_2 = \int_{A}^{+\infty} W(x)dx \tag{4.7}$$

must exist and $I_1 = -I_2$.

If it is assumed $W(x) = o(1/x^2)$, then double integration of (4.1) followed by integration by parts and imposition of (4.3) and (4.4) gives that

$$I_3 = \int_{-\infty}^{A} xW(x)dx \quad and \tag{4.8}$$

$$I_4 = \int_{A}^{\infty} xW(x)dx \tag{4.9}$$

must exist.

In the conditions (4.6) to (4.9), A is any point along the x direction. These conditions are necessary conditions for

the existence of a solution of the deformation problem. In the case of localized heating, the dynamical effects far away from the heat source decay exponentially with distance and thus $W(x)=o(1/x^2)$ is satisfied automatically. This is the case of most interest in practical application. For general interfaces, the above integrals can be used to estimate whether large deformation will occur when the cavities become longer and longer.

The necessary conditions for conditions (4.6) to (4.9) can be written as follows:

$$\int_{-\infty}^{\infty} W(x)dx=0 \tag{4.10}$$

$$\int_{-\infty}^{\infty} xW(x)dx=G \tag{4.11}$$

where G is an arbitrary constant.

The conditions (4.6) to (4.9) or (4.10) and (4.11) are valid for any Re and Ma. These conditions define the type of external heating applied to the interface that does not induce large deformation (and break-up) of the layer. In general, these conditions can be tested only a posteriori, since the relation between the external heating and the function h_{xx} is not explicit. In the special case of Re=Ma=0, this relation can be determined using Fourier transforms.

The Fourier transform $\hat{W}(k)$ of $W(x)$ is defined (following Krol, 1991) as

$$\hat{W}(k)=(2\pi)^{-1/2}\int_{-\infty}^{\infty} W(x)e^{ikx}\,dx \tag{4.12}$$

Existence conditions (4.10) to (4.11) can be expressed as

$$\hat{W}(0)=0, \qquad \frac{d\hat{W}(0)}{dk}=iG(2\pi)^{-1/2}, \tag{4.13}$$

where i denotes imaginary unit. $\hat{W}(k)$ can be evaluated as (Krol, 1991),

$$\hat{W}(k)=\frac{Bi\,\cosh(k)}{k\,\sinh(k)+Bi\,\cosh(k)}\;\frac{2k^3}{\sinh(2k)-2k}\;\hat{T}_g(k) \tag{4.14}$$

where $\hat{T}_g(k)$ stands for the Fourier transform of the temperature $T_g(x)$ of the gas phase. Equation (4.13) requires that

$$\hat{T}_g(0)=0\ , \qquad \frac{3}{2}\frac{d\hat{T}_g(0)}{dk}=iG(2\pi)^{-1/2}, \tag{4.15}$$

which, in view of the definition of the Fourier transform, requires that the external temperature field satisfies the following conditions

$$\int_{-\infty}^{\infty} T_g(x)dx=0 \ , \tag{4.16}$$

$$\int_{-\infty}^{\infty} xT_g(x)dx=2G/3 \ , \tag{4.17}$$

Equations (4.16) and (4.17) give explicit form of the existence conditions in the case of Re=Ma=0. The same form of conditions is also valid for Bi=∞, Re=0 and arbitrary Ma. A two-dimensional version of conditions (4.16) and (4.17) for the case of an interface being unaffected by the heating far away from the heating area was given by Floryan & Krol (1991).

4.3 Deformation Analysis

The behaviour of the interface subject to five types of external heating shown in Table 4.1 will be investigated. In order to simplify the following discussion, only the case of Re=Ma=0, Bi=∞ will be considered. This makes the temperature of the interface equal to the temperature of the gas phase $T_g(x)$.

Temperature distribution A (Table 4.1) describes a cavity whose ends are kept at constant (but different) temperatures. Conduction dominates in the gas phase leading to a linear temperature variation along the interface. The temperature gradient decreases as the length L of the cavity increases,

leading to a weaker thermocapillary effect. This heating was frequently studied before (e.g., Sen & Davis, 1982) and is included in our analysis for comparison purposes. It will be demonstrated that, because this heating violates the existence conditions, the large deformation will occur.

Table 4.1*

External temperature fields subject to the investigation and their moments.

	Temperature Distribution T(x)	$\int_{-\frac{1}{2}L}^{\frac{1}{2}L} T(x)dx$	$\int_{-\frac{1}{2}L}^{\frac{1}{2}L} xT(x)dx$
A	$-x/L$	0	$-L^2/12$
B	$-x$	0	$-L^3/12$
C	$10e^{-x^2}$	$10\pi^{1/2}\mathrm{erf}(L/2)$	0
D	$(4x^3-6x)e^{-x^2}$	0	$-L^3e^{-1/4}/2$
E	$(4x^3-6x)e^{-1.5x^2}$	0	$-0.96\mathrm{erf}(0.61L)$ $+0.67Le^{-0.3751.^2}$ $-0.33L^3e^{-0.3751.^2}$

* erf denotes the error function

The temperature distribution B (Table 4.1) describes the situation where the temperature gradient along the interface is constant. Again, this type of heating has been frequently studied in the literature (e.g.,Birikh, 1966). This temperature does not satisfy the existence conditions.

Temperature distribution C (Table 4.1) has been selected in order to (qualitatively) represent temperature fields that can be found when the liquid is subject to a heating using a localized heat source. This problem is of interest in various material processing techniques. The corresponding temperature distribution does not satisfy the existence conditions.

Temperature distribution D (Table 4.1) provides an example of heating that satisfies the existence condition with G=0 in equation (4.17). Temperature distribution E (Table 4.1) also satisfies the existence conditions, but with G=-1.44 in equation (4.17).

Figures (4.2) to (4.11) display results of the direct numerical solution of the flow problems corresponding to the temperature distributions A-E, respectively. Calculations shown had been obtained for Ca=0.024 and for the interface that was initially flat. The selected value of the capillary

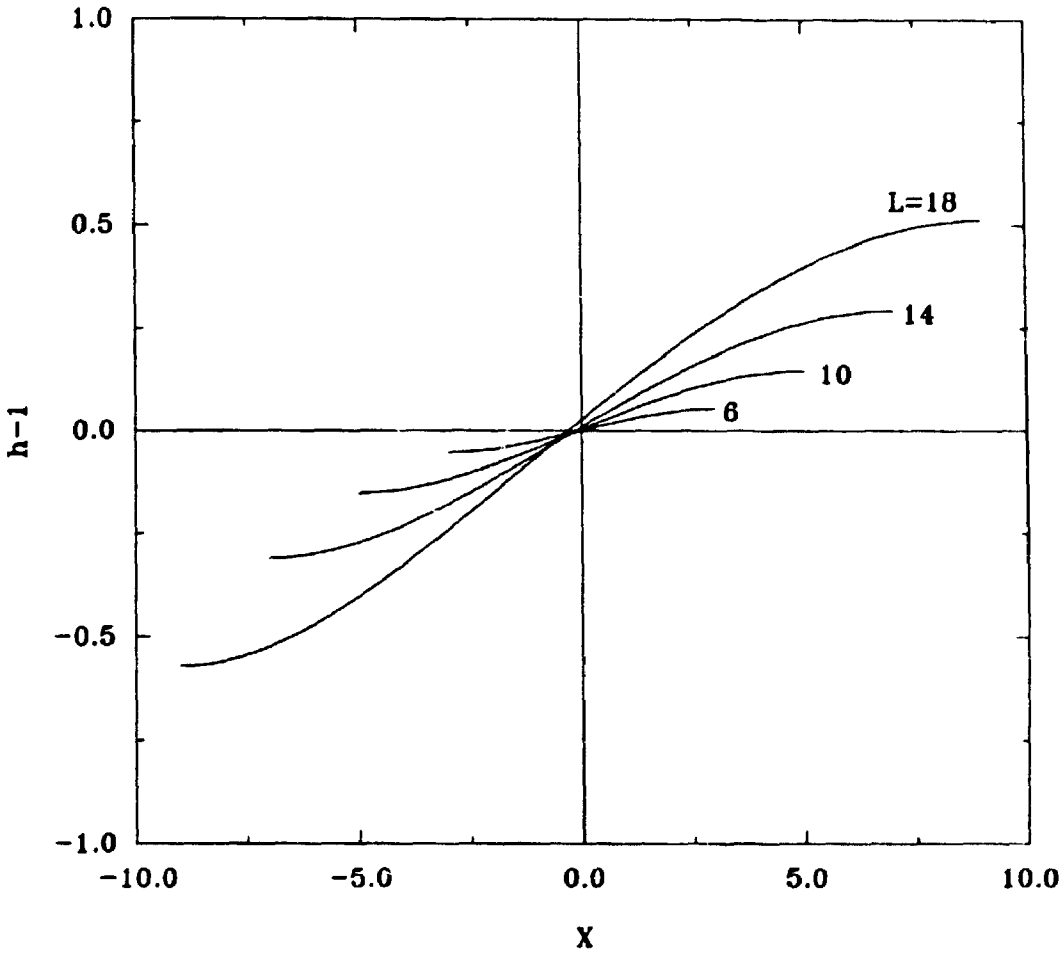

Figure 4.2 Interface deformation pattern. External heating of type A: $T_g(x)=-x/L$. Re=Ma=0, Bi=∞, fixed contact angles ($\theta_L=\theta_R=0$).

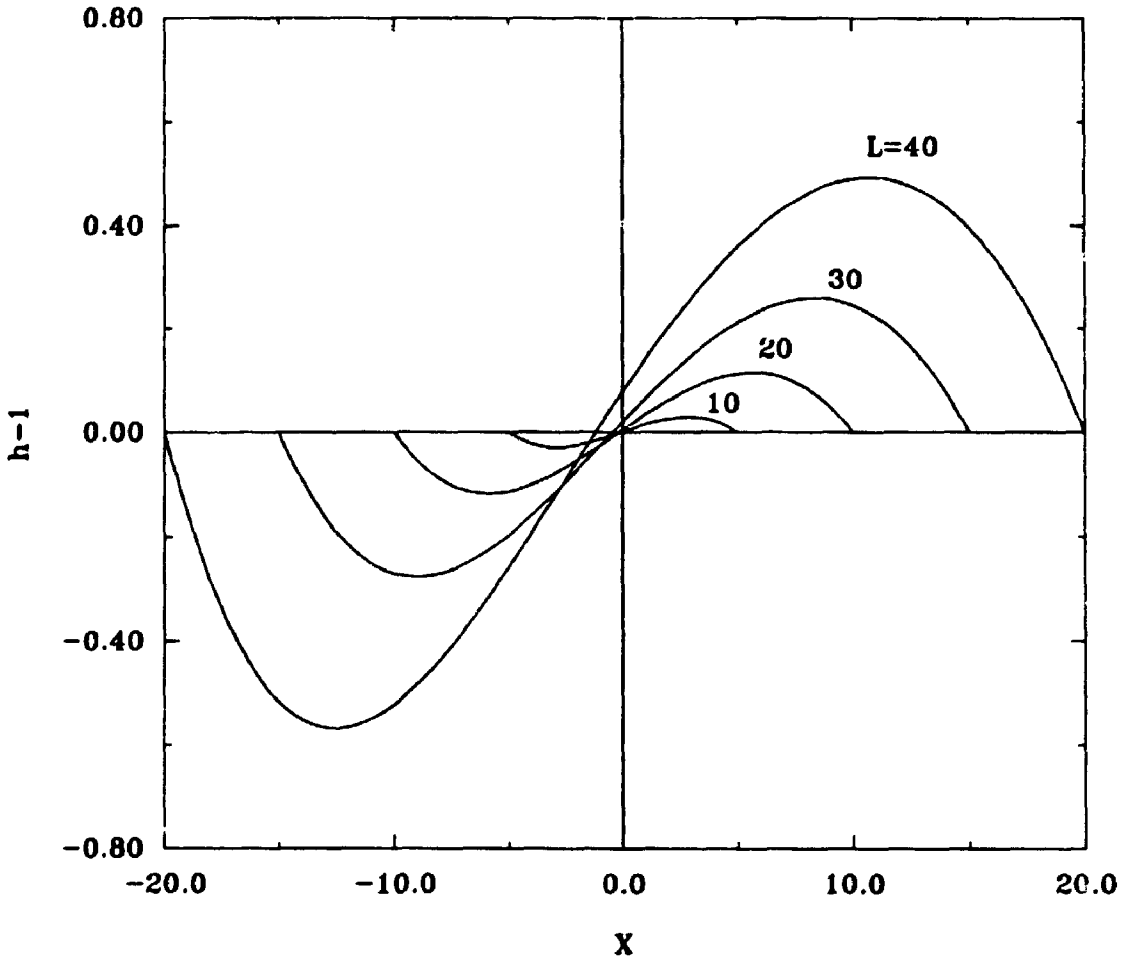

Figure 4.3 Interface deformation pattern. External heating of type A: $T_s(x)=-x/L$. Re=Ma=0, Bi=∞, fixed contact points ($h(-\frac{1}{2}L)=h(\frac{1}{2}L)=1$).

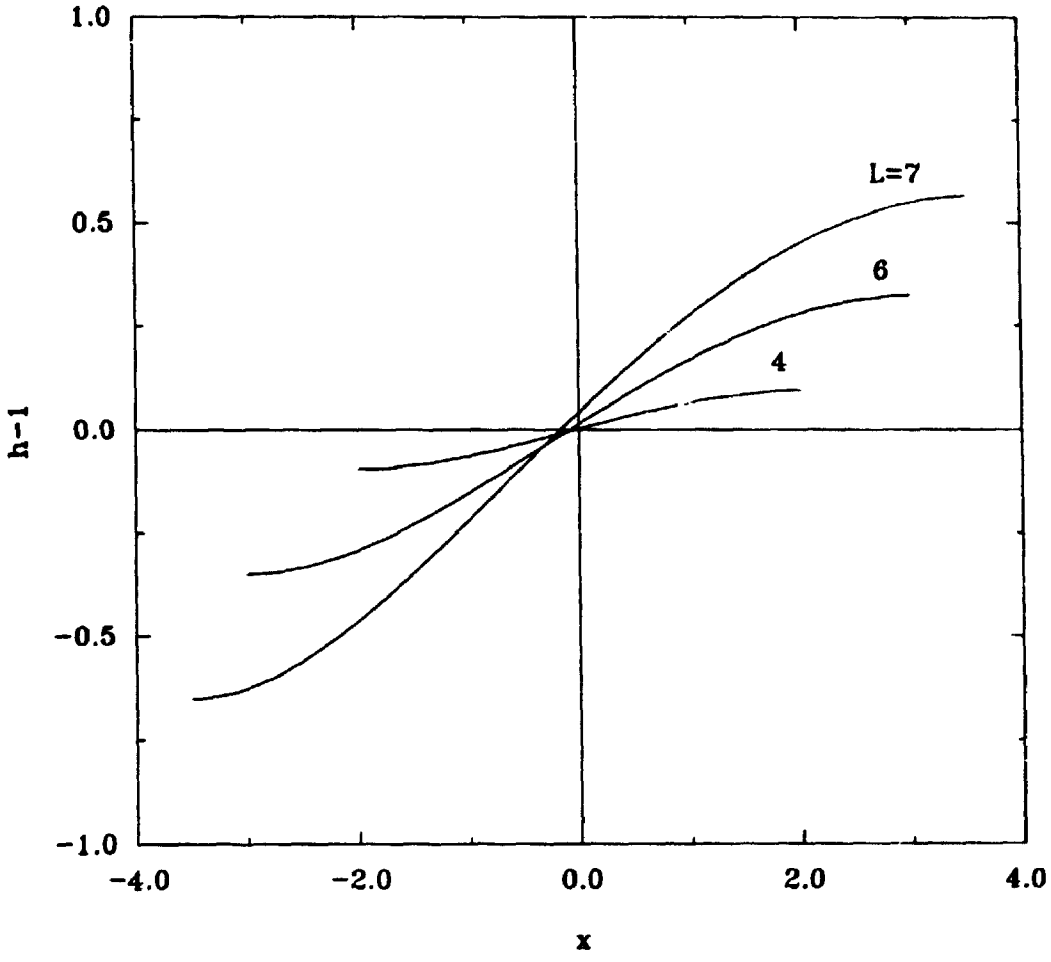

Figure 4.4 Interface deformation pattern. External heating of type B: $T_g(x)=-x$. All other conditions as in Figure 4.2.

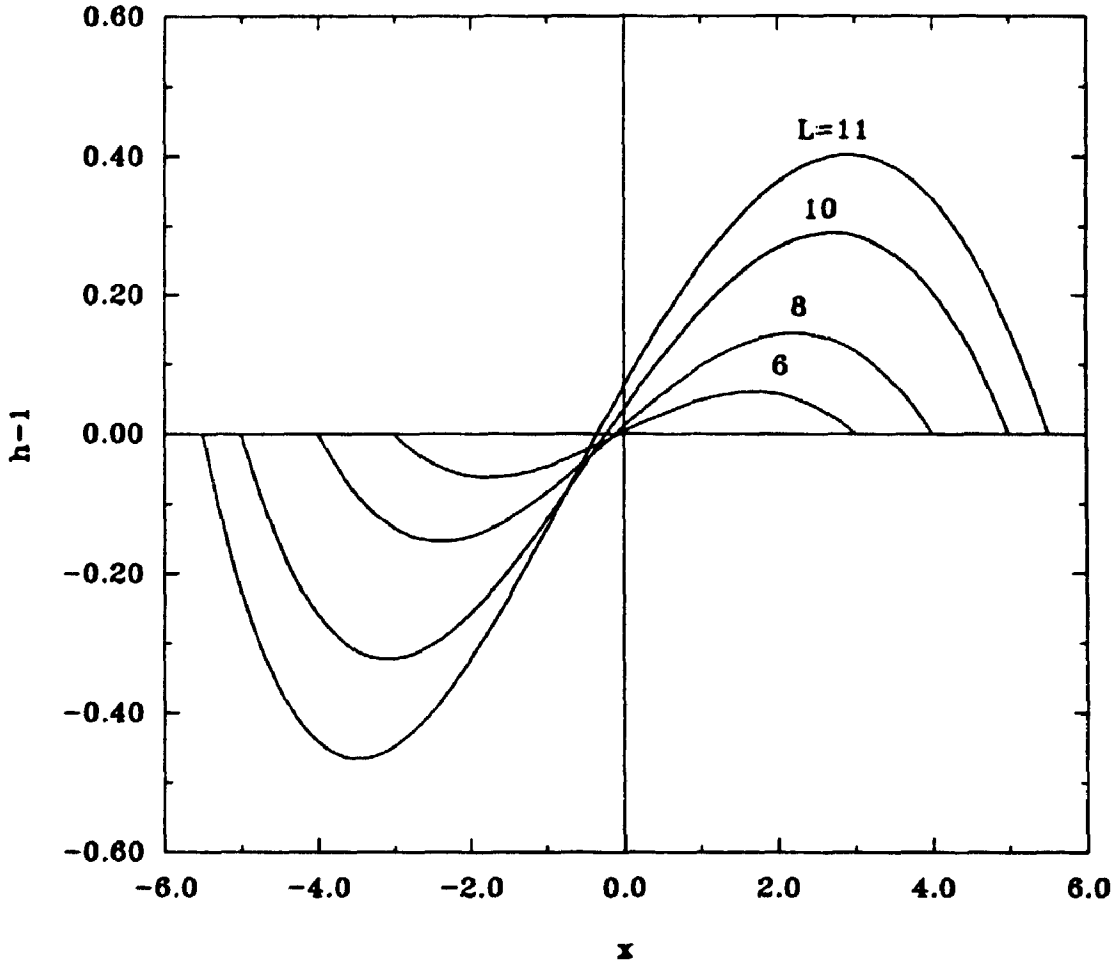

Figure 4.5 Interface deformation pattern. External heating of type B: $T_s(x)=-x$. All other conditions as in Figure 4.3.

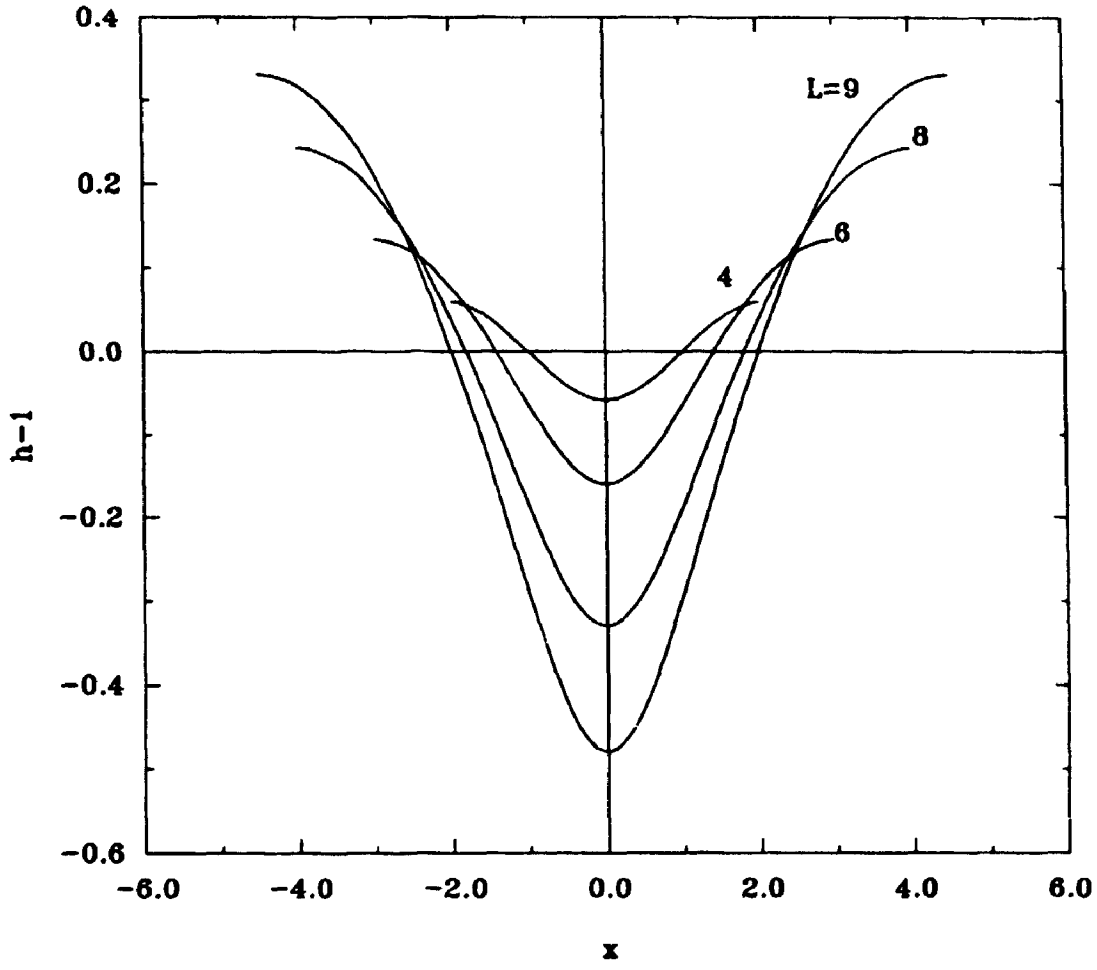

Figure 4.6 Interface deformation pattern. External heating of type C: $T_g(x)=10e^{-x^2}$. All other conditions as in Figure 4.2.

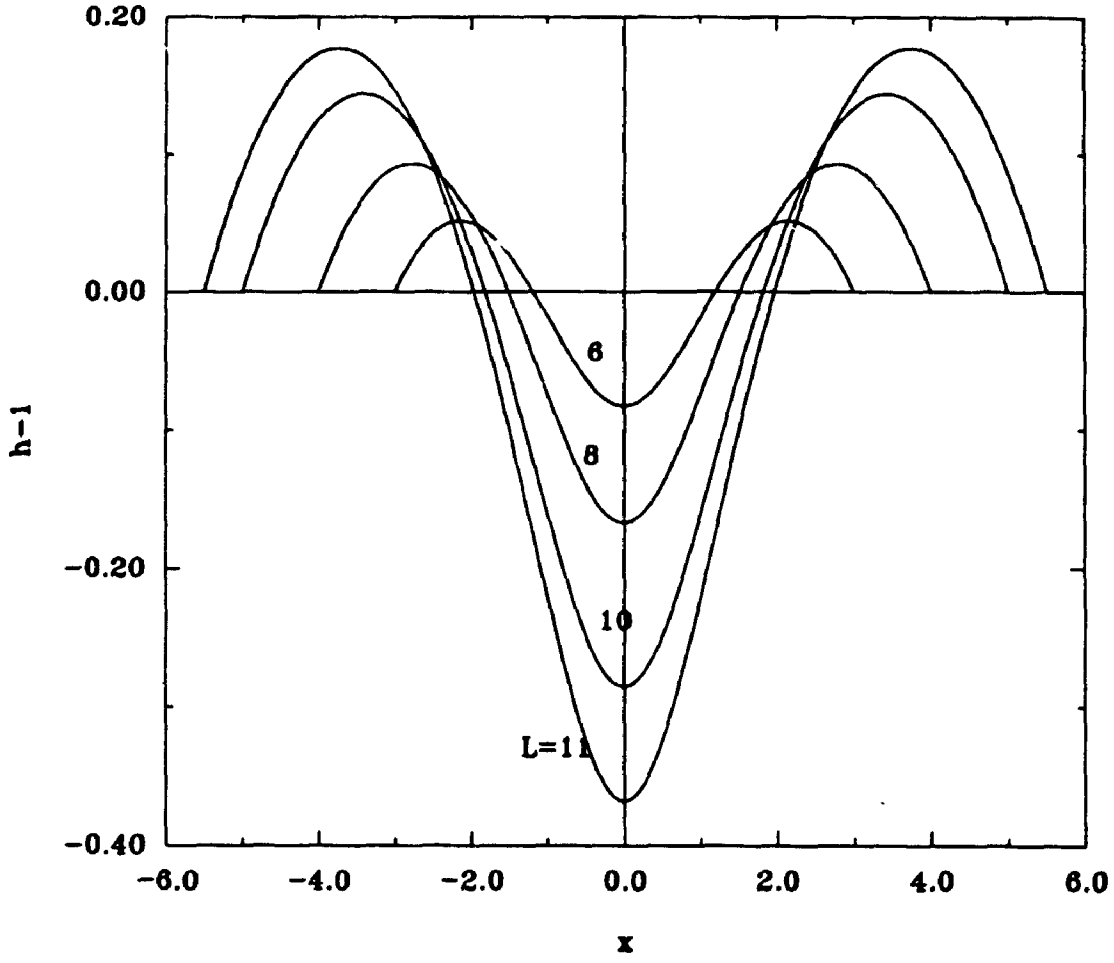

Figure 4.7 Interface deformation pattern. External heating of type C: $T_s(x)=10e^{-x^2}$. All other conditions as in Figure 4.3.

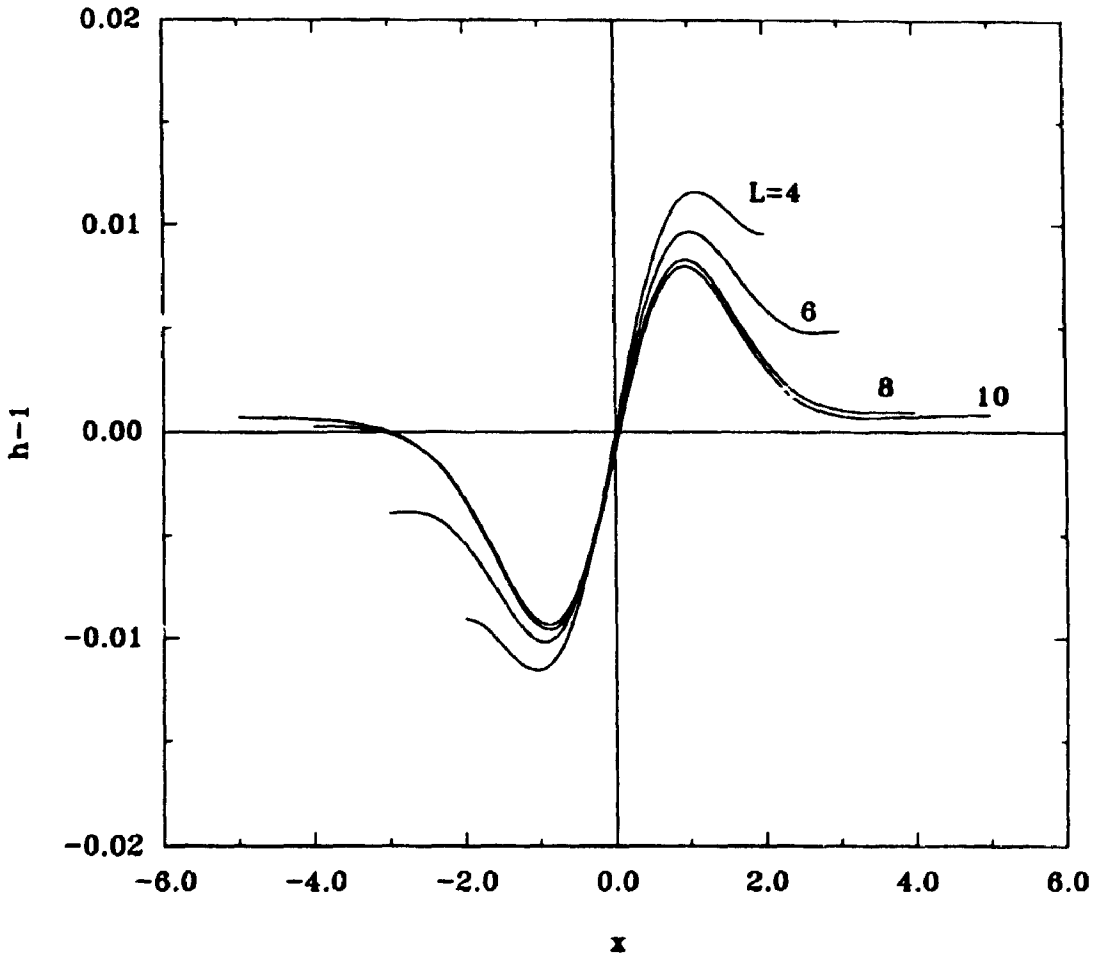

Figure 4.8 Interface deformation pattern. External heating of type D: $T_g(x)=(4x^3-6x)e^{-x^2}$. All other conditions as in Figure 4.2.

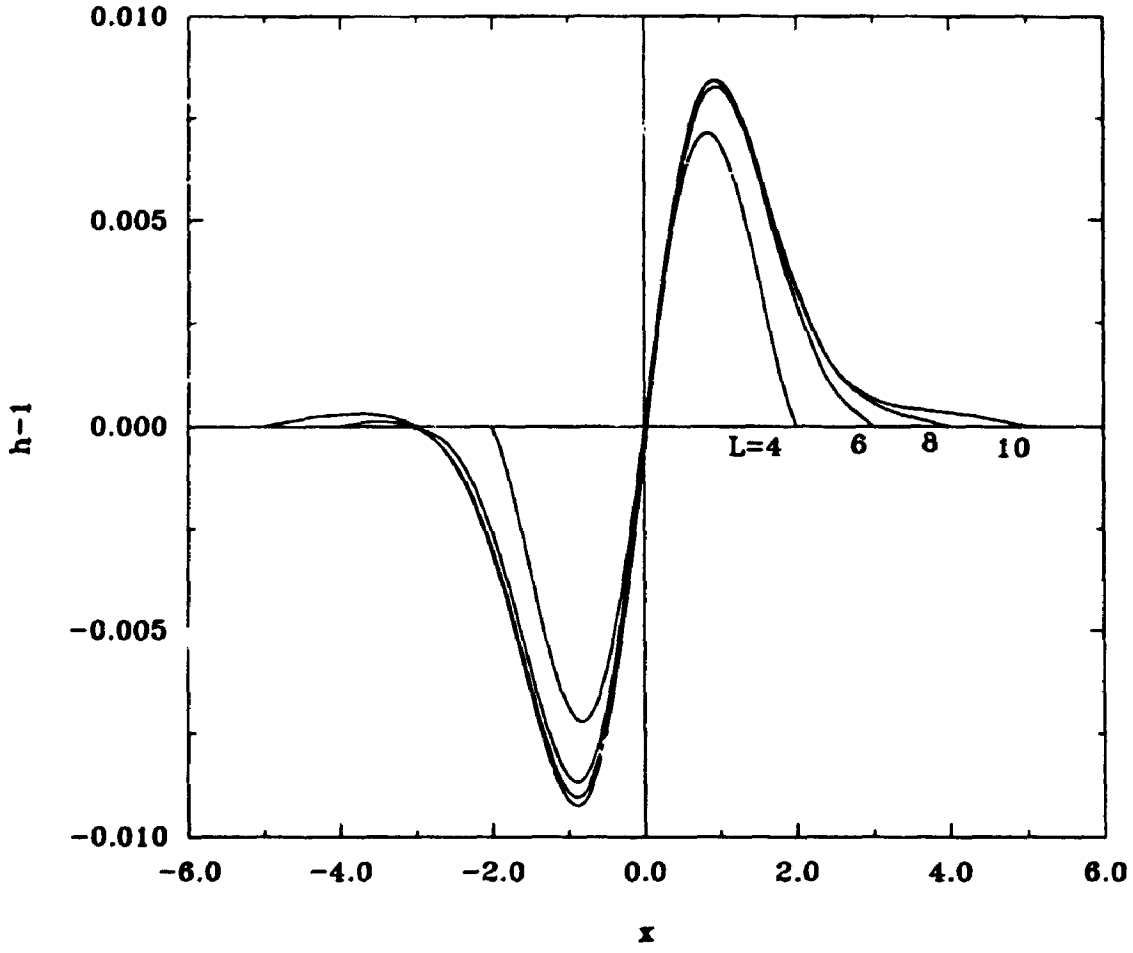

Figure 4.9 Interface deformation pattern. External heating of type D: $T_s(x)=(4x^3-6x)e^{-x^2}$. All other conditions as in Figure 4.3.

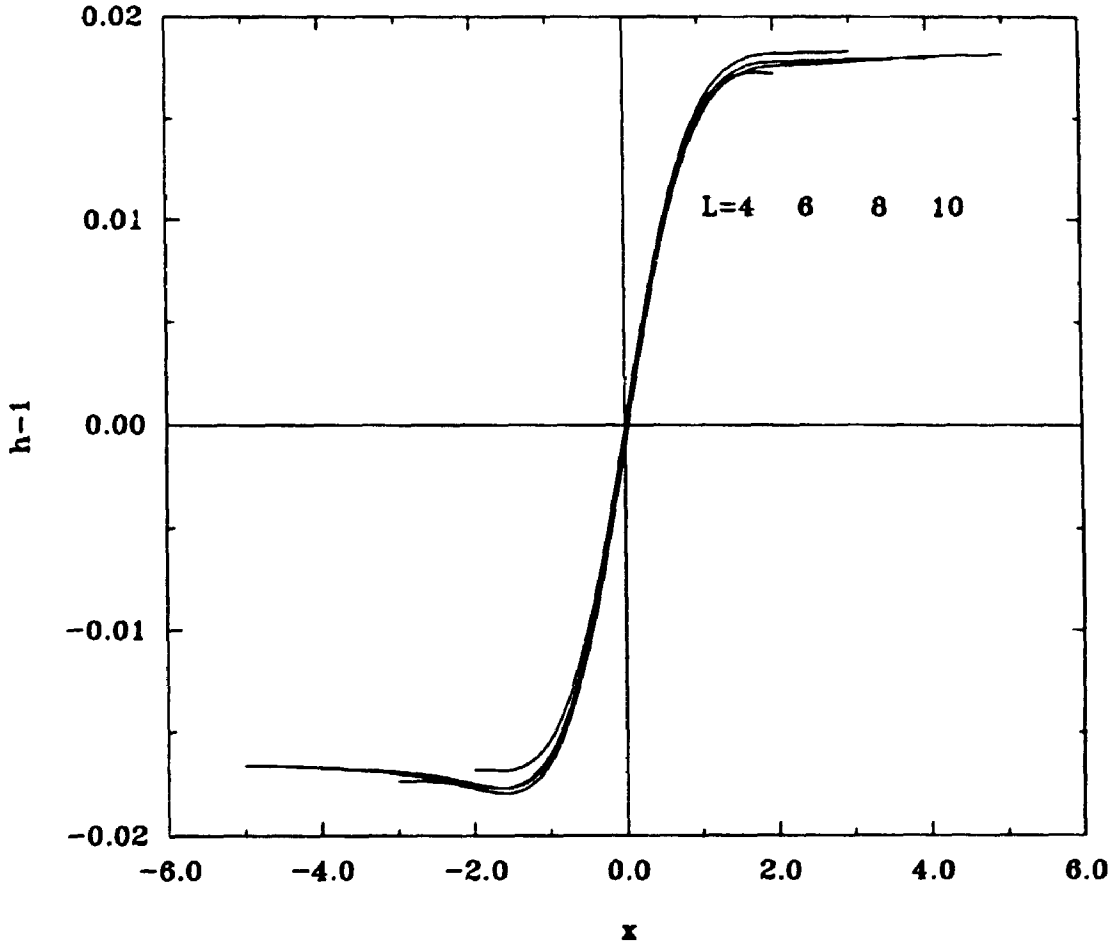

Figure 4.10 Interface deformation pattern. External heating of type E: $T_g(x)=(4x^3-6x)e^{-1.5x^2}$. All other conditions as in Figure 4.2.

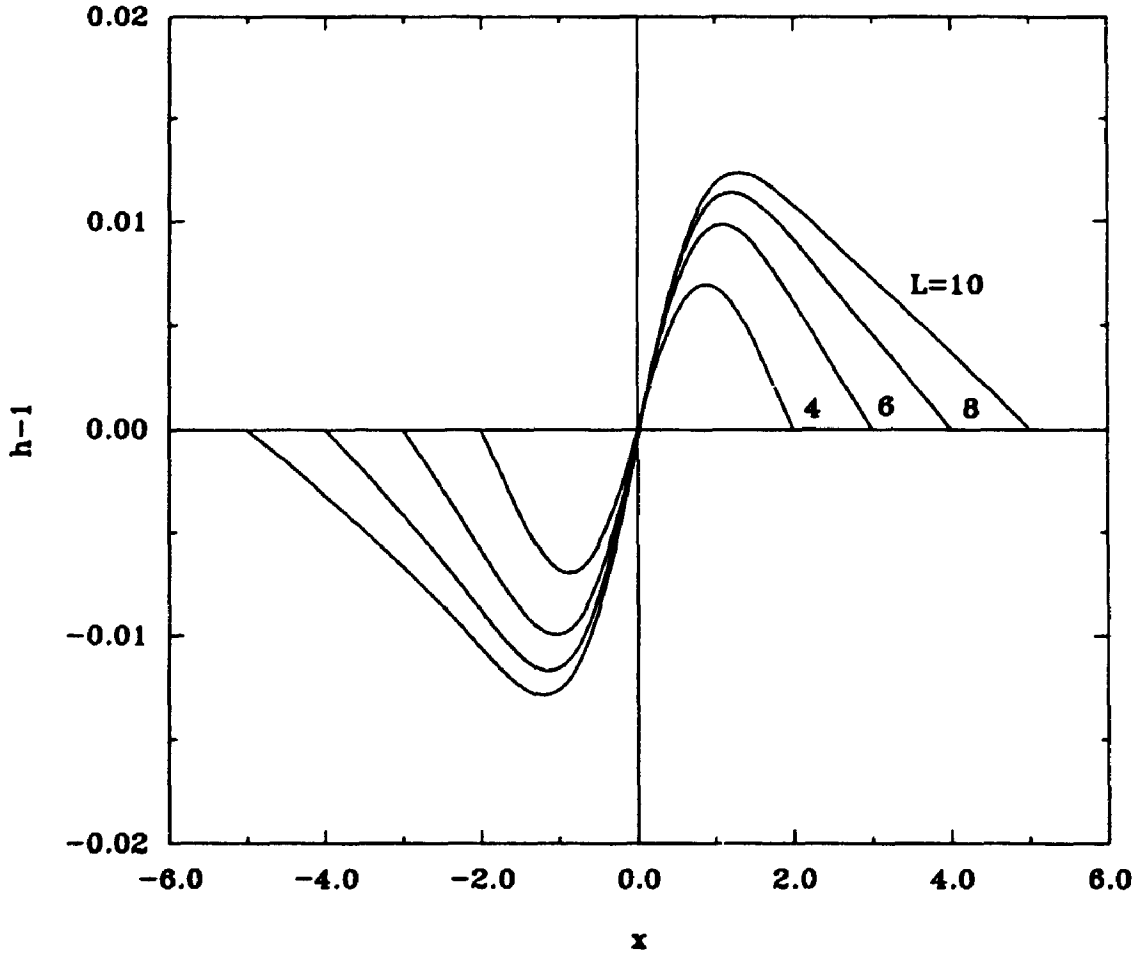

Figure 4.11 Interface deformation pattern. External heating of type D: $T_s(x)=(4x^3-6x)e^{-1.5x^2}$. All other conditions as in Figure 4.3.

number $Ca \to 0$ sufficiently small, so that one might be tempted to construct asymptotic solutions in the forms (3.46) and (3.47). Results shown in Figures 4.2, 4.4, and 4.6, which were obtained in the fixed contact angles case, demonstrate that the temperatures A, B and C induce large distortions and lead to the break-up of the interface in a sufficiently long cavity. The character and details of the break-up process strongly depend on the functional form of the external heating. Fixing contact points reduces the amplitude of the interface deformation but does not prevent break-up of the interface in a sufficiently long cavity, as shown in Figures 4.3, 4.5 and 4.7. Temperature distributions D and E satisfy the existence condition and give rise only to small deformations, as shown in Figures 4.8 to 4.11. Details will be discussed in the following sections.

4.3.1 External Heating in the Form T(x)=-x/L (Type A)

Study of this type of heating was initiated by Sen & Davis (1982) in the case of a very long cavity (cavity aspect ratio $H/L \to 0$) and with the small interface deformation assumption. The problem is peculiar in the sense that in the limiting process (as the cavity becomes longer) the interface temperature gradient and thus the thermocapillary effect become smaller (and disappear in the limit). Sen & Davis (1982) demonstrated that the flow field may be divided into a

core zone with the Couette-Poiseuille flow (with zero mass flux) and two turning zones, each at the opposite end of the cavity. Deformation of the interface is affected only by the core zone. Since this deformation increases without bounds for increasing length of the cavity, as demonstrated by the results shown in Figures 4.2 and 4.3, it is of interest to determine the physical reasons for the break-up of the liquid layer.

The flow in the core zone is driven by shear stress at the interface. There is a constant longitudinal pressure gradient required to generate back flow in order to conserve mass. While the pressure gradient becomes smaller in the limiting process, the total pressure variation from one end of the cavity to the other does not need to decrease, which is due to the increasing length of the cavity. It is simple to show that in the case of Couette-Poiseuille flow (with flat interface)

$$u(y)=\frac{3}{4L}z^2-\frac{1}{2L}z, \quad \frac{dp}{dx}=\frac{3}{2L} . \tag{4.18}$$

Solution of the (small) deformation problem (4.7) and (4.8) gives

$$h_1(x)=-x^3/4L+3Lx/16 \tag{4.19}$$

$$h_{1max}=h_1(\pm\frac{1}{2L})=L^2/16 \tag{4.20}$$

in the fixed contact angles case and

$$h_1(x)=-x^3/4L+Lx/16 \tag{4.21}$$

$$h_{1max}=h_1(\pm 12^{-1/2}L)=L^2/(48*3^{1/2}) \tag{4.22}$$

in the fixed contact points case. Equation (4.18) shows that the total pressure variations remain the same as L increases, while the amplitude of deformation increases as L^2 (equations (4.19) to (4.22)) due to the increased distance between the contact points. One may note that equation (4.17) predicts similar rate of increase (see Table 4.1 for the integral evaluation). The large deformation is eliminated in the solution of Sen & Davis (1982) by requiring that $Ca=O((H/L)^3)$ when $H/L\to 0$, which gives deformation in the form $h = 1 + Ca\ h_1 = 1 + (H/L)\bar{h}_1$, where $\bar{h}_1=O(1)$. Sen (1986) considered the case of $Ca=O((H/L)^2)$ and showed that deformations of O(1) are possible. The evolution of the interface deformation as a function of the cavity length L is illustrated in Tables 4.2 and 4.3.

The results show that the amplitude of deformation initially increases proportionally to L^2, and that the growth

process is well approximated using the core zone approximation of the flow field even for (h-1)=O(1), which confirms Sen's (1986) results. Comparison of Tables 4.2 and 4.3 shows that, while fixing of the location of the contact points strongly reduces the magnitude of the interface deformation, it does not affect qualitatively the rate of its growth as a function of L.

Table 4.2

Maximum interface deformation as a function of the cavity length. External heating of type A. Fixed contact angles.

	$\lvert h(\frac{1}{2}L)-1 \rvert$ (fixed contact angles) Ca=0.024		
Cavity length L	Asymptotic solution (Ca→0) with the core flow approximation (equation 4.19)	Asymptotic solution (Ca→0) with the complete flow field (Section 3.5.1)	Direct solution
6	0.054	0.0539	0.05385
10	0.15	0.1497	0.1527
14	0.294	0.2935	0.3112
18	0.486	0.4855	0.5714
19	0.5415	0.5412	0.6823

4.3.2 External Heating in the Form T(x)=-x (type B)

Study of this type of heating was initiated by Levich (1962) who analyzed flow in the central section of a long cavity. The interface was assumed to be flat and the flow was considered to be unaffected by the cavity ends and well approximated by the Couette-Poiseuille flow. Birikh (1966)

Table 4.3

Maximum interface deformation as a function of the cavity length. External heating of type A. Fixed contact points.

	$\lvert h-1 \rvert_{max}$ (fixed contact points) Ca=0.024		
Cavity length L	Asymptotic solution (Ca→0) with the core flow approximation (equation 4.21)	Asymptotic solution (Ca→0) with the complete flow field (Section 3.5.1)	Direct solution
6	0.0104	0.101	0.01
10	0.0287	0.0287	0.0288
20	0.1155	0.1150	0.1122
30	0.2598	0.2598	0.2769
40	0.4618	0.4618	0.5688

generalized this solution without, however, addressing the issue of the interface deformation.

The structure of the flow field is similar to the one already discussed in Section 4.3.1. The only difference is that the strength of the thermocapillary effect remains the same as the length of the cavity increases. Not surprisingly, the break-up of the interface occurs for much shorter cavities, as illustrated in Figures 4.4 and 4.5. Analysis similar to the one that lead to equations (4.18) to (4.22) results in

$$u(y)=\frac{3}{4}z^2-\frac{1}{2}z\ ,\quad \frac{dp}{dx}=\frac{3}{2} \tag{4.23}$$

and deformations in the fixed contact angles case in the form

$$h_1(x)=-x^3/4+3L^2x/16 \tag{4.24}$$

$$h_{1max}=h_1(\pm\frac{1}{2L})=L^3/16 \tag{4.25}$$

and in the fixed contact points case in the form

$$h_1(x)=-x^3/4+L^2x/16 \tag{4.26}$$

$$h_{1max}=h_1(\pm(12)^{-1/2}L)=L^3/(48*3^{1/2})\ . \tag{4.27}$$

Equation (4.23) shows that the total pressure variations along the interface increase proportionally to L, while amplitude of the interface deformation increases as L^3 (equations (4.24) to

(4.267). Such growth is predicted by equation (4.17) (see Table 4.1 for value of the integral).

Tables 4.4 and 4.5 illustrate evolution of the interface deformation as a function of L and confirms that this deformation grows initially proportionally to L^3 and that this growth is well approximated even for fairly large deformations by the core zone approximation.

Table 4.4

Maximum interface deformation as a function of the cavity length. External heating of type B. Fixed contact angles.

	$\lvert h(-\frac{1}{2}L)-1 \rvert$ (fixed contact angles) Ca=0.024		
Cavity length L	Asymptotic solution (Ca→0) with the core flow approximation (equation 4.24)	Asymptotic solution (Ca→0) with the complete flow field (Section 3.5.1)	Direct solution
4	0.096	0.096	0.0965
6	0.324	0.323	0.3504
7	0.515	0.5133	0.6516
7.1	0.5369	0.5354	0.7145

4.3.3. External Heating in the Form $T(x)=10e^{-x^2}$ (type C)

This particular temperature distribution has been selected in order to illustrate effects associated with heating of the liquid using a localized heat source. The existence conditions are not satisfied and the layer breaks-up in a sufficiently long cavity, as illustrated by results shown in Figures 4.6 and 4.7.

Table 4.5

Maximum interface deformation as a function of the cavity length. External heating of type B. Fixed contact points.

	(fixed contact points) Ca=0.$\|\Omega\|_{max}$		
Cavity length L	Asymptotic solution (Ca→0) with the core flow approximation (equation 4.26)	Asymptotic solution (Ca→0) with the complete flow field (Section 3.5.1)	Direct solution
6	0.0624	0.0607	0.0622
8	0.148	0.146	0.153
10	0.287	0.287	0.322
11	0.384	0.383	0.466
11.5	0.439	0.4375	0.579

The liquid is driven by surface tension gradients along the interface away from the point of maximum temperature. The back flow along the bottom of the cavity is forced by the pressure rise on both sides of the heating area. Since the velocity magnitude decreases approximately exponentially with distance away from the heat source, this pressure reaches a constant (non-zero) value sufficiently far away from the heat source, as illustrated in Figure 4.12. This constant pressure would extend to the ends of the cavity regardless of the cavity length if the interface was non-deformable. In the case of a finite Ca, the constant pressure jump across the interface generates large deformation regardless of the value of Ca, if the cavity is made sufficiently long. The deformation consists of bulging out at both ends of the cavity (high pressure areas) and bulging in the middle section (location of heat source, low pressure area), as shown in Figures 4.6 and 4.7.

4.3.4. External Heating in the Form $T(x)=(4x^3-6x)e^{-x^2}$ (type D)

The functional form of this temperature distribution has been specially selected in order to satisfy the existence conditions. This heating is characterized by G=0 in equation (4.17). Its form is plotted in Figure 4.13 and shows a pattern of localized heating and cooling. The resulting distribution of surface tension gradients is "balanced" in the sense that

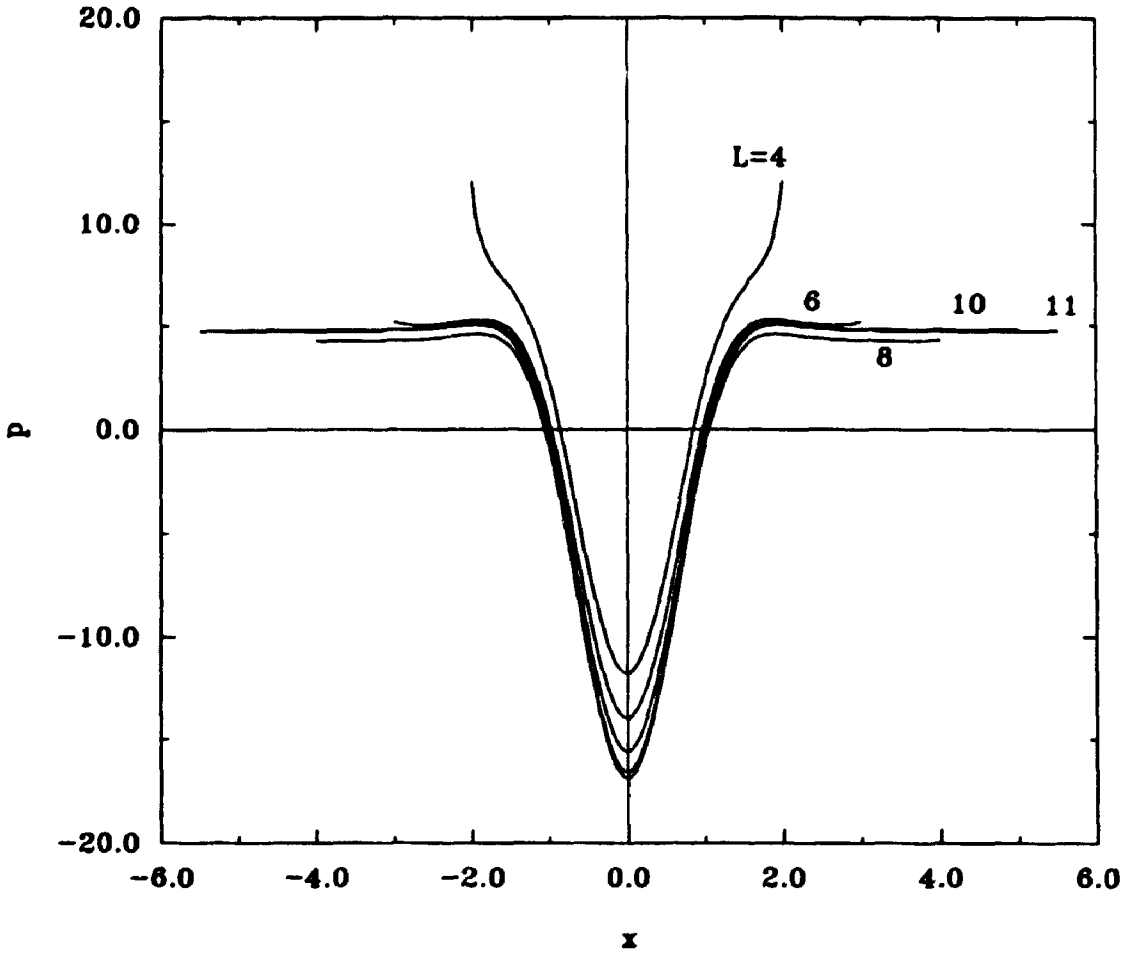

Figure 4.12 Interface pressure distribution p(x,1). External heating of type C (see Table 4.1). Fixed contact points.

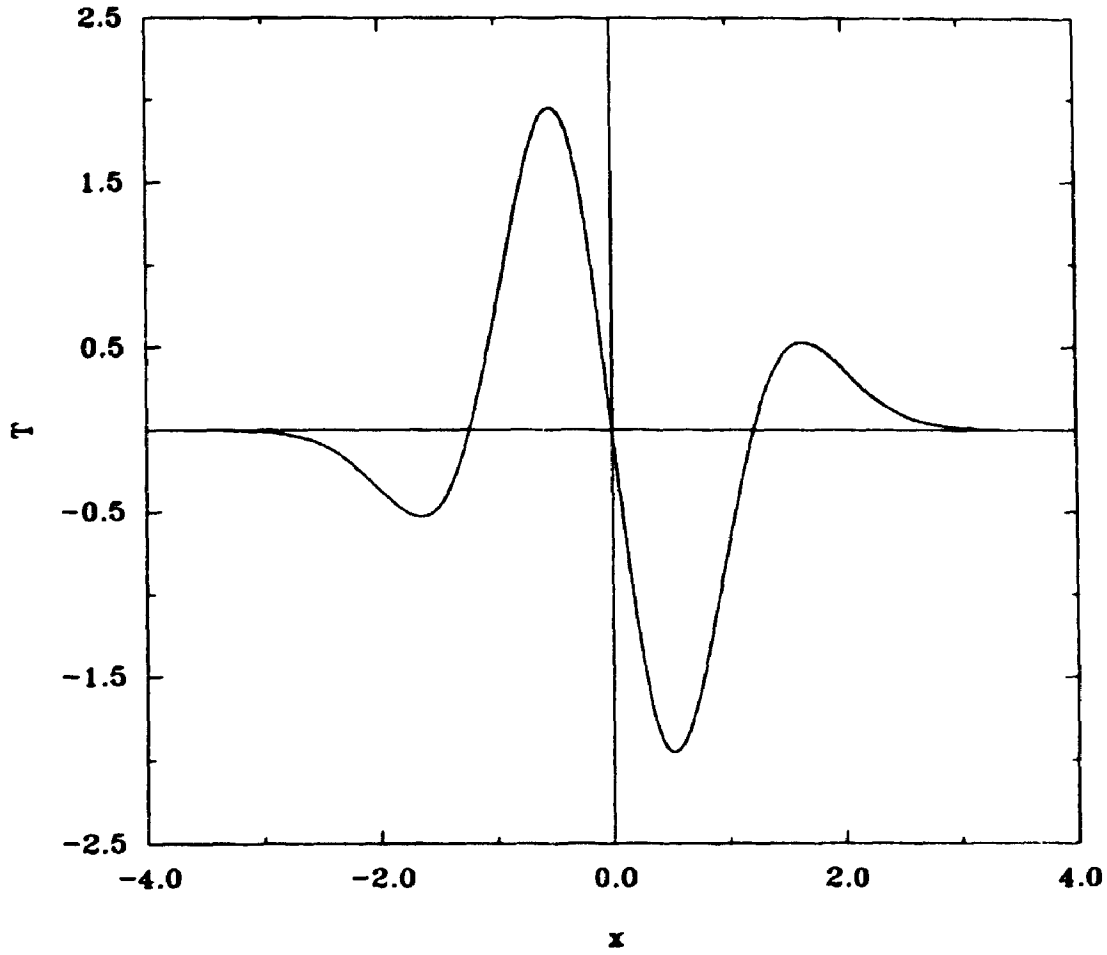

Figure 4.13 Interface temperature distribution T(x,1). External heating of type D (see Table 4.1).

it does not lead to any pressure changes far away from the heating area. Such changes were required in the case of heating discussed in the previous section in order to generate back flow. The pressure distribution is shown in Figure 4.14. The resulting interface deformation, shown in Figures 4.8 and 4.9, very rapidly approaches the infinite layer, with $h_1(-\frac{1}{2}L)$, $h_1(\frac{1}{2}L)\to 0$ as $L\to\infty$.

4.3.5. External Heating in the Form $T(x)=(4x^3-6x)e^{-1.5x^2}$ (type E)

This form of temperature distribution was selected specially in order to satisfy the existence conditions, but with $G\neq 0$ in equation (4.17) ($G=-1.44$). The heating causes change of elevation of the interface at $x=\pm\infty$ and this is inconsistent in the limit of very long cavity $L\to\infty$ with the fixed contact points condition.

The physical situation is analogous to the one discussed in Section 4.3.4. The pressure distribution displayed in Figure 4.15 shows that the pressure levels off to zero with distance away from the heating area. The pattern of the interface deformation in the fixed contact angles case is shown in Figure 4.10, with $h_1(-\frac{1}{2}L)\to -0.72$ and $h_1(\frac{1}{2}L)\to 0.72$ as $L\to\infty$. The deformation in the fixed contact points case is shown in Figure 4.11, but it does not offer any insight into what

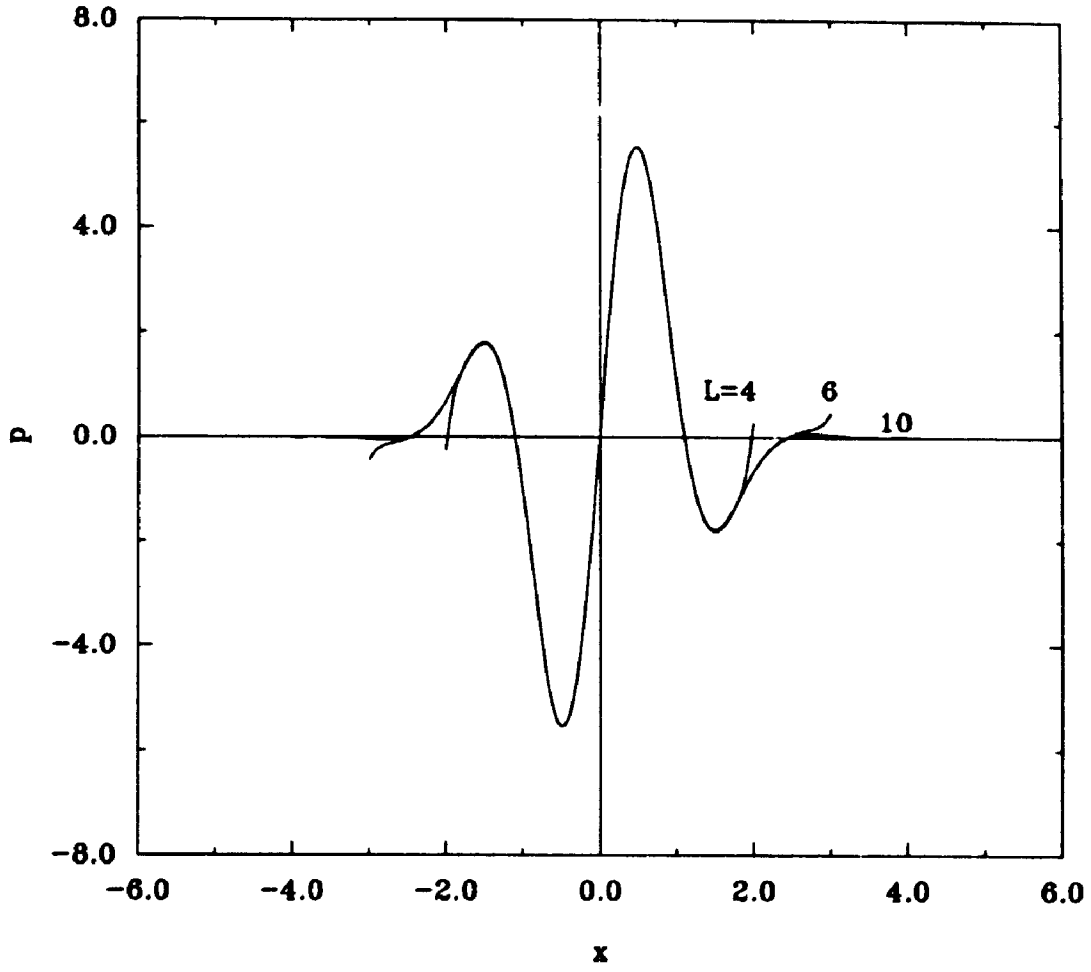

Figure 4.14 Interface pressure distribution p(x,1). External heating of type D (see Table 4.1).

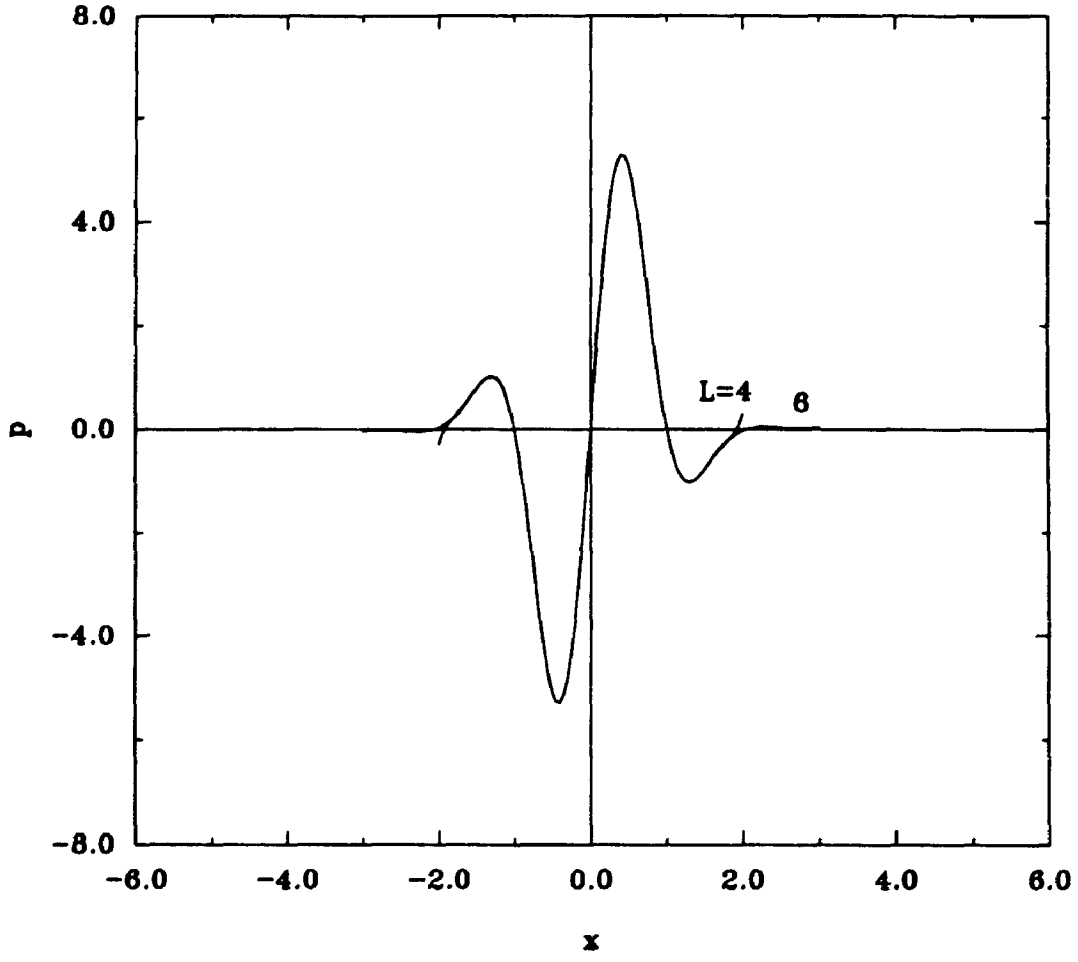

Figure 4.15 Interface pressure distribution p(x,1). External heating of type E (see Table 4.1).

happens as $L \to \infty$. One may recall that such a solution cannot exist for $L = \infty$. The maximum deformation increases as a function of L ($|h-1|_{max}$=0.0128, 0.0161, 0.018, 0.0195 for L=10, 20, 30, 40, respectively) which suggest possible occurrence of large deformations. The rate of increase is so small that it precludes detailed analysis of this phenomena using the present algorithm.

4.4 Interface Diagnostics

A direct relation between the external heating and the interface deformation cannot be established under general flow conditions. The occurrence of large deformation and, perhaps, break-up of the layer can be predicted by carrying out a direct solution of the whole problem using the method described in Chapter 3. A cheaper alternative is offered by carrying out a solution with the small deformation assumption, such as described in Section 3.5.1, and diagnosing the true behaviour of the interface by evaluating integrals appearing in Equations (4.6) to (4.9). A numerical solution of the Navier-Stokes equations still has to be carried out, but the geometry of the solution domain is simple and the location of the boundary conditions is fixed.

We shall begin discussion of the interface diagnostics by considering a cavity with fixed contact angles. The integrals

in equations (4.6) to (4.9) will be used for diagnostic purpose. Utility of such diagnostics is demonstrated by results of calculations, which are shown in Tables 4.6 to 4.10. The assumptions stated in Section 4.2 are satisfied in the cases analyzed here. The divergent behaviour of the integrals in cases that violate the existence conditions is clearly visible.

Results in the fixed contact point cases are given in Tables 4.11 to 4.15. They show behaviour of I_1, I_2, I_3 and I_4 consistent with the existence conditions (4.6) to (4.9).

Table 4.6

Evaluations of the integrals (4.6)to (4.9) as a function of the cavity length. External heating of type A. Fixed contact angles.

Length L	I_1	I_2	I_3	I_4
6	1.117	-1.117	-2.246	-2.246
10	1.870	-1.870	-6.238	-6.238
14	2.622	-2.622	-12.24	-12.24

Table 4.7

Evaluations of the integrals as a function of the cavity length. External heating of type B. Fixed contact angles.

Length L	I_1	I_2	I_3	I_4
4	2.954	-2.954	-4.021	-4.021
6	6.704	-6.704	-13.48	-13.48
7	9.141	-9.141	-21.39	-21.39

Table 4.8

Evaluations of the integrals as a function of the cavity length. External heating of type C. Fixed contact angles.

Length L	I_1	I_2	I_3	I_4
4	0	0	4.274	-4.274
6	0	0	9.981	-9.981
8	0	0	16.56	-16.56

Table 4.9

Evaluations of the integrals as a function of the cavity length. External heating of type D. Fixed contact angles.

Length L	I_1	I_2	I_3	I_4
4	0.7913	-0.7913	-0.4033	-0.4033
6	0.7196	-0.7196	-0.1967	-0.1967
8	0.6658	-0.6658	-0.0125	-0.01248
10	0.6630	-0.6630	-0.0001	-0.0001

Table 4.10

Evaluations of the integrals as a function of the cavity length. External heating of type E. Fixed contact angles.

Length L	I_1	I_2	I_3	I_4
4	0.9113	-0.9113	-0.7168	-0.7168
6	0.9264	-0.9264	-0.7434	-0.7434
8	0.9208	-0.9208	-0.7244	-0.7244
10	0.9206	-0.9206	-0.7236	-0.7236

Table 4.11

Evaluations of the integrals as a function of the cavity length. External heating of type A. Fixed contact points.

Length L	I_1	I_2	I_3	I_4
10	1.870	-1.870	-6.238	-6.238
20	3.748	-3.748	-24.98	-24.98
30	5.623	-5.623	-56.23	-56.23

Table 4.12

Evaluations of the integrals as a function of the cavity length. External heating of type B. Fixed contact points.

Length L	I_1	I_2	I_3	I_4
4	2.954	-2.954	-4.021	-4.021
6	6.704	-6.704	-13.48	-13.48
8	11.95	-11.95	-31.93	-31.93
10	18.70	-18.70	-62.38	-62.38
11	22.64	-22.64	-83.05	-83.05

Table 4.13

Evaluations of the integrals as a function of the cavity length. External heating of type C. Fixed contact points.

Length L	I_1	I_2	I_3	I_4
4	-3.311	-3.311	7.585	-7.585
6	-4.076	-4.706	17.04	-17.04
8	-5.528	-5.528	27.61	-27.61

Table 4.14

Evaluations of the integrals as a function of the cavity length. External heating of type D. Fixed contact points.

Length L	I_1	I_2	I_3	I_4
4	0.7913	-0.7913	-0.4033	-0.4033
6	0.7196	-0.7196	-0.1967	-0.1967
8	0.6658	-0.6658	-0.0125	-0.01248
10	0.6630	-0.6630	-0.0001	-0.0001

Table 4.15

Evaluations of the integrals as a function of the cavity length. External heating of type E. Fixed contact points.

Length L	I_1	I_2	I_3	I_4
4	0.9113	-0.9113	-0.7168	-0.7168
6	0.9264	-0.9264	-0.7434	-0.7434
8	0.9208	-0.9208	-0.7244	-0.7244
10	0.9206	-0.9206	-0.7236	-0.7236

The above discussion shows that integrals I_1, I_2, I_3 and I_4 can be used for a relatively simple prediction of whether a particular heating can generate large distortions (and possible break-up) of the interface.

4.5 Concluding Remarks

Analysis of thermocapillary effects in an infinite liquid layer in the absence of gravity was carried out. It was shown that the layer may exist only if the external temperature field satisfies existence conditions. The explicit form of these conditions was given in the case of negligible

convective transport. The form of the existence conditions shows that it may not be possible to enforce them in the case of a general flow (i.e. with convective effects present).

Analysis of a finite layer subject to carefully selected types of external heating was also carried out. Results show that if the external temperature field does not satisfy the existence conditions determined in the case of an infinite layer, large interfacial deformations occur, leading to break-up of the layer if the cavity is made sufficiently long. Since the temperature fields satisfying the existence conditions are rather unusual, the most likely response of the layer to an external heating in the case of a real experiment would consist of large interfacial distortions and, possibly, break-up of the layer.

CHAPTER 5

NUMERICAL RESULTS FOR NON-ZERO REYNOLDS NUMBER SITUATIONS

5.1 Introduction

In Chapter 4, thermocapillary convection in liquid layers was analyzed. The analysis was focused on the Stokes (Reynolds number Re=0) and conduction (Marangoni number Ma=0) limits. It was shown that the liquid layers would exist in a continuous form only if the external temperature field satisfied existence conditions. For finite liquid layers, large interface deformations might occur if the external temperature did not satisfy the existence conditions (determined in the case of an infinite layer). These deformations lead to break-up of the layer if the cavity was made sufficiently long. Since the temperature fields satisfying the existence conditions were unusual, the most likely response of the layer to an external heating in the case of a real experiment was expected to consist of large interfacial distortions and, possibly, break-up of the layer.

Another issue that remains unsolved is the question of the effects of convective transport on the interface deformation and on the convection in the interior of the

liquid. In particular, it remains to be determined: (i) whether it is possible to diagnose the possible appearance of large interfacial distortions for $Re \neq 0$, (ii) how an increase of Re affects interface deformation (qualitatively and quantitatively) and (iii) are there any new flow phenomena associated with the presence of convective effects such as the possible appearance of non-unique solutions. Because of the large number of parameters present in the problem, all conditions will be kept the same as in Chapter 4 and the investigation will include effects of cavity length, various types of external heating, different contact conditions, and variations of capillary number and Reynolds number.

Thermocapillary convection at non-zero Reynolds numbers has been studied previously by various authors with Re up to 10^5 (Rivas & Ostrach, 1989; Hadid and Roux, 1992; Laure et. al., 1990; Hadid & Roux, 1990; Carpenter and Homsy, 1990; Rivas, 1991; Zebib et al, 1985; Cowley and Davis, 1983). Results available in the literature were obtained with assumption of small (i.e. negligible) interface deformation, and, therefore, they can provide information about convection patterns only. It is not possible to determine whether these results provide an accurate description of the convection because conditions under which small deformation assumption is valid were not specified.

In order to simplify the following discussion, only the cavities whose interfaces are flat under isothermal conditions, i.e.,

$$h_0(x) = 1 \tag{5.1}$$

will be considered. These cavities are subject to an external heating and the resulting shape of the interface (including large deformations) is determined numerically using the algorithm described in Chapter 3. The response of the liquid to four types of external heating shown in Table 4.1 (without considering type A) will be investigated. In order to limit the number of parameters, the analysis will be focused on the case of Ma=0, Bi=∞. This makes the temperature of the interface equal to the temperature of the gas phase $T_g(x)$.

5.2 Variation of the Interface Deformation as a Function of the Reynolds Number

Figures 5.1-5.8 display results of the direct numerical simulation of the flow problems corresponding to the temperature distributions B-E, respectively. Calculations shown were obtained for Ca=0.024 and for the interface that was initially flat (Eq. 5.1). Results shown in Figures 5.1, 5.3, 5.5, and 5.7, for the fixed contact point cases demonstrate that the interface undergoes large deformations

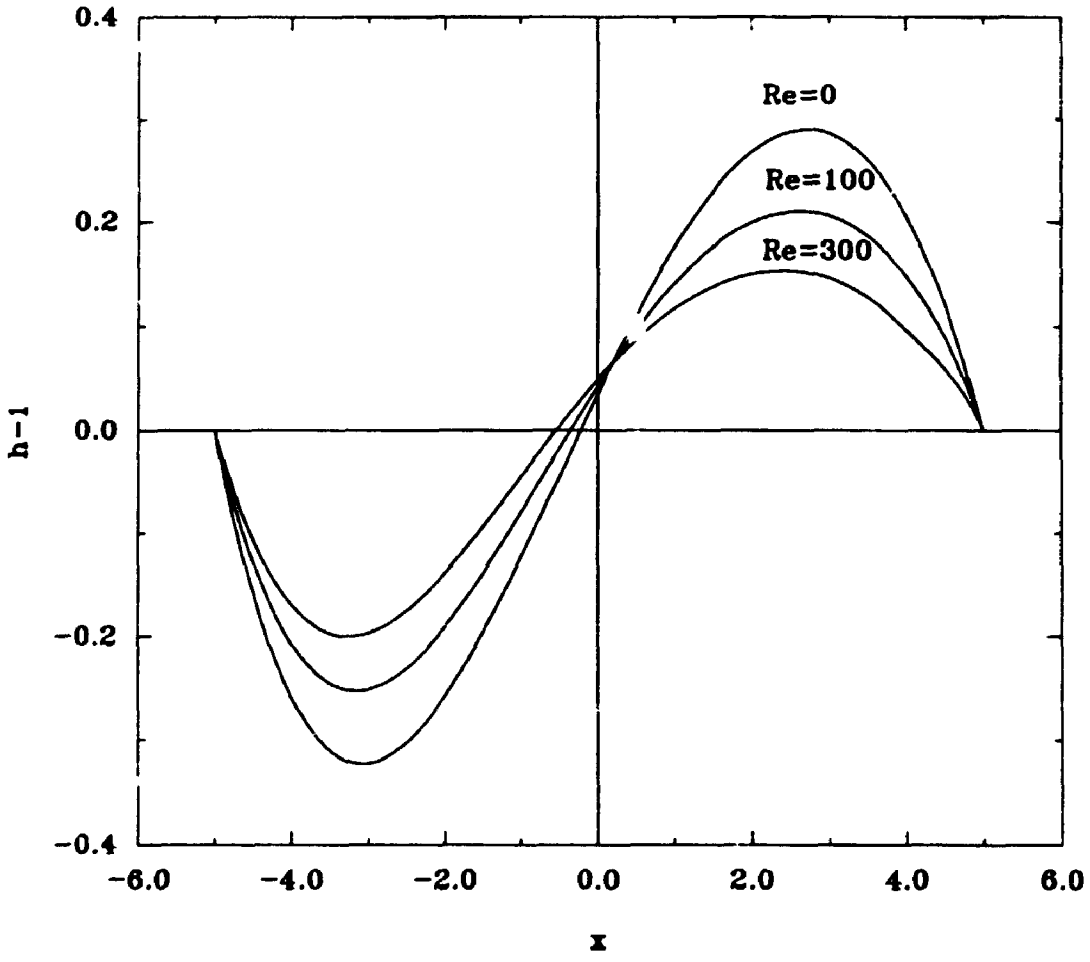

Figure 5.1 Interface deformation pattern. External heating of type B: $T_s(x)=-x$. Ma=0, Bi=∞, Ca=0.024, fixed contact points (h(-1/2L)=h(1/2L)=1).

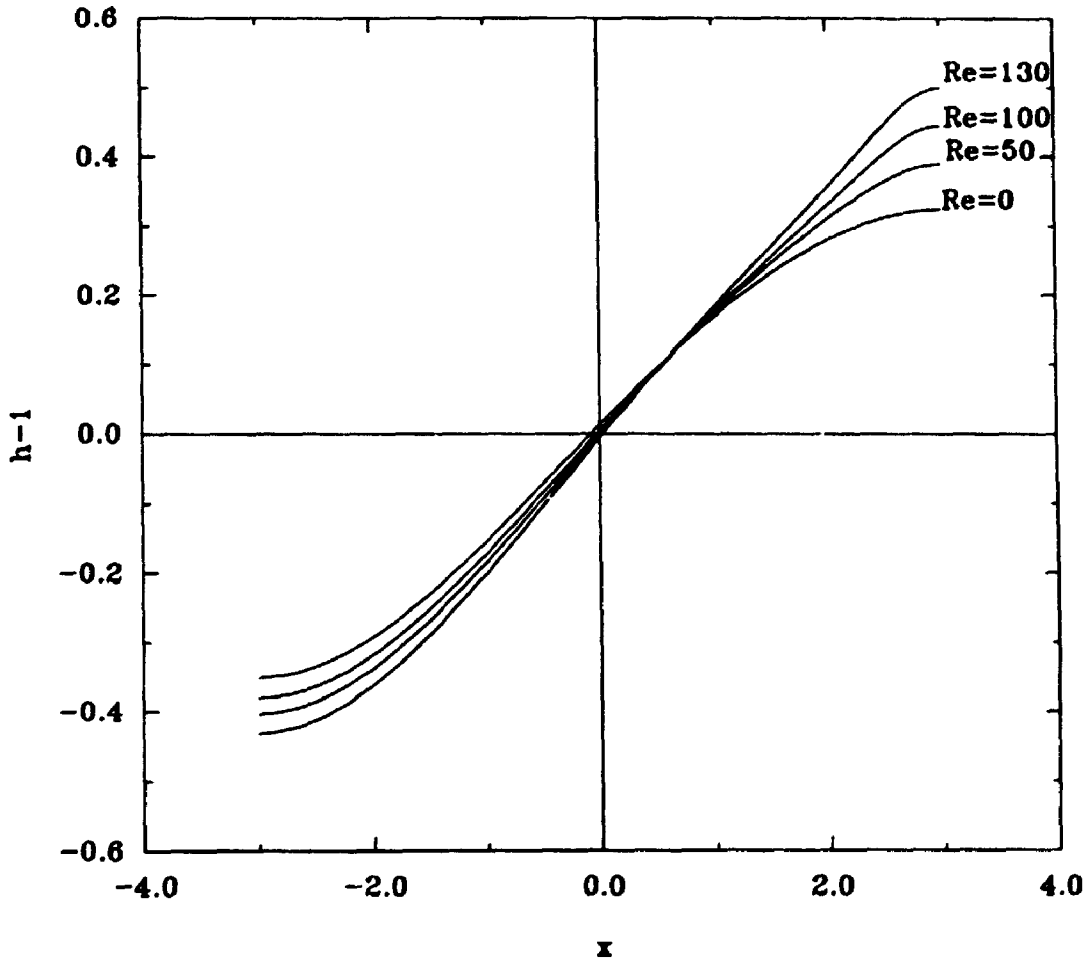

Figure 5.2 Interface deformation pattern. External heating of type B: $T_g(x)=-x$. Ma=0, Bi=∞, Ca=0.024, fixed contact angles ($h_x(-1/2L)=h_x(1/2L)=0$).

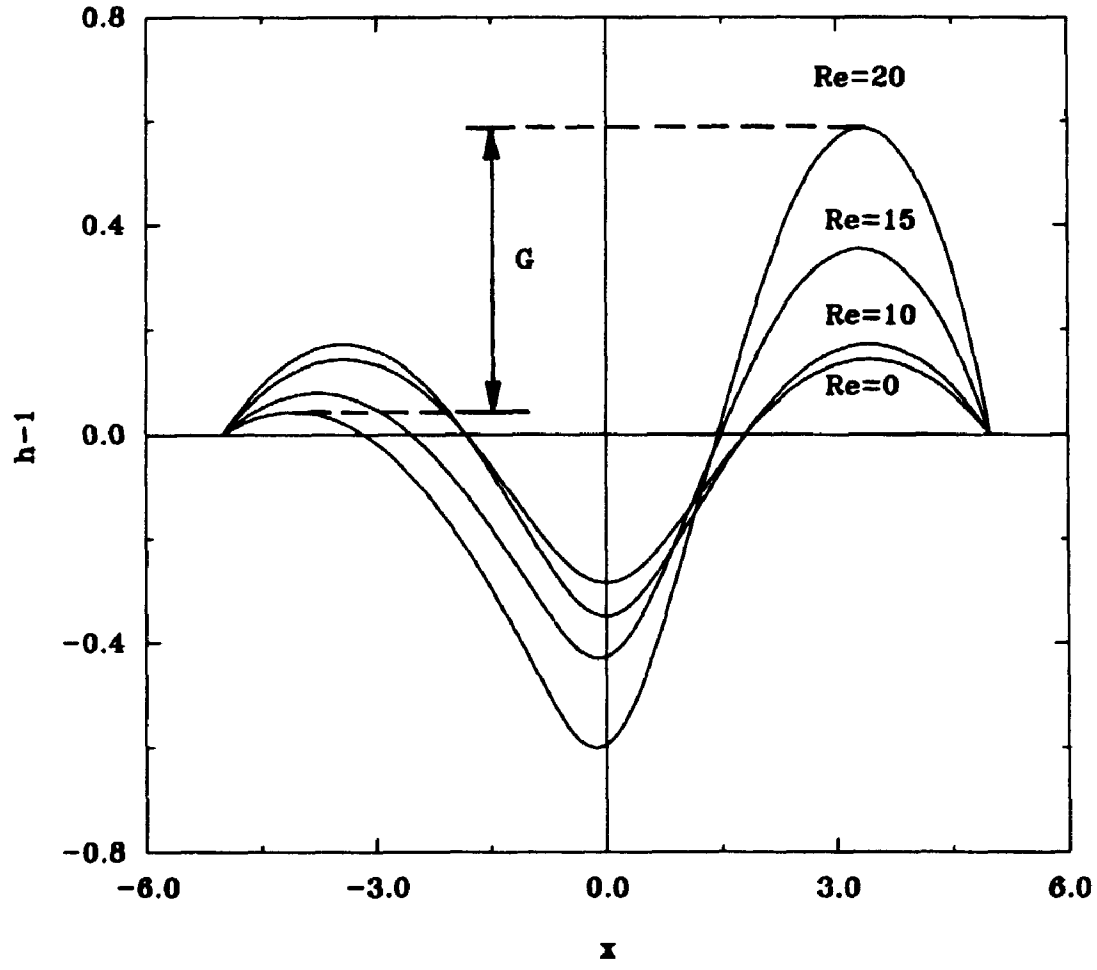

Figure 5.3 Interface deformation pattern. External heating of type C: $T_g(x)=10e^{-x^2}$, fixed contact points. All other conditions as in Fig. 5.1.

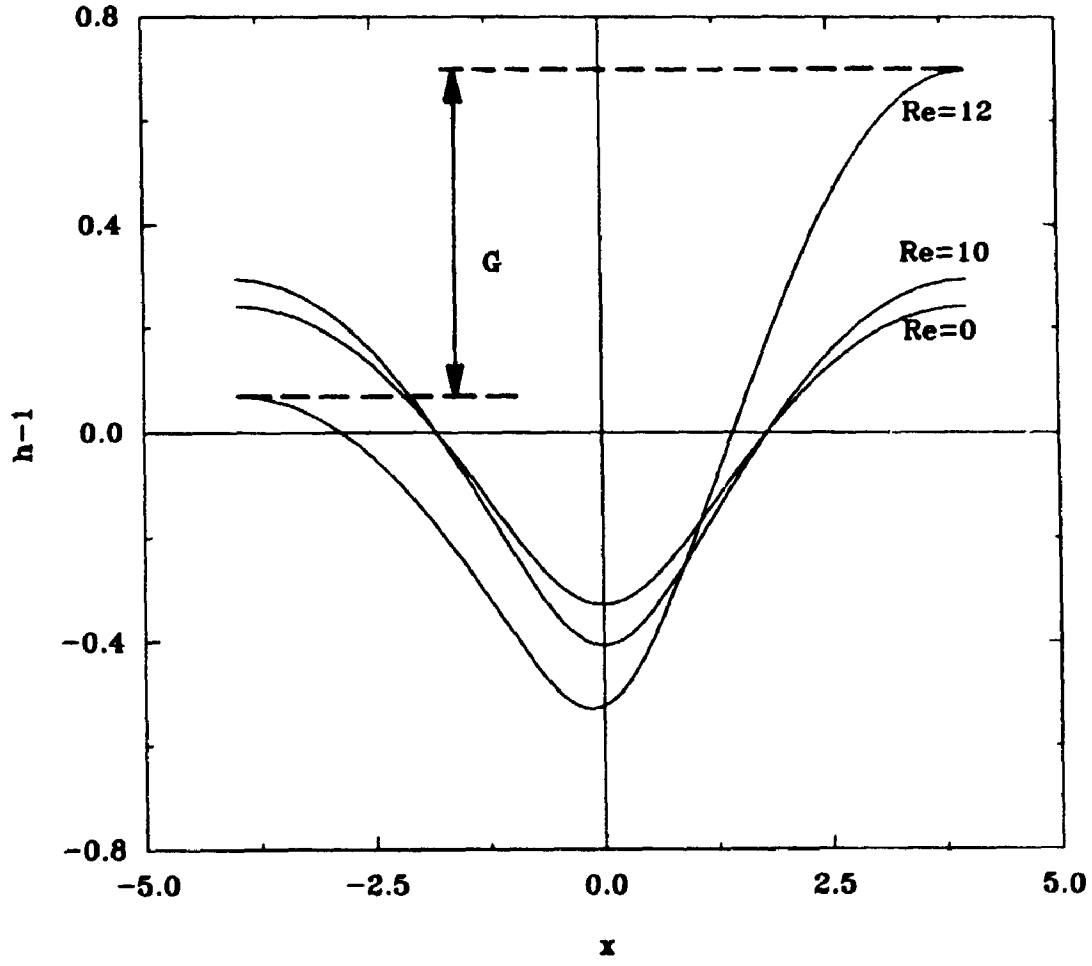

Figure 5.4 Interface deformation pattern. External heating of type C: $T_s(x)=10e^{-x^2}$, fixed contact angles. All other conditions as in Fig. 5.2.

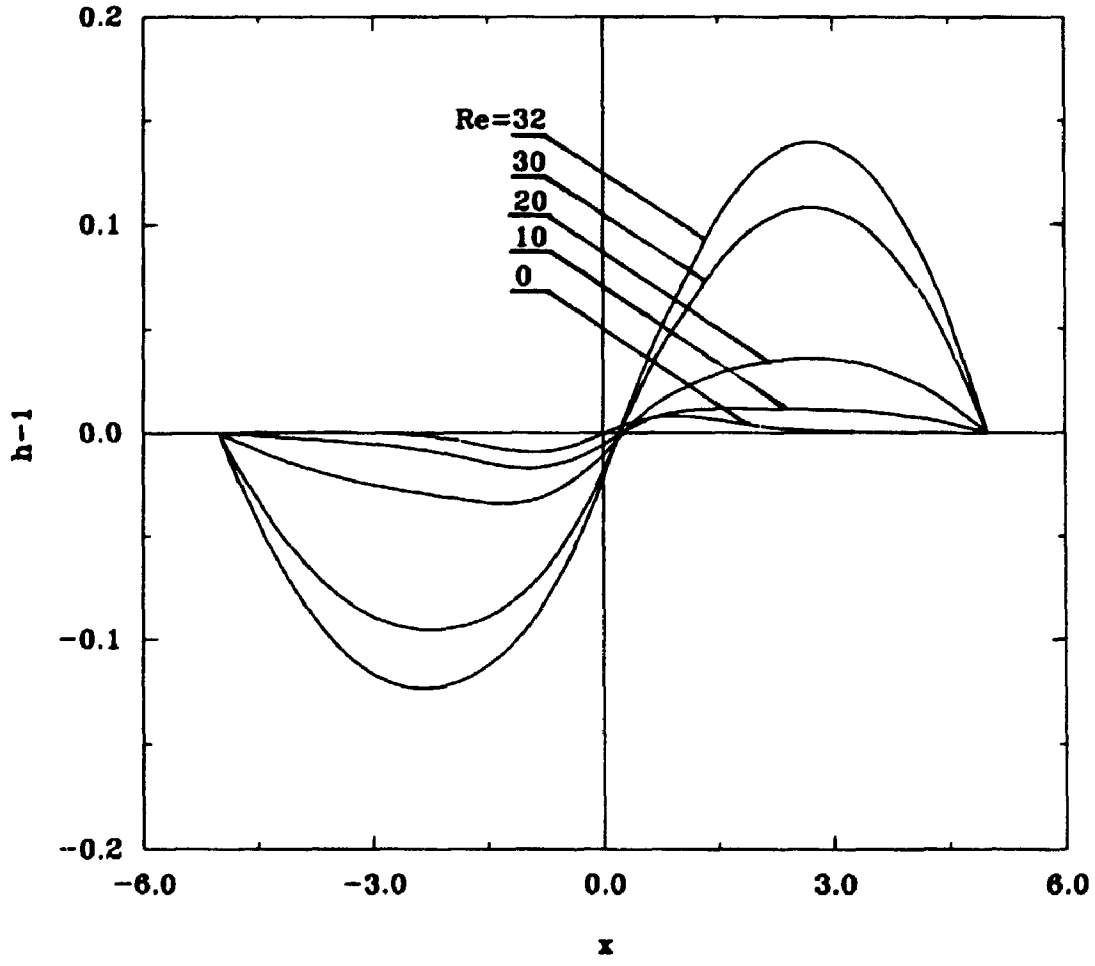

Figure 5.5 Interface deformation pattern. External heating of type D: $T_g(x)=(4x^3-6x)e^{-x^2}$, fixed contact points. All other conditions as in Fig. 5.1.

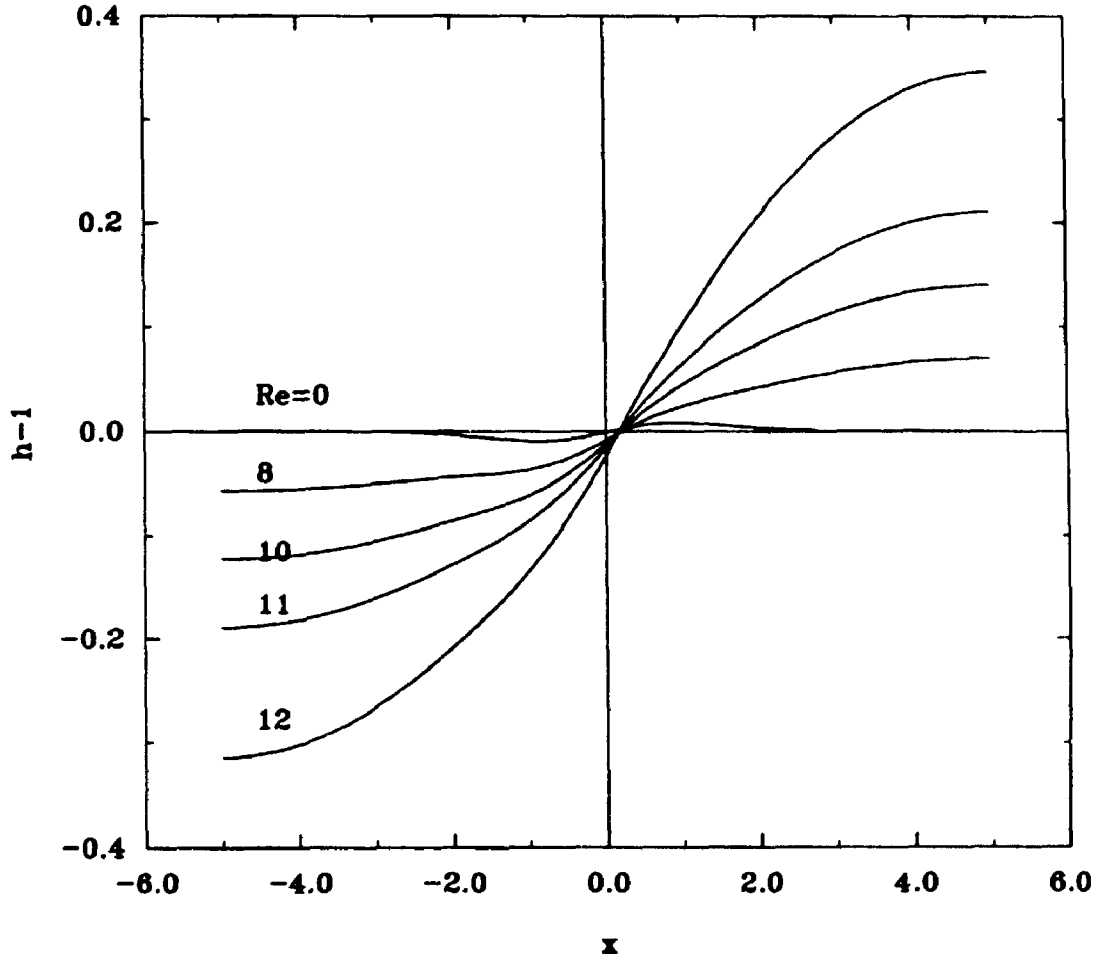

Figure 5.6 Interface deformation pattern. External heating of type D: $T_g(x)=(4x^3-6x)e^{-x^2}$, fixed contact angles. All other conditions as in Fig. 5.2.

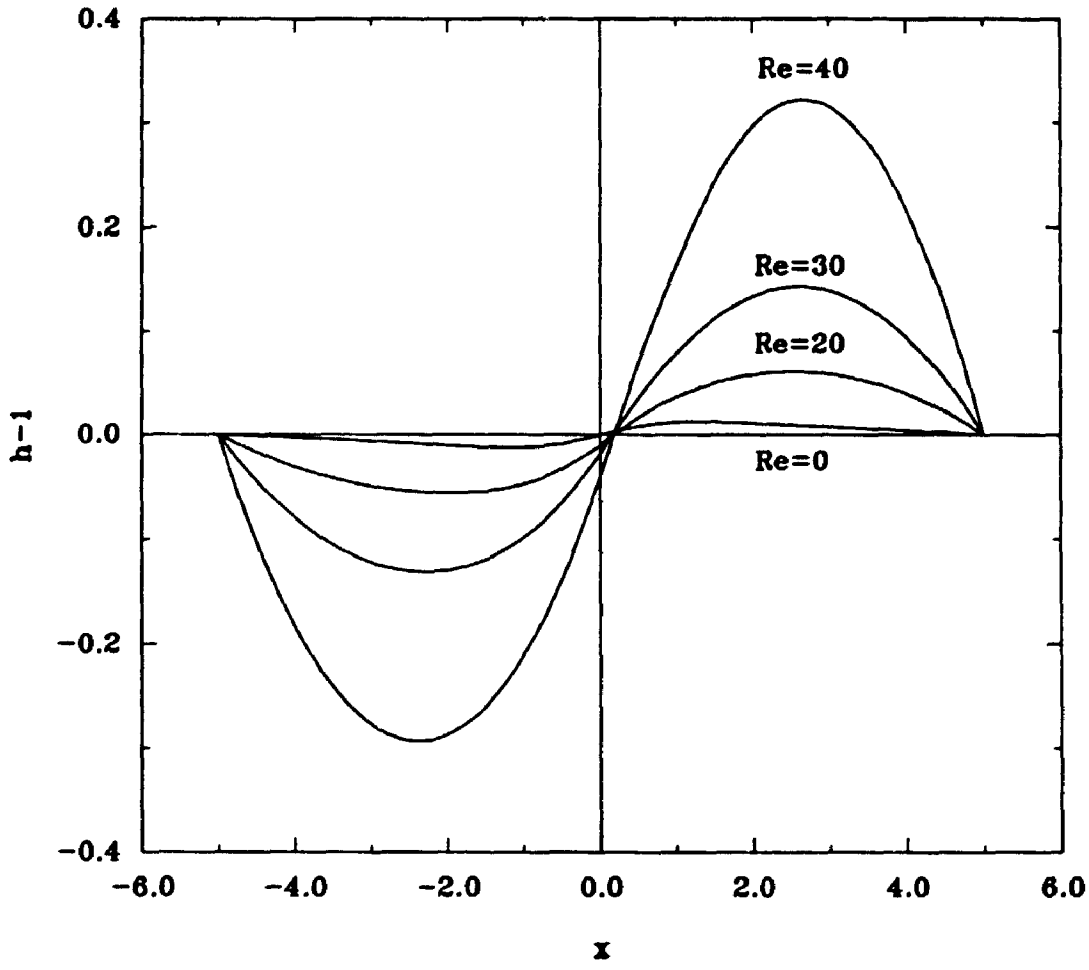

Figure 5.7 Interface deformation pattern. External heating of type E: $T_g(x)=(4x^3-6x)e^{-1.5x^2}$, fixed contact points. All other conditions as in Fig. 5.1.

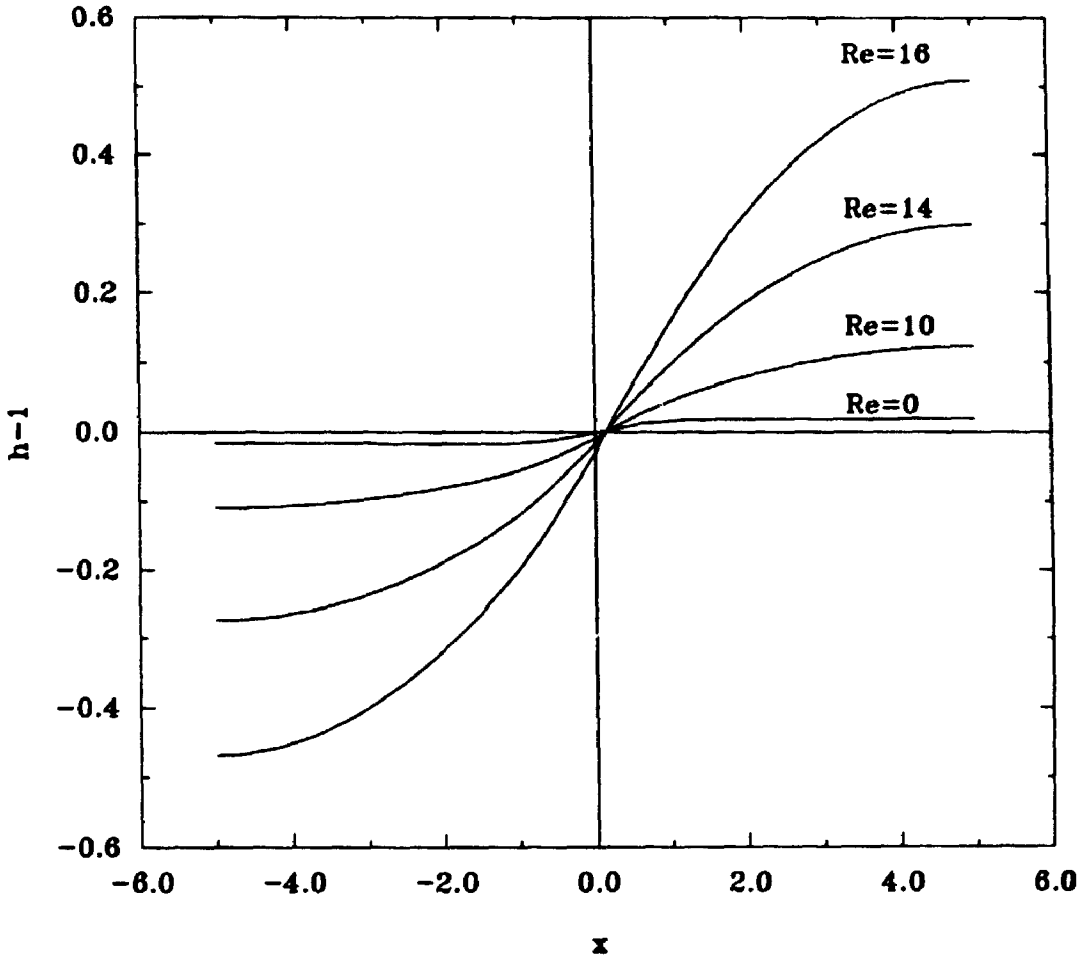

Figure 5.8 Interface deformation pattern. External heating of type E: $T_g(x)=(4x^3-6x)e^{-1.5x^2}$, fixed contact angles. All other conditions as in Fig. 5.1.

and that an increase of the Reynolds number generally increases the magnitude of the deformation. This increase is a strong function of the functional form of the external temperature field. Increase of Re from 0 to 10 doubles the magnitude of the deformation induced by heating C to 40% of the initial cavity depth (Figure 5.3). Change of Re from 0 to 30 increases the deformation induced by heating D from being negligible to almost 15% of the initial cavity depth (Figure 5.5), while in the case of heating E the deformation increases from being negligible to almost 30% of the original depth when Re increases from 0 to 40 (Figure 5.7). Thus, in all these cases, deformation is very sensitive to changes of Re. In contrast, results shown in Figure 5.1 demonstrate that the deformation actually decreases with an increase of Re when heating of type B is applied, and this deformation is comparatively insensitive to variations of Re (it takes an increase of Re from 0 to 300 in order to reduce deformation by 50%). This is a peculiar case and will be discussed again later.

Change of the contact conditions, from fixed contact points into fixed contact angles, increases the magnitude of the deformation induced by all types of heating being studied (Figure 5.2, 5.4, 5.6, and 5.8). In all cases, an increase of Re increased the magnitude of the deformation. This increase is modest for heating B (change of Re from 0 to 130 doubles

the magnitude of deformation - Figure 5.2) and it is very large for the remaining types of heating (see Figures 5.4, 5.6, and 5.8). These results show that the interface deformation is very sensitive to changes of Re in the fixed contact angle cases.

The reasons behind the increase in interface deformation with increasing Re can be explained by analyzing the pressure distribution at the interface. Figure 5.9 shows the pressure induced by heating D in the case of fixed contact point cases. When Re=0, the flow pattern is such that the pressure decreases to zero away from the heated area (as $x \rightarrow \pm \frac{1}{2}L$) and deformation remains small (as predicted by the analysis of Chapter 4), Figure 5.5. An increase of Re changes the flow pattern and leads to a constant non-zero pressure away from the heated area. This is the effect that produces large interface distortion.

The deformation induced by heating B (and its decrease with increase Re in the fixed point cases, Figure 5.1) will be discussed now. The reader may recall that in the present analysis only one parameter varies while all others are fixed. An increase of Re while keeping Ca fixed corresponds to a decrease of μ (see description of scaling in Chapter 2). This should lead to a reduced longitudinal pressure gradient in the cavity. The calculated pressure distribution along the

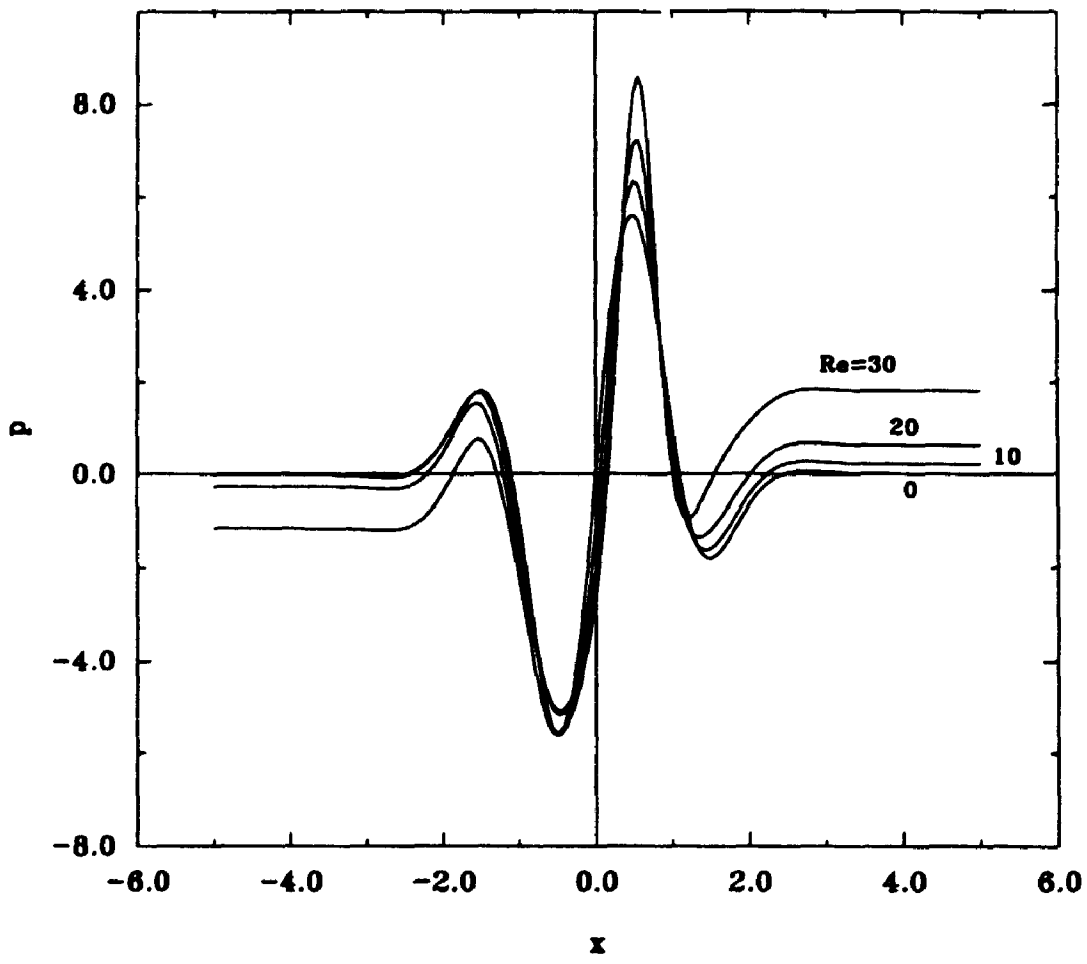

Figure 5.9 Interface pressure distribution. External heating of type D. Ma=0, Bi=∞, Ca=0.024, L=10, fixed contact point cases, direction solution.

interface in the fixed point cases is shown in Figure 5.10. The flow field can be divided into the core zone (where the pressure gradient is almost constant and the velocity field is well approximated by the Poiseuille solution with zero mass flux) and two turning zones. The pressure gradient in the core zone decreases with an increase of Re (as expected), while pressure peaks in the turning zones increase. Because the ends of the interface (where the pressure is high) are fixed, the magnitude of the deformation is determined by the pressure in the core zone. This results in a decrease of the deformation as Re increases. The same pressure distribution (in qualitative terms) is observed in the fixed contact angles cases (Figure 5.11). Since the ends of the interface (where the pressure is high) are allowed to move, the overall interface deformation increases as Re increases (see Figure 5.1).

The results discussed so far in this chapter show that an increase of Re increases interface deformation. The calculations are conservative as far as the magnitude of the deformation is concerned because Ca is kept constant. It has been shown previously that an increase of Ca and Re together would magnify this effect. This case is of interest because it can be interpreted as corresponding to increasing magnitude of heating (while all other parameters are kept constant). Evolution of the shape of the interface as a function of Re

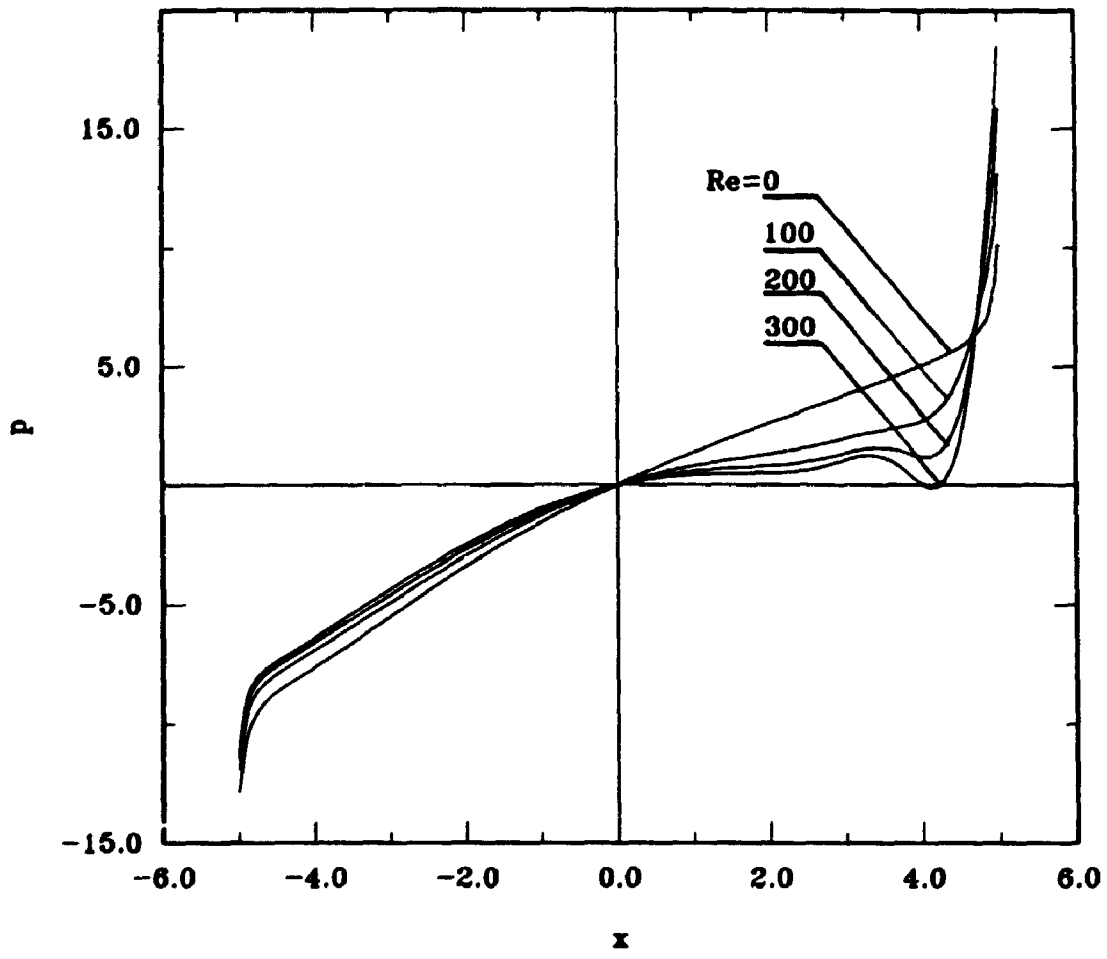

Figure 5.10 Interface pressure distribution. External heating of type B. Ma=0, Bi=∞, Ca=0.024, L=10, fixed contact points.

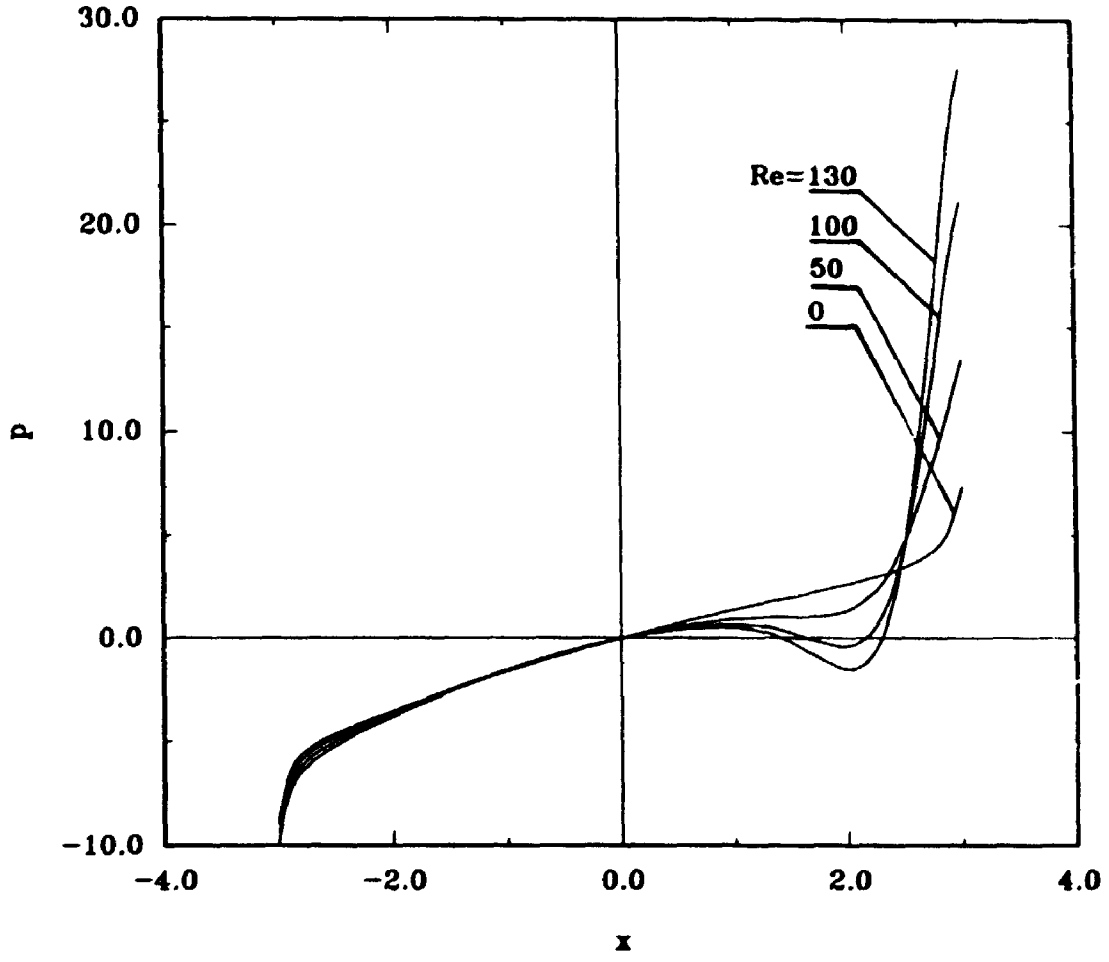

Figure 5.11 Interface pressure distribution. External heating of type B. Ma=0, Bi=∞, Ca=0.024, L=6, fixed contact angles.

and Ca for heating B and fixed constant point cases is shown in Figure 5.12. The calculation started with Ca=0.001 and Re=5, and then both parameters were increased by the same mount (i.e., $\gamma\Delta T$ increase). Results demonstrate a very rapid increase in the magnitude of the interface deformation.

In summary, one may conclude that (even a modest) increase of Re significantly increases the magnitude of the interface deformation. The rate of the increase depends strongly on the functional type of the external temperature field and on the type of contact conditions.

5.3 Small Interface Deformation

It is rather obvious that it must be possible to have an external temperature field that induces only small interface deformation. Results shown in Figures 5.1-5.8 suggest that such a temperature field may have to have a different functional form for different values of Re, even if all other parameters are fixed.

Conditions guaranteeing small interface deformations are expressed by Equation (4.6) to (4.9). Because of their implicit form, it is not possible to predict a priori whether any particular heating can satisfy them. One possible approach is to use conditions (4.16) and (4.17) determined for Re=0 and

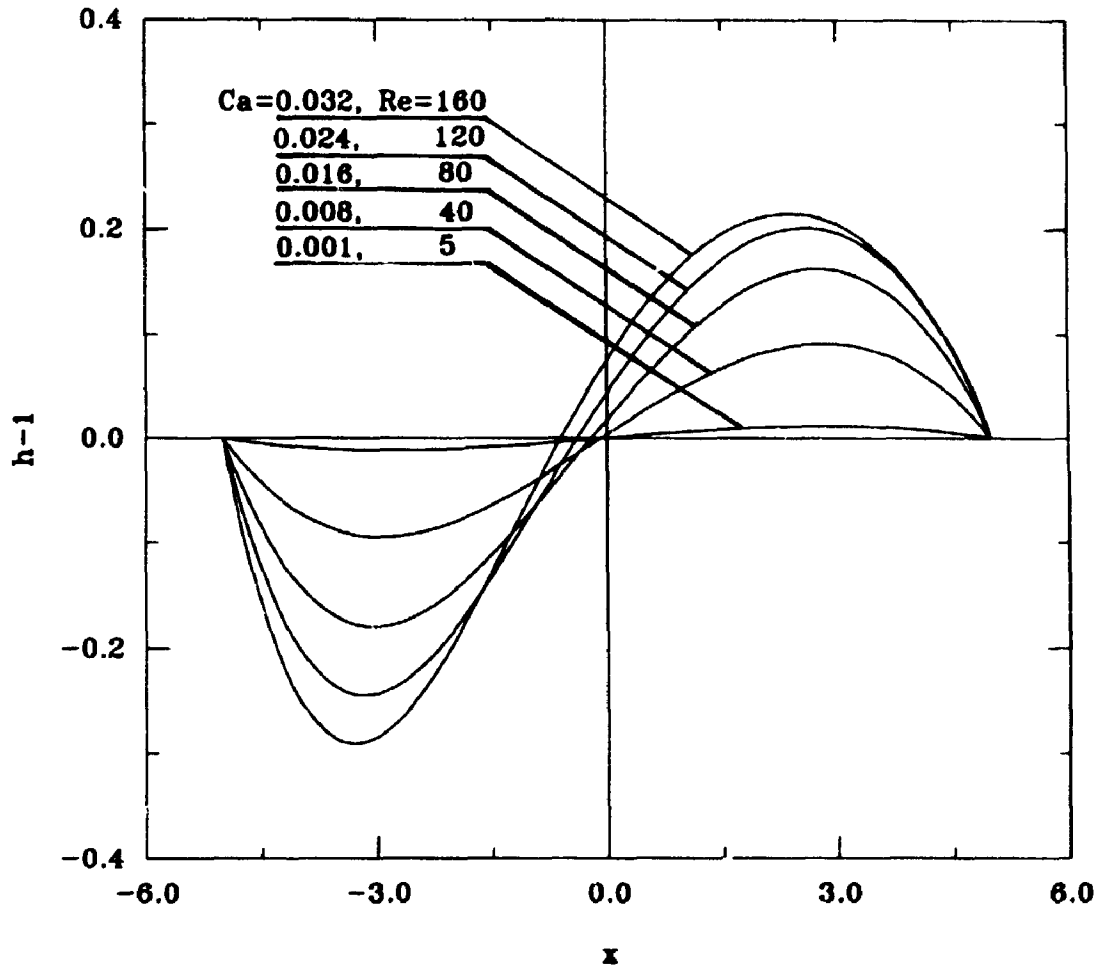

Figure 5.12 Interface deformation pattern as a function of Re and Ca. Heating B, L=10, Ma=0, Bi=∞, fixed contact points.

to check whether they can provide any useful guideline for $Re \neq 0$. Heating D and E satisfy conditions (4.16) and (4.17), but the results obtained in these cases (see Figure 5.5-5.8) demonstrate that a very rapid increase of the magnitude of the deformation takes place when Re increases. Thus, conditions (4.16) and (4.17) do not offer any insight into what happens when $Re \neq 0$.

The possible occurrence of small deformations can be diagnosed, without solving the complete problem, by assuming the existence of a small deformation, then carrying out the solution as described in Chapter 3 and, at the end, evaluating integrals appearing in (4.6) to (4.9) (thus checking the existence conditions a posteriori). If these integrals diverge as a function of Re, clearly, small deformations cannot exist. This procedure requires a numerical solution of the full Navier-Stokes equations, but the geometry of the solution domain is simple and the location of the boundary conditions is fixed. Thus, this approach is much cheaper than the direct solution of the complete moving boundary problem using the method described in Chapter 3. The indirect diagnosing of the behaviour of the interface, as described above, could be sufficient for many applications.

Fixed contact point cases will be considered first. The utility of the above diagnostics is demonstrated by the

results of calculations give in Table 5.1-5.4. The results, which were obtained for cavity length L=10, clearly demonstrate divergent behaviour of I_1, I_2, I_3 and I_4 as a function of Re for heatings C-E. Thus, the interface deformation cannot be small, as confirmed by the results of the direct numerical simulation displayed in Figures 5.3-5.8. Heating B is somewhat peculiar, as discussed in Section 5.1.

The utility of above diagnostics for fixed contact angles is again demonstrated by the results of calculations (Table 5.5-5.8). The above results are for the same cavity length as shown in Figures 5.1-5.8. The divergent behaviour of the diagnostic integrals is clearly visible, and the occurrence of large deformations is confirmed by the results displayed in Figures 5.1-5.8.

The above discussion shows that intergrals I_1, I_2, I_3, and I_4 can be used for a relatively simple prediction of whether a particular heating can generate large distortions of the interface. In the case of doubt, a full solution of the flow equations, as described in Chapter 3, has to be carried out.

Table 5.1

Evaluations of the integrals as a function of the Reynolds number. External heating of type B. Fixed contact points.

Re	I_1	I_2	I_3	I_4
0	18.70	-18 70	-62.38	-62.38
25	18.53	-18.84	-61.51	-63.11
50	18.32	-18.32	-60.47	-63.71
75	18.06	-18.99	-59.29	-64.19
100	17.77	-19.01	-57.99	-64.55

Table 5.2

Evaluations of the integrals as a function of the Reynolds number. External heating of type C. Fixed contact points.

Re	I_1	I_2	I_3	I_4
0	-5.930	-5.930	38.03	-38.03
10	-7.776	-7.776	49.04	-49.04
20	-9.486	-9.486	59.01	-59.01
30	-10.86	-10.86	66.83	-66.83

Table 5.3

Evaluations of the integrals as a function of the Reynolds number. External heating of type D. Fixed contact points.

Re	I_1	I_2	I_3	I_4
0	0.6630	-0.6630	0	0
10	0.7474	-1.090	0.4695	-1.756
20	1.254	-1.929	-0.1273	-4.506
30	1.999	-2.984	-1.320	-7.704

Table 5.4

Evaluations of the integrals as a function of the Reynolds number. External heating of type E. Fixed contact points.

Re	I_1	I_2	I_3	I_4
0	0.9206	-0.9206	-0.7236	-0.7236
10	1.085	-1.313	-0.6936	-2.208
20	1.724	-2.178	-1.901	-4.915
30	2.663	-3.339	-3.881	-8.352

Table 5.5

Evaluations of the integrals as a function of the Reynolds number. External heating of type B. Fixed contact angles.

Re	I_1	I_2	I_3	I_4
0	6.704	-6.704	-13.48	-13.48
25	6.684	-6.684	-13.23	-13.65
50	6.626	-6.626	-12.92	-13.76
75	6.535	-6.535	-12.57	-13.81
100	6.412	-6.412	-12.19	-13.80

Table 5.6

Evaluations of the integrals as a function of the Reynolds number. External heating of type C. Fixed contact angles.

Re	I_1	I_2	I_3	I_4
0	0	0	16.56	-16.56
10	0	0	20.74	-20.74
20	0	0	24.25	24.25
30	0	0	26.76	26.76

Table 5.7

Evaluations of the integrals as a function of the Reynolds number. External heating of type D. Fixed contact angles.

Re	I_1	I_2	I_3	I_4
0	0.6630	-0.6630	0	0
10	0.9187	-0.9187	-0.0412	-0.1328
20	1.591	-1.591	-0.9706	-3.662
30	2.492	-2.492	-2.552	-6.472

Table 5.8

Evaluations of the integrals as a function of the Reynolds number. External heating of type E. Fixed contact angles.

Re	I_1	I_2	I_3	I_4
0	0.9206	-0.9206	-0.7236	-0.7236
10	1.199	-1.199	-0.9791	-1.923
20	1.951	-1.951	-2.470	-4.347
30	3.001	-3.001	-4.725	-7.508

5.4 Non-uniqueness of Steady Solutions

In this Section, the possibility of a non-unique response of the liquid to external heating will be discussed. It will be demonstrated that the non-uniqueness occurs at very low Reynolds numbers, and its appearance is associated with the interface deformability. The following discussion will focus on the heating of type C (simulated point heating).

For system (3.6) to (3.16), its solutions ($\mathbf{x}$, $\mathbf{p}$) for a particular range of the values of vector $\mathbf{p}$ will be found. Here, $\mathbf{x}$ consists of values of ψ, ω and h, and $\mathbf{p}$ contains parameters L, Re, Ca. The total number of solutions varies as a function of vector $\mathbf{p}$. If more than one solution exists, then it is said that multiple solutions exist (non-uniqueness of solutions) for a given value of $\mathbf{p}$.

Usually, a bifurcation diagram is used in describing the multiplicity of solutions. A bifurcation diagram presents an overall picture of dependence of solution $\mathbf{x}$ on vector $\mathbf{p}$. Such a diagram is obtained by plotting a characteristic value of a solution. The dependence $\mathbf{x}(\mathbf{p})$ can consist of various branches, but it is unique on each particular branch.

A large number of numerical procedures can be used for finding the relation $\mathbf{x}(\mathbf{p})$. The simplest one, a sequential

procedure, is used in the present study. A certain interval of $\mathbf{p}$ values is divided by the nodes $\mathbf{p}_0$, $\mathbf{p}_1$, ..., $\mathbf{p}_n$ into sections. The solution $\mathbf{x}(\mathbf{p}_i)$, which is obtained by the method described in Chapter 3, is used as an estimate of the solution for $\mathbf{p}=\mathbf{p}_{i+1}$. This way the form of a single branch can be determined. But when one passes through a bifurcation point, the behaviour of the algorithm is more or less random.

5.4.1 Existence of Non-unique Steady Solutions

Consider the case in which L=10, Ca=0.024, and Re=20. According to the discussion in Section 3.5.4, grid size was chosen as $\Delta\xi=1/20$ and $\Delta\eta=1/40$. The results shown in Figure 5.3 demonstrate that interface deformation has a symmetric form at Re=0. An increase of Re leads to an increase of the magnitude of the deformation, initially in a symmetric form and then, for higher Re, in an asymmetric form. The asymmetric shape shown in Figure 5.3 is characterized by the right bulge extending much further out as compared to the left bulge. This form will be referred to as the right asymmetry. The interface with the left bulge being larger than the right one for the same value of Re also was obtained. This shape will be referred as left asymmetry. Either one can be obtained by making minor changes in the algorithm such as, for example, changing the sweep direction in the Gauss-Seidel iteration

procedure. Therefore, the multiple solutions exist indeed for the present system.

5.4.2 Check of the Non-uniqueness Phenomena

In the above primary calculation, non-unique steady solutions have been found. The important question to be addressed now is confirmation that this non-uniqueness is the property of the physical system, and not a property of its numerical analog.

5.4.2.1 Effects of Convergence Criteria

The convergence criteria used in above section was $\varepsilon=10^{-6}$ (see Section 3.4). A series of calculations were carried out with ε reduced to 10^{-9}. The results showed that when ε was decreased, only the last few digits of the solution changed. When ε was less than 10^{-9}, the first eight digits did not change while the 9th digit changed randomly. Reduction of ε below 10^{-9} was counterproductive due to the finite resolution of the computer word and the finite accuracy of the algorithm.

5.4.2.2 Effects of Grid Density

The second check is to conduct computations on different grid sizes. The results are shown in Tables 5.9 and 10. It can

be seen that the maximum difference among different results are less than 2%. Figure 5.13 shows the interface obtained on different grid sizes. Again, it is found that when taking into account all constraints, the grid size $\Delta\xi$=1/20 and $\Delta\eta$=1/40 is the most optimal. From the above discussion, it can be concluded that the multiplicity of steady solutions is a property of the physical system.

5.5 Dependence of Steady Solution on Control Parameters

Conditions leading to the appearance of the non-unique solutions are well described by adopting the difference G between the height of the right and the left bulges (see

Table 5.9

Results obtained from different grid sizes

(Re=20, Ca=0.024, Bi=∞, L=10, fixed contact angles)

Grid Size		$\lvert\psi\rvert_{max}$	$\lvert\omega\rvert_{max}$	$\lvert h\rvert_{max}$	$\lvert p\rvert_{max}$
$\Delta\xi$	$\Delta\eta$				
1/20	1/20	0.1422	8,0067	1.5874	41.77
1/20	1/40	0.1445	8.0360	1.5869	41.39
1/40	1/40	0.1445	8.0361	1.5872	41.42
1/30	1/60	0.1450	8.0435	1.5869	41.33

Table 5.10

Relative difference between the results

(same conditions as in the Table 5.9)

Grid size		$\frac{\lvert\Delta\psi_{max}\rvert}{\lvert\psi\rvert_{max}}$	$\frac{\lvert\Delta\omega_{max}\rvert}{\lvert\omega\rvert_{max}}$	$\frac{\lvert\Delta h_{max}\rvert}{\lvert h\rvert_{max}}$	$\frac{\lvert\Delta p_{max}\rvert}{\lvert p\rvert_{max}}$
$\Delta\xi$	$\Delta\eta$	%	%	%	%
1/20	1/20	1.9	0.46	0.08	1.1
1/20	1/40	0.34	0.09	0.00	0.37
1/40	1/40	0.34	0.09	0.05	0.45

Figure 5.3) as a measure of asymmetry of the interface. In the following sections, the results will be presented in the form of bifurcation diagrams, with Ca, L or Re on the horizontal axis and G on the vertical axis.

Figure 5.14 shows bifurcation diagrams resulting from the increase of Re for various values of Ca. The complete diagram is shown only for Ca=0.024 and the discussion will focus on this case (only upper halves of the diagrams are shown for other values of Ca). The bifurcation appears to occur at Re≈14. Three flow patterns that may exist at Re=15.5 are

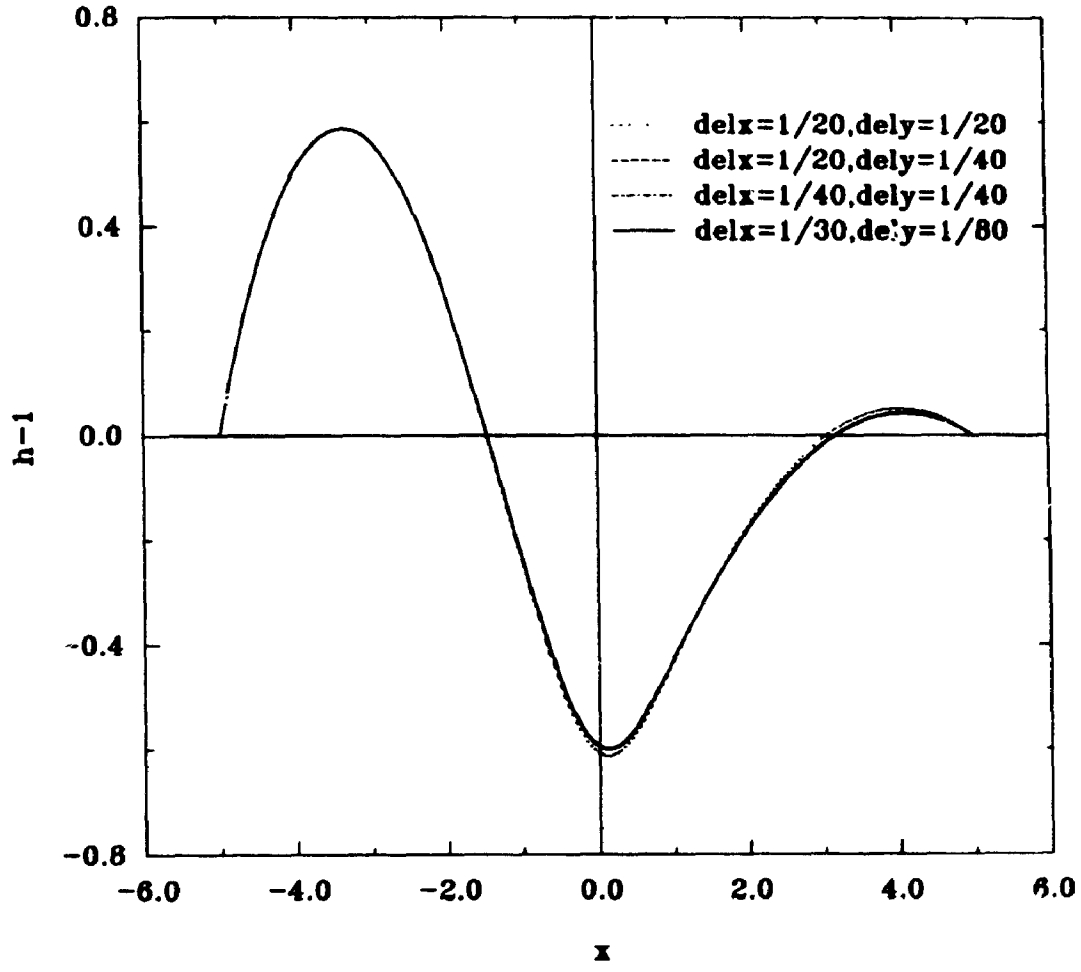

Figure 5.13 Interface deformation $h_1(x)$ obtained with different grid sizes. Heating C, L=10, Re=20, Ca=0.024, Ma=0, Bi=∞.

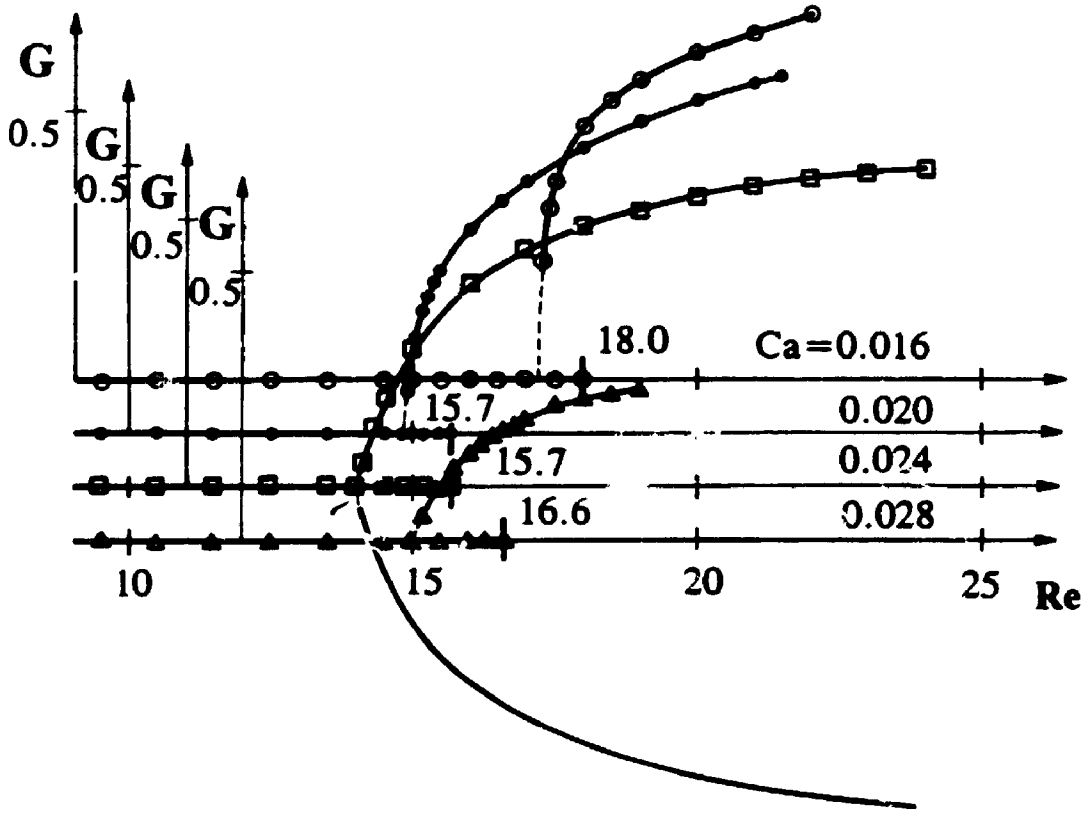

Figure 5.14 Bifurcation diagram describing existence of nonunique (symmetric and nonsymmetric) flow patterns induced by the external temperature of type C as a function of Reynolds number Re for various capillary numbers Ca. G denotes a measure of asymmetry (see Fig. 5.3). L=10, Ma=0, Bi=∞, fixed contact points. Complete diagram is shown only for Ca=0.024. Only upper halves of the diagrams are shown for other values of Ca. Discrete points shown on the diagrams correspond to computed solutions. ○ - Ca=0.016, • - Ca=0.020, □ - Ca=0.024, △ - Ca=0.028 Vertical bars show maximum values of Re for which we were able to compute symmetric solutions.

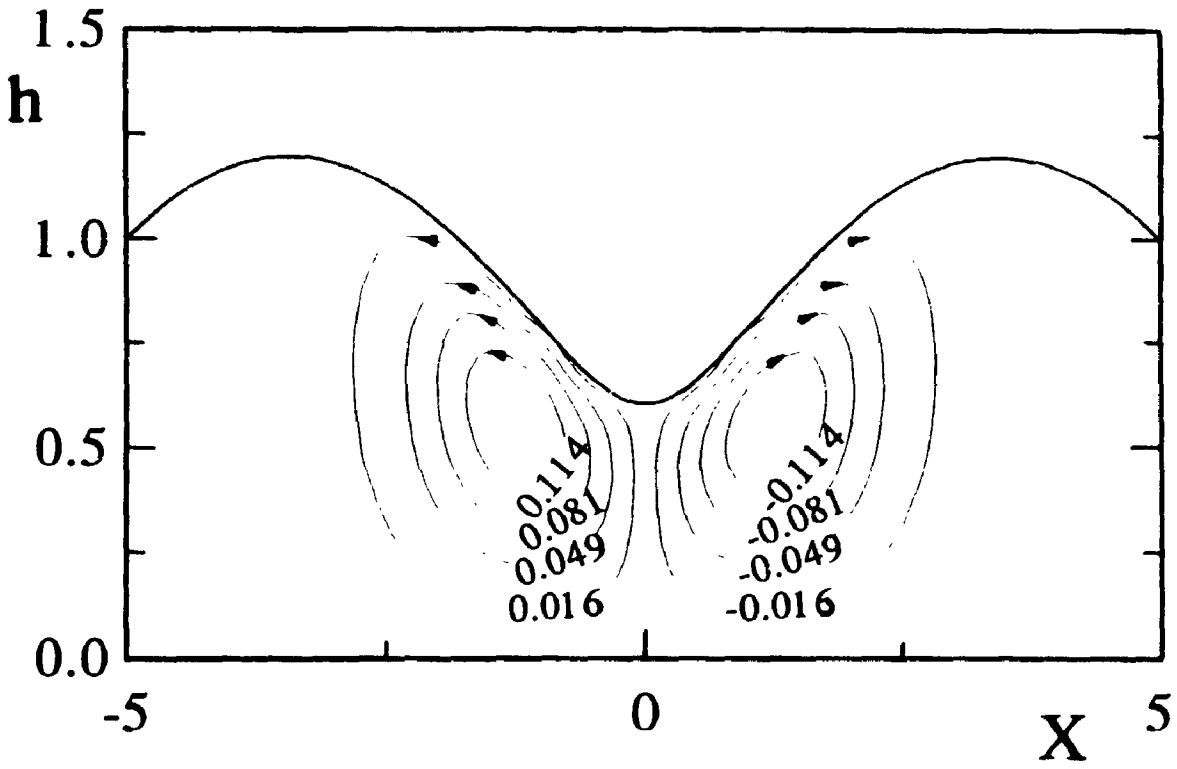

Figure 5.15A Flow pattern induced by the external temperature of type C. e=15.5, L=10, Ma=0, Bi=∞, Ca=0.024, fixed contact points, symmetric flow.

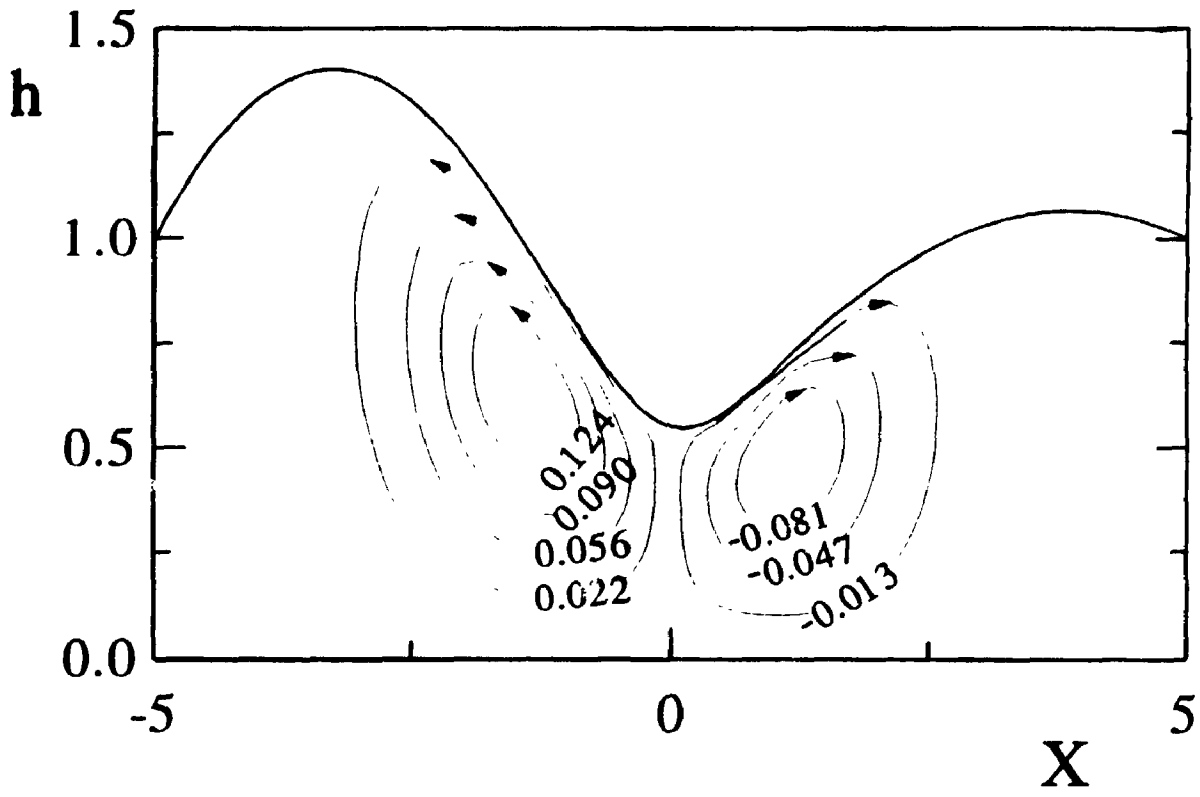

Figure 5.15B Flow pattern induced by the external temperature of type C. Re=15.5, L=10, Ma=0, Bi=∞, Ca=0.024, fixed contact points, asymmetric flow (left asymmetry).

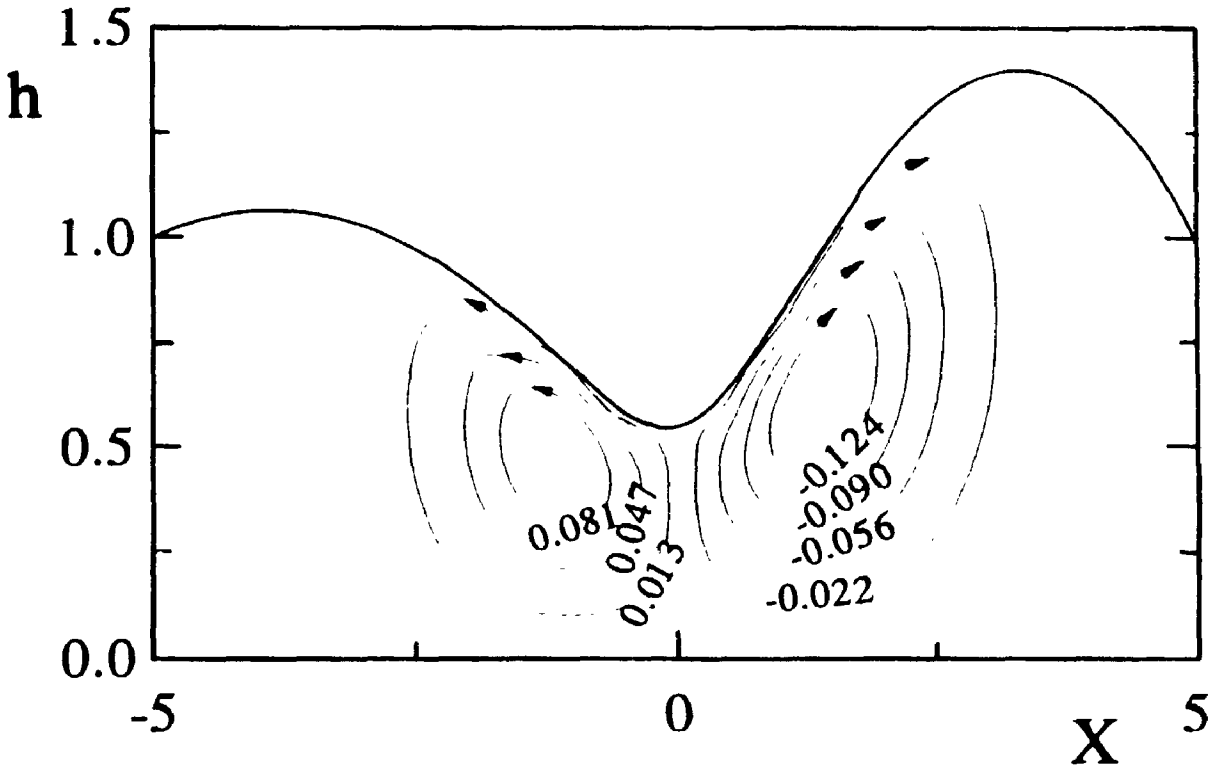

Figure 5.15C Flow pattern induced by the external temperature of type C. Re=15.5, L=10, Ma=0, Bi=∞, Ca=0.024, fixed contact points, asymmetric flow (right asymmetry).

displayed in Figure 5.15. The present calculations were able to compute symmetric solutions for Re up to Re=15.7 (by starting with Re=0 and computing a sequence of solutions with increasing Re and using the last solution as an initial guess for the solution corresponding to the next value of Re). For higher values of Re the iterative process would converge to either one of the asymmetric solutions (even when increasing Re by 0.1 and using strong under-relaxation of order 0.01). Asymmetric branches were traced by calculating asymmetric solutions for higher values of Re and then tracing these branches back by reducing Re. The asymmetric branches approach the symmetric one (within numerical error) at Re≈14. Thus it appears that the bifurcation has a supercritical character. It cannot, however, be excluded that the bifurcation occurs at Re≈15.7 (which is the last symmetric solution obtained) and has a subcritical character. Hundreds of solutions have been calculated and the experience is that while following the asymmetric branch it is possible to come arbitrarily close (within numerical error) to the symmetric one (at Re≈14). This points towards supercritical bifurcation. This point of view will be adopted and further discussion will be carried out with understanding that the final settling of this question requires linear stability analysis (not attempted here).

A short digression regarding our numerical algorithm is appropriate at this point. One may argue that an iterative

algorithm of the type used here should not be able to capture solutions corresponding to unstable branches. Thus, bifurcation occurs at Re=15.7 and is subcritical. This, however, may not be the case. It will be shown later in the text that the bifurcation occurs solely because of deformability of the interface. The part of the present algorithm that deals with the interface solves the deformation equation directly using the Newton-Raphson linearization and thus is capable of capturing unstable branches. The properties of the present algorithm, therefore, do not exclude the possibility of having supercritical bifurcation (which is the view adopted here as discussed earlier).

The deformability of the interface (or strength of the surface tension) is described by capillary number Ca (very small Ca corresponds to very strong mean surface tension and an interface that is "stiff"). The effect of changing of Ca is illustrated in Figure 5.14. The bifurcation is supercritical and of the pitch-fork type for all values of Ca investigated. The bifurcation Reynolds number and measure of asymmetry G are both non-monotonic functions of Ca; they at first increase and then decrease as Ca increases. Figure 5.16, which displays diagrams of G as a function of Ca for fixed Re, gives, perhaps, a more explicit view of the effects of Ca. For Ca sufficiently small, a unique symmetric solution is always

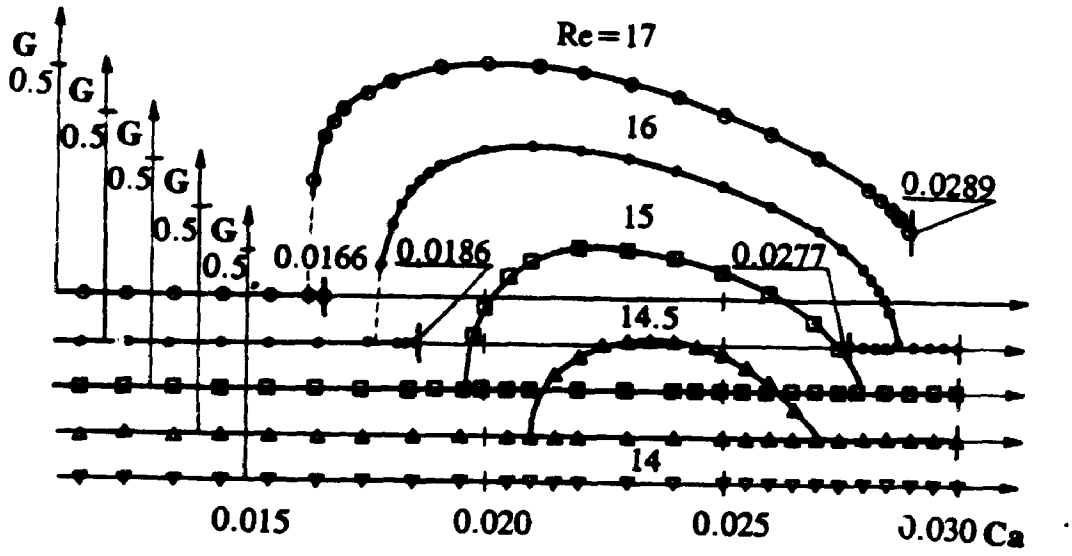

Figure 5.16 Bifurcation diagrams describing existence of nonunique flow patterns induced by the external temperature of type C as a function of capillary number Ca for various Reynolds numbers Re. G denotes a measure of asymmetry (see Fig. 5.3). L=10, Ma=0, Bi=∞, fixed contact points. Only upper halves of the diagrams are shown. Discrete points shown on the diagrams correspond to computed solutions. ○ - Re=17, • - Re=16, □ - Re=15, △ - Re=14.5, ▽ - Re=14. Vertical bars show the extent to which we were able to compute various branches.

obtained regardless of the value of Re. Thus, it can be concluded that non-unique solutions arise only because of deformability of the interface. These solutions appear only if Re is sufficiently large. For Re=14 no non-unique solutions were found within the range of values for Ca studied. At Re=14.5, a range of values of Ca was found where both symmetric and nonsymmetric solutions coexisted. At Re=15, a range of values of Ca was found where only nonsymmetric solutions exist. At Re=16 and Re=17, once the first bifurcation point was passed as Ca was increasing, essentially only asymmetric solutions can be obtained.

Figure 5.16 shows that it is difficult to make any general conclusions regarding how "stiffness" (or deformability) of the interface affects behaviour of the flow system. One trend is clear, that is, that only unique symmetric solutions can be obtained when the interface is sufficiently "stiff" (Ca sufficiently small). When the interface becomes more "elastic" (easier to deform), multiple solutions exist, however further increase of Ca leads to unique solutions again. The other trend that is clear is that for a sufficiently small Re we have only unique solutions. The smallest Reynolds number for which non-unique solutions were found is by itself very small (Re>14). An increase of Re was found to increase the asymmetry as measure by G (see Fig. 5.14) in all cases studied.

Figure 5.17 illustrates the evolution of the shape of the interface as Ca increases for a fixed value for Re=16. One may note an initial decrease (increase) of the left (right) bulge as computations move to the right along the asymmetric branch of the bifurcation diagram shown in Figure 5.16. It is followed by a reversed of this trend as the asymmetric branch approaches the symmetric one with further increase of Ca. The symmetric solutions at higher values of Ca give a much higher magnitude of the deformation as compared to the symmetric solution at low Ca. Figure 5.18 illustrates the same process at a slightly higher value of Re (Re=17). One may see that for a certain range of values of Ca, the left bulge completely disappears resulting in a qualitatively different topology of the interface.

Figure 5.19 illustrates the effect of changing length of the cavity (for fixed Ca=0.024). Bifurcation diagrams are qualitatively similar to those shown in Figure 5.14. The general trend is (in the range of parameters studied) that an increase of the length of the cavity makes it "more difficult" for non-unique solutions to appear, i.e., it increases the Reynolds number at which bifurcation takes place and reduces the magnitude of asymmetry G. In all cases, an increase of Re leads to an increase of G. The effects of Ca for different cavity lengths (for fixed Re=17) are illustrated in Figure

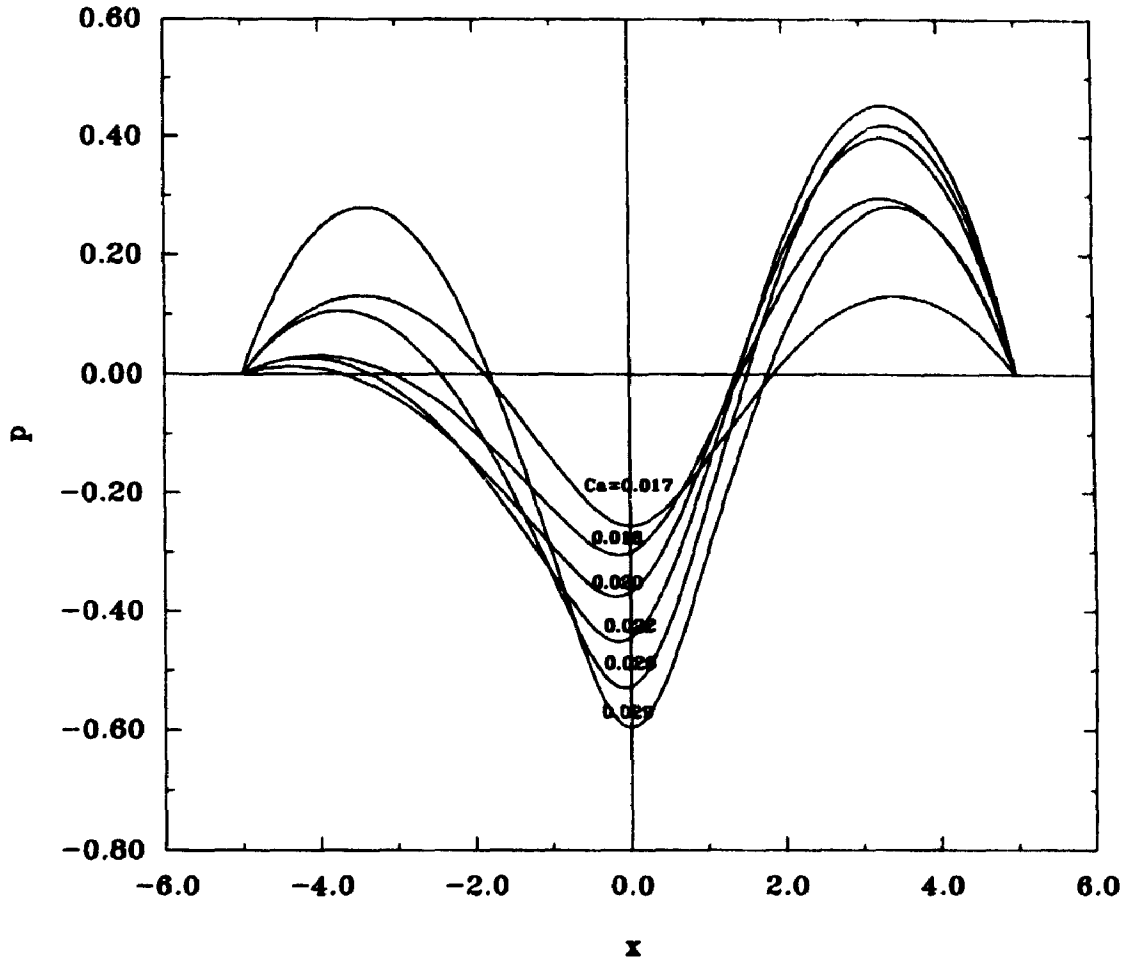

Figure 5.17 Evolution of the interface as a function of Ca. External heating of type C. L=10, Ma=0, Bi=∞, Re=16, fixed contact points. Sequence of solutions shown corresponds to the asymmetric branch displayed in Fig. 5.16.

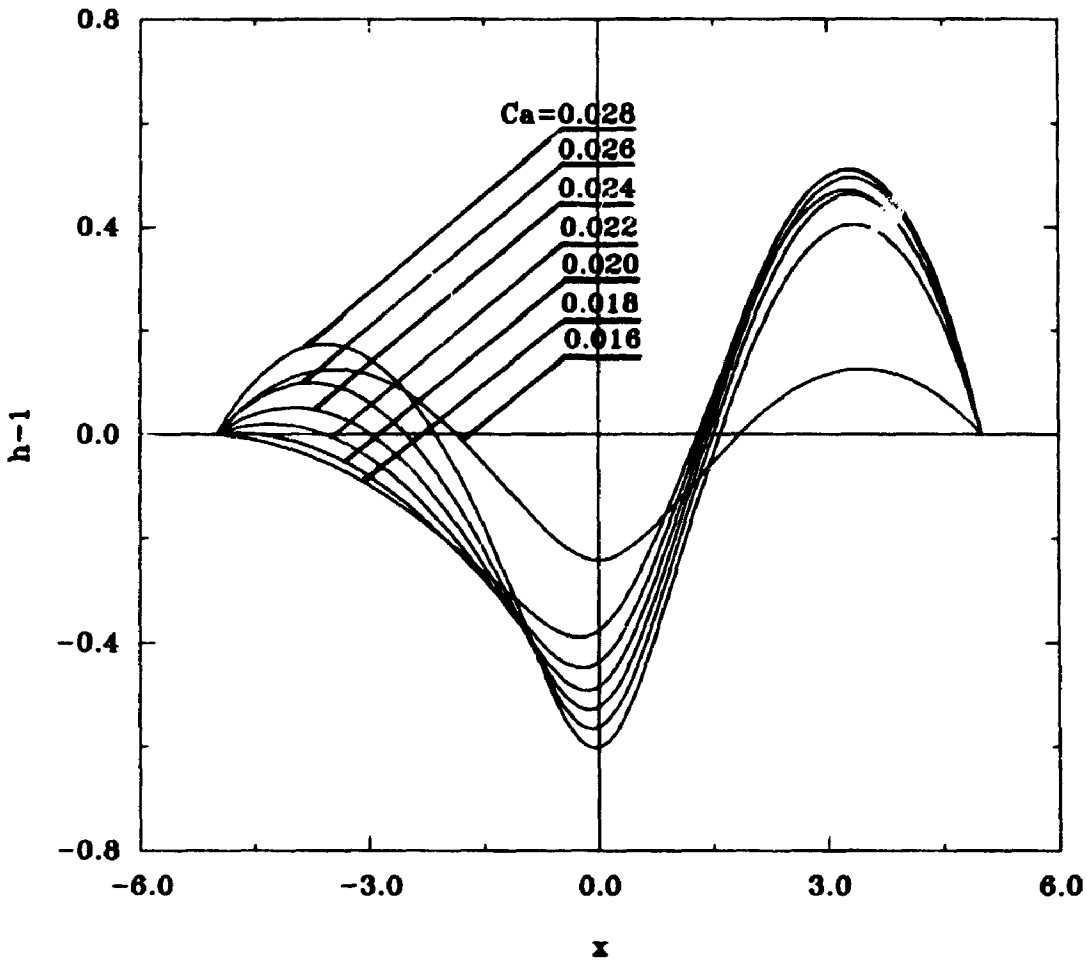

Figure 5.18 Evolution of the interface as a function of Ca for Re=17. Other conditions as in Fig. 5.16.

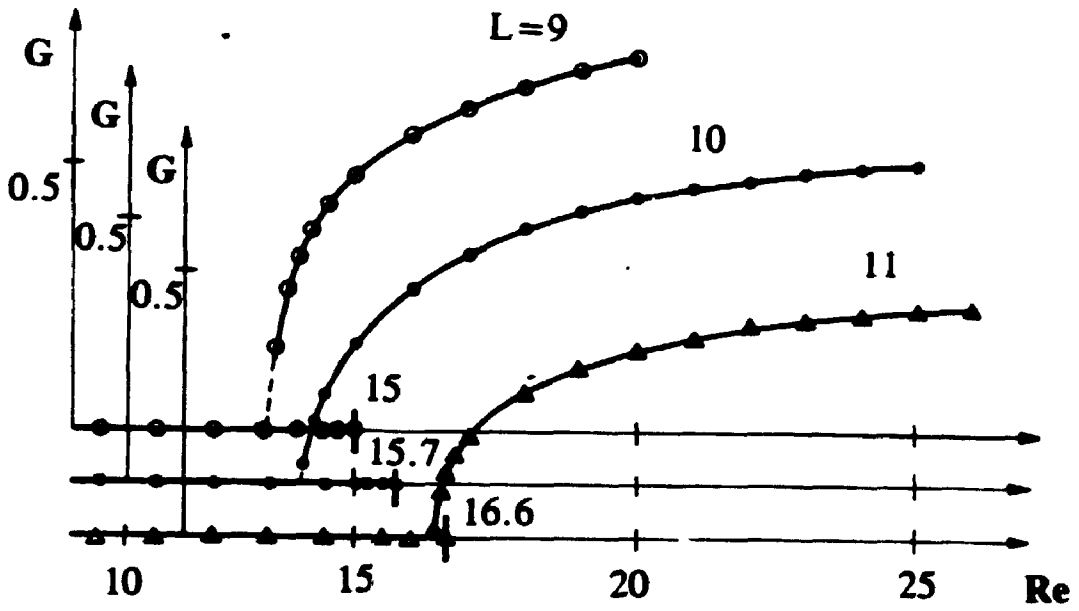

Figure 5.19 Bifurcation diagrams describing existence of nonunique flow patterns induced by the external temperature of type C as a function of Reynolds number Re for various cavity lengths L. Ca=0.024, Bi=∞, Ma=0, fixed contact points. ○ - L=9, • - L=10, △ - L=11. Discrete points shown on the diagrams correspond to computed solutions. Vertical bars show maximum values of Re for which we were able to compute symmetric solutions. Only upper halves of the diagrams are shown.

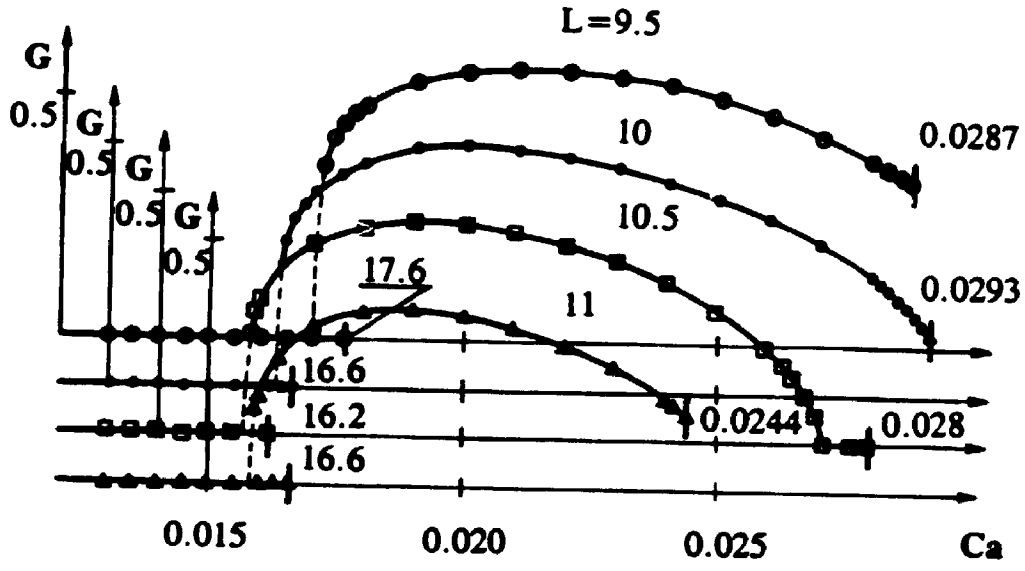

Figure 5.20 Bifurcation diagrams describing existence of nonunique flow patterns induced by the external temperature of type C as a function of capillary number Ca for various cavity lengths L. Re=17, Ma=0, Bi=∞, fixed contact points. Discrete points shown in the diagrams correspond to computed solutions. ○ - L=9.5, • - L=10, □ - L=10.5, △ - L=11. Only upper halves of the diagrams are shown.

5.20. In all cases studied, only a unique (symmetric) solution was found for sufficiently small and sufficiently large values of Ca, in qualitative agreement with the results shown in Figure 5.16. Similarly, in all cases, an increase of the length of the cavity reduced the magnitude of asymmetry (with exception of conditions corresponding to the neighbourhood of the left bifurcation point).

A change of contact conditions from fixed contact points into fixed contact angles allows the end points of the interface to move and, as a result, it increases the magnitude of the deformation. This effect is clearly seen in Figures 5.1-5.8. The increased ease with which the interface deforms leads to an earlier appearance of non-unique solutions (compare Figure 5.21 with Figure 5.14). Bifurcation diagrams describing the behaviour of the liquid as a function of Reynolds number Re for various values of capillary number Ca are displayed in Figure 5.21. Bifurcations are supercritical and of the pitch-fork type in all cases studied. An example of non-unique flow patterns that co-exist at Re=9.8 and Ca=0.020 is displayed in Figure 5.22.

The effect of "stiffness" of the interface is illustrated in Figure 5.23, which displays bifurcation diagrams resulting from variations of capillary number Ca while Reynolds number Re is kept constant. It is seen that unique solutions exist

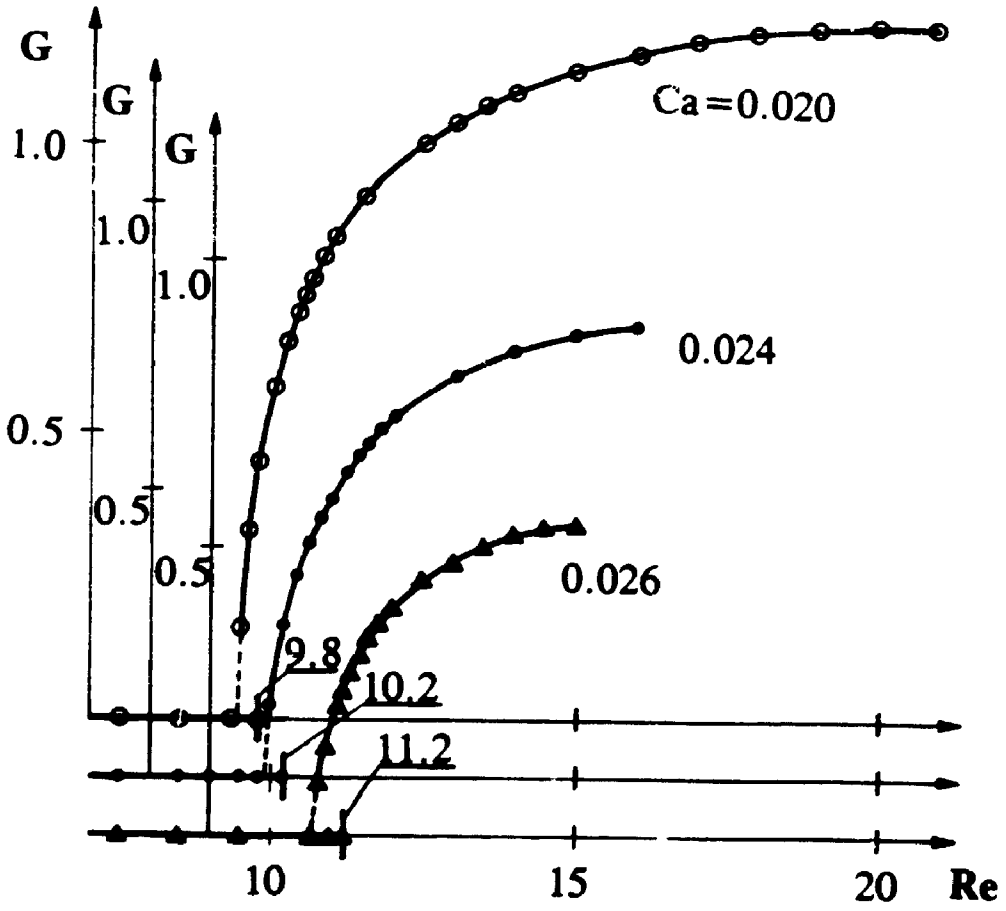

Figure 5.21 Bifurcation diagrams describing existence of nonunique flow patterns induced by the external temperature of type C as a function of Reynolds number Re for various capillary number Ca. Fixed contact angles, L=8. Other conditions as in Fig. 5.14. Discrete points shown on the diagrams correspond to computed solutions. o - Ca=0.020, • - Ca=0.024, ▵ - Ca=0.026. Only upper halves of the diagrams are shown. Vertical bars show maximum value of Re for which we were able to compute symmetric solutions.

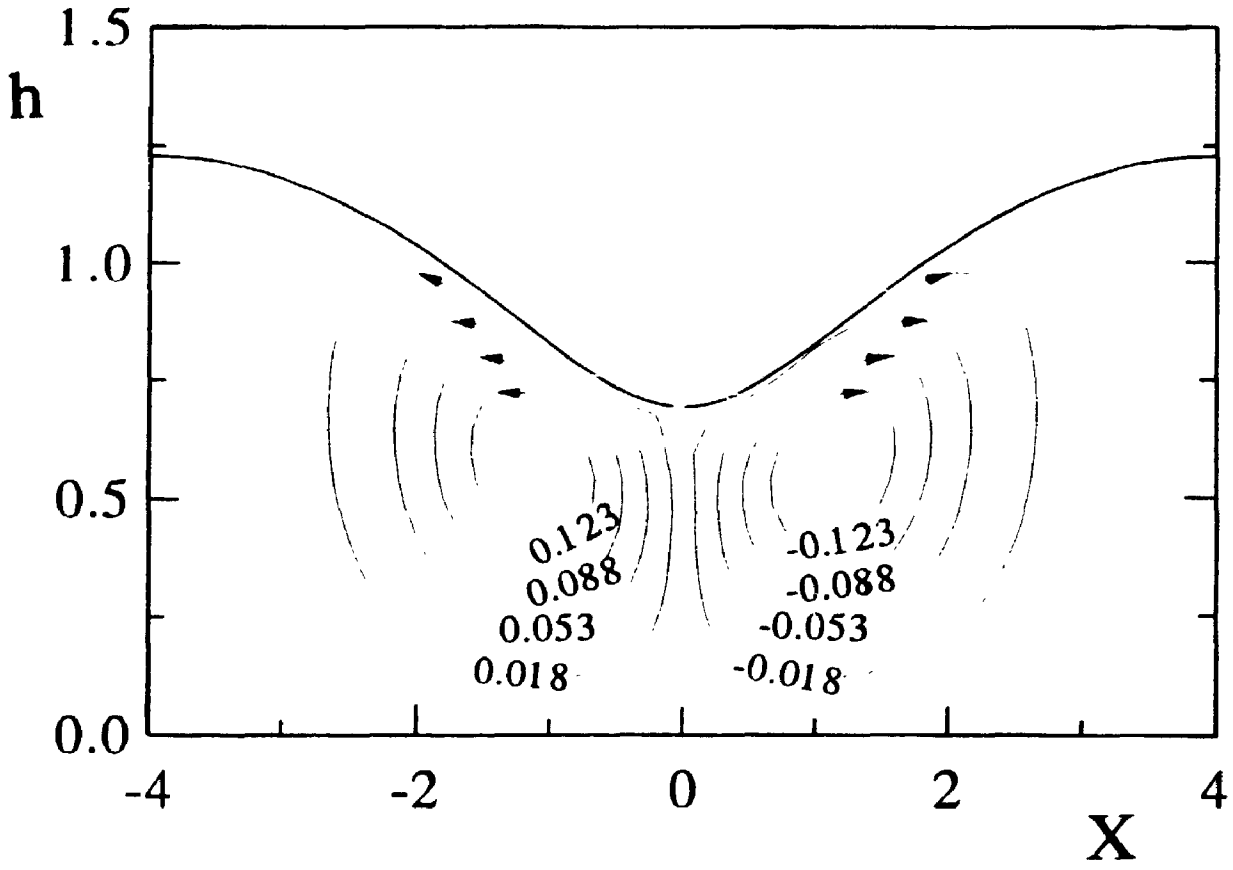

Figure 5.22A. Flow pattern induced by the external temperature of type C. Re=9.8, L=8, Ca=0.020, fixed contact angles, symmetric flow.

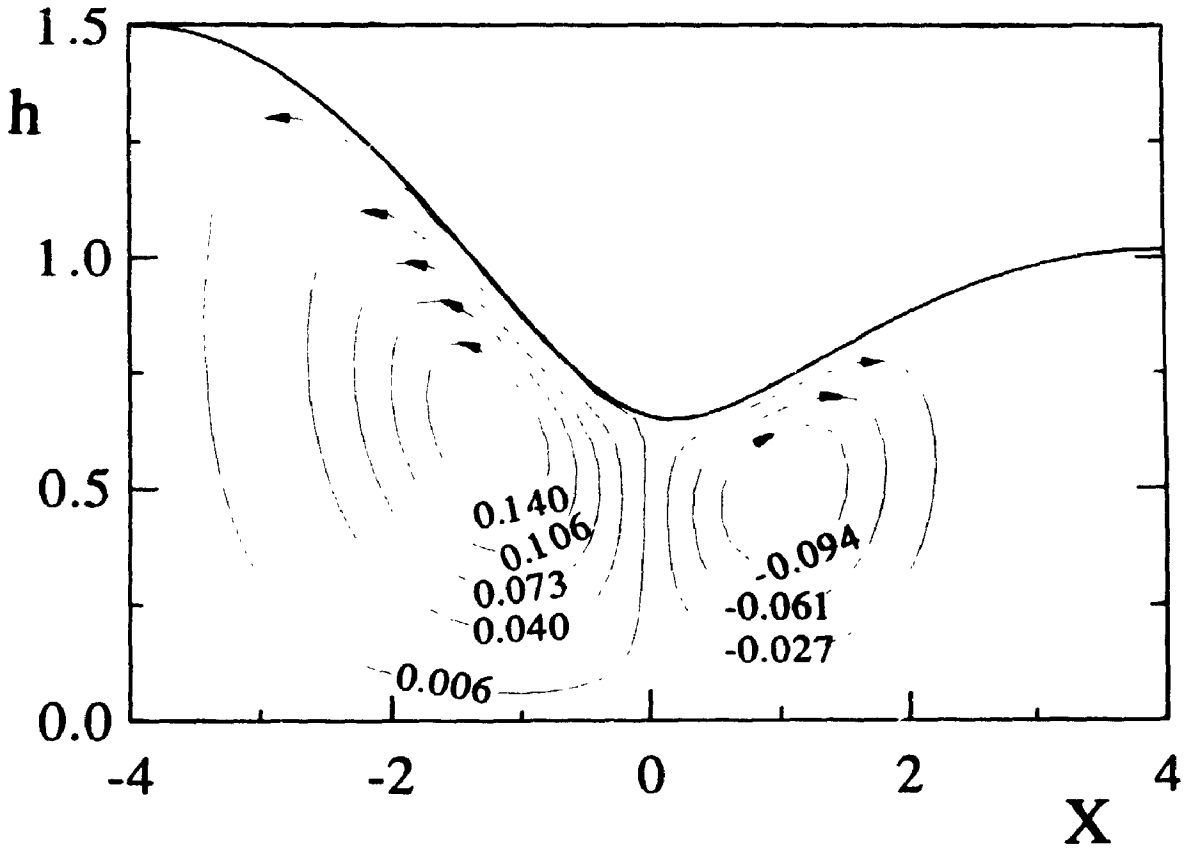

Figure 5.22B Flow pattern induced by the external temperature of type C. Re=9.8, L=8, Ca=0.020, fixed contact angles, asymmetric flow (left asymmetry).

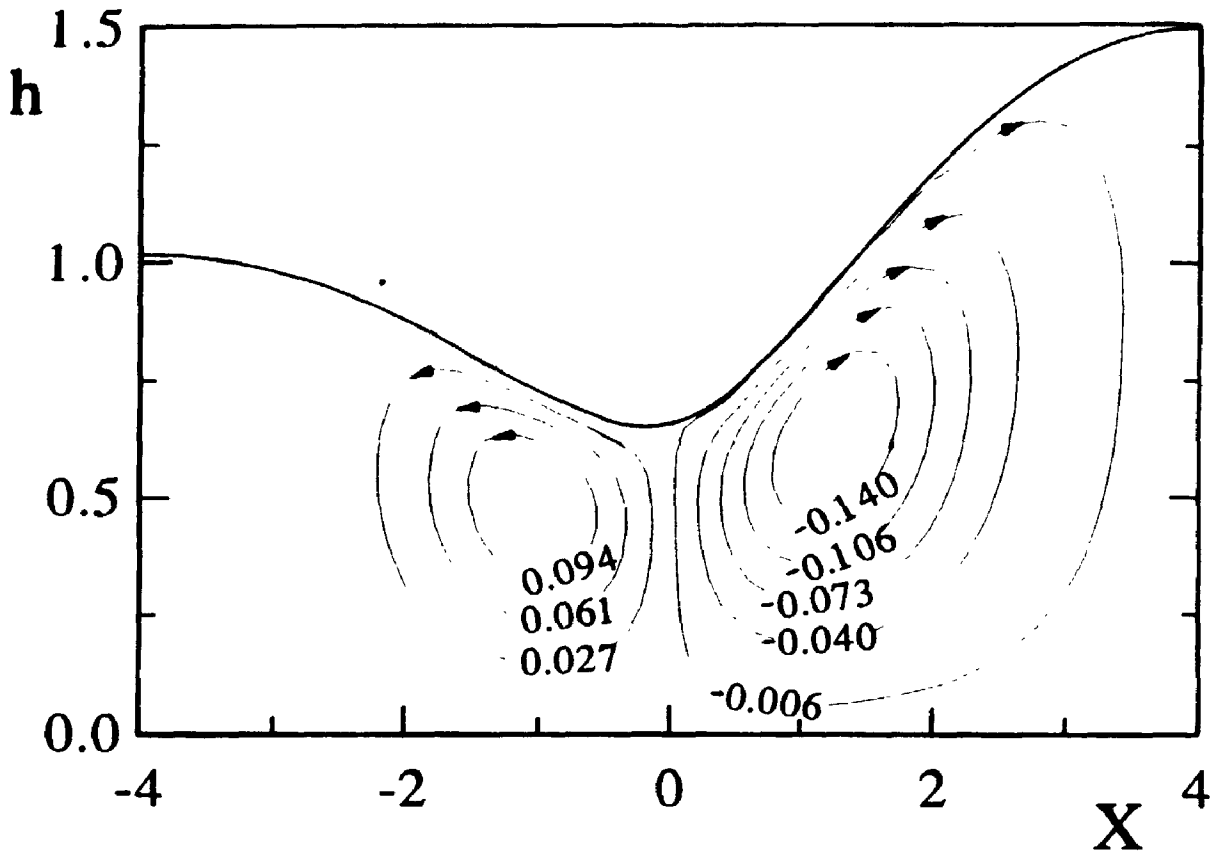

Figure 5.22C Flow pattern induced by the external temperature of type C. Re=9.8, L=8, Ca=0.020, fixed contact angles, asymmetric flow (right asymmetry).

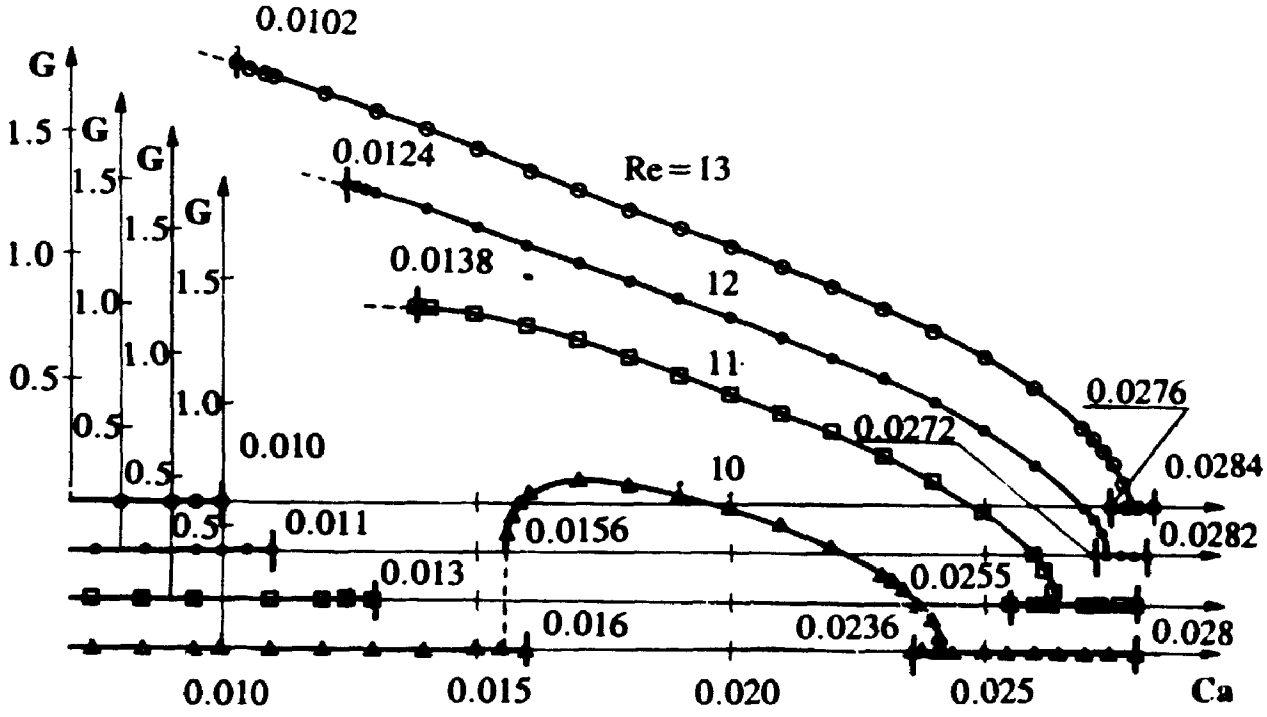

Figure 5.23 Bifurcation diagrams describing existence of nonunique flow patterns induced by the external temperature of type C as a function of capillary number Ca for various Reynolds numbers Re. L=8, fixed contact points. All other conditions as in Fig. 5.16. Discrete points shown on the diagrams correspond to computed solutions. ○ - Re=13, • - Re=12, □ - Re=11, △ - Re=10. Only upper halves of the diagrams are shown. Vertical bars show the extent to which we were able to compute various branches.

for sufficiently small and sufficiently large Ca, in qualitative agreement with the case of fixed contact points (see Figure 5.16). One may note that the flow system undergoes very rapid changes around the left bifurcation point. We were unable to reproduce the corresponding sections of the bifurcation branche due to convergence problems. The form of the bifurcation diagram shows that the flow system may be very difficult to control under such conditions. Evolution of the shape of the interface as a function of Ca for a fixed value of Re=10 is illustrated in Figure 5.24 (the corresponding bifurcation branch is shown in Figure 5.23). The deformation of the interface has a symmetric form at Ca=0.007, then it becomes asymmetric, and then it regains symmetry at a sufficiently high value of Ca. One should note a large increase of the absolute value of the deformation as Ca increases.

The above discussion shows that the change of the contact conditions, from fixed contact points into fixed contact angles, does not affect the behaviour of the flow system in qualitative terms. It does, however, reduce the bifurcation Reynolds and capillary numbers, and significantly increases the magnitude of the deformation.

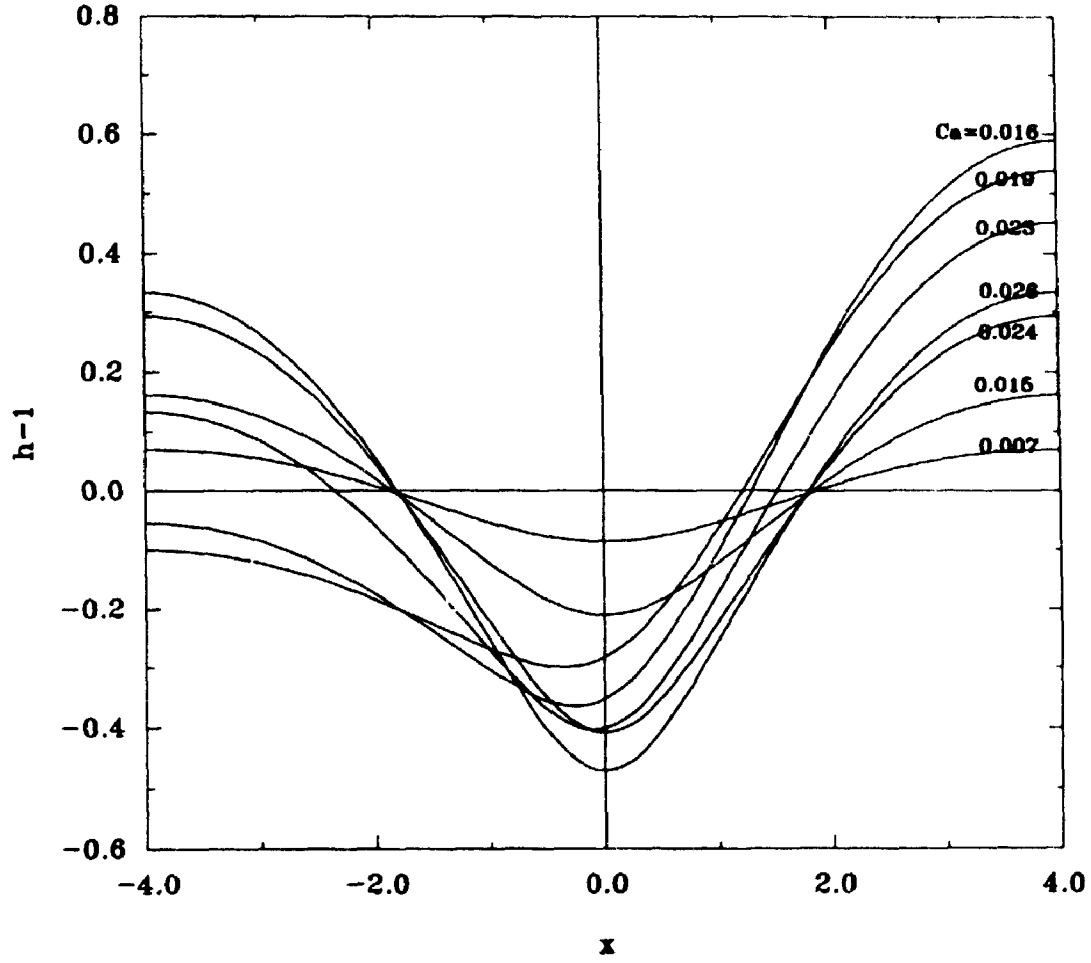

Figure 5.24 Evolution of the interface as a function of capillary number Ca. External heating of type C. L=8, Re=10, Ma=0, Bi=∞, fixed contact angles. Sequence of solutions shown corresponds to the asymmetric branch dispalyed in Fig. 5.23.

5.6 Sensitivity of Solutions

In the previous Sections, we have investigated the response of the flow system to a specified external heating. Such heating, regardless of what its functional form might be, can be reproduced only approximately in a real experiments. This brings us to the question of sensitivity of the flow system to small changes in the external heating. The following discussion will focus on the heating of type C.

External temperature of type C simulates heating using a localized heat source placed above the center of the cavity. It is likely that in a real experiment this heat source may be placed slightly off the center. Alternatively, one may want to (intentionally) slightly misplace the heat source in order to destroy symmetry of the heating and (possibly) prevent the appearance of the non-unique solutions. One might hope that this strategy will result in a better control of the system. The effect of dislocating the heat source can be analyzed by modifying temperature C to the form $T_\varepsilon(x)=10e^{-(x+\varepsilon)^2}$, where $\varepsilon>0$ is a measure of the error in the location of the heat source. Figure 5.25 shows the form of the interface resulting from such a heating in the case of fixed contact points. The results show that the right bulge is bigger (we have referred to such a shape in the previous subsection as the right asymmetry), and that no symmetric solution is possible when

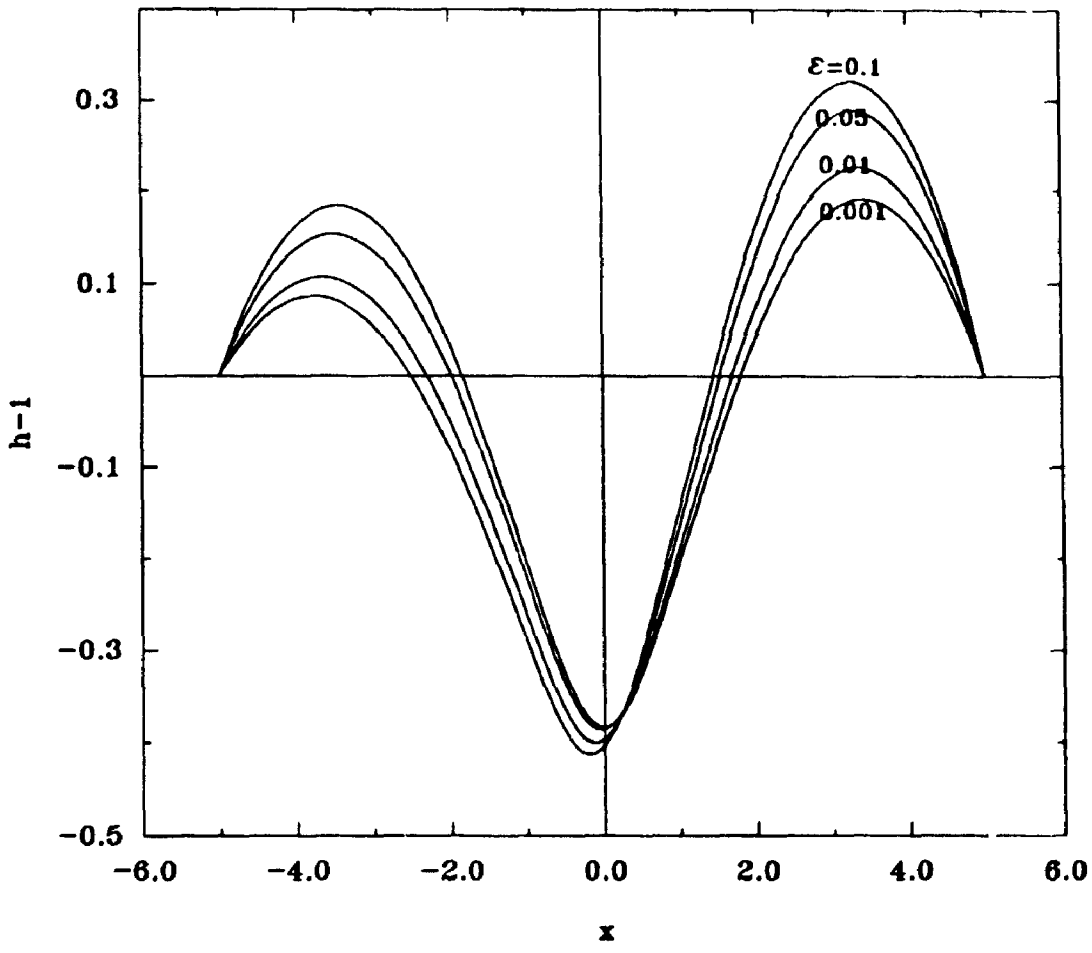

Figure 5.25 Evolution of the interface as a function of the distance between heat source and the center of the cavity. External heating in the form $T_s(x)=10e^{-(x+\varepsilon)^2}$. Ca=0.024, Re=14, L=10, Ma=0, Bi=∞, fixed contact points.

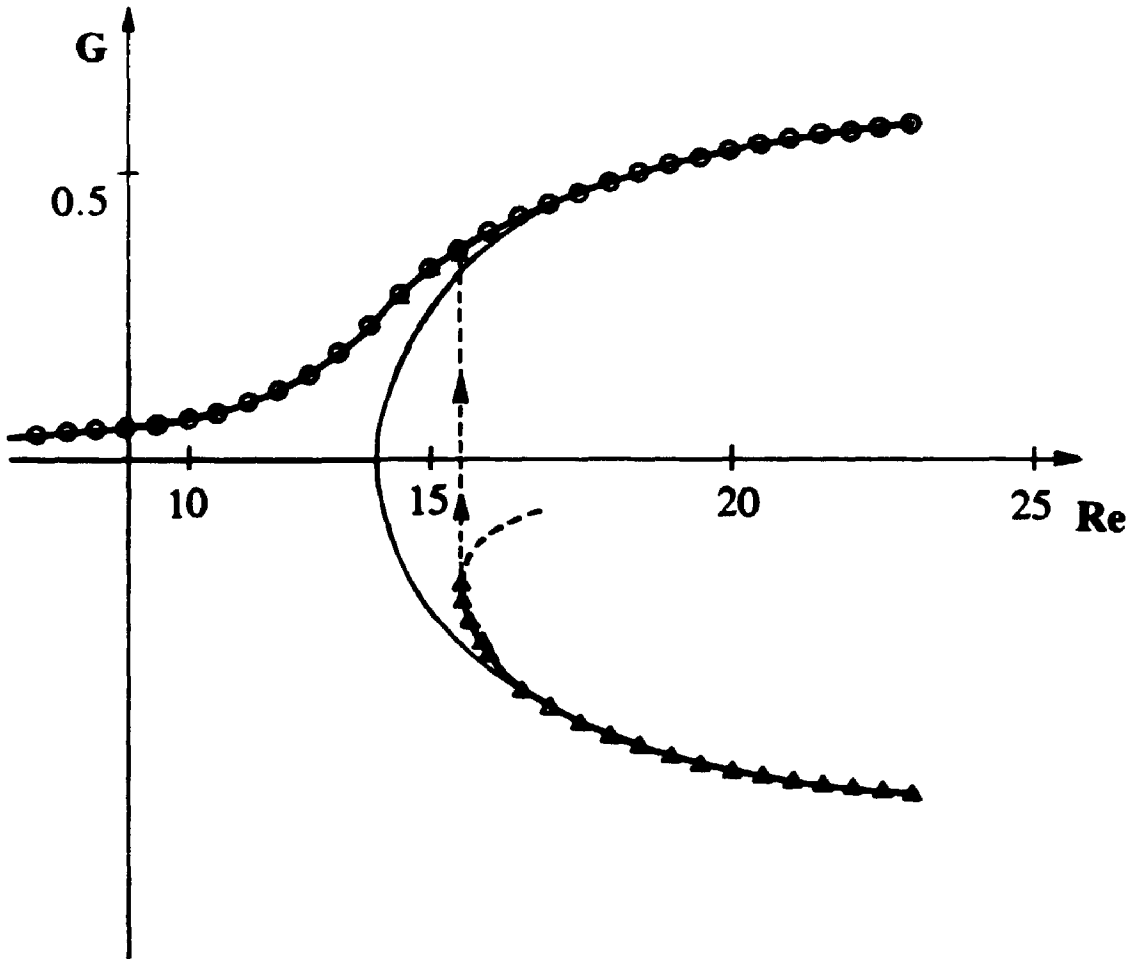

Figure 5.26 Bifurcation diagram describing existence of nonunique flow patterns induced by the external temperature in the form $T_g(x)=10e^{-(x+\varepsilon)^2}$, $\varepsilon=0.1$, as a function of Reynolds number Re. L=10, Ca=0.024, Ma=0, Bi=∞, fixed contact points. Discrete points shown in the diagram correspond to computed solutions. o - upper branch, Δ - lower branch. An identical (mirror image) diagram can be constructed for $\varepsilon=-0.1$.

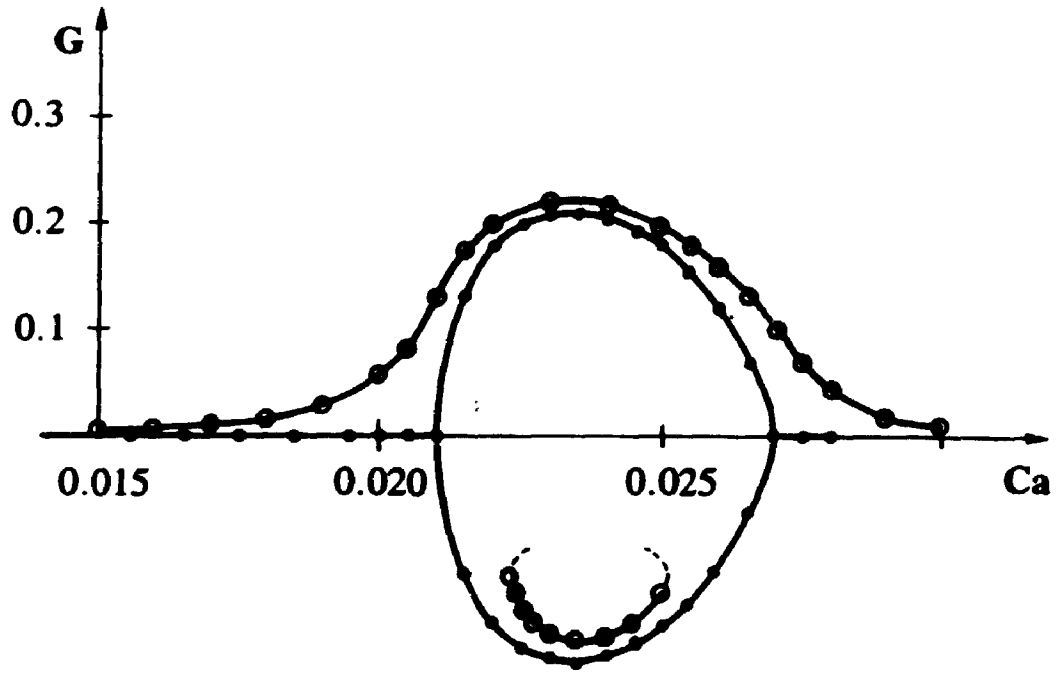

Figure 5.27 Bifurcation diagram describing existence of nonunique flow patterns induced by the external temperature in the form $T_g(x)=10e^{-(x+\varepsilon)^2}$, $\varepsilon=0.01$, as a function of capillary number Ca. L=10, Re=14.5, Ma=0, Bi=∞, fixed contact points. Discrete points shown in the diagram correspond to computed solutions. An identical (mirror image) diagram can be constructed for $\varepsilon=-0.01$.

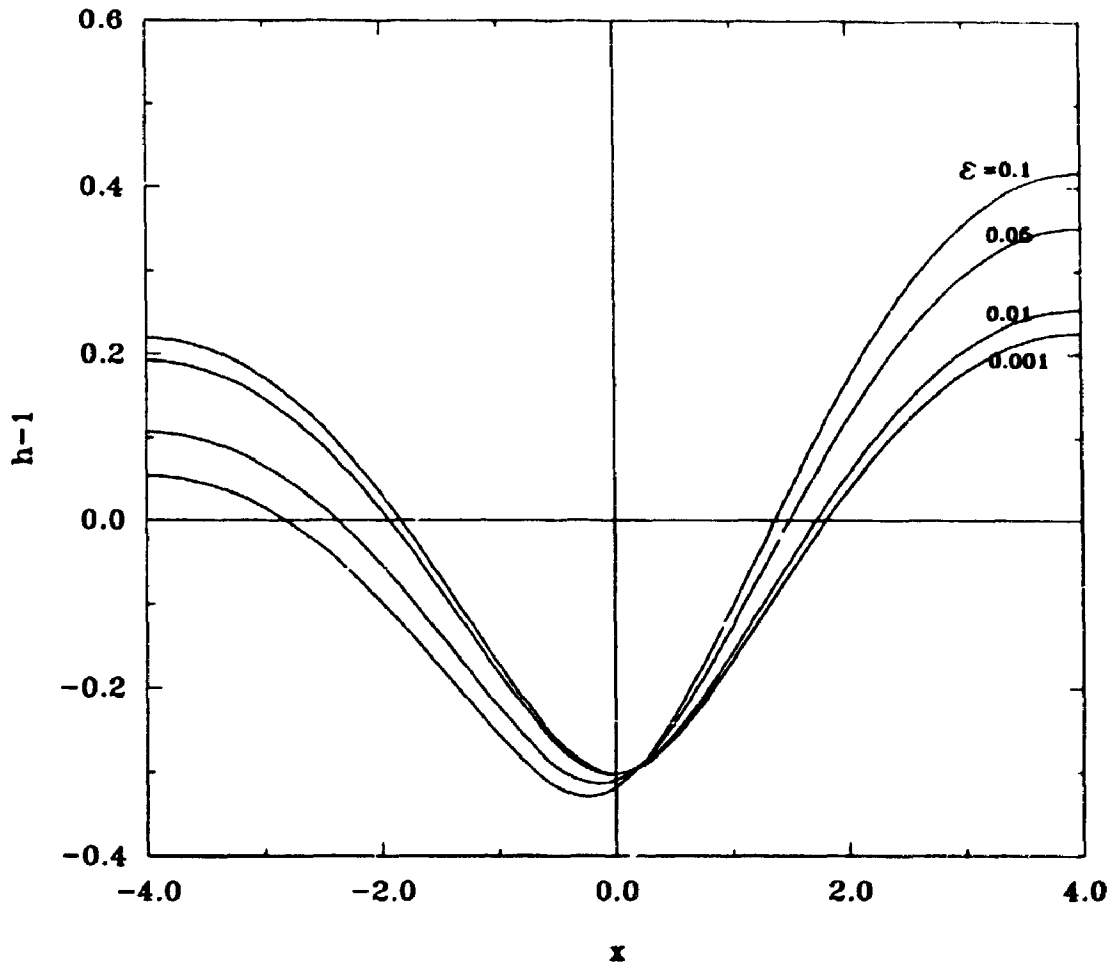

Figure 5.28 Evolution of the interface as a function of the distance between heat source and the center of the cavity. External heating in the form $T_g(x)=10e^{-(x+\varepsilon)^2}$. Ca=0.020, Re=9, L=8, Ma=0, Bi=∞, fixed contact angles.

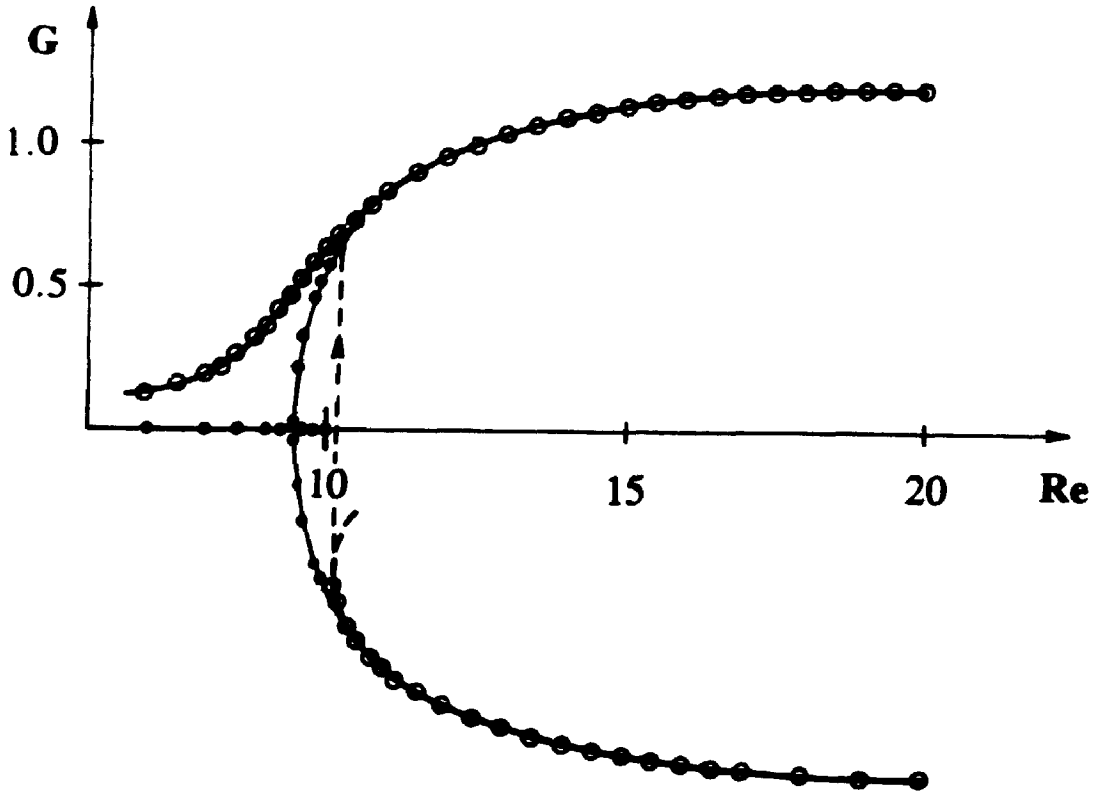

Figure 5.29 Bifurcation diagram describing existence of nonunique flow patterns induced by the external temperature in the form $T_g(x)=10e^{-(x+\varepsilon)^2}$, $\varepsilon=0.1$, as a function of Reynolds number Re. L=8, fixed contact angles. All other conditions as in Fig. 5.26.

able to compute (practically) overlap with those corresponding to perfect bifurcation once Re is increased above the perfect bifurcation point.

5.7 Concluding Remarks

Reynolds number effects on the thermocapillary convection in cavities and liquid layers have been studied. It is shown that the increase of Reynolds number will significantly increase the magnitude of the interface deformation. The rate of the increase depends strongly on the functional type of the external temperature field and the type of contact conditions.

Non-unique stable solutions have been found even for very low values of the Reynolds and capillary numbers. The primary bifurcation as a function of Reynolds number is of the pitchfork type, while in the capillary number cases the structure is more complicated and cannot be easily categorized. The system is very sensitive with respect to external heating, and control parameters, such as Reynolds number, capillary number, and length of the cavity.

CHAPTER 6

Control of Thermocapillary Convection Using Encapsulation

6.1 Introduction

The ability to control the dynamics of thin liquid layers is important in many material processing applications. The primary considerations are avoidance of rupture of the layer and the prevention of development of unsteady phenomena, such as oscillatory convection. It was shown in Chapters 4 and 5 that convection cannot be avoided in thin liquid layers. But its intensity can be reduced through a proper control procedure. The proposed method is to cover the liquid layer with a blanket of another liquid.

The objective of this chapter is to investigate whether the intensity of the convection can be reduced through appropriate selection of the thickness and material properties of the covering liquid. Since the direct numerical solution for a double-layer system is very time consuming, the domain perturbation method will be used. For simplicity, an infinite length double layer system will be considered instead of a finite length cavity.

As mentioned in Chapter 4, there are many publications focusing on single liquid layer systems. However, not much has been done on double-layer systems. Results available are limited exclusively to parallel flows, where the transverse velocity component is negligible (D. Villers & J.K. Plateen, 1990, H.Q. Yang & K.T. Yang, 1990, and A.A. Nepomnyashchii & I.B. Simanovskii,1984). There is a lack of formalism that allows the evaluation of interface effects. In what follows, an investigation will be presented which studies thermocapillary convection in a double-layer system including cases with a large transverse velocity component and the resulting interface deformation. Finally, the possibilities of reducing the intensity of the convection will be discussed.

6.2 Problem Formulation

Consider two superposed layers made of immiscible liquids, infinite in the x and y directions, bounded below by a solid nonisothermal plate and above by an insulated plate, as shown in Figure 6.1. The plates are flat, parallel to each other and set apart by a distance H. The temperature of the lower plate $\tilde{T}_w(x,y)$ is fixed by external means and considered to be known. The lower liquid (liquid A) is incompressible, Newtonian, has density ρ_A, thermal conductivity k_A, specific heat per unit mass c_A, thermal

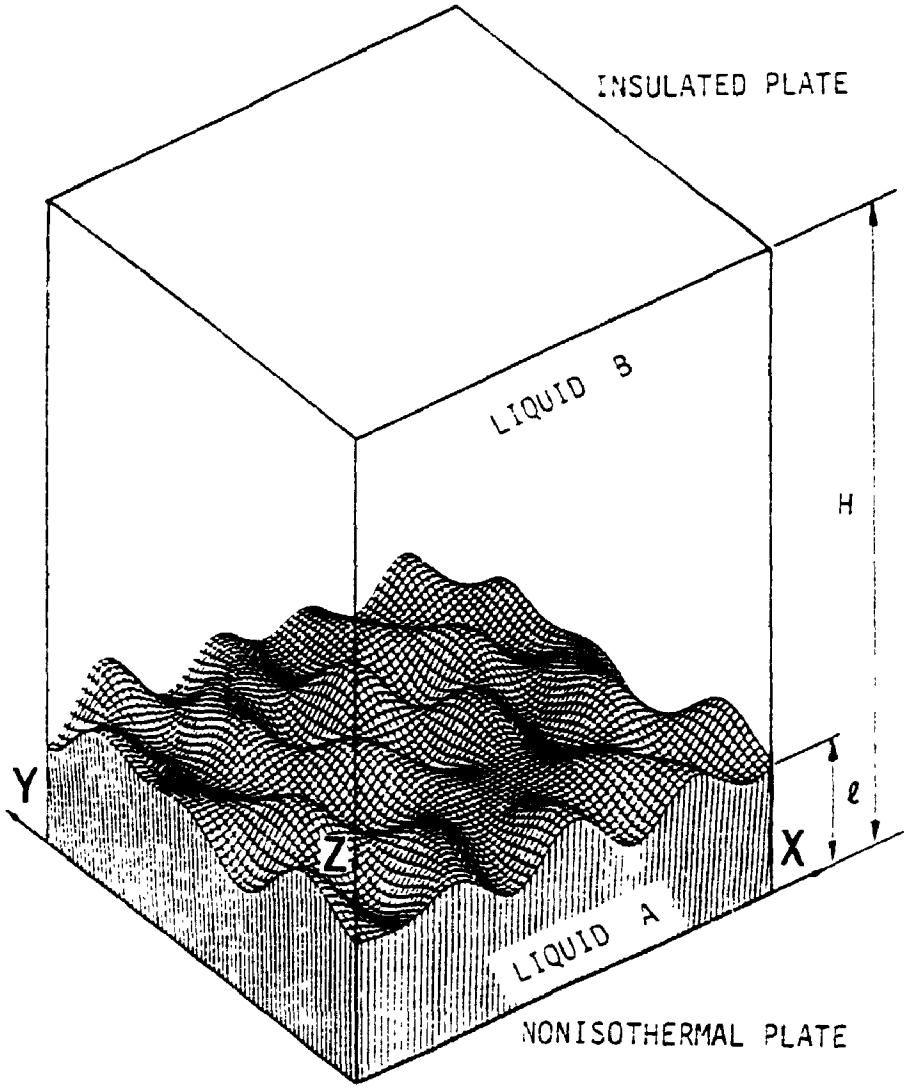

Figure 6.1 Sketch of the flow system. Liquid B is introduced in order to reduce convection in liquid A.

diffusivity $\kappa_A=K_A/\rho_A c_A$, kinematic viscosity ν_A, dynamic viscosity μ_A, and average thickness ℓ. The upper liquid (liquid B) has similar characteristics and its properties are denoted as ρ_B, K_B, c_B, κ_B, ν_B, μ_B. The interface, described by $z=h(x,y)$, has an associated surface tension σ, which depends on the local temperature.

While the governing equations are similar to those in Chapter 2, they are to be extended to three dimensions, as follows

$$u_{Ax}+v_{Ay}+w_{Az}=0, \tag{6.1}$$

$$u_A u_{Ax}+v_A u_{Ay}+w_A u_{Az}=-\rho_A^{-1}p_{Ax}+\nu_A\,(u_{Axx}+u_{Ayy}+u_{Azz}), \tag{6.2}$$

$$u_A v_{Ax}+v_A v_{Ay}+w_A v_{Az}=-\rho_A^{-1}p_{Ay}+\nu_A\,(v_{Axx}+v_{Ayy}+v_{Azz}), \tag{6.3}$$

$$u_A w_{Ax}+v_A w_{Ay}+w_A w_{Az}=-\rho_A^{-1}p_{Az}+\nu_A\,(w_{Axx}+w_{Ayy}+w_{Azz}), \tag{6.4}$$

$$u_A T_{Ax}+v_A T_{Ay}+w_A T_{Az}=\kappa_A\,(T_{Axx}+T_{Ayy}+T_{Azz})+\nu_A c_A^{-1}D_A, \tag{6.5}$$

$$u_{Bx}+v_{By}+w_{Bz}=0, \tag{6.6}$$

$$u_B u_{Bx}+v_B u_{By}+w_B u_{Bz}=-\rho_B^{-1}p_{Bx}+\nu_B\,(u_{Bxx}+u_{Byy}+u_{Bzz}), \tag{6.7}$$

$$u_B v_{Bx}+v_B v_{By}+w_B v_{Bz}=-\rho_B^{-1}p_{By}+\nu_B\,(v_{Bxx}+v_{Byy}+v_{Bzz}), \tag{6.8}$$

$$u_B W_{Bx} + v_B W_{By} + w_B W_{Bz} = -\rho_B^{-1} p_{Bz} + \nu_B (W_{Bxx} + W_{Byy} + W_{Bzz}) , \tag{6.9}$$

$$u_B T_{Bx} + v_B T_{By} + w_B T_{Bz} = \kappa_B (T_{Bxx} + T_{Byy} + T_{Bzz}) + \nu_B C_B^{-1} D_B , \tag{6.10}$$

$z=0$: $$u_A = v_A = w_A = 0 , \quad T_A = \bar{T}_w(x, y) , \tag{6.11}$$

$z=H$: $$u_B = v_B = w_B = 0 , \quad T_{Bz} = 0 , \tag{6.12}$$

$z=h(x,y)$: $$u_A = u_B , \quad v_A = v_B , \quad w_A = w_B , \quad T_A = T_B , \tag{6.13}$$

$$w_A = u_A h_x + v_A h_y , \tag{6.14}$$

$$(s_{Aij} - s_{Bij}) n_j n_i = 2\sigma\Lambda , \tag{6.15}$$

$$(s_{Aij} - s_{Bij}) n_j t_i^x = \sigma_{sx} , \tag{6.16}$$

$$(s_{Aij} - s_{Bij}) n_j t_i^y = \sigma_{sy} , \tag{6.17}$$

$$k_A T_{An} = k_B T_{Bn} , \tag{6.18}$$

where D stands for the dissipation function, and subscripts A and B refer to liquids A and B, respectively. Other symbols have the same means as those in Chapter 2. The unit normal vector **n**, the tangent vector in the (x, z)-plane $\mathbf{t}^x$, and the unit tangent vector in the (y, z)-plane $\mathbf{t}^y$ are defined as follows:

$$n = \frac{-h_x i - h_y j + k}{N} , \tag{6.19}$$

$$t^x = \frac{i + h_x k}{N^x} , \quad t^y = \frac{j + h_y k}{N^y} , \tag{6.20}$$

with

$$N=(1+h_x^2+h_y^2)^{1/2}, \quad N^x=(1+h_x^2)^{1/2}, \quad N^y=(1+h_y^2)^{1/2}. \qquad (6.21)$$

The mean curvature Λ of the interface in equation (6.15) has the definition

$$\Lambda=-\frac{1}{2}n_{j,j}=\frac{1}{2}\frac{h_{xx}(1+h_y^2)-2h_xh_yh_{xy}+h_{yy}(1+h_x^2)}{N^3}. \qquad (6.22)$$

Apart from boundary conditions (6.11)-(6.18), the liquids must also satisfy the mass conservation constraint. Since both liquids are assumed to be incompressible, their total volumes V_A and V_B must remain constant, respectively, i.e.,

$$V_A=constant, \quad V_B=constant. \qquad (6.23)$$

The explicit forms of the above conditions will be given in Section 6.4 which deals with the analysis of isothermal conditions.

The equation of state for surface tension, equation (2.18), has a linear form.

The temperature of the lower wall $\tilde{T}_w(x, y)$ is written as

$$\tilde{T}_w(x, y)=T_w(x, y)+B, \qquad (6.24)$$

where B is a constant and $T_w(x, y)$ is either periodic or decays to zero as $x, y\to\pm\infty$. It will be shown in Section 6.6

that $T_w(x, y)$ has to satisfy additional constraint conditions for steady convection to exist.

Similarly to Chapter 2, the problem can be scaled in terms of lubrication-type variables by using ℓ, u_*, $\mu_A u_*/\ell$ and σ_0 as length, velocity, pressure and surface tension scales, respectively. Temperatures T_A' and T_B' are defined as:

$$T_A=(T_{max}-T_{min})T_A', \quad T_B=(T_{max}-T_{min})T_B', \quad B-T_*=(T_{max}-T_{min})B'. \tag{6.25}$$

Here, T_{max} and T_{min} denote a measure of maximum and minimum interface temperature, respectively. And the velocity scale u_* is

$$u_*=\gamma\frac{T_{max}-T_{min}}{\mu_A}. \tag{6.26}$$

With the above scales the dimensionless equations (with the primes dropped) can be written in the form

$$u_{Ax}+v_{Ay}+w_{Az}=0, \tag{6.27}$$

$$Re_A(u_A u_{Ax}+v_A u_{Ay}+w_A u_{Az})=-p_{Ax}+u_{Axx}+u_{Ayy}+u_{Azz}, \tag{6.28}$$

$$Re_A(u_A v_{Ax}+v_A v_{Ay}+w_A v_{Az})=-p_{Ay}+v_{Axx}+v_{Ayy}+v_{Azz}, \tag{6.29}$$

$$Re_A(u_A w_{Ax}+v_A w_{Ay}+w_A w_{Az})=-p_{Az}+w_{Axx}+w_{Ayy}+w_{Azz}, \tag{6.30}$$

$$Ma_A(u_A T_{Ax}+v_A T_{Ay}+w_A T_{Az})=T_{Axx}+T_{Ayy}+T_{Azz}+Br_A D_A, \tag{6.31}$$

$$u_{Bx}+v_{By}+w_{Bz}=0, \tag{6.32}$$

$$Re_B(u_B u_{Bx}+v_B u_{By}+w_B u_{Bz})=-p_{Bx}+u_{Bxx}+u_{Byy}+u_{Bzz}, \tag{6.33}$$

$$Re_B(u_B v_{Bx}+v_B v_{By}+w_B v_{Bz})=-p_{By}+v_{Bxx}+v_{Byy}+v_{Bzz}, \tag{6.34}$$

$$Re_B(u_B w_{Bx}+v_B w_{By}+w_B w_{Bz})=-p_{Bz}+w_{Bxx}+w_{Byy}+w_{Bzz}, \tag{6.35}$$

$$Ma_B(u_B T_{Bx}+v_B T_{By}+w_B T_{Bz})=T_{Bxx}+T_{Byy}+T_{Bzz}+Br_B D_B. \tag{6.36}$$

The Reynolds numbers Re_A and Re_B, the Marangoni numbers Ma_A and Ma_B and the Brinkman numbers Br_A and Br_B have the standard definitions, i.e.,

$$Re_A=\frac{u_*\ell}{\nu_A}=\frac{\gamma(T_{max}-T_{min})\ell}{\mu_A\nu_A}, \quad Re_B=\frac{u_*\ell}{\nu_B}=\frac{\gamma(T_{max}-T_{min})\ell}{\mu_A\nu_B},$$

$$Ma_A=\frac{u_*\ell}{\kappa_A}=\frac{\gamma(T_{max}-T_{min})\ell}{\mu_A\kappa_A}, \quad Ma_B=\frac{u_*\ell}{\kappa_B}=\frac{\gamma(T_{max}-T_{min})\ell}{\mu_A\kappa_B}, \tag{6.37}$$

$$Br_A=\frac{\mu_A u_*^2}{(T_{max}-T_{min})k_A}=\frac{\gamma^2(T_{max}-T_{min})}{\mu_A k_A}, \quad Br_B=\frac{\mu_B u_*^2}{(T_{max}-T_{min})k_B}=\frac{\gamma^2(T_{max}-T_{min})}{\mu_B k_B}\frac{\mu_B^2}{\mu_A^2}.$$

The boundary conditions (6.11) to (6.18) are then transformed to

$z=0$: $$u_A=v_A=w_A=0, \quad T_A=T_w(x,y), \tag{6.38}$$

$z=H$: $$u_B=v_B=w_B=0, \quad T_{Bz}=0, \tag{6.39}$$

$$z=h(x,y): \qquad u_A=u_B, \quad v_A=v_B, \quad w_A=w_B, \quad T_A=T_B, \tag{6.40}$$

$$w_A=u_A h_x+v_A h_y, \tag{6.41}$$

$$\begin{aligned} &-p_A+2N^{-2}[h_x^2u_{Ax}+h_y^2v_{Ay}+w_{Az}+h_xh_y(u_{Ay}+v_{Ax})-h_x(w_{Ax}+u_{Az}) \\ &-h_y(v_{Az}+w_{Ay})]+K\{-P_B+2N^{-2}[h_x^2u_{Bx}+h_y^2v_{By}+w_{Bz} \\ &+h_xh_y(u_{By}+v_{Bx})-h_x(w_{Bx}+u_{Bz})-h_y(v_{Bz}+w_{By0})]\} \\ &=Ca^{-1}N^{-3}[h_{xx}(1+h_y^2)-2h_xh_yh_{xy}+h_{yy}(1+h_x^2)](1-CaT), \end{aligned} \tag{6.42}$$

$$\begin{aligned} &2h_x(-u_{Ax}+w_{Az})-h_y(u_{Ay}+v_{Az})+(1-h_x^2)(w_{Ax}+u_{Az})-h_xh_y(v_{Az}+w_{Ay}) \\ &K[2h_x(-u_{Bx}+w_{Bz})-h_y(u_{By}+v_{Bx})+(1-h_x^2)(w_{Bx}+u_{Bz})-h_xh_y(v_{Bz}+w_{By})] \\ &=-(T_x+h_xT_{Az})N, \end{aligned} \tag{6.43}$$

$$\begin{aligned} &2h_y(w_{Az}-v_{Ay})-h_x(u_{Ay}+v_{Ax})+(1-h_y^2)(v_{Az}+w_{Ay})-h_xh_y(w_{Ax}+u_{Az}) \\ &K[2h_y(w_{Bz}-v_{By})-h_x(u_{By}+v_{Bx})+(1-h_y^2)(v_{Bz}+w_{By})-h_xh_y(w_{Bx}+u_{Bz})] \\ &=-(T_y+h_yT_z)N, \end{aligned} \tag{6.44}$$

$$-h_xT_{Ax}-h_yT_{Ay}+T_{Az}=G(-h_xT_{Bx}-h_yT_{By}+T_{Bz}). \tag{6.45}$$

In the above, Ca is the capillary number. K and G denote ratios of viscosities and thermal conductivities of both fluids, i.e.,

$$K=\frac{\mu_B}{\mu_A}, \qquad G=\frac{k_B}{k_A}. \tag{6.46}$$

6.3 Small Deformation Theory

Similar to Section 3.5.2, consider the case of very large mean surface tension as compared to the amplitude of its thermal variations. Note that power expansions (in terms of Ca) (3.47) and (3.48) are still valid, with q standing for each of u_A, v_A, w_A, T_A, u_B, v_B, w_B, T_B, and h, and p for p_A and p_B. Substitution of expansions (3.47) and (3.48) into the field equations (6.27) to (6.36) and boundary conditions (6.38) to (6.45) leads to a sequence of problems of order Ca^{-1}, Ca^0, Ca^1, etc. Only the leading-order equations are given below.

The problem of order Ca^{-1}:

$$p_{Asx}=0, \tag{6.47}$$

$$p_{Asy}=0, \tag{6.48}$$

$$p_{Asz}=0, \tag{6.49}$$

$$p_{Bsx}=0, \tag{6.50}$$

$$p_{Bsy}=0, \tag{6.51}$$

$$p_{Bsz}=0, \tag{6.52}$$

with boundary condition

$$-(p_{As}-p_{Bs})=[h_{0xx}(1+h_{0y}^2)-2h_{0x}h_{0y}h_{0xy}+h_{0yy}(1+h_{0x}^2)]N^{-3/2}. \tag{6.53}$$

The problem of order Ca^0:

$$u_{A0x}+v_{A0y}+w_{A0z}=0, \tag{6.54}$$

$$Re_A(u_{A0}u_{A0x}+v_{A0}u_{A0y}+w_{A0}u_{A0z})=-p_{A0x}+u_{A0xx}+u_{A0yy}+u_{A0zz}, \tag{6.55}$$

$$Re_A(u_{A0}v_{A0x}+v_{A0}v_{A0y}+w_{A0}v_{A0z})=-p_{A0y}+v_{A0xx}+v_{A0yy}+v_{A0zz}, \tag{6.56}$$

$$Re_A(u_{A0}w_{A0x}+v_{A0}w_{A0y}+w_{A0}w_{A0z})=-p_{A0z}+w_{A0xx}+w_{A0yy}+w_{A0zz}, \tag{6.57}$$

$$Ma_A(u_{A0}T_{A0x}+v_{A0}T_{A0y}+w_{A0}T_{A0z})=T_{A0xx}+T_{A0yy}+T_{A0zz}+Br_AD_{A0}, \tag{6.58}$$

$$u_{B0x}+v_{B0y}+w_{B0z}=0, \tag{6.59}$$

$$Re_B(u_{B0}u_{B0x}+v_{B0}u_{B0y}+w_{B0}u_{B0z})=-p_{B0x}+u_{B0xx}+u_{B0yy}+u_{B0zz}, \tag{6.60}$$

$$Re_B(u_{B0}v_{B0x}+v_{B0}v_{B0y}+w_{B0}v_{B0z})=-p_{B0y}+v_{B0xx}+v_{B0yy}+v_{B0zz}, \tag{6.61}$$

$$Re_B(u_{B0}w_{B0x}+v_{B0}w_{B0y}+w_{B0}w_{B0z})=-p_{B0z}+w_{B0xx}+w_{B0yy}+w_{B0zz}, \tag{6.62}$$

$$Ma_B(u_{B0}T_{B0x}+v_{B0}T_{B0y}+w_{B0}T_{B0z})=T_{B0xx}+T_{B0yy}+T_{B0zz}+Br_BD_{B0}, \tag{6.63}$$

with boundary conditions:

$z=0$: $$u_{A0}=v_{A0}=w_{A0}=0, \quad T_{A0}=T_W(x,y)+B, \tag{6.64}$$

$z=H$: $$u_{B0}=v_{B0}=w_{B0}=0, \quad T_{B0z}=0, \tag{6.65}$$

$z=1$: $$u_{A0}=u_{B0}, \quad v_{A0}=v_{B0}, \quad w_{A0}=w_{B0}, \quad T_{A0}=T_{B0}, \tag{6.66}$$

$$w_{A0}=u_{A0}h_{0x}+v_{A0}h_{0y}, \tag{6.67}$$

$$
\begin{aligned}
&-p_{A0}+2\left(1+h_{0x}^2+h_{0y}^2\right)^{-1}\left[h_{0x}^2 u_{A0x}+h_{0y}^2 v_{A0y}+w_{A0z}+h_{0x}h_{0y}\left(u_{A0y}+v_{A0x}\right)\right.\\
&\left.-h_{0x}\left(w_{A0x}+u_{A0z}\right)-h_{0y}\left(v_{A0z}+w_{A0y}\right)\right]-K\{-p_{0B}+2\left(1+h_{0x}^2+h_{0y}^2\right)^{-1}\left[h_{0x}^2 u_{B0x}\right.\\
&\left.+h_{0y}^2 v_{B0y}+w_{B0z}+h_{0x}h_{0y}\left(u_{B0y}+v_{B0x}\right)-h_{0x}\left(w_{B0x}+u_{B0z}\right)-h_{0y}\left(v_{B0z}+w_{B0y}\right)\right]\}\\
&=\{-\left[h_{0xx}\left(1+h_{0y}^2\right)-2h_{0x}h_{0y}h_{0xy}+h_{0yy}\left(1+h_{0x}^2\right)\right]\left[T_{A0}+3\left(1+h_{0x}^2+h_{0y}^2\right)^{-1}*\right.\\
&\left.\left(h_{0x}h_{1x}+h_{0y}h_{1y}\right)\right]+h_{1xx}\left(1+h_{0y}^2\right)+2h_{0y}h_{1y}h_{0xx}-2\left(h_{0x}h_{1y}h_{0xy}+h_{1x}h_{0y}h_{0xy}\right.\\
&\left.+h_{0x}h_{0y}h_{1xy}\right)+\left(1+h_{0x}^2\right)h_{1yy}+2h_{0x}h_{1x}h_{0yy}\}\left(1+h_{0x}^2+h_{0y}^2\right)^{-3/2},
\end{aligned}
\tag{6.68}
$$

$$
\begin{aligned}
&2h_{0x}\left(-u_{A0x}+w_{A0z}\right)-h_{0y}\left(u_{A0y}+v_{A0x}\right)+\left(1-h_{0x}^2\right)\left(u_{A0z}+w_{A0x}\right)\\
&\quad-h_{0x}h_{0y}\left(v_{A0z}+w_{A0y}\right)-K\left[2h_{0x}\left(-u_{B0x}+w_{B0z}\right)-h_{0y}\left(u_{B0y}+v_{B0x}\right)\right.\\
&\quad\left.+\left(1-h_{0x}^2\right)\left(w_{B0x}+u_{B0z}\right)-h_{0x}h_{0y}\left(v_{B0z}+w_{B0y}\right)\right]\\
&=-\left(T_{A0x}+h_{0x}T_{A0z}\right)\left(1+h_{0x}^2+h_{0y}^2\right)^{1/2},
\end{aligned}
\tag{6.69}
$$

$$
\begin{aligned}
&2h_{0y}\left(w_{A0z}-v_{A0y}\right)-h_{0x}\left(u_{A0y}+v_{A0x}\right)+\left(1-h_{0y}^2\right)\left(v_{A0z}+w_{A0y}\right)\\
&\quad-h_{0x}h_{0y}\left(w_{A0x}+u_{A0z}\right)-K\left[2h_{0y}\left(w_{B0z}-v_{B0y}\right)-h_{0x}\left(u_{B0y}+v_{B0x}\right)\right.\\
&\quad\left.+\left(1-h_{0y}^2\right)\left(v_{B0z}+w_{B0y}\right)-h_{0x}h_{0y}\left(w_{B0x}+u_{B0z}\right)\right]\\
&=-\left(T_{A0y}+h_{0y}T_{A0z}\right)\left(1+h_{0x}^2+h_{0y}^2\right)^{1/2},
\end{aligned}
\tag{6.70}
$$

$$
-h_{0x}T_{A0x}-h_{0y}T_{A0y}+T_{A0z}=G\left(-h_{0x}T_{B0x}-h_{0y}T_{B0y}+T_{B0z}\right). \tag{6.71}
$$

In the above, the leading-order expressions for the dissipation functions are denoted by D_{A0} in equation (6.58) and D_{B0} in equation (6.63), respectively. Equations governing higher-order terms in the asymptotic expansions (3.47) and (3.48) can be written in an analogous way. Since the analysis given in this study is limited to the determination of the leading-order approximation of the flow field and surface deformation only, these equations will not be listed here.

6.4 Isothermal Conditions

When temperature gradients are negligible (leading-order approximation), the mechanism that drives the liquids is absent and the liquids remain in the state of static equilibrium governed by equations (6.47) to (6.53). It follows from equations (6.47) to (6.52) that the static pressures p_{As} and p_{Bs} are constant. Equation (6.53) is known as the Young-Laplace equation and its solutions describe menisci supporting a constant pressure difference. The actual value of $p_{As}-p_{Bs}$ is to be determined from the volumetric constraint (6.23) and from conditions imposed on the interface when $x\to\pm\infty$, $y\to\pm\infty$. Note that it is possible to determine only the difference $p_{As}-p_{Bs}$, not the absolute values of p_{As} and p_{Bs}.

Now let us concentrate on a particular solution of equations (6.47) to (6.53):

$$h_0=1, \tag{6.72}$$

$$p_{As}=p_{Bs}=const, \tag{6.73}$$

which corresponds to a flat interface. In order to check its static stability, consider a small volume-conserving deformation in the form

$$h_0=1+\varepsilon\hat{h}(x,y), \tag{6.74}$$

$$p_{As}-p_{Bs}=\varepsilon p_1, \tag{6.75}$$

where, $\hat{h}(x,y)$ denotes deformation bounded for $x\to\pm\infty$, $y\to\pm\infty$, ε is a small parameter measuring the magnitude of the deformation ($\varepsilon<<1$), and p_1 stands for the change in the pressure jump across the interface associated with the deformation $\hat{h}$. The deformation has to satisfy the volumetric constraint, i.e.,

$$\int_{-\infty}^{\infty}\int_{-\infty}^{\infty}\hat{h}(x,y)\,dxdy=0. \tag{6.76}$$

Substitution of equation (6.74) into equation (6.53) results, after linearization, in the following equation

$$\hat{h}_{xx}+\hat{h}_{yy}=-p_1. \tag{6.77}$$

Of which a general solution has the form

$$\hat{h}=\hat{h}_1-\frac{1}{4}p_1(x^2+y^2), \tag{6.78}$$

where $\hat{h}_1$ is governed by

$$\hat{h}_{1xx}+\hat{h}_{1yy}=0. \tag{6.79}$$

Since $\hat{h}$ is bounded, p_1 must be zero and $\hat{h}_1$ must be bounded. Since $\hat{h}_1$ is analytic by virtue of equation (6.79), it must be constant (Liouville's theorem). This constant must be zero due to the volumetric constraint condition (6.76). It can be concluded that equation (6.74) does not admit small non-trivial deformation of a flat interface, i.e., a flat interface is statically stable and capillary instability does not occur.

6.5 Thermocapillary Convection

When the flow and temperature fields are described by the equations (6.54) to (6.63) and subjected to the conditions (6.64) to (6.71), the problem is a fixed boundary problem since the location of the interface h_0 has already been, in principle, determined, and the analysis will be limited only to the flat interface described by equation (6.72). Boundary condition (6.68) is associated with interface deformation $h_1(x,y)$, however, this condition is not required to close the system of flow equations. Note that, while it is possible to determine velocity and temperature fields completely, the pressure field can be determined with accuracy up to a constant only.

The solution of the flow problem described above is a function of the following parameters: Re_A, Ma_A, Br_A, Re_B, Ma_B, Br_B, K, G, H and $T_W(x,y)$. There are many flow phenomena that may occur depending on the location in the parameter space. In the present study it is assumed that both liquid layers are sufficiently thin to make convection effects negligible, i.e., $Re_A=Re_B=Ma_A=Ma_B=0$. Also neglected are effects of dissipation, i.e., $Br_A=Br_B=0$. Therefore, this study focuses on the effects of different heat loading $T_W(x,y)$ applied to the bottom wall and of the ratios of viscosities and thermal conductivities, i.e., G and K of both liquids.

The assumptions regarding Re_A, Ma_A, Br_A, Re_B, Ma_B, Br_B lead to the decoupling of the energy equations (6.58) and (6.63) from the flow equations (6.54) to (6.57) and (6.59) to (6.62). Boundary conditions (6.64), (6.65), and (6.71) permit determination of the temperature field independently from the flow field, while the flow field is coupled to the temperature field through the boundary conditions (6.69) and (6.70).

6.5.1 Heat Transport

The assumptions described above reduce the heat transport problem to the following form:

$$T_{AOxx}+T_{AOyy}+T_{AOzz}=0, \tag{6.80}$$

$$T_{BOxx}+T_{BOyy}+T_{BOzz}=0, \tag{6.81}$$

$$z=0: \qquad T_{AO}=T_W(x,y)+B, \tag{6.82}$$

$$z=H: \qquad T_{BOz}=0, \tag{6.83}$$

$$z=1: \qquad T_{AO}=T_{BO}, \qquad T_{AOz}=GT_{BOz}, \tag{6.84}$$

where $T_W(x,y)+B$ is the temperature of the bottom wall.

To solve this problem, define a two-dimensional Fourier transform as

$$\hat{T}(k_1,k_2;z)=\frac{1}{2\pi}\int_{-\infty}^{\infty}\int_{-\infty}^{\infty}T(x,y,z)\,e^{i(k_1x+k_2y)}dxdy, \qquad (6.85)$$

which transforms equations (6.80) to (6.84) to become

$$\hat{T}_{AOzz}-k^2\hat{T}_{AO}=0, \qquad (6.86)$$

$$\hat{T}_{BOzz}-k^2\hat{T}_{BO}=0, \qquad (6.87)$$

$z=0$: $$\hat{T}_{AO}=\hat{T}_w(k_1,k_2)+\delta(k_1,k_2), \qquad (6.88)$$

$z=H$: $$\hat{T}_{BOz}=0, \qquad (6.89)$$

$z=1$: $$\hat{T}_{AO}=\hat{T}_{BO}, \qquad \hat{T}_{AOz}=G\hat{T}_{BOz}, \qquad (6.90)$$

The solution of the above system leads to the following expressions of the temperature:

$$T_{AO}(x,y,x)=\frac{1}{2\pi}\int_{-\infty}^{\infty}\int_{-\infty}^{\infty}\frac{D_1(k,H,z)-GD_2(k,H,z)}{D_3(k,H,G)}s(k_1,k_2)\,dk_1dk_2+B, \qquad (6.91)$$

$$T_{BO}(x,y,z)=\frac{1}{2\pi}\int_{-\infty}^{\infty}\int_{-\infty}^{\infty}\frac{D_1(k,H,z)-D_2(k,H,z)}{D_3(k,H,G)}s(k_1,k_2)\,dk_1dk_2+B, \qquad (6.92)$$

where

$$s(k_1,k_2)=\hat{T}_w(k_1,k_2)\,e^{-i(k_1x+k_2y)}, \qquad (6.93)$$

$$D_1(k,H,z)=\cosh(k\bar{H})\ \cosh[k(z-1)], \qquad (6.94)$$

$$D_2(k,H,z)=\sinh(k\bar{H})\sinh[k(z-1)], \qquad (6.95)$$

$$D_3(k,H,z)=\cosh(k)\cosh(k\bar{H})+G\sinh(k)\sinh(k\bar{H}), \qquad (6.96)$$

$$\bar{H}=H-1. \tag{6.97}$$

The temperature of the bottom wall has to satisfy conditions assuring existence of its Fourier transform. Expressions for the temperature field given above describe the mechanism for generation of temperature gradients along the interface that are responsible for the thermocapillary convection. The only source of temperature variations is the temperature of the bottom wall. The characteristic of this temperature distribution determines the topology of the flow: the heat flow between liquids A and B disappears when $G\to 0$; the interface becomes isothermal when $G\to\infty$; and the amplitude of temperature variations drops exponentially with distance away from the bottom wall for k sufficiently large. This discussion suggests that an increase of either G or k should lead to a reduction of the intensity of the convection.

For illustration purposes, consider a particular case of wall temperature distribution:

$$T_w(x,y)=T_{\alpha\beta}\sin(\alpha x)\sin(\beta y), \tag{6.98}$$

which can be viewed as describing one of the Fourier modes present in an arbitrary wall temperature. Then

$$T_{A0}(x,y,z)=\frac{D_1(\lambda,H,z)-GD_2(\lambda,H,z)}{D_3(\lambda,H,G)}T_{\alpha\beta}\sin(\alpha x)\sin(\beta y), \tag{6.99}$$

$$T_{B0}(x,y,z)=\frac{D_1(\lambda,H,z)-D_2(\lambda,H,z)}{D_3(\lambda,H,G)}T_{\alpha\beta}\sin(\alpha x)\sin(\beta y), \qquad (6.100)$$

where

$$\lambda=(\alpha^2+\beta^2)^{1/2}. \qquad (6.101)$$

6.5.2 Motion of the Liquid

Equations describing motion of the liquid reduce to the following form:

$$u_{A0x}+v_{A0y}+w_{A0z}=0, \qquad (6.102)$$

$$u_{A0xx}+u_{A0yy}+u_{A0zz}=p_{A0x}, \qquad (6.103)$$

$$v_{A0xx}+v_{A0yy}+v_{A0zz}=p_{A0y}, \qquad (6.104)$$

$$w_{A0xx}+w_{A0yy}+w_{A0zz}=p_{A0z}, \qquad (6.105)$$

$$u_{B0x}+v_{B0y}+w_{B0z}=0, \qquad (6.106)$$

$$u_{B0xx}+u_{B0yy}+u_{B0zz}=p_{B0x}, \qquad (6.107)$$

$$v_{B0xx}+v_{B0yy}+v_{B0zz}=p_{B0y}, \qquad (6.108)$$

$$w_{B0xx}+w_{B0yy}+w_{B0zz}=p_{B0z}, \qquad (6.109)$$

$z=0$: $$u_{A0}=v_{A0}=w_{A0}=0, \qquad (6.110)$$

$z=H$: $$u_{B0}=v_{B0}=w_{B0}=0, \qquad (6.111)$$

$z=1$:

$$u_{AO}=u_{BO}, \quad v_{AO}=v_{BO}, \quad w_{AO}=w_{BO}=0, \tag{6.112}$$

$$u_{AOz}-Ku_{BOz}=-T_{AOx}, \tag{6.113}$$

$$v_{AOz}-Kv_{BOz}=-T_{AOy}. \tag{6.114}$$

The motion is driven by specifying $T_w(x,y)$ in equations (6.91) and (6.92). Solution for an arbitrary distribution of $T_w(x,y)$ is found by introducing the two-dimensional Fourier transform of equations (6.102) to (6.114), where the transform of each particular component of the flow field is defined as

$$\hat{q}(k_1,k_2;z)=\frac{1}{2\pi}\int_{-\infty}^{\infty}\int_{-\infty}^{\infty}q_0(x,y,z)e^{-i(k_1x+k_2y)}dxdy \tag{6.115}$$

with q_0 standing for any flow variable.

Equations (6.102) to (6.114) are then transformed to the following form:

$$\hat{w}_{AOz}-i(k_1\hat{u}_{AO}+k_2\hat{v}_{AO})=0, \tag{6.116}$$

$$\hat{u}_{AOzz}-k^2\hat{u}_{AO}=-ik_1\hat{p}_{AO}, \tag{6.117}$$

$$\hat{v}_{AOzz}-k^2\hat{v}_{AO}=-ik_2\hat{p}_{AO}, \tag{6.118}$$

$$\hat{w}_{AOzz}-k^2\hat{w}_{AO}=\hat{p}_{AOz}, \tag{6.119}$$

$$\hat{w}_{BOzz}-i(k_1\hat{u}_{BO}+k_2\hat{v}_{BO})=0, \tag{6.120}$$

$$\hat{u}_{BOzz}-k^2\hat{u}_{BO}=-ik_1\hat{p}_{BO}, \tag{6.121}$$

$$\hat{v}_{BOzz}-k^2\hat{v}_{BO}=-ik_2\hat{p}_{BO}, \tag{6.122}$$

$$\hat{w}_{BOzz}-k^2\hat{w}_{BO}=\hat{p}_{BOz}, \tag{6.123}$$

$z=0$: $$\hat{u}_{AO}=\hat{v}_{AO}=\hat{w}_{AO}=0, \tag{6.124}$$

$z=H$: $$\hat{u}_{BO}=\hat{v}_{BO}=\hat{w}_{BO}=0, \tag{6.125}$$

$z=1$: $$\hat{u}_{AO}=\hat{u}_{BO}, \quad \hat{v}_{AO}=\hat{v}_{BO}, \quad \hat{w}_{AO}=\hat{w}_{BO}=0, \tag{6.126}$$

$$\hat{u}_{AOz}-K\hat{u}_{BOz}=ik_1\hat{T}_{AO}, \tag{6.127}$$

$$\hat{v}_{AOz}-K\hat{v}_{BOz}=ik_2\hat{T}_{AO}. \tag{6.128}$$

The solution of the above system leads to the following expressions for the flow components:

$$u_{AO}(x,y,z)=\frac{1}{2\pi}\int_{-\infty}^{\infty}\int_{-\infty}^{\infty}\frac{ik_1g_3(k,H)}{2F(k,H,K)}F_1(k,z)r(k_1,k_2)\,dk_1dk_2, \tag{6.129}$$

$$v_{AO}(x,y,z)=\frac{1}{2\pi}\int_{-\infty}^{\infty}\int_{-\infty}^{\infty}\frac{ik_2g_3(k,H)}{2F(k,H,K)}F_1(k,z)r(k_1,k_2)\,dk_1dk_2, \tag{6.130}$$

$$w_{AO}(x,y,z)=\frac{1}{2\pi}\int_{-\infty}^{\infty}\int_{-\infty}^{\infty}\frac{kg_3(k,H)}{2F(k,H,K)}F_2(k,z)r(k_1,k_2)\,dk_1dk_2, \tag{6.131}$$

$$p_{AO}(x,y,z)=\frac{1}{2\pi}\int_{-\infty}^{\infty}\int_{-\infty}^{\infty}\frac{k^2g_3(k,H)}{F(k,H,K)}F_5(k,z)r(k_1,k_2)\,dk_1dk_2+A_A, \tag{6.132}$$

$$u_{BO}(x,y,z)=\frac{1}{2\pi}\int_{-\infty}^{\infty}\int_{-\infty}^{\infty}\frac{ik_1g_2(k,H)}{2F(k,H,K)}F_3(k,z)r(k_1,k_2)\,dk_1dk_2, \tag{6.133}$$

$$v_{BO}(x,y,z) = \frac{1}{2\pi}\int_{-\infty}^{\infty}\int_{-\infty}^{\infty}\frac{ik_2 g_2(k,H)}{2F(k,H,K)}F_3(k,z)\,r(k_1,k_2)\,dk_1dk_2, \qquad (6.134)$$

$$w_{BO}(x,y,z) = \frac{1}{2\pi}\int_{-\infty}^{\infty}\int_{-\infty}^{\infty}\frac{kg_2(k,H)}{2F(k,H,K)}F_4(k,z)\,r(k_1,k_2)\,dk_1dk_2, \qquad (6.135)$$

$$p_{BO}(x,y,z) = \frac{1}{2\pi}\int_{-\infty}^{\infty}\int_{-\infty}^{\infty}-\frac{k^2 g_2(k,H)}{F(k,H,K)}F_6(k,z)\,r(k_1,k_2)\,dk_1dk_2+A_B, \qquad (6.136)$$

where

$$F(k,H,K) = k\{Kg_2(k)\,[\sinh(k\bar{H})\cosh(k\bar{H}) - k\bar{H}] + g_3(k,H)\,[\sinh(k)\cosh(k) - k]\}, \qquad (6.137)$$

$$F_1(k,z) = -g_1(k)\sinh(kz) + k^2 z\sinh(k)\sinh(kz) - kg_1(k)\,z\cosh(kz), \qquad (6.138)$$

$$F_2(k,z) = k\sinh(k)\sinh(kz) - k^2 z\sinh(k) * \cosh(kz) + kzg_1(k)\sinh(kz), \qquad (6.139)$$

$$F_3(k,H,z) = g_4(k,H)\sinh[k(z-H)] + k^2\bar{H}(z-H)\sinh(k\bar{H})\sinh[k(z-H)] + kg_4(k,H)\,(z-H)\cosh[k(z-H)], \qquad (6.140)$$

$$F_4(k,H,z) = k\bar{H}\sinh(k\bar{H})\sinh[k(z-H)] - k^2\bar{H}(z-H)\sinh(k\bar{H}) * \cosh[k(z-H)] - kg_4(k,H)\,(z-H)\cosh[k(z-H)], \qquad (6.141)$$

$$F_5(k,z) = g_1(k)\sinh(kz) - k\sinh(k)\cosh(kz), \qquad (6.142)$$

$$F_6(k,H,z) = g_4(k,H)\sinh[k(z-H)] + k\bar{H}\sinh(k\bar{H})\cosh[k(z-H)], \qquad (6.143)$$

$$g_1(k) = k\cosh(k) - \sinh(k), \qquad (6.144)$$

$$g_2(k) = \sinh^2(k) - k^2, \tag{6.145}$$

$$g_3(k,H) = \sinh^2(k\bar{H}) - k^2\bar{H}^2, \tag{6.146}$$

$$g_4(k,H) = k\bar{H}\cosh(k\bar{H}) - \sinh(k\bar{H}), \tag{6.147}$$

$$r(k_1,k_2) = \hat{T}_i(k_1,k_2)\, e^{-i(k_1x+k_2y)}, \tag{6.148}$$

and $\hat{T}_i$ (k_1, k_2) denotes the Fourier transform of the interface temperature arising due to the wall temperature $T_w(x,y)$, i.e.,

$$\hat{T}_i(k_1,k_2) = \frac{\cosh(k\bar{H})}{\cosh(k)\cosh(kH) + G\sinh(k)\sinh(kH)}\hat{T}_w(k_1,k_2). \tag{6.149}$$

The arbitrary constants A_A and A_B in the pressure fields have to be determined from analysis of the interface deformation.

Analysis of the vorticity fields shows that the vorticity vectors

$$\Omega_{A0} = \Omega_{A0x}\mathbf{i} + \Omega_{A0y}\mathbf{j} + \Omega_{A0z}\mathbf{k} \text{ and } \Omega_{B0} = \Omega_{B0x}\mathbf{i} + \Omega_{B0y}\mathbf{j} + \Omega_{B0z}\mathbf{k}$$

are always parallel to the (x,y)-plane, i.e.,

$$\Omega_{A0x} = -\frac{i}{2\pi}\int_{-\infty}^{\infty}\int_{-\infty}^{\infty}\frac{k_2 g_3(k,H)}{2F(k,H,K)}\zeta_1(k,z)\, r(k_1,k_2)\, dk_1\, dk_2, \tag{6.150}$$

$$\Omega_{A0y} = \frac{i}{2\pi}\int_{-\infty}^{\infty}\int_{-\infty}^{\infty}\frac{k_1 g_3(k,H)}{2F(k,H,K)}\zeta_1(k,z)\, r(k_1,k_2)\, dk_1\, dk_2, \tag{6.151}$$

$$\Omega_{A0z} = 0. \tag{6.152}$$

Expressions for components of Ω_{B0} are similar with $g_3(k,H)$ replaced by $g_2(k)$, and $\zeta_1(k,z)$ by $\zeta_2(k,z,H)$. The definitions of $g_2(k)$ and $g_3(k)$ are as before

$$\zeta_1(k,z) = 2k^2\sinh(k)\sinh(kz) - 2kg_1(k)\cosh(kz), \quad (6.153)$$

$$\zeta_2(k,z,H) = 2k^2\bar{H}\sinh(k\bar{H})\sinh[k(z-H)] + 2kg_4(k,H)\cosh[k(z-H)]. \quad (6.154)$$

The vortex lines form planes parallel to the (x,y)-plane and their topology is described by constant values of the function $W_A(x,y)$ defined as

$$W_A(x,y) = \frac{1}{2\pi}\int_{-\infty}^{\infty}\int_{-\infty}^{\infty}\frac{g_3(k,H)}{2F(k,H,K)}\xi_1(k,z)\,r(k_1,k_2)\,dk_1dk_2, \quad (6.155)$$

where $\Omega_{Ax}=\partial W/\partial y$, $\Omega_{Ay}=\partial W/\partial x$. A similar function can be defined for fluid B.

One may note that all the above expressions demonstrate explicitly that the pattern of the flow in the (x,y)-plane is completely determined by the wall temperature.

For illustration purposes, consider a particular case of a flow induced by the temperature distribution (6.98). The results are as follows:

$$u_{A0}(x,y,z) = -\frac{\alpha T_{in} g_3(\lambda,z)F_1(\lambda,z)}{2F(\lambda,H,K)}\cos(\alpha x)\sin(\beta y), \quad (6.156)$$

$$v_{A0}(x,y,z) = -\frac{\beta T_{in} g_3(\lambda,H)F_1(\lambda,z)}{2F(\lambda,H,K)}\sin(\alpha x)\cos(\beta y), \quad (6.157)$$

$$w_{A0}(x,y,z) = \frac{\lambda T_{in} g_3(\lambda,H)F_2(\lambda,z)}{2F(\lambda,H,K)}\sin(\alpha x)\sin(\beta y), \quad (6.158)$$

$$p_{A0}(x,y,z) = \frac{\lambda^2 T_{in} g_3(\lambda,H) F_5(\lambda,H)}{F(\lambda,H,K)} \sin(\alpha x)\sin(\beta y) + A_A, \quad (6.159)$$

$$u_{B0}(x,y,z) = -\frac{\alpha T_{in} g_2(\lambda) F_3(\lambda,H,z)}{2F(\lambda,H,K)} \cos(\alpha x)\sin(\beta y), \quad (6.160)$$

$$v_{B0}(x,y,z) = -\frac{\beta T_{in} g_2(\lambda) F_3(\lambda,H,z)}{2F(\lambda,H,K)} \sin(\alpha x)\cos(\beta y), \quad (6.161)$$

$$w_{B0}(x,y,z) = \frac{\lambda T_{in} g_2(\lambda) F_4(\lambda,H,z)}{2F(\lambda,H,K)} \sin(\alpha x)\sin(\beta y), \quad (6.162)$$

$$p_{B0}(x,y,z) = -\frac{\lambda^2 T_{in} g_2(\lambda) F_6(\lambda,H,z)}{F(\lambda,H,K)} \sin(\alpha x)\sin(\beta y) + A_B, \quad (6.163)$$

where T_{in} denotes amplitude of the interface temperature variations, i.e.,

$$T_{in} = \frac{T_{\alpha\beta}\cosh(\lambda\bar{H})}{\cosh(\lambda)\cosh(\lambda\bar{H}) + G\sinh(\lambda)\sinh(\lambda\bar{H})}. \quad (6.164)$$

The above expressions can be interpreted as describing a fundamental Fourier mode associated with the convection being studied.

6.6 Interface Deformation

The interface deformation is described by equation (6.68) subject to the volumetric constraint (6.23). The explicit form of this constraint is

$$\int_{-\infty}^{\infty}\int_{-\infty}^{\infty} h_1(x,y)\,dxdy=0. \qquad (6.165)$$

We shall limit consideration to an interface that is initially flat, i.e. it is described by equation (6.72). The interface deformation equation reduces to

$$h_{1xx}+h_{1yy}=-p_{A0}(x,y,1)+2w_{A0z}(x,y,1)+A_A \\ -K[p_{B0}(x,y1)+2w_{B0z}(x,y,1)+A_B], \qquad (6.166)$$

which is valid for arbitrary values of the transport parameters Re_A, Ma_A, Br_A, Re_B, Ma_B, Br_B. However, an explicit solution of this equation can only be found for the case where $Re_A=Ma_A=Br_A=Re_B=Ma_B=Br_B=0$.

The inhomogeneous part of the solution of equation (6.166) when the flow is driven by arbitrary interface traction τ_1 and τ_2, $\bar{h}_1$ can be found via Fourier transforms, i.e.,

$$\bar{h}_1(x,y)= \frac{1}{2\pi}\int_{-\infty}^{\infty}\int_{-\infty}^{\infty}\{\frac{i\hat{M}(k_1,k_2)}{KF(k,H,K)}[g_3(k,H)-Kg_2(K)\bar{H}^2] \\ -\frac{A_A-KA_B}{k^2}2\pi\delta(k_1)\delta(k_2)\}e^{-i(k_1x+k_2y)}dk_1dk_2, \qquad (6.167)$$

where $\hat{M}=k_1\hat{\tau}_1(k_1, k_2)+k_2\hat{\tau}_2(k_1, k_2)$ with $\hat{\tau}_1$ and $\hat{\tau}_2$ denoting Fourier transform of τ_1, τ_2, respectively, and δ Direct delta function. $A_A=A_B=0$ has bo be satisfied if $\hat{h}$ is to be bounded for arbitrary K.

It follows from the Liouville's theorem that the only possible homogeneous solution of equation (6.166) is a constant, and this constant has to be zero in view of the volumetric constraint (6.165). Thus, the expression for the interface deformation takes the form:

$$\bar{h}_1(x,y) = \frac{1}{2\pi}\int_{-\infty}^{\infty}\int_{-\infty}^{\infty} \frac{i\hat{M}(k_1,k_2)}{F(k,H,K)}\left[g_3(k,H) - Kg_2(k)\bar{H}^2\right] * e^{-i(k_1x+k_2y)}dk_1dk_2, \qquad (6.168)$$

The volumetric constraint condition (6.165) applied to equation (6.168) results in

$$\int_{-\infty}^{\infty}\int_{-\infty}^{\infty} \frac{\hat{M}(k_1,k_2)\left[g_3(k,H) - Kg_2(k)\bar{H}^2\right]}{F(k,H,K)}\delta(k_1)\,\delta(k_2)\,dk_1dk_2 = 0. \qquad (6.169)$$

The above is always satisfied when $\tau_1(x,y)$ and $\tau_2(x,y)$ are both periodic in at least one direction. When the conditions of periodicity do not arise, equation (6.169) imposes constraints on the class of acceptable surface traction distributions in the form:

$$f_1 = o(k^3), \quad f_2 = o(k^3), \qquad \text{when } k \to 0. \qquad (6.170)$$

These conditions are identical to the ones found in the case of a single liquid layer (Floryan & Krol, 1991). When the surface traction occurs due to thermocapillary effect, the interface deformation takes the form:

$$h_1(x,y) = -\frac{1}{2\pi}\int_{-\infty}^{\infty}\int_{-\infty}^{\infty}\frac{k^2\hat{T}_i(k_1,k_2)\,[g_3(k,H) - Kg_2(k,H)\bar{H}^2]}{F(k,H,K)} * e^{-i(k_1x+k_2y)}dk_1dk_2 \qquad (6.171)$$

and leads to the constraint condition

$$\int_{-\infty}^{\infty}\int_{-\infty}^{\infty}\frac{k^2\hat{T}_i(k_1,k_2)\,[g_3(k,H) - Kg_2(k,H)\bar{H}^2)\,]}{F(k,H,K)}\delta(k_1)\,\delta(k_2)\,dk_1dk_2, \qquad (6.172)$$

where $\hat{T}_i(k_1, k_2)$ is given by equation (6.153). The above condition is satisfied if

$$\hat{T}_w(k_1,k_2) = o(k^2). \qquad (6.173)$$

This implies that

$$\int_{-\infty}^{\infty}\int_{-\infty}^{\infty} m(x,y)\,T_w(x,y)\,dxdy = 0. \qquad (6.174)$$

where $m(x,y)=1,x,y,xy$, as shown in Floryan & Krol (1991).

The results derived above clearly show that only a certain restricted class of temperature distributions applied to the liquid layers leads to a steady interface deformation and thus steady thermocapillary convection. The form of the existence conditions will not be affected by the presence and properties of the upper layer.

The temperature distribution described by equation (6.98), which satisfies the existence conditions, leads to the interface deformation in the form

$$h_1(x,y) = -\frac{\lambda^2 T_m}{F(\lambda,H,K)}[g_3(\lambda,H) - Kg_2(\lambda)\bar{H}^2]\sin(\alpha x)\sin(\beta y) . \quad (6.175)$$

6.7 Discussion of the Results

It has been shown in the previous sections that the presence of an additional layer does not affect conditions describing a continuous layer, i.e., the external temperature field applied to the liquid has to satisfy the same conditions as in the case of a single layer system. What remains to be discussed is the characteristics of the convection when the existence conditions are satisfied. Since the convection is affected by the ratio of thermal conductivity G, the ratio of viscosity K, the depth of upper layer, and wave number λ, this chapter will focus on the question of how these parameters change the characteristics of the convection.

6.7.1 The Fundamental Mode of the Convection

Thermocapillary convection induced by a special wall temperature distribution, equation (6.98), is considered here. This temperature distribution can be proved, in fact, to correspond to a typical Fourier mode present in the problem. An example of such a temperature distribution in the lower layer is shown in Figure 6.2, where $\alpha=\pi$ and $\beta=2\pi$. The topology

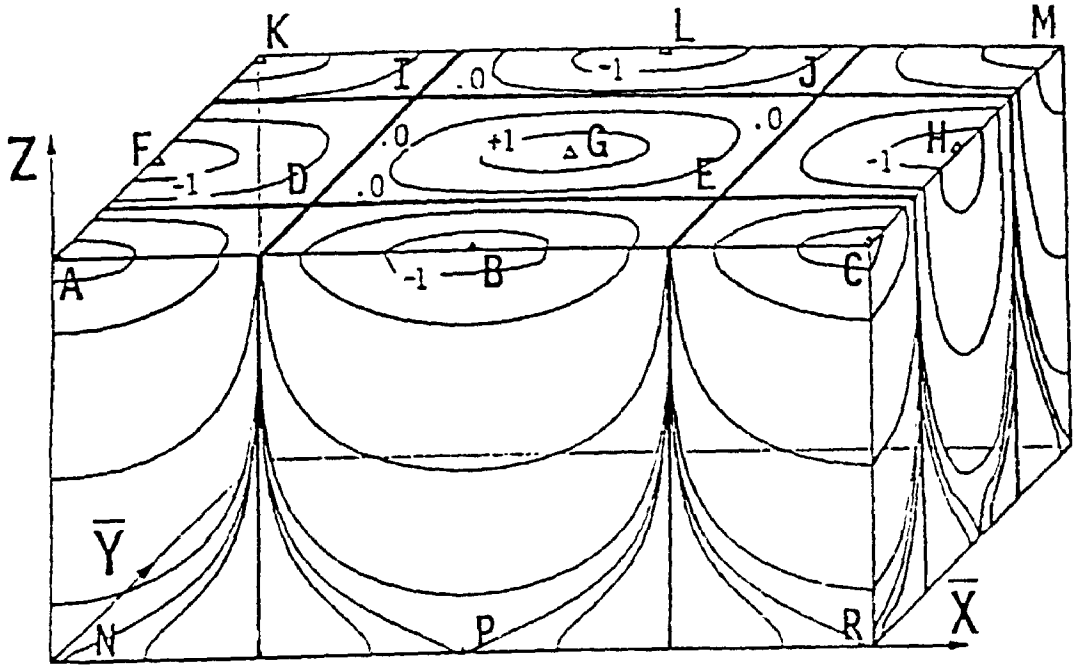

Figure 6.2 Temperature distribution corresponding to a typical mode in the temperature field. Here, $\bar{x}=x-0.5$, $\bar{y}=y-0.25$ and the plot extends to $\bar{x}=2.0$ and $\bar{y}=1.0$. Points A,C,G,K, and M denote interface temperature maxima while points B,F,H, and L denote interface temperature minima.

of the corresponding flow field in the bottom layer is shown in Figure 6.3. Note that the flow field distribution in the upper layer is qualitatively similar and forms a mirror image of the flow in the lower layer, with stretching accounting for the effects of different thicknesses of the two layers.

Figure 6.3 shows that the flow is driven along the interface from hot to cold spots. Because of the conservation of mass, the fluid turns towards the interior of the liquid layer as it approaches the cold spots and is drawn from within the interior of the layer around the hot spots. The flow topology on the interface is completely determined by the distribution of shear stress.

Figure 6.4 portrays the interface deformation as induced by thermocapillary effects. The character of this deformation is determined by interactions between the following two competing factors. The first one is of a static nature and is associated with variations of surface tension, i.e., the variation of the mean curvature of the interface has to be inversely proportional to that of the surface tension in order to maintain constant pressure inside the liquid. This effect would bulge the interface outwards at the hot spots and inwards at the cold spots. The second factor is a dynamic one

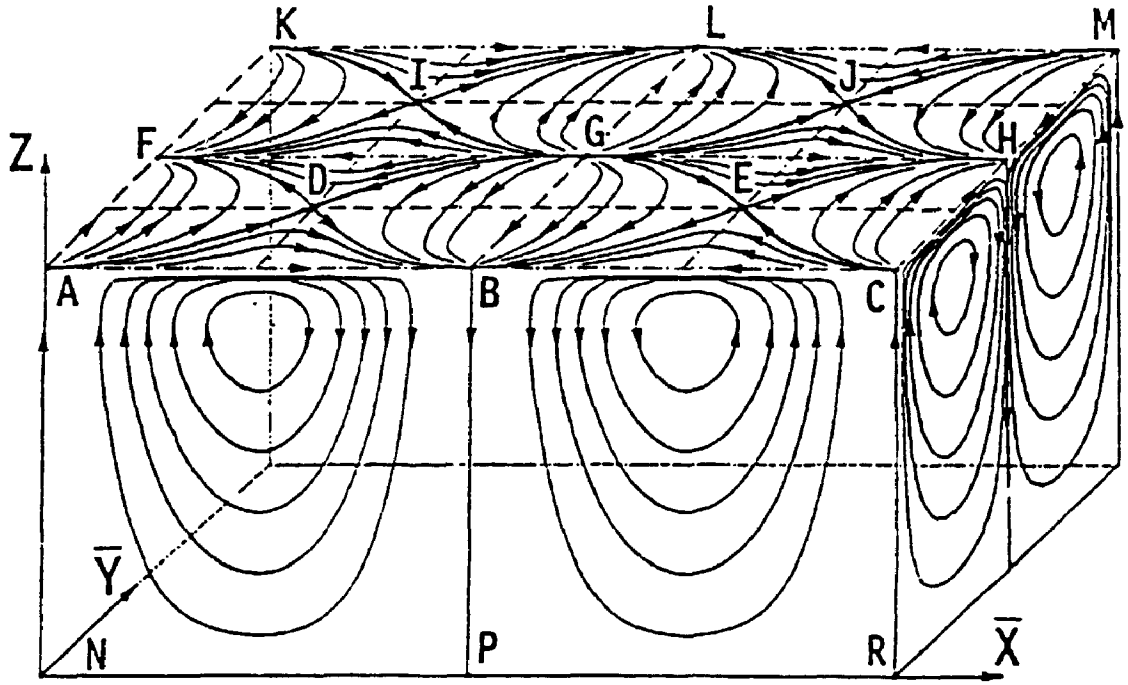

Figure 6.3 Topology of the flow field induced by the temperature field displayed in Fig. 6.2. Dash lines identify locations where the x-component of surface stress is zero, while dash-dot lines identify locations where the y-component of surface stress is zero. Intersections of the dash and dash-dot lines identify locations of the nodal and saddle (stagnation) points. See Fig. 6.2 for further details.

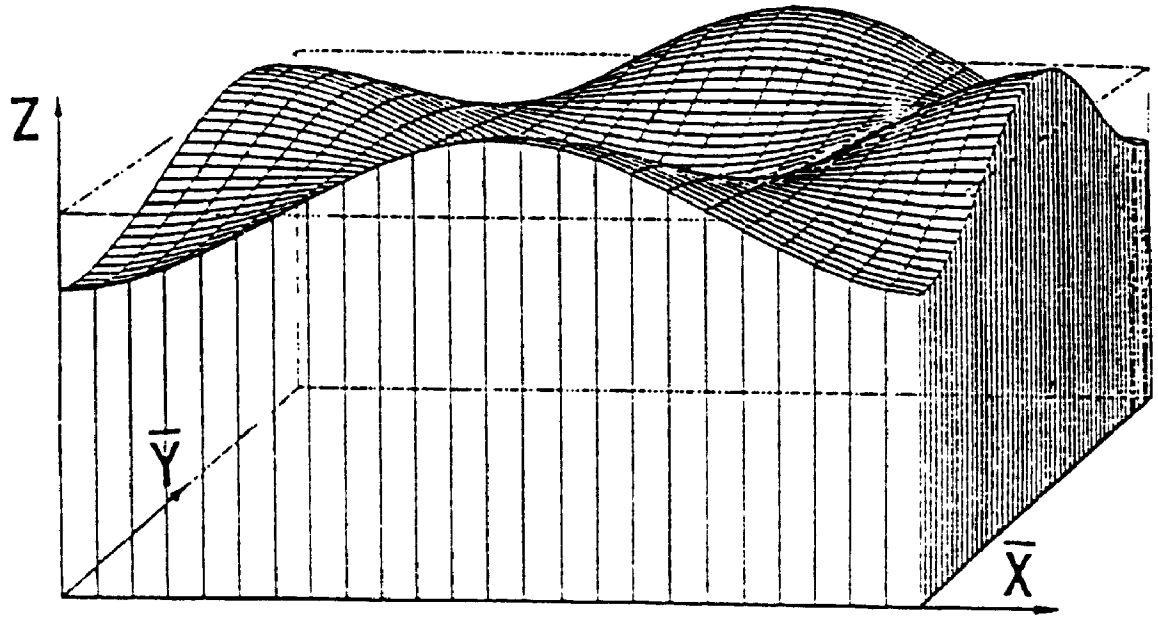

Figure 6.4 Surface deformation induced by flow and temperature fields displayed in Figs. 6.2 and 6.3. See Figs. 6.2 and 6.3 for further details.

concerning the motion of the liquid. When the liquid is drawn towards the cold spots, there is a pressure rise such that the liquid can be re-directed towards the interior of the layer. Similarly, when liquid is drawn away from the hot spots, there is a pressure drop so as to draw the liquid from within the interior of the layer. The resulting pressure distribution would, therefore, tend to bulge the interface outwards at the cold spots and inwards at the hot spots. By looking at Figure 6.4, it is clear that the dynamic effect dominates.

6.7.2 The Effects of the Ratio of Conductivity, G

Since maximum convection occurs at the interface, the discussion of the effects of properties of the upper layer on the convection in the lower layer can be conveniently carried out in terms of the amplitude of the interface velocity vector as defined by

$$V=(u_{max}^2+v_{max}^2)^{1/2}=\frac{\lambda g_3(\lambda,\bar{H})\,g_2(\lambda)}{F(\lambda,\bar{H},K)}*T_{in}, \qquad (6.176)$$

where T_{in} is the amplitude of temperature distribution at the interface and equal to

$$T_{in}=\frac{T_w\cosh(\lambda\bar{H})}{\cosh(\lambda)\cosh(\lambda\bar{H})+G\sinh(\lambda)\sinh(\lambda\bar{H})}, \qquad (1.177)$$

and λ is defined by equation (6.101).

The heat transfer process occurring in the two layers depends on G. Since the temperature field changes as G changes, the effect of convection on the shape of the interface will change accordingly. In other words, G has effects on convection by affecting the temperature distributions between the two layers, or the effects of G are indirect. This conclusion can also be obtained by analyzing equations (6.176) and (6.177) in which G affects V by showing up only in T_{in}. As a matter of fact, analysis of equations (6.156) to (6.162) reveals that the velocity can be written as

$$v(x,y,z)=L(\lambda,\bar{H},G)\ V_1(x,y,z,\lambda,\bar{H}) \qquad (6.178)$$

in which

$$L(\lambda,\bar{H},G)=\frac{\cosh(\lambda\bar{H})}{\cosh(\lambda)\cosh(\lambda\bar{H})+G\sinh(\lambda)\sinh(\lambda H)}, \qquad (6.179)$$

with v standing for u_{A0}, v_{A0}, w_{A0}, u_{B0}, v_{B0}, and w_{B0}. $V_1(x,y,z,\lambda,\bar{H})$ may be considered as serving as a measuring unit such that L is a measurement of velocity in terms of V_1. Therefore, the larger the value of L, the larger is the variation in the interface temperature, which in turn, generates a stronger convection. Furthermore, one may note , from equation (6.177), that L is the ratio of the interface temperature and the wall temperature, i.e.,

$$\frac{T_{in}(x,y)}{T_w(x,y)}=L(\lambda,\bar{H},G)\,. \qquad (6.180)$$

Hence, L can be considered as the transfer function between the two temperatures. Meanwhile, Krol (1991) reported a transfer function for single layer cases, i.e.,

$$L_1 = \frac{Bi\cosh(\lambda)}{\lambda\sinh(\lambda) + Bi\cosh(\lambda)}. \qquad (6.181)$$

Therefore, if and only if $L<L_1$ will the strength of convection in double layer system be weaker than in the original one-layer system. It can be proved that the corresponding necessary and sufficient condition is

$$G \geq \frac{\lambda\sinh(\lambda) + Bi\cosh(\lambda) - Bi\cosh^2(\lambda)}{Bi\sinh(\lambda)\cosh(\lambda)} \tanh(\lambda\bar{H}). \qquad (6.182)$$

Therefore the larger the values of G, the weaker the resulting convection is.

To observe the quantitative effects of G on convection, the relations between G, L and G, V are studied and shown in Figures 6.5 to 6.7, where $\bar{H}$ and λ are treated as parameters. Figures 6.5 to 6.7 demonstrate that L and V decrease with the increase of G (in fact, one can prove that L is a monotonically decreasing function for all of its arguments: G, $\bar{H}$, and λ). L assumes its maximum at G=0 and minimum as $G\to\infty$. $G\to 0$ corresponds to the case in which the thermal conductivity of liquid B is very small compared with that of liquid A (so that the interface becomes insulated and the temperature of liquid B is independent of that of liquid A). On the other

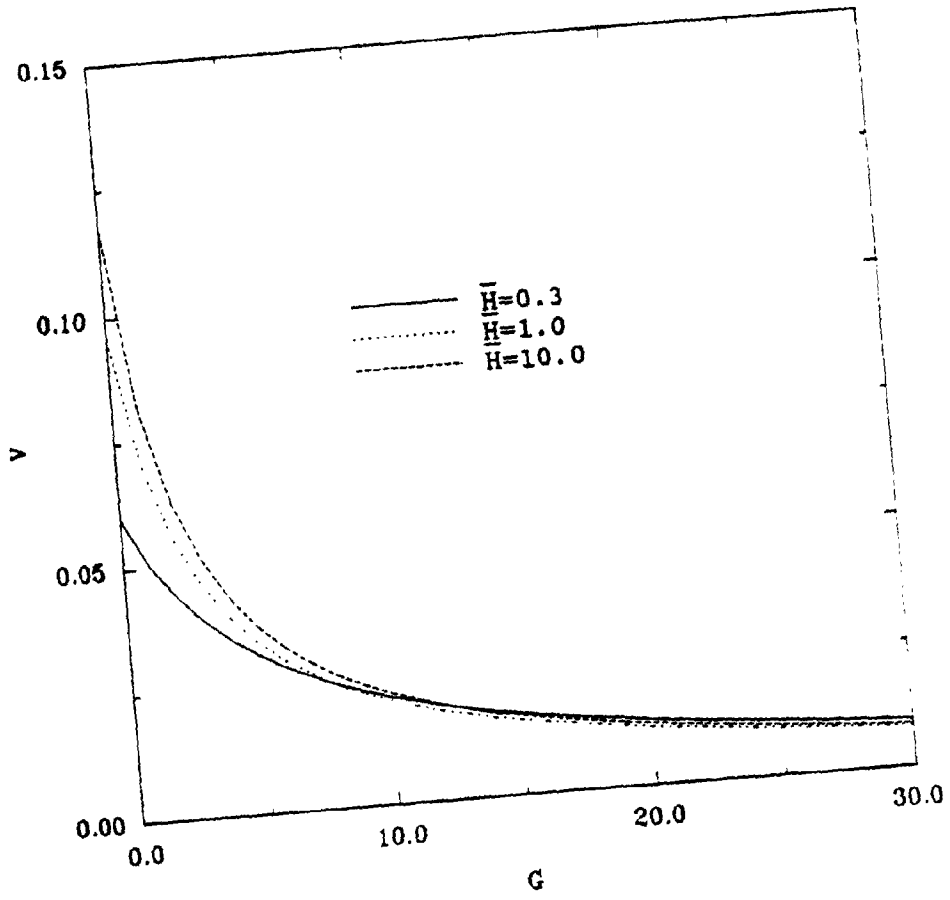

Figure 6.5 Variation of the amplitude V of the interface velocity vector induced by the temperature field (6.98) as a function of the relative conductivity of the upper liquid G for K=1.0 and λ=1.0.

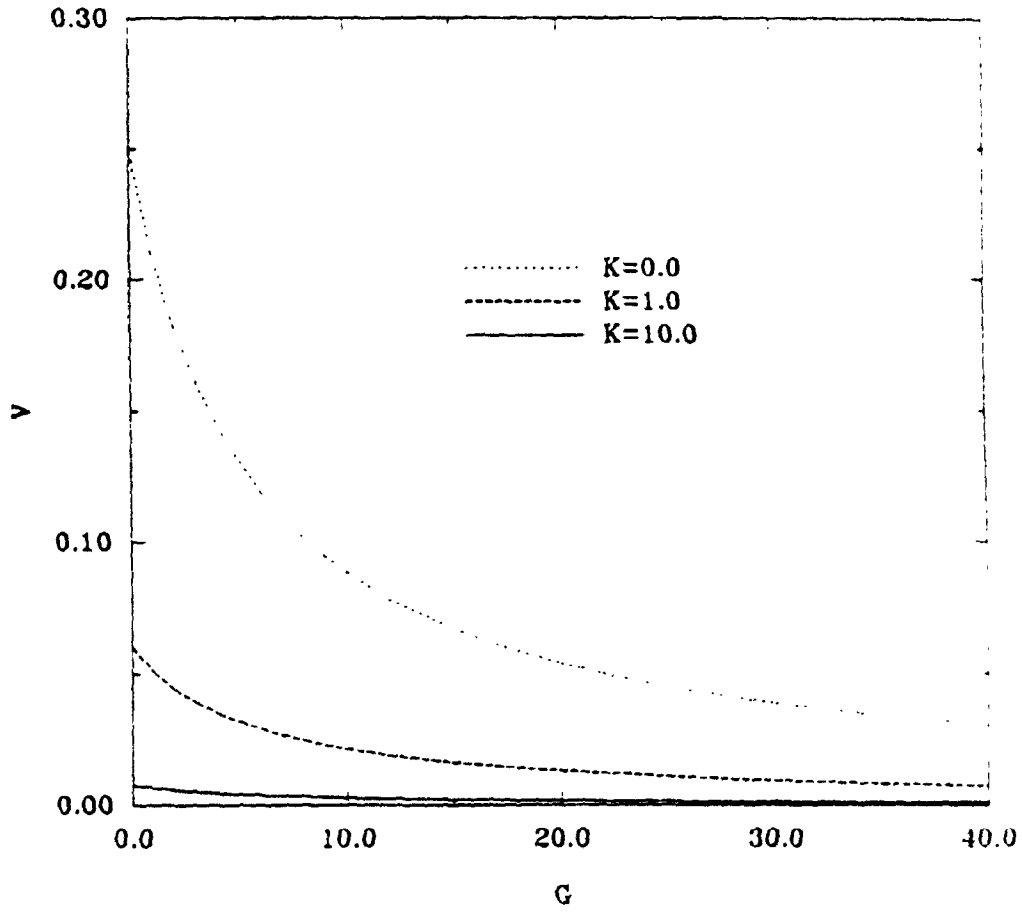

Figure 6.6 Variation of the amplitude V of the interface velocity vector induced by the temperature field (6.98) as a function of the relative conductivity of the upper liquid G for $\bar{H}$=0.3 and λ=1.0.

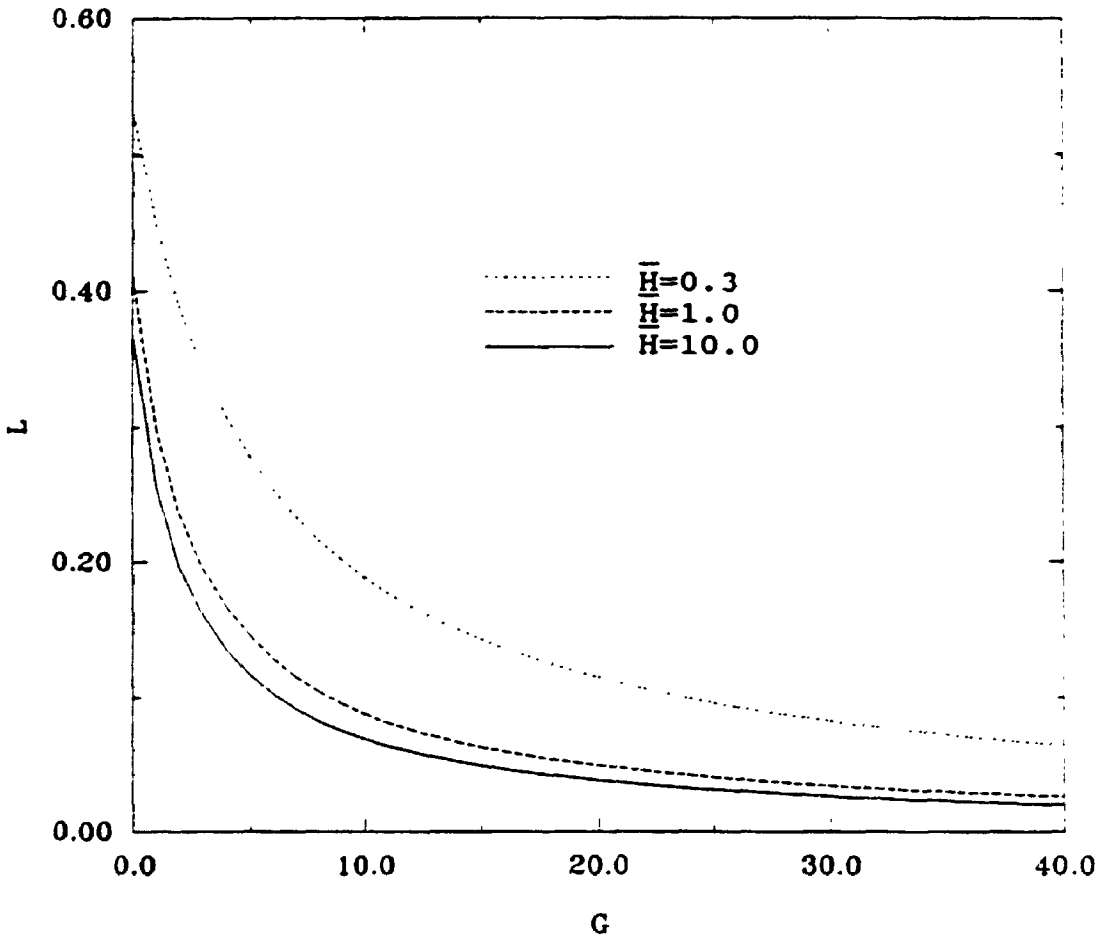

Figure 6.7 Variation of the amplitude L of the transfer function (6.180) as a function of the relative conductivity of the upper liquid G for K=1.0 and λ=1.0.

hand, the case of $G \to \infty$ represents a very weak heat conduction in liquid A resulting in the interface being almost isothermal. In this case there is no driving force for the flow and both of the liquids remain static.

One may also note that the maximum of L is 1 which indicates that the interface temperature is always lower than the wall temperature.

6.7.3 The Effects of the Ratio of Viscosities K

In Section 6.7.2, the change of temperature has been studied. In this section, the effects of K, the ratio of the viscosities, on the convection will be discussed (for fixed interface temperature). Note that K determines the jump in the shear stress which in turn, has to be in balance with the surface tension gradient at the interface. In the present study, since the temperature field is decoupled from the flow field, the temperature distribution will not be affected by K, and only the changes of flow field with K will be looked into.

Consider first the case where $K \to 0$. This happens when μ_A is very large compared with μ_B so that liquid A dominates the flow. In this case, equations (6.178) become

$$V = \frac{[\sinh^2(\lambda) - \lambda^2]T_m}{\sinh(2\lambda) - 2\lambda}. \qquad (6.183)$$

Comparing the above equation with the corresponding formula for single layer from Krol (1991), one can find that they are exactly the same. Thus, K→0 means a double layer system reduces to a single layer system. Liquid B then has no effect on the motion of liquid A.

The second case to look at is when K→∞. This case corresponds to μ_B which is very large compared with μ_A so that liquid B is dominant. The system equations for this case can be re-cast by using the properties of liquid B. And the results are found to be similar to those based on liquid A.

An example of the numerical study of the system equations for arbitrary values of K can be seen in Figure 6.8 which illustrates that increasing K decreases the intensity of the convection.

One may note that formula (6.176) is a function which decreases monotonically for any K>0. It takes its maximum at K=0. Recalling that K>0 represents a double layer system, this implies that the intensity of convection in a double layer system is always weaker than that in a single layer system or,

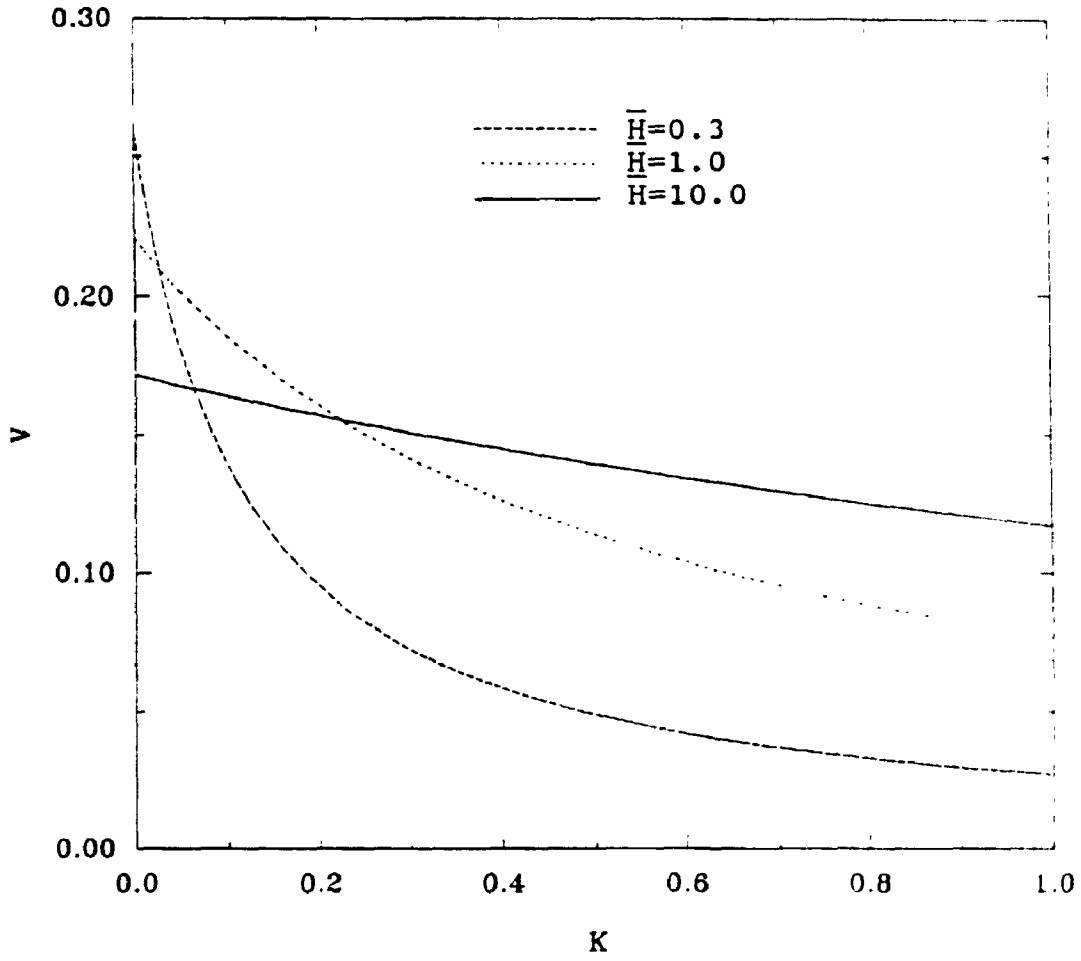

Figure 6.8 Variation of the amplitude V of the interface velocity vector induced by the temperature field (6.98) as a function of the relative viscosity of the upper liquid K for G=1.0 and λ=1.0.

in other words, the coating of one liquid layer by another will always reduce the convection. From a purely physical viewpoint, one can draw the same conclusion as follows: since the gradient of the surface tension is the driving force of the motion and shear stress has to balance the gradient, one can view the shear stress as a load for surface tension. Following Newton's second law of motion, a larger load will cause a weaker motion for a given driving force. In a single layer system, the shear stress can only come from the movement of liquid A, while both liquid A and B contribute to the shear stress in a double layer system. As a result, as the movement in liquid A decreases, and the larger the shear stress that liquid B produces, the weaker the movement of liquid A. Note that the shear stress coming from liquid B has a magnitude that is proportional to K, so that increasing K will no doubt decrease the intensity of convection.

6.7.4 The Effects of Thickness of the Upper Layer $\bar{H}$

The thickness of the upper layer, $\bar{H}=H-1$, affects the convection by changing both the viscous stresses and interface temperature gradient. Concerning the temperature field, it is known (Section 6.7.2) that the transfer function between the interface and wall temperature decreases monotonically and that increasing $\bar{H}$ will decrease the interface temperature, thus decrease the intensity of the convection.

Now, consider the effects of $\bar{H}$ on the flow field, given that the interface temperature is fixed. Assuming that the upper boundary is a solid wall, more constraints will be imposed on the flow as $\bar{H}$ decreases. At the extreme, i.e., when $\bar{H}$=0, there will be no interface and driving force disappears. In this case the velocity field is zero. As $\bar{H}$ increases, the constraint effect imposed by the solid wall decreases but more fluid will be driven. These two trends will eventually arrive at an equilibrium state so that the changes in $\bar{H}$ cease to generate any more effects on the flow distribution. In fact, analysis of equations (6.156) to (6.163) reveals that

$$q=q_0(\lambda,x,y,z)+q_1(x,y,z,\lambda,K)\bar{H}^2e^{-2\lambda\bar{H}}+O(e^{-4\lambda\bar{H}}), \quad (6.184)$$

where q stands for flow parameters. It can then be seen that

$$q\to q_0 \qquad when \quad \bar{H}\to\infty. \quad (6.185)$$

Figure 6.9 shows the distributions of the horizontal velocity component for various values of $\bar{H}$. It reveals that the addition of the upper liquid layer can decrease the horizontal component of velocity and thus the convection. This is especially true when the second liquid layer is thin (see the curve of $\bar{H}$=0.3 in Figure 6.9).

When H=1, the velocity and pressure fields are symmetric, for both liquid A and B, about the interface. Due to the

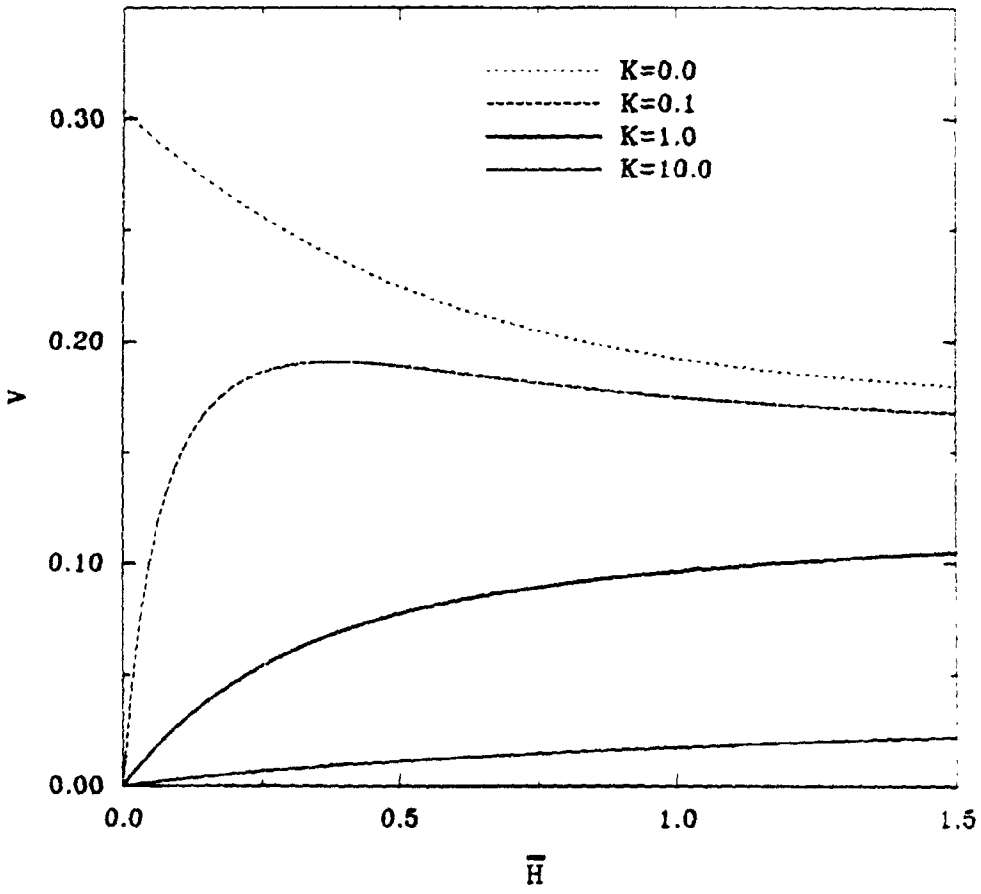

Figure 6.9 Variation of the amplitude V of the interface velocity vector induced by the temperature field (6.98) as a function of the thichness $\bar{H}$ of the upper liquid K for G=1.0 and λ=1.0.

conservation of mass, the vertical velocity component will be antisymmetric.

6.7.5 The Effects of the Wave Number λ

Figures 6.10 and 6.11 portray the velocity magnitude as a function of wave number λ. The entire double layer system acts as a bandwidth filter which filters out both high and low wave-number components. Since the temperature gradient along the interface is proportional to λ, the driving force is very small when λ is very small. On the other hand, the amplitude of the interface temperature is very small when λ is large enough. Eventually, the driving force will disappear too.

When the wall temperature is periodic, the temperature, velocity and pressure in both liquid layers can be expressed explicitly (Section 6.5 and 6.6). Otherwise, numerical results have to be sought. One approach, which is based on results obtained in Section 6.5 and 6.6 and a discrete Fourier transform (DFT) method, is developed in Appendix E.

6.8 Concluding Remarks

It follows from the above discussions that, assuming that it is possible to maintain a nonisothermal layer, the convection within this layer can be effectively controlled by

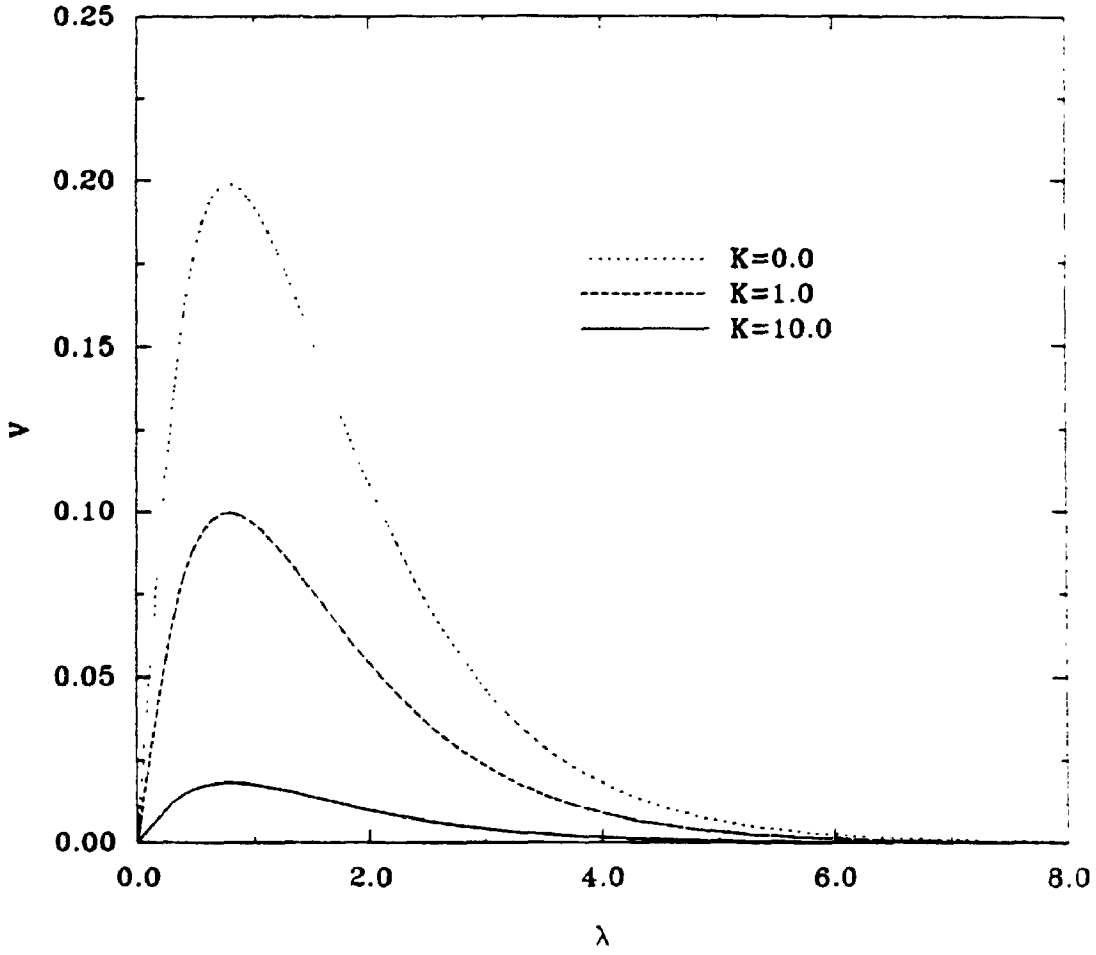

Figure 6.10 Variation of the amplitude V of the interface velocity vector induced by the temperature field (6.98) as a function of λ for G=1.0 and $\bar{H}$=1.0

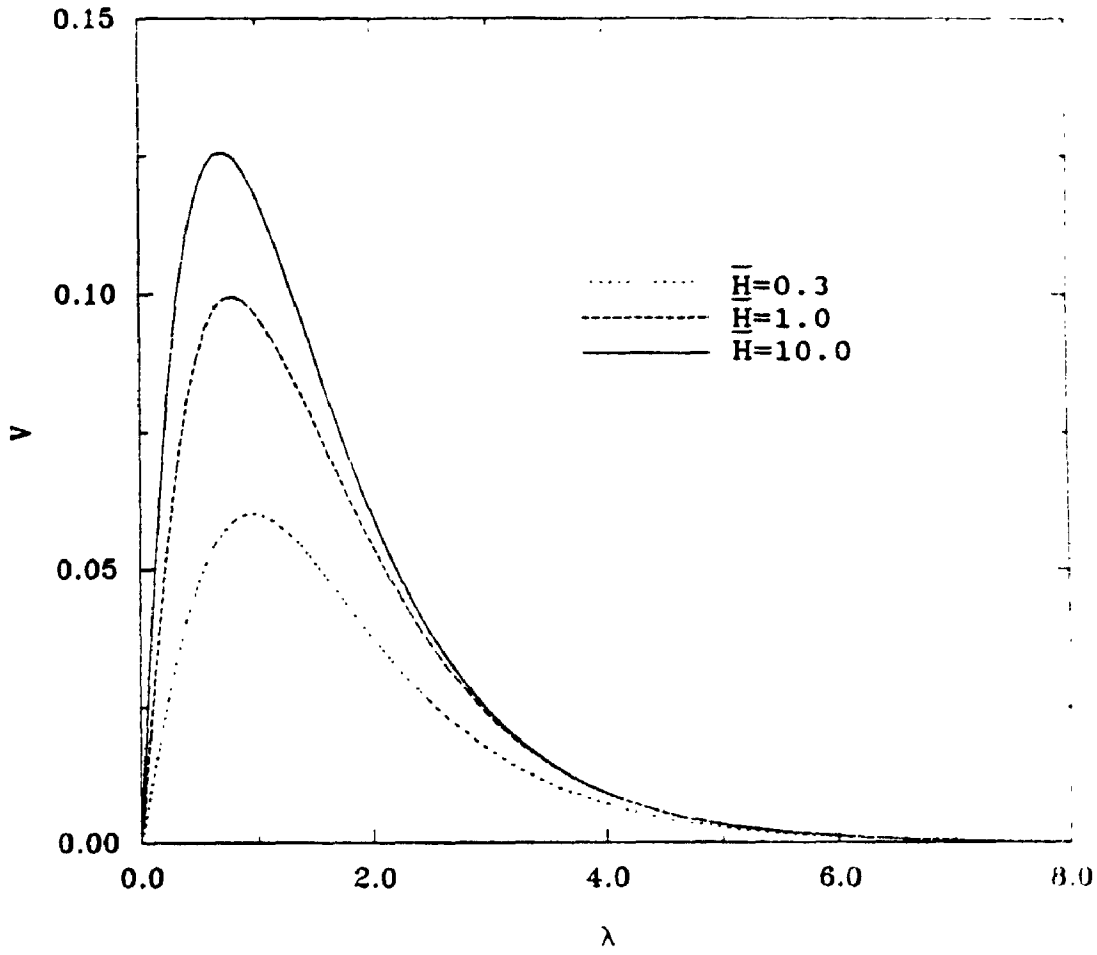

Figure 6.11 Variation of the amplitude V of the interface velocity vector induced by the temperature field (6.98) as a function of λ for G=1.0 and K=1.0.

properly selecting the properties of the upper layer. While the introduction of such an additional layer always reduces the convection, a significantly higher reduction can be obtained by reducing the thickness of the covering layer, and increasing both its viscosity and thermal conductivity.

CHAPTER 7

SUMMARY AND CONCLUSIONS

The problem of steady thermocapillary convection in a cavity with an upper free surface in the absence of gravity was studied. The flow was driven by a temperature gradient parallel to the interface.

An effective algorithm for numerical simulation of the flow field was developed. The algorithm was based on a coordinate transformation method, streamfunction-vorticity formulation, and second-order finite-difference discretization. The unknown physical domain was mapped onto a rectangular computational domain, with the explicit form of the mapping function not being known. The field variables and the mapping function were determined simultaneously using a Picard-type iteration.

Different methods were employed to check the algorithm. The numerical results are shown to be in good agreement with previous asymptotic results in the small deformation cases. The algorithm delivered the second-order accuracy even for very large interfacial distortion. The results obtained on grid size $\Delta\xi=1/20$ and $\Delta\eta=1/20$ provided an accuracy no worse than 5%. The

grid size $\Delta\xi=1/20$ and $\Delta\eta=1/40$ was preferred to the grid size $\Delta\xi=1/40$ and $\Delta\eta=1/40$ in cases where a higher accuracy was needed.

Analysis of thermocapillary effects in an infinite liquid layer in the absence of gravity was carried out. It was shown that the layer may exist only if the external temperature field satisfies existence conditions. The explicit form of these conditions was given in the case of negligible convective transport.

Extensive parametric studies have been carried out for cavities. Results showed that if the external temperature field does not satisfy the existence conditions determined in the case of an infinite layer, large interfacial deformations can occur, leading to a break-up of the layer if the cavity is made sufficiently long. Since the temperature fields satisfying the existence conditions are rather unusual, the most likely response of the layer to an external heating in the case of a real experiment would consist of large interfacial distortions and, possibly, break-up of the layer.

Non-unique stable solutions have been found even for very low values of the Reynolds and capillary numbers. The primary bifurcation as a function of Reynolds number is of the pitchfork type, while in the capillary number cases the structure is more complicated and cannot be easily categorized. The system is very

sensitive with respect to external heating, and control parameters, such as Reynolds number, capillary number, and length of the cavity.

Double liquid layer systems have been studied in order to assess the potential of encapsulation techniques for control of the thermocapillary convection. A detailed analysis of the flow and temperature field was carried out. The results show that the thermocapillary convection can be effectively controlled by properly selecting the properties of the encapsulating liquid. While the introduction of an additional layer always reduces the convection, a significantly higher reduction can be obtained by reducing the thickness of the covering layer, and increasing both its viscosity and thermal conductivity.

Appendix A

Finite-Difference Approximation of Mixed Partial Derivatives at the Interface

The derivatives of the dependent variables appearing in the partial differential equations must be expressed as approximate expressions so that a digital computer can be employed to obtain a solution. Some of the approximations have been given in Section 3.3. Besides these standard finite-difference formulas, a mixed derivative appears in the normal stress boundary condition. Since this condition is applied at the upper boundary, a backward difference formula has to be constructed. One out of the many available methods is the one based on the Taylor series expansion for the two variables. The derivation is described below:

Given a function $f(\xi,\eta)$, which is analytical, $f(\xi+\Delta\xi, \eta+\Delta\eta)$ can be expressed in terms of Taylor series centered at (ξ, η) in the form,

$$\begin{aligned} f(\xi+\Delta\xi,\eta+\Delta\eta) = f(\xi,\eta) &+\Delta\xi f_{\xi}+\Delta\eta f_{\eta}+\frac{\Delta\xi^2}{2}f_{\xi\xi}+\frac{\Delta\eta^2}{2}f_{\eta\eta} \\ &+\Delta\xi\Delta\eta f_{\xi\eta}+\frac{\Delta\xi^3}{6}f_{\xi\xi\xi}+\frac{\Delta\eta^3}{6}f_{\eta\eta\eta} \\ &+\Delta\xi^2\Delta\eta f_{\xi\xi\eta}+\Delta\xi\Delta\eta^2 f_{\xi\eta\eta}+O[\Delta\xi^4,\Delta\eta^4]. \end{aligned} \tag{A.1}$$

Using indices i,N to represent a grid point at the top boundary, expansion (A.1) yields

$$f_{i-1,N-1}=f_{i,N}-\Delta\xi f_{\xi}-\Delta\eta f_{\eta}+\frac{\Delta\xi^2}{2}f_{\xi\xi}+\frac{\Delta\eta^2}{2}f_{\eta\eta}+\Delta\xi\Delta\eta f_{\xi\eta}$$
$$+\frac{\Delta\xi^3}{6}f_{\xi\xi\xi}-\frac{\Delta\eta^3}{6}f_{\eta\eta\eta}-\Delta\xi^2\Delta\eta f_{\xi\xi\eta}-\Delta\xi\Delta\eta^2 f_{\xi\eta\eta}+O(\Delta\xi^4,\Delta\eta^4)\,, \tag{A.2}$$

$$f_{i+1,N-1}=f_{i,N}+\Delta\xi f_{\xi}-\Delta\eta f_{\eta}+\frac{\Delta\xi^2}{2}f_{\xi\xi}+\frac{\Delta\eta^2}{2}f_{\eta\eta}-\Delta\xi\Delta\eta f_{\xi\eta}$$
$$+\frac{\Delta\xi^3}{6}f_{\xi\xi\xi}-\frac{\Delta\eta^3}{6}f_{\eta\eta\eta}-\Delta\xi^2\Delta\eta f_{\xi\xi\eta}+\Delta\xi\Delta\eta^2 f_{\xi\eta\eta}+O(\Delta\xi^4,\Delta\eta^4)\,, \tag{A.3}$$

$$f_{i-1,N-2}=f_{i,N}-\Delta\xi f_{\xi}-2\Delta\eta f_{\eta}+\frac{\Delta\xi^2}{2}f_{\xi\xi}+2\Delta\eta^2 f_{\eta\eta}+2\Delta\xi\Delta\eta f_{\xi\eta}$$
$$-\frac{\Delta\xi^3}{6}f_{\xi\xi\xi}-\frac{4\Delta\eta^3}{3}f_{\eta\eta\eta}-2\Delta\xi^2\Delta\eta f_{\xi\xi\eta}-4\Delta\xi\Delta\eta^2 f_{\xi\eta\eta}+O(\Delta\xi^4,\Delta\eta^4)\,, \tag{A.4}$$

$$f_{i+1,N-2}=f_{i,N}+\Delta\xi f_{\xi}-2\Delta\eta f_{\eta}+\frac{\Delta\xi^2}{2}f_{\xi\xi}+2\Delta\eta^2 f_{\eta\eta}-2\Delta\xi\Delta\eta f_{\xi\eta}$$
$$+\frac{\Delta\xi^3}{6}f_{\xi\xi\xi}-\frac{4\Delta\eta^3}{3}f_{\eta\eta\eta}-2\Delta\xi^2\Delta\eta f_{\xi\xi\eta}+4\Delta\xi\Delta\eta^2 f_{\xi\eta\eta}+O(\Delta\xi^4,\Delta\eta^4)\,, \tag{A.5}$$

$$f_{i+1,N}=f_{i,N}+\Delta\xi f_{\xi}+\frac{\Delta\xi^2}{2}f_{\xi\xi}+\frac{\Delta\xi^3}{6}f_{\xi\xi\xi}+O(\Delta\xi^4)\,, \tag{A.6}$$

$$f_{i-1,N}=f_{i,N}-\Delta\xi f_{\xi}+\frac{\Delta\xi^2}{2}f_{\xi\xi}-\frac{\Delta\xi^3}{6}f_{\xi\xi\xi}+O(\Delta\xi^4)\,. \tag{A.7}$$

Subtracting Equation (A.2) from Equation (A.3) yields

$$f_{i+1,N-1}-f_{i-1,N-1}=2\Delta\xi f_{\xi}-2\Delta\xi\Delta\eta f_{\xi\eta}+\frac{\Delta\xi^3}{3}f_{\xi\xi\xi}$$
$$+2\Delta\xi\Delta\eta^2 f_{\xi\eta\eta}+O(\Delta\xi^4,\Delta\eta^4)\,. \tag{A.8}$$

subtracting of Equation (A.4) from Equation (A.5) gives

$$f_{i+1,N-2}-f_{i-1,N-2}=2\Delta\xi f_{\xi}-4\Delta\xi\Delta\eta f_{\xi\eta}+\frac{\Delta\xi^3}{3}f_{\xi\xi\xi}$$
$$+8\Delta\xi\Delta\eta^2 f_{\xi\eta\eta}+O(\Delta\xi^4,\Delta\eta^4)\,. \tag{A.9}$$

Multiply Equation (A.8) by -4 and add it to Equation (A.9) to get

$$f_{i+1,\,N-2}-f_{i-1,\,N-2}-4\,[f_{i-1,\,N-1}-f_{i-1,\,N-1}] \\ =4\Delta\xi\Delta\eta\,f_{\xi\eta}-6\Delta\xi\,f_{\xi}-\Delta\xi^{3}f_{\xi\xi\xi}+O(\Delta\xi^{4},\Delta\eta^{4})\,. \tag{A.10}$$

Subtraction of Equation (A.7) from Equation (A.6) results in

$$f_{i+1,\,N}-f_{i-1,\,N}=2\Delta\xi\,f_{\xi}+\frac{\Delta\xi^{3}}{3}f_{\xi\xi\xi}+O(\Delta\xi^{4})\,. \tag{A.11}$$

Equations (A.10) can be simplified using Equation (A.11) and re-arranged in order to get the desired expression for the mixed derivative:

$$f_{\xi\eta}=\frac{3\,[f_{i+1,\,N}-f_{i-1,\,N}]-4\,[f_{i+1,\,N-1}-f_{i-1,\,N-1}]+f_{i+1,\,N-2}-f_{i-1,\,N-2}}{4\Delta\xi\Delta\eta} \\ +O(\Delta\xi^{2},\Delta\eta^{2})\,. \tag{A.12}$$

Appendix B

On Quasi-Tridiagonal Systems

This appendix describes an algorithm for direct solution of the following system of linear algebraic equations:

$$A_i\hat{h}_{i-1}+B_i\hat{h}_i+C_i\hat{h}_{i+1}+N_iK=M_i, \qquad i=2,\ldots,M-1 \tag{B.1}$$

$$\sum_{i=1}^{i=M} D_i\hat{h}_i=V \tag{B.2}$$

where A_i, B_i, C_i, D_i, N_i, M_i and V are known. $\hat{h}_i$ and K are unknowns to be determined.

B.1 Case I - Fixed Contact Point Cases

Assume that fixed contact point conditions are imposed ard, therefore, the values of the $\hat{h}$ at i=1 and i=M are given. The set of equations can be written in matrix formula as

$$\begin{bmatrix} B_2 & C_2 & . & . & & & & & N_2 \\ A_3 & B_3 & C_3 & . & & & & & N_3 \\ . & A_4 & B_4 & C_4 & & & & & N_4 \\ & & & & & & & & . \\ & & & & A_{M-3} & B_{M-3} & C_{M-3} & & N_{M-3} \\ & & & & . & A_{M-2} & B_{M-2} & C_{M-2} & N_{M-2} \\ & & & & . & . & A_{M-1} & B_{M-1} & N_{M-1} \\ D_2 & D_3 & D_4 & D_5 & . & D_{M-4} & D_{M-3} & D_{M-2} & . \end{bmatrix} \begin{bmatrix} \hat{h}_2 \\ \hat{h}_3 \\ \hat{h}_4 \\ \\ \hat{h}_{M-3} \\ \hat{h}_{M-2} \\ \hat{h}_{M-1} \\ K \end{bmatrix} = \begin{bmatrix} M_2 \\ M_3 \\ M_4 \\ . \\ M_{M-3} \\ M_{M-2} \\ M_{M-1} \\ W \end{bmatrix} \tag{B.3}$$

where only the non-zero elements are shown. In the above,

$$W=V-D_1\hat{h}_1-D_M\hat{h}_M. \tag{B.4}$$

The above system is similar to a tridiagonal system except that the last row and column at the matrix are not null. A very efficient solution procedure can be developed by taking advantage of the quasi-tridinagonal nature of the coefficient matrix.

The diagonal terms are eliminated leading to a solution with the form:

$$\hat{h}_i=H_i\hat{h}_{i+1}+G_i+E_iK, \tag{B.5}$$

where

$$\begin{aligned} H_i&=\frac{C_i}{B_i-A_iH_{i-1}},\\ G_i&=\frac{M_i-A_iG_{i-1}}{B_i-A_iH_{i-1}},\\ E_i&=\frac{N_i+A_iE_{i-1}}{A_iH_{i-1}-B_i}. \end{aligned} \tag{B.6}$$

Coefficients H_i, G_i, E_i are evaluated for i=1,...,M-1 by noting that $H_1=0$, $E_1=0$, $G_1=\hat{h}_1$. The bottom row of the matrix is eliminated by writing a partial sum in the form

$$S_i=P_i\hat{h}_i+R_i+F_iK, \tag{B.7}$$

where

$$P_i=-P_{i-1}H_{i-1}+D_i,$$
$$R_i=P_{i-1}G_{i-1}+R_{i-1}, \qquad \text{(B.8)}$$
$$F_i=P_{i-1}E_{i-1}+F_{i-1}.$$

These sums are evaluated for i=2,...,M by noting that $S_2=D_2\hat{h}_2$, thus $P_2=D_2$, $R_2=0$ and $F_2=0$; also, $D_M=0$. The constant K in the last row is evaluated from the total sum as

$$K=\frac{W-P_M\hat{h}_M-R_M}{F_M}. \qquad \text{(B.9)}$$

The complete solution procedure involves evaluation of H_i, G_i, E_i from (B.6) followed by evaluation of P_i, R_i, and F_i from (B.8), K from (B9) and $\hat{h}_i$ from (B.5).

B.2 Case II - Fixed Contact Angle Cases

The change of the fixed contact point condition into fixed contact angle condition does not change the nature of above system. Assume that the fixed contact angle conditions are imposed and, therefore, the values of $\hat{h}_{1\xi}$ at i=1 and i=M are given, i.e.,

$$\hat{h}_{1\xi}=M_1, \qquad \hat{h}_{M\xi}=M_M. \qquad \text{(B.10)}$$

Suppose the following expressions are used for the approximation of the contact conditions at both ends

$$h_{1\xi}=(-3\hat{h}_1+4\hat{h}_2-\hat{h}_3)/2\Delta\xi+O(\Delta\xi^2)=M_1 \qquad \xi=-\frac{1}{2}L \qquad \text{(B.11)}$$

$$h_{1\xi}=(3\hat{h}_M-4\hat{h}_{M-1}+\hat{h}_{M-2})/2\Delta\xi+O(\Delta\xi^2)=M_M \qquad \xi=\frac{1}{2}L \qquad \text{(B.12)}$$

resulting in a matrix equation of the following structure

$$\begin{bmatrix} B_1 & C_1 & A_1 & . & & & & & N_1 \\ A_2 & B_2 & C_2 & . & & & & & N_2 \\ . & A_3 & B_3 & C_3 & & & & & N_3 \\ & & & & & & & & . \\ & & & & & & & & . \\ & & & & A_{M-2} & B_{M-2} & C_{M-2} & . & N_{M-2} \\ & & & & . & A_{M-1} & B_{M-1} & C_{M-1} & N_{M-1} \\ & & & & . & C_M & A_M & B_M & . \\ D_1 & D_2 & D_3 & D_4 & \ldots & D_{M-3} & D_{M-2} & D_{M-1} & D_M \end{bmatrix} \begin{bmatrix} \hat{h}_1 \\ \hat{h}_2 \\ \hat{h}_3 \\ \\ \\ \hat{h}_{M-2} \\ \hat{h}_{M-1} \\ \hat{h}_M \\ K \end{bmatrix} = \begin{bmatrix} M_1 \\ M_2 \\ M_3 \\ . \\ . \\ M_{M-2} \\ M_{M-1} \\ M_M \\ V \end{bmatrix} \qquad \text{(B.13)}$$

Equation (B.5) is used with H_i, G_i, and E_i defined by (B.6) for $i=1,\ldots,M$, with

$$H_1=\frac{C_1C_2-B_2A_1}{B_1C_2-A_2A_1},$$

$$G_1=\frac{M_1C_2-M_2A_1}{B_1C_2-A_2A_1}, \qquad \text{(B.14)}$$

$$E_1=\frac{N_2A_1}{B_1C_2-A_2A_1}.$$

Partial sums are defined by (B.7) for i=1,...,M with $P_1=D_1$, $R_1=0$, $F_1=0$. An expression for the constant K has the form

$$K=\frac{(V-R_M)A^*+C^*P_M}{F_MA^*-P_MB^*}, \tag{B.15}$$

with

$$\begin{aligned} A^* &= -A_MA_{M-1}H_{M-1}+B_{M-1}C_MH_{M-1}+B_MA_{M-1}-C_{M-1}C_M, \\ B^* &= A_MA_{M-1}E_{M-1}-B_{M-1}C_ME_{M-1}+N_{M-1}C_M, \\ C^* &= A_MA_{M-1}G_{M-1}-B_{M-1}C_MG_{M-1}-M_MA_{M-1}+M_{M-1}C_M. \end{aligned} \tag{B.16}$$

The value of $\hat{h}_M$ at i=M is

$$\hat{h}_M=\frac{(V-R_M)B^*+C^*F_M}{P_MB^*-A^*F_M} \tag{B.17}$$

and all the remaining points can be evaluated from the recursive relation (B.5).

APPENDIX C

General Solution of Equations of Motion for Arbitrary Surface Traction

The general solution of Equations (6.102) to (6.114) has the following form:

$$u_{A0}=\frac{1}{2\pi}\int_{-\infty}^{\infty}\int_{-\infty}^{\infty}[C_1S_1(kz)+C_3zS_1(kz)+C_4zS_2(kz)] * r_1(k_1,k_2)\,dk_1dk_2, \tag{C.1}$$

$$v_{A0}=\frac{1}{2\pi}\int_{-\infty}^{\infty}\int_{-\infty}^{\infty}[C_5S_1(kz)+\frac{k_2}{k_1}C_3zS_1(kz)+\frac{k_2}{k_1}C_4zS_2(kz)] * r_1(k_1,k_2)\,dk_1dk_2, \tag{C.2}$$

$$w_{A0}=\frac{1}{2\pi}\int_{-\infty}^{\infty}\int_{-\infty}^{\infty}\frac{ig_3(k,H)M(\tau_1,\tau_2)}{2kF(k,H,K)}\{-[g_1(k)z+S_1(k)]S_1(kz) +kzS_1(k)S_2(kz)\}r_1(k_1,k_2)\,dk_1dk_2, \tag{C.3}$$

$$p_{A0}=\frac{1}{2\pi}\int_{-\infty}^{\infty}\int_{-\infty}^{\infty}\frac{ig_3(k,H)M(\tau_1,\tau_2)}{kF(k,H,K)}[-g_1(k)S_1(kz)+ kS_1(k)S_2(kz)]r_1(k_1,k_2)\,dk_1dk_2, \tag{C.4}$$

$$u_{B0}=\frac{1}{2\pi}\int_{-\infty}^{\infty}\int_{-\infty}^{\infty}\{D_1S_1[k(z-H)]+D_3(z-H)S_1[k(z-H)]+ D_4(z-H)S_2[k(z-H)]\}r_1(k_1,k_2)\,dk_1dk_2, \tag{C.5}$$

$$v_{B0}=\frac{1}{2\pi}\int_{-\infty}^{\infty}\int_{-\infty}^{\infty}\{D_5S_1[k(z-H))]+\frac{k_2}{k_1}D_3(z-H)S_1[k(z-H)] +\frac{k_2}{k_1}D_4(z-H)S_2[k(z-H)]\}r_1(k_1,k_2)\,dk_1dk_2, \tag{C.6}$$

$$w_{BO}=\frac{1}{2\pi}\int_{-\infty}^{\infty}\int_{-\infty}^{\infty}\frac{ig_2(k)M(\tau_1,\tau_2)}{2kF(k,H,K)}\{[g_4(k,H)(z-H)-\bar{H}S_1(k\bar{H})] * S_1[k(z-H)]+k\bar{H}(z-H)S_1(k\bar{H})S_2[k(z-H)]\}r(k_1,k_2)dk_1dk_2, \tag{C.7}$$

$$p_{BO}=\frac{1}{2\pi}\int_{-\infty}^{\infty}\int_{-\infty}^{\infty}\frac{ig_2(k)M(\tau_1,\tau_2)}{kF(k,H,K)}\{g_4(k,H)S_1[k(z-H)]+k\bar{H}S_1(k\bar{H})S_2[k(z-H)\}r_1(k_1,k_2)dk_1dk_2, \tag{C.8}$$

where

$$C_1=-\frac{(A_1K+A_2)\hat{r}_1(k_1,k_2)+(B_1K+B_2)\hat{r}_2(k_1,k_2)}{2k^2F(k,H,K)F_7(k,H)}, \tag{C.9}$$

$$C_3=\frac{k_1S_1(k)[S_1^2(k\bar{H})-k^2\bar{H}^2]M(\hat{r}_1,\hat{r}_2)}{2F(k,H,K)}, \tag{C.10}$$

$$C_4=-\frac{k_1[kS_2(k)-S_1(k)][S_1^2(k\bar{H})-k^2\bar{H}^2]M(\hat{r}_1,\hat{r}_2)}{2kF(k,H,K)}, \tag{C.11}$$

$$C_5=-\frac{(A_3K+A_4)\hat{r}_1(k_1,k_2)+(B_3K+B_4)\hat{r}_2(k_1,k_2)}{2k^2F(k,H,K)F_7(k,H)k_1}, \tag{C.12}$$

$$D_1=-\frac{(A_5K+A_6)\hat{r}_1(k_1,k_2)+(B_5K+B_6)\hat{r}_2(k_1+k_2)}{2k^2F(k,H,K)F_7(k,H)}, \tag{C.13}$$

$$D_3=\frac{k_1\bar{H}S_1(k\bar{H})[S_1^2(k)-k^2]M(\hat{r}_1,\hat{r}_2)}{2F(k,H,K)}, \tag{C.14}$$

$$D_4=\frac{k_1[k\bar{H}S_2(k\bar{H})-S_1(k\bar{H})][S_1^2(k)-k^2]M(\hat{r}_1,\hat{r}_2)}{2kF(k,H,K)}, \tag{C.15}$$

$$D_5 = -\frac{(A_7K+A_8)\,f_1(k_1,k_2)+(B_7K+B_8)\,f_2(k_1,k_2)}{2k_1k^2F(k,H,K)\,F_7(k,H)}, \tag{C.16}$$

$$F_7 = S_1(k)\,S_2(k\bar{H})+S_1(k\bar{H})\,S_2(k), \tag{C.17}$$

$$S_1(x) = \sinh(x), \tag{C.18}$$

$$S_2(x) = \cosh(x), \tag{C.19}$$

$$M(f_1,f_2) = f_1k_1+f_2k_2, \tag{C.20}$$

$$r_1(k_1,k_2) = e^{-i(k_1x+k_2y)}, \tag{C.21}$$

$$\begin{aligned} A_1 = {} & -k_1^2k^3\bar{H}^2S_2(k)\,S_1(k)\,S_2(k\bar{H})-2k^3k_2^2S_1(k\bar{H})+k_1^2k^2\bar{H}^2S_1^2(k)\,S_2(k\bar{H}) \\ & +2k^2k_2^2S_2(k\bar{H})\,S_1^2(k\bar{H})+kk_1^2S_1(k)\,S_2(k)\,S_2(k\bar{H})\,S_1^2(k\bar{H}) \\ & -(k^2+k_2^2)\,S_1^2(k\bar{H})\,S_2^2(k\bar{H})\,S_1^2(k)+2kk_2^2\bar{H}S_1(k\bar{H})\,S_1^2(k), \end{aligned} \tag{C.22}$$

$$\begin{aligned} A_2 = {} & -k^3k_1^2\bar{H}^2S_1(k\bar{H})\,S_2^2(k)-2k^3k_2^2\bar{H}S_1(k\bar{H})+k^4\bar{H}^2S_1(k\bar{H})\,S_1(k)\,S_2(k) \\ & +k^2k_2^2\bar{H}^2S_1(k\bar{H})\,S_2(k)\,S_1(k)+kk_1^2S_1^3(k\bar{H})\,S_2^2(k)+2kk_2^2S_1^3(k\bar{H}) \\ & -k^2S_1(k)\,S_2(k)\,S_1^3(k\bar{H})-k_2^2S_1(k)\,S_2(k)\,S_1^3(k\bar{H}), \end{aligned} \tag{C.23}$$

$$\begin{aligned} A_3 = {} & -k^3k_1^2k_2\bar{H}^2S_1(k)\,S_2(k)\,S_2(k\bar{H})+2k_1^2k^3k_2\bar{H}S(k\bar{H}) \\ & -2k^2k_1^2k_2S_2(k\bar{H})\,S_1^2(k\bar{H})+k^2k_1^2k_2\bar{H}^2S_2(k\bar{H})\,S_1^2(k) \\ & +kk_1^2k_2S_1(k)\,S_2(k)\,S_2(k\bar{H})\,S_1^2(k\bar{H}) \\ & -kk_1^2k_2\bar{H}S_1(k\bar{H})\,S_1^2(k)+k_1^2k_2S_1^2(k\bar{H})\,S_1^2(k)\,S_2(k\bar{H}), \end{aligned} \tag{C.24}$$

$$A_4=2k^3k_1^2k_2\bar{H}^2S_1(k\bar{H})-k^3\bar{H}^2k_1^2k_2S_2^2(k)S_1(k\bar{H})$$
$$-k_2k^2k_1^2\bar{H}^2S_1(k)S_2(k)S_1(k\bar{H})-2kk_1^2k_2S_1^3(k\bar{H}) \qquad (C.25)$$
$$+kk_1^2k_2S_2^2(k)S_1^3(k\bar{H})+k_1^2k_2S_1(k)S_2(k)S_1^3(k\bar{H}),$$

$$A_5=k^3k_1^2\bar{H}S_1(k)S_2^2(k\bar{H})+2k^3k_2^3\bar{H}S_1(k)-k^4S_1(k\bar{H})S_1(k)S_2(k)$$
$$-k^2k_2^2S_1(k)S_1(k\bar{H})S_2(k\bar{H})-kk_1^2\bar{H}S_1^3(k)S_2^2(k\bar{H}) \qquad (C.26)$$
$$-2kk_2^2\bar{H}S_1^3(k)+(k^2+k_2^2)S_1^3(k)S_1(k\bar{H})S_2(k\bar{H}),$$

$$A_6=k^3k_1^2\bar{H}S_1(k\bar{H})S_2(k\bar{H})S_2(k)+2k^3k_2^2\bar{H}^2S(k)-k^2k_1^2S_2(k)S_1^2(k\bar{H})$$
$$-2k^2k_2^2\bar{H}^2S_2(k)S_1^2(k)-kk_1^2\bar{H}S_1(k\bar{H})S_2(k\bar{H})S_1^2(k)S_2(k) \qquad (C.27)$$
$$-2k_2kS_1(k)S_1^2(k\bar{H})+(k_2^2+k^2)S_1^2(k)S_2(k)S_1^2(k\bar{H}),$$

$$A_7=-k^3k_1^2k_2\bar{H}S(k)+k^3k_1^3k_2\bar{H}S_1(k)S_1^2(k\bar{H})$$
$$+k^2k_1^2k_2S_1(k)S_1(k\bar{H})S_2(k\bar{H})-k_1^2kk_2\bar{H}S_1^3(k)S_1^2(k\bar{H}) \qquad (C.28)$$
$$+kk_1^2k_2\bar{H}S_1^3(k)-k_1^2k_2S_1^3(k)S_1(k\bar{H})S_2(K\bar{H}),$$

$$A_8=-2k^3k_1^2k_2\bar{H}^2S_1(k)+k^3k_1^2k_2\bar{H}S_2(k)S_1(k\bar{H})S_2(k\bar{H})$$
$$-k^2k_1^2k_2S_2(k)S_1^2(k\bar{H})+2k^2k_1^2k_2\bar{H}^2S_1^2(k)S_2(k)$$
$$+2kk_1^2k_2S_1(k)S_1^2(k\bar{H})-k_1^2k_2S_1^2(k)S_2(k)S_1^2(k\bar{H}) \qquad (C.29)$$
$$-kk_1^2k_2\bar{H}S_1(k)S_2(k)S_1(k\bar{H})S_2(k\bar{H}),$$

$$B_1=2k^3k_1k_2\bar{H}S_1(k\bar{H})-k^3k_1k_2\bar{H}^2S_1(k)S_2(k)S_2(k\bar{H})$$
$$+k^2k_1k_2\bar{H}^2S_1^2(k)S_1k\bar{H})-2k^2k_1k_2S_1^2(k\bar{H})S_2(k\bar{H})$$
$$+kk_1k_2S_1(k)S_2(k)S_1^2(k\bar{H})S_2(k\bar{H}) \qquad (C.30)$$
$$-2kk_1k_2\bar{H}S_1^2(k)S_1(k\bar{H})+k_1k_2S_1^2(k)S_1^2(k\bar{H})S_2(k\bar{H}),$$

$$B_2=2k^3k_1k_2\bar{H}^2S_1(k\bar{H})-k^3k_1k_2\bar{H}^2S_1(k\bar{H})S_2^2(k)$$
$$-k^2k_1k_2\bar{H}^2S_1(k)S_2(k)S_1(k\bar{H})+kk_1k_2S_2^2(k)S_1^3(k\bar{H}) \qquad (C.31)$$
$$-2kk_1k_2S_1^3(k\bar{H})+k_1k_2S_1^3(k\bar{H})S_1(k)S_2(k)\,,$$

$$B_3=-2k^3k_1^3\bar{H}S_1(k\bar{H})-2k^2k_1^3S_1^2(k\bar{H})S_2(k\bar{H})+2kk_1^3\bar{H}S_1^2(k)S_1(k\bar{H})$$
$$-k^3k_1k_2\bar{H}^2S_1(k)S_2(k)S_1(k\bar{H})+k^2k_1k_2^2\bar{H}^2S_1^2(k)S_2(k\bar{H}) \qquad (C.32)$$
$$+k_2^2kk_1S_1(k)S_2(k)S_1^2(k\bar{H})S_2(k\bar{H})+k_1k_2^2S_1^2(k)S_1^2(k\bar{H})S_2(k\bar{H})$$
$$-2k^2k_1S_1^2(k)S_1^2(k\bar{H})S_2(k\bar{H})\,,$$

$$B_4=-2k^3k_1^3\bar{H}^2S_1(k\bar{H})+k^4k_1\bar{H}^2S_1(k)S_2(k)S_1(k\bar{H})$$
$$+k^2k_1^3\bar{H}^2S_1(k)S_2(k)S_1(k\bar{H})+2kk_1^3S_1^3(k\bar{H}) \qquad (C.33)$$
$$-k^2k_1S_1(k)S_2(k)S_1^3(k\bar{H})-k_1^3S_1(k)S_2(k)S_1^3(k\bar{H})$$
$$+kk_1k_2^2S_2^2(k)S_1^3(k\bar{H})-k^3k_2^2k_1\bar{H}^2S_2^2(k)S_1(k\bar{H})\,,$$

$$B_5=k^3k_1k_2\bar{H}S_1(k)S_1^2(k\bar{H})-k^3k_1k_2\bar{H}S_1(k)+k^2k_1k_2S_1(k\bar{H})S_1(k)S_2(k\bar{H}) \qquad (C.34)$$
$$+kk_1k_2\bar{H}S_1^3(k)-kk_1k_2\bar{H}S_1^2(k)S_1^2(k\bar{H})-k_1k_2S_1^3(k)S_1(k\bar{H})S_2(k\bar{H})\,,$$

$$B_6=-2k^3k_1k_2\bar{H}^2S(k)+k^3k_1k_2\bar{H}S_2(k)S_1(k\bar{H})S_2(k\bar{H})+$$
$$2k^2k_1k_2\bar{H}^2S_1^2(k)S_2(k)-k_1k_2k^2S_2(k)S_1^2(k\bar{H}) \qquad (C.35)$$
$$+2k_1k_2S_1(k)S_1^2(k\bar{H})-kk_1k_2\bar{H}S_1^2(k)S_2(k)S_1(k\bar{H})S_2(k\bar{H})$$
$$-k_1k_2S_1^2(k)S_2(k)S_1^2(k\bar{H})\,,$$

$$
\begin{aligned}
B_7 = {} & 2k^3k_1^3\bar{H}S_1(k) - k^2k_1^3S_1(k)S_1(k\bar{H})S_2(k\bar{H}) \\
& - k^4k_1S_1(k)S_1(k\bar{H})S_2(k\bar{H}) - 2kk_1^3\bar{H}S_1^3(k) \\
& + k_1^3S_1^3(k)S_1(k\bar{H})S_2(k\bar{H}) + k^2k_1S_1^3(k)S_1(k\bar{H})S_2(k\bar{H}) \\
& + k^3k_1k_2^2\bar{H}S_1(k)S_2^2(k\bar{H}) - kk_1k_2^2\bar{H}S_1^3(k)S_2^2(k\bar{H}) ,
\end{aligned}
\tag{C.36}
$$

$$
\begin{aligned}
B_8 = {} & 2k^3k_1^3\bar{H}^2S_1(k) - 2k^2k_1^3\bar{H}^2S_1^2(k)S_2(k) - 2kk_1^3S_1(k)S_1^2(k\bar{H}) + \\
& k^2k_1S_1^2(k)S_2(k)S_1^2(k\bar{H}) + k_1^3S_1^2(k)S_2(k)S_1^2(k\bar{H}) \\
& - k^2k_1k_2S_2(k)S_1^2(k\bar{H}) + k^3k_1k_2^2\bar{H}S_2(k)S_1(k\bar{H})S_2(k\bar{H}) \\
& - kk_1k_2^2\bar{H}S_1^2(k)S(k)S_1(k\bar{H})S_2(k\bar{H}) .
\end{aligned}
\tag{C.37}
$$

Appendix D

Thermocapillary Convection in a Double Layer System with Two Interfaces

In Chapters 6, thermocapillary convection in a double layer system was discussed. Here, a more general case, two interface system will be studied. Consider the system shown in Figure 6.1. If the liquid B is not bounded by a solid wall but exposed to gas, the second interface h_B will present (Figure D.1).

The governing equations remain to be Navier-Stokes, continuity and energy equations (Equations (6.1)-(6.10)), and the boundary conditions at the bottom solid wall and the interface between the two liquids (h_A) are still Equations (6.11) and (6.13)-(6.18)). Yet the boundary conditions at the top solid wall are replaced by following equations (after scaling):

$$\begin{aligned} &-p_B+2N_B^{-2}[u_{Bx}h_{Bx}^2+v_{By}h_{By}^2+w_{Bz}+(u_{By}+v_{Bx})h_{Bx}h_{By}-(u_{Bz}+w_{Bx})h_{Bx}-(v_{Bz}+w_{By})h_{By}] \\ &=\frac{\mu_A\gamma_B}{\mu_B\gamma_A}\frac{1-Ca_BT_B}{Ca_B}[h_{Bxx}(1+h_{By}^2)-2h_{Bx}h_{By}h_{Bxy}+h_{Byy}(1+h_{Bx}^2)]N_B^{-3}, \end{aligned} \tag{D.1}$$

$$\begin{aligned} &2h_{By}(w_{Bz}-v_{By})+(v_{Bz}+w_{By})(1-h_{By}^2)-(u_{By}+v_{Bx})h_{Bx}-(u_{Bz}+w_{Bx})h_{By}h_{Bx} \\ &=-\frac{\mu_A\gamma_B}{\mu_B\gamma_A}N_B(T_{By}+h_{By}T_{Bz}), \end{aligned} \tag{D.2}$$

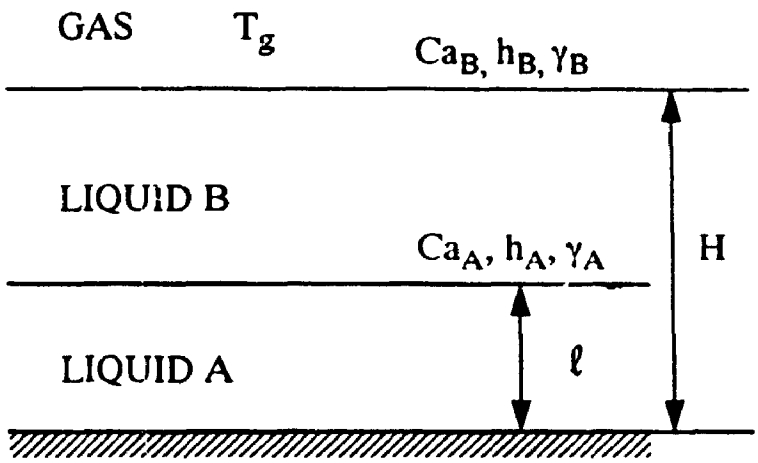

Figure D.1 Sketch of the flow system with two interfaces.

$$2h_{Bx}(w_{Bz}-u_{Bx})+(u_{Bz}+w_{Bx})(1-h_{Bx}^2)-(v_{Bz}+w_{By})h_{Bx}h_{By}-(u_{By}+v_{Bx})h_{By}$$
$$=-\frac{\mu_A\gamma_B}{\mu_B\gamma_A}(T_{Bx}+T_{Bz}h_{Bx})N_B, \tag{D.3}$$

$$N_B^{-1/2}(-h_{Bx}T_{Bx}-h_{By}T_{By}+T_{Bz})+\frac{H_g\ell}{\kappa_B}[T_B-T_g(x,y)]=0, \tag{D.4}$$

where h_B is the interface between liquid B and gas (upper interface), Ca_B the capillary number at the interface h_B, γ_B the negative of the derivative of the surface tension with respect to temperature at the interface h_B, κ_B the conductivity of the liquid B, H_g the heat transfer coefficient between the liquid B and the gas, and $T_g(x,y)$ the gas temperature. And N_B is defined as

$$N_B=(1+h_{Bx}^2+h_{By}^2)^{1/2}. \tag{D.5}$$

Introduction of expansion (3.47) and (3.48) gives the following equations for above boundary conditions:

problem $O(Ca_B^{-1})$:

$$-p_{Bs}=\frac{\mu_A\gamma_B Ca_A}{\mu_B\gamma_A Ca_B}[h_{B0xx}(1+h_{B0y}^2)-2h_{B0x}h_{B0y}h_{B0xy}+h_{B0yy}(1+h_{B0x}^2)](1+h_{B0x}^2+h_{B0y}^2)^{-3/2}. \tag{D.6}$$

problem $O(Ca_B^0)$:

$$
\begin{aligned}
&-P_{B0}+2(1+h_{B0x}^2+h_{B0y}^2)^{-1}[h_{B0x}^2 u_{B0x}+h_{B0y}^2 v_{B0y}+w_{B0z} \\
&\quad +h_{B0x}h_{B0y}(u_{B0y}+v_{B0x})-h_{B0x}(w_{B0x}+u_{B0z})-h_{B0y}(v_{B0z}+w_{B0y}) \\
&=N_B^{-3/2}\{-[(1+h_{B0y}^2)h_{B0xx}-2h_{B0x}h_{B0y}h_{B0xy}+(1+h_{B0x}^2)h_{B0yy}] \\
&\quad *[T_g+3\frac{Ca_A}{Ca_B}N_B^{-1}(h_{B0x}h_{B1x}+h_{B0y}h_{B1y})] \\
&\quad +[(1+h_{B0y}^2)h_{B1xx}+2h_{B0y}h_{B1y}h_{B0xx}-2(h_{B1x}h_{B0y}+h_{B0x}h_{B1y})h_{B0y} \\
&\quad -2h_{B1xy}h_{B0y}h_{B0x}+(1+h_{B0x}^2)h_{B1yy}+2h_{B0y}h_{B1x}h_{B0xy}]\frac{Ca_A}{Ca_B}\}\frac{\mu_A\gamma_B}{\mu_B\gamma_B},
\end{aligned}
\tag{D.7}
$$

$$
\begin{aligned}
&2h_{B0x}(w_{B0z}-u_{B0x})+(u_{B0z}+w_{B0x})(1-h_{B0x}^2)-(u_{B0y}+v_{B0x})h_{B0y}-(v_{B0z}+w_{B0y})h_{B0x}h_{B0y} \\
&=-\frac{\mu_A\gamma_B}{\mu_B\gamma_A}(T_{B0x}+T_{B0z}h_{B0x})(1+h_{B0x}^2+h_{B0y}^2)^{1/2},
\end{aligned}
\tag{D.8}
$$

$$
\begin{aligned}
&2h_{B0y}(w_{B0z}-v_{B0y})+(v_{B0z}+w_{B0y})(1-h_{B0y}^2)-(u_{B0y}+v_{B0x})h_{B0x}-(u_{B0z}+w_{B0x})h_{B0x}h_{B0y} \\
&=-\frac{\mu_A\gamma_B}{\mu_B\gamma_A}(T_{B0y}+T_{B0z}h_{B0y})(1+h_{B0x}^2+h_{B0y}^2)^{1/2},
\end{aligned}
\tag{D.9}
$$

$$
(1+h_{B0x}^2+h_{B0y}^2)^{-1/2}(-h_{B0x}T_{B0x}-h_{B0y}T_{B0y}+T_{B0z})+\frac{H_g\ell}{\kappa_B}[T_{B0}-T_g(x,y)]=0. \tag{D.10}
$$

Similar to Chapter 6, consider an initially flat interface

$$
h_A=1. \qquad h_B=H. \tag{D.11}
$$

Then the complete set of equations and boundary conditions for problem $O(Ca^0)$:

temperature field:

$$T_{A0xx}+T_{A0yy}+T_{A0zz}=0, \tag{D.12}$$

$$T_{B0xx}+T_{B0yy}+T_{B0zz}=0, \tag{D.13}$$

z=0: $$T_{A0}=T_w(x,y), \tag{D.14}$$

z=1: $$T_{A0}=T_{B0}, \qquad T_{A0z}=GT_{B0z}, \tag{D.15}$$

z=H: $$T_{B0z}+Bi[T_{B0}-T_g(x,y)]=0, \tag{D.16}$$

flow field:

$$u_{A0x}+v_{A0y}+w_{A0z}=0, \tag{D.17}$$

$$u_{A0xx}+u_{A0yy}+u_{A0zz}=p_{A0x}, \tag{D.18}$$

$$v_{A0xx}+v_{A0yy}+v_{A0zz}=p_{A0y}, \tag{D.19}$$

$$w_{A0xx}+w_{A0yy}+w_{A0zz}=p_{A0z}, \tag{D.20}$$

$$u_{B0x}+v_{B0y}+w_{B0z}=0, \tag{D.21}$$

$$u_{B0xx}+u_{B0yy}+u_{B0zz}=p_{B0x}, \tag{D.22}$$

$$v_{B0xx}+v_{B0yy}+v_{B0zz}=p_{B0y}, \tag{D.23}$$

$$w_{B0xx}+w_{B0yy}+w_{B0zz}=p_{B0z}, \tag{D.24}$$

z=0: $$u_{A0}=v_{A0}=w_{A0}=0, \tag{D.25}$$

z=1: $$u_{A0}=u_{B0}, \quad v_{A0}=v_{B0}, \quad w_{A0}=w_{B0}=0, \tag{D.26}$$

$$u_{A0z}-Ku_{B0z}=-T_{A0x}, \tag{D.27}$$

$$v_{A0z} - K v_{B0z} = -T_{A0y}, \tag{D.28}$$

$z=H$:

$$u_{B0z} = -\frac{m}{K} T_{B0x}, \tag{D.29}$$

$$v_{B0z} = -\frac{m}{K} T_{B0y}, \tag{D.30}$$

$$w_{B0} = 0, \tag{D.31}$$

deformation problem:

$z=1$:

$$-p_{A0} + 2w_{A0z} - K(-p_{B0} + 2w_{B0z}) = h_{A1xx} + h_{A1yy}, \tag{D.32}$$

$z=H$:

$$-p_{B0} + 2w_{B0z} = \frac{m}{McK}(h_{B1xx} + h_{B1yy}), \tag{D.33}$$

where

$$Bi = \frac{H_g \ell}{\kappa_B}, \tag{D.34}$$

$$G = \frac{\kappa_B}{\kappa_A}, \tag{D.35}$$

$$K = \frac{\mu_B}{\mu_A}, \tag{D.36}$$

$$m = \frac{\gamma_B}{\gamma_A}, \tag{D.37}$$

$$Mc = \frac{Ca_B}{Ca_A}. \tag{D.38}$$

The solutions for above system are:

temperature:

$$T_{A0}(x,y)=\frac{1}{2\pi}\int_{-\infty}^{\infty}\int_{-\infty}^{\infty}\{\frac{C_{n1}\sinh(kz)}{C_{d1}}+\hat{T}_w(k_1,k_2)\cosh(kz)\}r(k_1,k_2)dk_1dk_2, \quad \text{(D.39)}$$

$$T_{B0}=\frac{1}{2\pi}\int_{-\infty}^{\infty}\int_{-\infty}^{\infty}\frac{C_{n3}\sinh(kz)+C_{n4}\cosh(kz)}{C_{d1}}r(k_1,k_2)dk_1dk_2, \quad \text{(D.40)}$$

where

$$\begin{aligned}C_{n1}= {} & \hat{T}_w[Gk\cosh(k)+Bik\sinh(k)][\sinh(kH)\cosh(k)-\cosh(kH)\sinh(k)]+\\ & \hat{T}_w[GBi\cosh(kH)+k\sinh(k)][\cosh(k)\cosh(kH)-\sinh(k)\sinh(kH)]-Bi\hat{T}_gG,\end{aligned} \quad \text{(D.41)}$$

$$C_{n3}=\hat{T}_w[k\sinh(kH)+Bi\cosh(kH)]+\hat{T}_gBi[G\sinh^2(k)-\cosh^2(k)], \quad \text{(D.42)}$$

$$C_{n4}=-\hat{T}_w[k\cosh(kH)+Bi\sinh(kH)]+\hat{T}_gBi(1-G)\sinh(k)\cosh(k), \quad \text{(D.43)}$$

$$\begin{aligned}C_{d1}= {} & [Gk\sinh(k)+Bi\cosh(k)][\sinh(k)\cosh(kH)-\cosh(k)\sinh(kH)]\\ & +[GBi\sinh(k)+k\cosh(k)][\sinh(k)\sinh(kH)-\cosh(k)\cosh(kH)].\end{aligned} \quad \text{(D.44)}$$

Flow field:

$$u_{A0}(x,y,z)=\frac{1}{2\pi}\int_{-\infty}^{\infty}\int_{-\infty}^{\infty}[C_{v1}\sinh(kz)+C_{v2}z\sinh(kz)+C_{v3}z\cosh(kz)]r(k_1,k_2)dk_1dk_2, \quad \text{(D.45)}$$

$$\begin{aligned}v_{A0}(x,y,z)= {} & \frac{1}{2\pi}\int_{-\infty}^{\infty}\int_{-\infty}^{\infty}[C_{v4}\sinh(kz)+C_{v2}\frac{k_2}{k_1}z\sinh(kz)+\\ & C_{v3}\frac{k_2}{k_1}z\cosh(kz)]r(k_1,k_2)dk_1dk_2,\end{aligned} \quad \text{(D.46)}$$

$$w_{AO}(x,y,z) = \frac{i}{2\pi}\int_{-\infty}^{\infty}\int_{-\infty}^{\infty}[-\frac{C_{v2}}{k_1}\sinh(kz)+\frac{k}{k_1}C_{v2}z\cosh(kz) + \frac{k}{k_1}C_{v3}z\sinh(kz)] * r(k_1,k_2)dk_1dk_2, \quad (D.47)$$

$$p_{AO}(x,y,z)=\frac{1}{2\pi}\int_{-\infty}^{\infty}\int_{-\infty}^{\infty}\frac{i}{k_1}[2C_{v3}k\sinh(kz)+2C_{v2}k\cosh(kz)]r(k_1,k_2)dk_1dk_2, \quad (D.48)$$

$$u_{BO}(x,y,z) = \frac{1}{2\pi}\int_{-\infty}^{\infty}\int_{-\infty}^{\infty}\{C_{v5}\sinh[k(z-H)]+C_{v6}\cosh[k(z-H)] + C_{v7}(z-H)\sinh[k(z-H)]+C_{v8}(z-H)\cosh[k(z-H)]\}r(k_1,k_2)dk_1dk_2, \quad (D.49)$$

$$v_{BO}(x,y,z) = \frac{1}{2\pi}\int_{-\infty}^{\infty}\int_{-\infty}^{\infty}\{C_{v9}\sinh[k(z-H)]+C_{v10}\cosh[k(z-H)]+ \frac{k_2}{k_1}C_{v7}(z-H)\sinh[k(z-h)]+\frac{k_2}{k_1}C_{v8}(z-H)\cosh[k(z-H)]\}r(k_1,k_2)dk_1dk_2, \quad (D.50)$$

$$w_{BO}(x,y,z) = \frac{1}{2\pi}\int_{-\infty}^{\infty}\int_{-\infty}^{\infty}i\{(\frac{k_1}{k}C_{v6}+\frac{k_2}{k}C_{v10}-\frac{C_{v7}}{k_1})\sinh[k(z-H)] + \frac{k}{k_1}C_{v7}(z-H)\cosh[k(z-H)]+\frac{k}{k_1}C_{v8}(z-H)\sinh[k(z-H)]\}r(k_1,k_2)dk_1dk_2, \quad (D.51)$$

$$p_{BO}=\frac{1}{2\pi}\int_{-\infty}^{\infty}\int_{-\infty}^{\infty}\frac{i}{k_1}\{2C_{v8}k\sinh[k(z-H)]+2C_{v7}k\cosh[k(z-H)]\}r(k_1,k_2)dk_1dk_2, \quad (D.52)$$

$$C_{v1}=\frac{ik_1}{2kF_v}[k\cosh(k)-\sinh(k)](\hat{T}_{AO}g_{v1}+\hat{T}_{BO}mg_{v2}), \quad (D.53)$$

$$C_{v2}=-\frac{ikk_1}{2F_v}\sinh(k)(\hat{T}_{AO}g_{v1}+\hat{T}_{BO}mg_{v2}), \quad (D.54)$$

$$C_{v3}=\frac{ik_1}{2F_v}[k\cosh(k)-\sinh(k)](\hat{T}_{A0}g_{v1}+\hat{T}_{B0}mg_{v2}), \tag{D.55}$$

$$C_{v4}=\frac{ik_2}{2kF_v}[k\cosh(k)-\sinh(k)](\hat{T}_{A0}g_{v1}+\hat{T}_{B0}mg_{v2}), \tag{D.56}$$

$$C_{v5}=\frac{ik_1m}{2kK}\hat{T}_{B0}, \tag{D.57}$$

$$\begin{aligned}C_{v6}= &-\frac{ik_1}{2kF_v}\{\hat{T}_{A0}g_{v2}[\sinh^2(k)-k^2]+\hat{T}_{B0}mg_{v1}[\sinh^2(k)-k^2]\\ &+\frac{m}{K}\hat{T}_{B0}[\cosh(k)\sinh(k)-k][\sinh^2(k-kH)-k^2(1-H)^2]\},\end{aligned} \tag{D.58}$$

$$\begin{aligned}C_{v7}= &-\frac{ik_1}{2F_v}\{\hat{T}_{A0}[k^2-\sinh^2(k)]\sinh[k(1-H)]+\hat{T}_{B0}m[k^2-\sinh^2(k)]\\ &*\cosh[k(1-H)]\sinh[k(1-H)]+\frac{\hat{T}_{B0}m}{K}[\cosh(k)\sinh(k)-k]\sinh^2[k(1-H)]\},\end{aligned} \tag{D.59}$$

$$C_{v8}=\frac{ik_1m}{2K}\hat{T}_{B0}, \tag{D.60}$$

$$C_{v9}=\frac{ik_2m}{2kK}\hat{T}_{B0}, \tag{D.61}$$

$$\begin{aligned}C_{b10}=&-\frac{ik_2}{2k_{F_v}}\{\hat{T}_{A0}g_{v2}[\sinh^2(k)-k^2]+\hat{T}_{B0}mg_{v1}[\sinh^2(k)-k^2]\\ &+\frac{\hat{T}_{B0}m}{K}[\sinh^2(k-kH)-k^2(1-H)^2][\sinh(k)\cosh(k)-k]\},\end{aligned} \tag{D.62}$$

$$g_{v1}=k(1-H)-\cosh[k(1-H)]\sinh[k(1-H)], \tag{D.63}$$

$$g_{v2}=k(1-H)\cosh[k(1-H)]-\sinh[k(1-H)] \tag{D.64}$$

$$\begin{aligned} F_v=&\{K\sinh^2(k-kH)[k^2-\sinh^2(k)] \\ &+[k-\sinh(k)\cosh(k)][k(1-H)-\sinh(k-kH)\cosh(k-kH)]\}. \end{aligned} \tag{D.65}$$

Deformation:

$$h_{AO}=\frac{1}{2\pi}\int_{-\infty}^{\infty}\int_{-\infty}^{\infty}\frac{1}{k^2}\frac{C_{nA}}{C_{dA}}r(k_1,k_2)dk_1dk_2, \tag{D.66}$$

$$h_{BO}(x,y)=\frac{1}{2\pi}\int_{-\infty}^{\infty}\int_{-\infty}^{\infty}\frac{K}{k^2}\frac{Mc}{m}\frac{C_{nB}}{C_{dB}}r(k_1,k_2)dk_1dk_2, \tag{D.67}$$

where

$$\begin{aligned} C_{nA}=&\hat{T}_{AO}k_1k^4\{k[k(1-H)-\cosh(k-kH)\sinh(k-kH)]+K(1-H)[\sinh^2-k^2]\} \\ &+\hat{T}_{BO}mk_1k^4\{(1-H)[k-\sinh(k)\cosh(k)]\sinh(k-kH) \\ &+k[(1-H)\cosh(k-kH)-\sinh(k-kH)]+K(1-H)\cosh(k-kh)\cosh^2(k)\}, \end{aligned} \tag{D.68}$$

$$\begin{aligned} C_{dA}=&\ Kk^2k_1[k^2-\sinh^2(k)]\sinh^2(k-kH) \\ &+k_1k^2[\cosh(k)\sinh(k)-k][\cosh(k-KH)\sinh(k-kH)-k(1-H)], \end{aligned} \tag{D.69}$$

$$\begin{aligned} C_{nB}=&\hat{T}_{AO}k^4(1-H)\cosh(k-kH)[\sinh^2(k)-k^2] \\ &+\hat{T}_{BO}mk^4(1-H)\{\sinh^2(k)-k^2+\frac{k}{K}(1-H)[k-\cosh(k)\sinh(k)]\}, \end{aligned} \tag{D.70}$$

$$C_{dB} = Kk^2[k^2-\sinh^2(k)]\sinh^2(k-kH) + k^2[\cosh(k)\sinh(k)-k][\cosh(k-kH)\sinh(k-kH)-k(1-H)]. \quad \text{(D.71)}$$

Analyzing the above results, we can show that the existence condition still has the form of Equation (6.174), i.e.,

$$\int_{-\infty}^{\infty}\int_{-\infty}^{\infty} T_w(x,y)dxdy = \int_{-\infty}^{\infty}\int_{-\infty}^{\infty} T_g(x,y)dxdy = 0. \quad \text{(D.72)}$$

Appendix E

Solution Procedure with DFT Methods for Small Deformation Cases

When the wall temperature is periodic, the temperature, velocity and pressure in both liquid layers can be expressed explicitly (Sections 6.5 and 6.6). Otherwise, numerical results have to be sought. Since direct numerical solution of a double layer system is very time-consuming, another approach, which is based on results obtained in Sections 6.5 and 6.6 and discrete Fourier transform (DFT) method, is to be developed in this section. For simplicity, only one-dimensional double liquid layer cases are considered, in which the wall temperature has the form of $T_w(x)$. Note that the proposed method can be easily extended to two-dimensional double liquid layer systems.

The basic idea of the method is, (1) using DFT method to obtain numerical values of $\hat{T}_w(k)$; (2) discretizing functions (6.94)-(6.96) and (6.137)-(6.148) in the k-plane (frequency domain); and (3) using inverse discrete Fourier transform (IDFT) method on the multiplication of $\hat{T}_w(k)$ and corresponding functions to get solutions of temperature, velocity and pressure, etc. This method treats the wall temperature as an

input signal and the temperature, velocity, pressure as output signals, while the system transform matrix is defined by equations (6.91)-(6.97) and (6.129)-(6.148).

Since the wall temperature and the system are continuous and exist over the entire interval $(-\infty, \infty)$ and DFT can only handle finite discrete number sequence, two important factors, the windowing and sampling of data, must be considered before any computation is implemented.

E.1 Truncating or Windowing of a Signal

Since the input signal $T_w(x)$ covers the entire x axis, it must first be truncated or windowed so as to be applicable for DFT. A signal is windowed by multiplying it by a window function $g(x)$. Among the many different window functions, the simplest and most widely used one seems to be the rectangular window. It has the following form:

$$\begin{aligned} g(t) &= 1 \qquad |x| \le x_0, \\ g(t) &= 0 \qquad |x| > x_0, \end{aligned} \tag{E.1}$$

which is also chosen as the windowing function of the present study. Using this window, only the signals within the interval $[-x_0/2, x_0/2]$ are picked up. The truncation will cause leakage and introduce ripples. When $x_0 \to \infty$, these side effects will be diminished. Usually x_0 is limited by the capacity of

computers. It should be decided by balancing all the factors. In the present study it is selected by numerical experiments.

E.2 Pulse-Amplitude Modulation or Sampling of a Signal

A continuous function $T_w(x)$ must be discretized before DFT is applied. The discretization procedure is called pulse-amplitude modulation or sampling which, in fact, is the multiplication of function $T_w(x)$ and a pulse train $p(x)$. An idealized sampling is used here which is,

$$p(x) = \delta(x - K\tau) \qquad \tau = \frac{1}{\omega_s}, \tag{E.2}$$

where δ is the impulse function, K any integer, ω_s sampling rate. The sampled signal $T_w(x)p(x)$ is therefore given by

$$T_w(x)p(x) = \sum_{K=-\infty}^{\infty} T_w(K\tau)\,\delta(x - K\tau). \tag{E.3}$$

Thus, in idealized sampling, the sampled signal is an impulse train whose weights are the instantaneous values of the signal $T_w(x)$ at the sampling times $x=K\tau$. A key question here is whether or not the sampled signal $T_w(x)p(x)$ is a good approximation of the original signal $T_w(x)$. The answer to it is the famous Shannon theorem: *If the signal $T_w(x)$ has bandwidth B, the sampling frequency ω_s should be greater than or equal to 2B.* The minimum sampling frequency $\omega_s=2B$ is called the Nyquist sampling frequency. However, as mentioned above, the windowed $T_w(x)$ has a finite bandwidth ω_s. Hence, sampling

a signal with a finite sampling rate ω_s, no matter how large ω_s is, will always produce error. In the present study this error is found to be negligible for suitably large values of ω_s. These values are again chosen by numerical experiments.

E.3 The Procedure of the Solution

From the above discussions, there are two parameters to be determined through numerical experiments. Therefore, the following iteration procedure is proposed.

(i) Choosing arbitrarily a sampling rate and a length of window;

(ii) Obtaining DFT of the wall temperature and the system equations;

(iii) Obtaining flow parameters by carrying out IDFT on the multiplication of $\hat{\Gamma}_w$ and suitable transform functions;

(iv) Repeating steps (i)-(iii) using an increased sampling rate and length of window; and

(v) Comparing the two results. If the difference between them is smaller than the predefined value, stopping the iteration. Otherwise, repeating step (iv).

As an example, consider the following wall temperature

$$T_w(x) = (4x^3 - 6x)e^{-x^2}. \qquad \text{(E.4)}$$

Note that this temperature distribution satisfies the existence condition, accordingly, the formulas in Sections 6.5 and 6.6 are valid.

The above procedures are then verified by comparing the results obtained here and obtained by the methods described in Chapter 3 for a single liquid system. Figure E.1 shows that the differences among those three results are smaller than 5%. Therefore, it can be concluded that the above procedures are effective. This also confirms the effectiveness of the method described in Chapter 3, from another viewpoint.

As mentioned in Chapter 4, there are many publications focusing on single liquid layer systems. However, not much has been done on double-layer systems. Results available are limited exclusively to parallel flows, where the transverse velocity component is negligible (D. Villers & J.K. Plateen, 1990, H.Q. Yang & K.T. Yang, 1990, and A.A. Nepomnyashchii & I.B. Simanovskii,1984). There is a lack of formalism that allows the evaluation of interface effects. In what follows, an investigation will be presented which studies thermocapillary convection in a double-layer system including cases with a large transverse velocity component and the resulting interface deformation. Finally, the possibilities of reducing the intensity of the convection will be discussed.

6.2 Problem Formulation

Consider two superposed layers made of immiscible liquids, infinite in the x and y directions, bounded below by a solid nonisothermal plate and above by an insulated plate, as shown in Figure 6.1. The plates are flat, parallel to each other and set apart by a distance H. The temperature of the lower plate $\tilde{T}_w(x,y)$ is fixed by external means and considered to be known. The lower liquid (liquid A) is incompressible, Newtonian, has density ρ_A, thermal conductivity k_A, specific heat per unit mass c_A, thermal

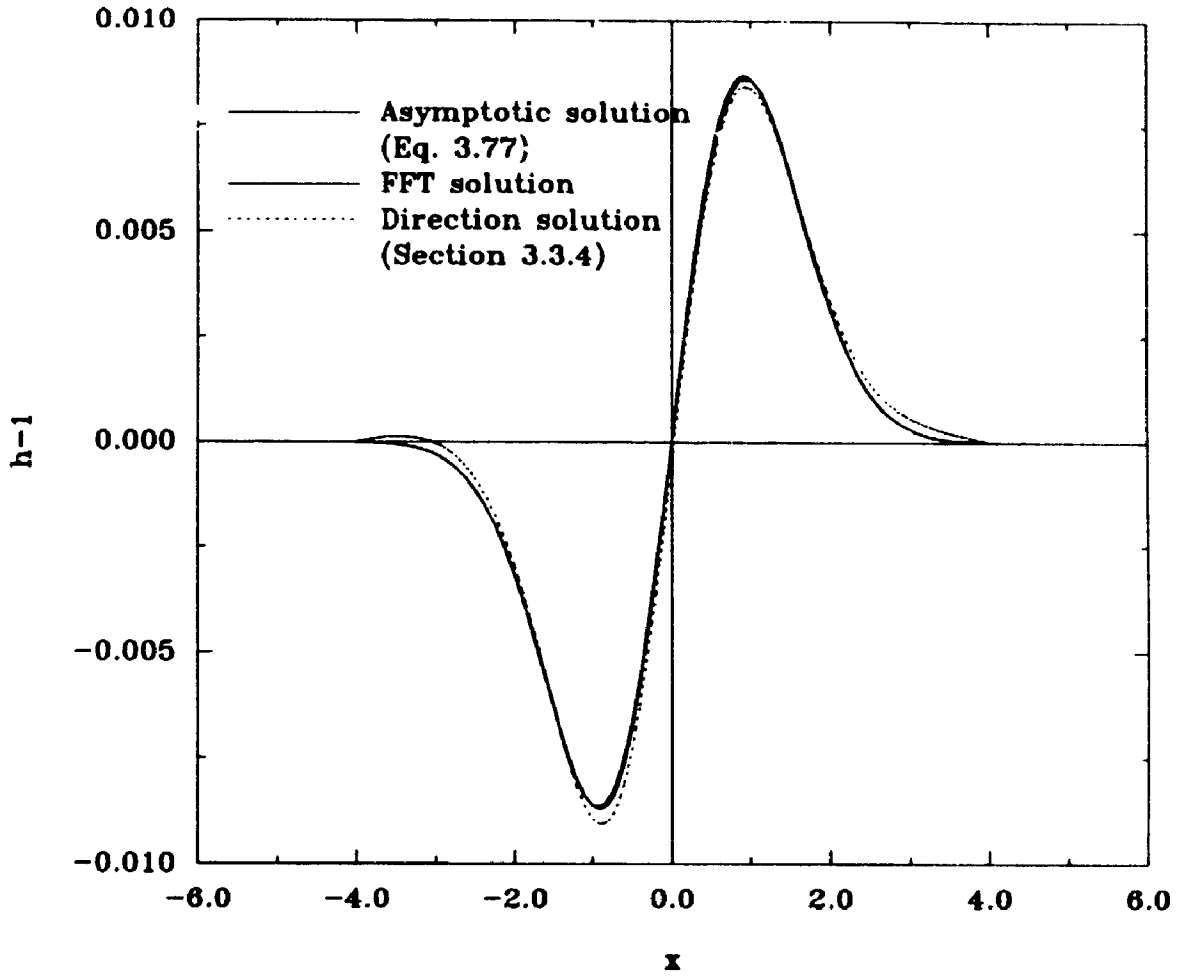

Figure E.1 Interface deformation $h_1(x)$ obtained by different methods for initially flat interface (Re=Ma=0, Bi=∞, Ca=0.024, $T_s=(4x^3-6x)e^{-x^2}$).

REFERENCES

1. Adler, J. and Sowerby, L., 1970, "Shallow Three-Dimensional Flows with Variable Surface Tension", J. Fluid Mech., Vol. 42, p549.

2. Bergman, T.L. and Webb, B.W., 1990, "Simulation of Pure Metal Melting with Buoyancy and Surface Tension Forces in the Liquid Phase", Int. J. Heat, Mass Transfer, Vol. 33, No.1, p139.

3. Birikh, R.V., 1966, "Thermocapillary Convection in a Horizontal layer of Liquid", J. Appl. Mech. and Tech. Phys., Vol. 3, p43.

4. Brown, R.A., 1988, "Theory of Transport Processes in Single Crystal Growth from the Melt", AIChE Journal, Vol. 34, p881.

5. Carpenter, B.M and Homsy, G.M., 1985, "The Effect of Surface Contamination on Thermocapillary Flow in a Two-Dimensional Slot. Part 2: Partially Contaminated Interfaces", J. Fluid Mech., Vol. 155, p429.

6. Carpenter, B.M. & Homsy, G.M., 1990, "High Marangoni Number Convection in a Square Cavity Part II", Phys. Fluids A, Vol. 2, No. 2, p137.

7. Chen, C. and Floryan, J.M., 1993, "Numerical Simulation of Nonisothermal Capillary Interfaces", To appear in the Journal of Computational Physics.

8. Chen, H. and Lee, Y., 1993, "Numerical Analysis of Thermocapillary Convection and Heat Transfer in Two-Dimensional Capillary Cavity", Computational Fluid Dynamics Journal, Vol. 1, No. 4, p477.

9. Chen, J.C., Chen, W.C and Hwu, F.S., 1991, "Numerical Computations of Unsteady Thermocapillary Convection in a Rectangular Cavity with Surface Deformation", HTD-Vol. 162, Heat Transfer in Metals and Containerless Processing and Manufacturing, ASME 1991, p89.

10. Chen, J.C., Sheu, J.C. and Jwu, S.S., 1990, "Numerical Computation of Thermocapillary Convection in a Rectangular Cavity", Numerical Heat Transfer, Part A, Vol. 17, p287.

11. Christov, C.I. and Volkov, P.K., 1985, "Numerical Investigation of the Steady Viscous flow Past a Stationary Deformable Bubble", J. Fluid Mech., Vol. 158, p341.

12. Coriell, S.R., McFadden, G.B. and Sekerka, R.F., 1985, "Cellular Growth During Directional Solidification", Ann. Rev. Mater. Sci., Vol. 15, p119.

13. Cowley, S.J. and Davis, S.H., 1983, "Viscous Thermocapillary Convection on High Marangoni Number", J. Fluid Mech., Vol. 135, p175.

14. Davis, S.H., 1987, "Thermocapillary Instabilities", Ann. Rev. Fluid Mech., Vol. 19, p403.

15. Dijkstra, H.A and van de Vooren, A.I, 1989, "Multiplicity and Stability of Steady Solutions for Marangoni Convection in a Two-Dimensional Rectangular Container with Rigid Sidewalls", Numerical Heat Transfer, Part A, Vol. 16, p59.

16. Doi, T. and Koster, J., 1993, "Thermocapillary Convection in Two Immiscible Liquid Layers with Free Surface", Phys. Fluids A, Vol. 5, No. 8, p1914.

17. Drazin, P.G. and Reid, W.H., 1981, "Hydrodynamic Stability", Cambridge Univ. Press.

18. Dubovik, K.G. and Slavchev, S.G., 1991, "Numerical Modeling of Thermocapillary Convection in a Liquid Layer with a Nonlinear Dependence of the Surface Tension on Temperature", Fluid Dynamics, Vol. 26, No. 5, p114.

19. Eyer, A and Leiste, H., 1985, "Striation-Free Silicon Crystals by Float-Zoning with Surface-Coated Melt", J. Crystal Growth, Vol. 71, p249.

20. Feuerbacher, B., Hamacher, H. and Naumann, R.J., 1986, "Materials Sciences in Space", Springer Verlag, Berlin.

21. Floryan, J.M. and Rasmussen, H., 1989, "Numerical Methods for Viscous Flows with Moving Boundaries", Appl. Mech. Rev., Vol. 42, No. 12, p323.

22. Floryan, J.M. and Krol, S., 1991, "On Thermocapillary Convection and Existence of Thin Nonisothermal Liquid Layers in the Absence of Gravity", Adv. Space Res., Vol. 11, No. 7, p125.

23. Glicksman, M.E., Coriell, S.R. and McFadden, G.B., 1986, "Interaction of Flows with the Crystal-Melt Interface", Ann. Rev. Fluid Mech. Vol. 18, p307.

24. Gouesbet, G., Maquet, J., Roze, C. and Darrigo, R., 1990, "Surface-Tension- and Coupled Buoyancy-Driven Instability in a Horizontal Liquid Layer. Overstability and Exchange of Stability", Phys. Fluids A, Vol. 2, No. 6, p903.

25. Goussis, D.A, and Kelly, R.Z, 1990, "On the Thermocapillary Instabilities in a Liquid Layer Heated from Below", Int. J. Heat, Mass Transfer, Vol. 33, No. 10, p2237.

26. Gupalo, Yu.P., Ryazantsev, Yu.S. and Skvortsova, A.V., 1990, "Effect of Thermocapillary Forces on Free-Surface Fluid Motion", Fluid Dynamics, Vol. 24, No. 5, p657.

27. Guo, K.H. and Yang, W.J, 1991, "Linear Oscillatory Cellular Thermocapillary Convection in Liquid Layers", J. Thermophysics, Vol. 5, No. 1, p96.

28. Hadid, H.B. and Roux, B., 1990, "Thermocapillary Convection in Long Horizontal Layers of Low-Prandtl-Number Melts Subject to a Horizontal Temperature Gradient", J. Fluid Mech., Vol. 221, p77.

29. Hadid, H.B. and Roux, B., 1992, "Buoyancy- and Thermocapillary-Driven Flows in Differentially Heated Cavities for Low-Prandtl-Number Fluids", J. Fluid Mech., Vol. 235, p1.

30. Henry, D. and Roux, B., 1988, "Stationary and Oscillatory Instabilities for Mixture Subjected to Soret Effect in Vertical Cylinder with Axial Temperature Gradient", J. Fluid Mech. Vol. 195, p175.

31. Hirt, C.W. and Nichols, B.D., 1981, "Volume of Fluid (VOF) Method for the Dynamics of Free Boundaries", J. Comput. Phys., Vol. 39, p201.

32. Hoffmann, K.A., 1989, "Computational Fluid Dynamics for Fngineers", Engineering Education System, Austin, Texas.

33. Homsy, G.M. and Meiburg, E., 1984, "The Effect of Surface Contamination on Thermocapillary Flow in a Two-dimensional Slot", J. Fluid Mech., Vol. 139, p443.

34. Hyman, J.M., 1984, "Numerical Methods for Tracking Interfaces", Physica, Vol. 12D, p396.

35. Jimenez-Fernandez, J. & Garcia-Sanz, J., 1989, "Surface Deflection in Benard - Marangoni Convection", Physics Letters A, Vol. 141, No.3-4, p161.

36. Kania, A.A., 1987, "Numerical Algorithms for Analysis of Dynamics of Ideal Fluid with Free/Moving Boundaries", Ph.D. Thesis, The University of Western Ontario, London, Ontario.

37. Krol, S, 1991, "Thermocapillary Convection in the Absence of Gravity", Master Thesis, The University of Western Ontario, London, Ontario.

38. Keller, J.R. and Bergman, T.L., 1990, "Thermocapillary Cavity Convection in Wetting and Nonwetting Liquids", Numerical Heat Transfer Part A, Vol. 18, p33.

39. Kim, Y.J. and Kou, S., 1989, "Thermocapillary Convection in Zone-Melting Crystal Growth - an Open-Boat Physical Simulation", J. Crystal Growth, Vol. 98, p637.

40. Kopbosynov, B.K. and Pukhnachev, V.V., 1986, Fluid Mechanics Soviet Research, Vol. 15, p95.

41. Lai, C.L. and Chai, A.T., 1986, Acta Astronantica, Vol. 13, p655.

42. Laure, P., Roux B. and Hadid, H.B. 1990, "Nonlinear Study of the Flow in a Long Rectangular Cavity Subjected to Thermocapillary Effect", Phys. Fluids A, Vol. 2, p516.

43. Levich, V.G., 1962, "Physicochemical Hydrodynamics", Prentice-Hall.

44. Loh, C.Y., 1985, "Numerical Techniques for Free Surface Problems in Viscous Incompressible and Porous Flows", Ph. D. Thesis, The University of Western Ontario, London, Ontario.

45. Loh, C.Y. and Rasmussen, H, 1987, "A Numerical Procedure for Viscous Free Surface Flows", Appl. Numer. Math, Vol. 3, p479.

46. McFadden, G.B., Coriell, S.R. and Boisvert, R.F., 1985, "Double-diffusive Convection with Sidewalls", Phys. Fluids, Vol. 28, p2716.

47. Mundrane, M and Zebib, A, 1993, "Two- and Three-dimensional Buoyant Thermocapillary Convection", Phys. Fluids A, Vol. 5, p810.

48. Nataf, H.C., Moreno, S. and Cardin, Ph, 1988, "What is Responsible for Thermal Coupling in Layered Convection", J. Phys. France, Vol. 49, p1707.

49. Nepomnyashchii, A.A. and Simanovskii, I.B., 1983a, "Thermocapillary Convection in a Two-layer System", Sov. Phys. Dokl. Vol. 28, p838.

50. Nepomnyashchii, A.A. and Simanovskii, I.B., 1983b, "Thermocapillary Convection in a Two-layer System", Fluid Dyn ..ics, Vol. 18, p629.

51. Nepomnyashchii, A.A. and Simanovskii, I.B., 1984, "Thermocapillary and Thermogravitational Convection in a Two-Layer System with Curved Interface", Fluid Dynamics, Vol. 19, No. 3, p494.

52. Nepomnyashchii, A.A. and Simanovskii, I.B., 1990a, "Onset of Thermocapillary Convection in a Two-Layer System with the Release of Heat at the Interface", J. Applied Mechanics and Technical Physics, Vol. 31, No. 1, p64.

53. Nepomnyaschii, A.A. and Simanovskii, I.B., 1990b, "Long-Wave Thermocapillary Convection in Layers with Deformable Interfaces", Applied Mathematics and Mechanics, Vol. 54, No. 4, p490.

54. Oda, K, Stito, T., Nishihama, J. and Ishihara, T, 1989, "Numerical Simulation of the Boat Growth Method", J. Crystal Growth, Vol. 97, p186.

55. Ostrach, S., 1980, "Natural Convection with Combined Driving Forces", PCH Physico. Chem. Hydrodyn., Vol. 1, p233.

56. Ostrach, S., 1982, "Low-Gravity Fluid Flows", Ann. Rev. Fluid Mech., Vol. 14, p313.

57. Ostrach, S., 1983, "Fluid Mechanics in Crystal Growth - The 1982 Freeman Scholarly Lecture", J. Fluids Engineering, Vol. 105, p5.

58. Ostrach, S., Kamotani, Y. and Lai, C.L., 1985, "Oscillatory Thermocapillary Flows", PCH Physico. Chem. Hydrodyn., Vol. 6, p585.

59. Pearson, J.R., 1958, "On Convection Cells Induced by Surface Tension", J. Fluid Mech., Vol. 4, p489.

60. Perez-Garcia, C. and Carneiro, G., 1991, "Linear Stability Analysis of Benard - Marangoni Convection in Fluids with a Deformable Free Surface", Phys. Fluids A, Vol 3, No. 2, p292.

61. Pimputkar, S.M. and Ostrach, S., 1980, "Transient Thermocapillary Flow in Thin Liquid Layers", Phys. Fluids, Vol. 23, p1281.

62. Pimputkar, S.M. and Ostarch, S., 1981, "Convective Effects in Crystal Grown from Melts", J. Crystal Growth, Vol. 55, p644.

63. Polezhaev, V.I., 1984, "Hydrodynamics of Heat and Mass Transfer during Crystal Growth", Springer.

64. Pshenichnikov, A.F. and Tokmenina, G.A., 1983, "Deformation of the Free Surface of a Liquid by Thermocapillary Motion", Fluid Dynamics, Vol. 18, No. 3, p463.

65. Rahman, M.M., Faghri, A, Hankey, L. and Swanson, T.D, 1990, "Computation of the Free Surface Flow of a Thin Liquid Film at Zero and Normal Gravity", Numer. Heat Transfer, Vol. 17A, p53.

66. Rahman, M.M, Hankey, W.L. and Faghri, A, 1991, "Analysis of the Fluid Flow and Heat Transfer in a Thin Liquid Film in the Presence and Absence of Gravity", Int. J. Heat Mass Transfer, Vol. 14, No. 1, p103.

67. Rivas, D. and Ostrach, S., 1989, "Low-Prandtl-number Thermocapillary Flows in Shallow Enclosures", PCH PhysicoChem. Hydrodyn., Vol. 11, p765.

68. Rivas, D., 1991, Phys. Fluids A, Vol. 3, p280.

69. Roach, P.J., 1976, Computational Fluid Dynamics, Hermosa Publishers, Albuquerque, NM.

70. Rosenberger, F., 1979, "Fundamentals of Crystal Growth", Springer.

71. Rybicki, A. and Floryan, J.M., 1987a, "Thermocapillary Effects in Liquid Bridges. I. Thermocapillary Convection", Phys. Fluids, Vol. 30, p1956.

72. Rybicki, A. and Floryan, J.M., 1987b, "Thermocapillary Effects in Liquid Bridges. II. Deformation of the Interface and Capillary Instability", Phys. Fluids, Vol. 30, p1973.

73. Ryskin, G. and Leal L.G., 1984, "Numerical Solution of Free-Boundary Problems in Fluid Mechanics. Part 1. The Finite-Difference Technique", J. Fluid Mech., Vol. 148, p1.

74. Sanochkin, Yu. V., 1983, "Thermocapillary Convection in a Thin Liquid Layer Locally Heated from Above", J. Applied Mechanics and Technical Physics, Vol. 24, p887.

75. Sanochkin, Yu. V., 1984, "Steady Thermocapillary Motion in a Horizontal Layer of Liquid Metal Locally Heated from Above", Fluid Dynamics, Vol. 19, No. 6, p986.

76. Sanochkin, Yu. V., 1989, "Thermocapillary Convection in a Thin Layer of Nonuniformly Heated Fluid", Fluid Dynamics, Vol. 24, No. 2, p264.

77. Schwabe, D., 1988, "Surface-tension Driven Flow in Crystal Growth Melts", Crystals, Growth, Applications and Properties, ed. Freyhardt, H.C., Vol. 11, p75, Springer Verlag, Berlin.

78. Schwabe, D. and Scharmann, A., 1981, "Marangoni Convection in Open Boat and Crucible", J. Crystal Growth, Vol. 52, p435.

79. Sen, A.K. and Davis, S.H., 1982, "Steady Thermocapillary Flows in Two-Dimensional Slots", J. Fluid Mech., Vol. 121, p163.

80. Sen, A.K., 1986, Phys. Fluids, Vol. 29, p3881.

81. Shokoohi, F. and Elrod, H.G., 1987, "Numerical Investigation of the Disintegration of Liquid Jets", J. Comput. Phys., Vol. 71, p324.

82. Silliman, W.J and Scriven, L.E., 1980, "Separating Flow near a Static Contact Line: Slip at a Wall and Shape of a Free Surface", J. Comput. Phys., Vol. 34, p 287.

83. Smith, M.K. and Davis, S.H., 1983a, "Instabilities of Dynamic Thermocapillary Liquid Layers. Part 1: Convective Instabilities", J. Fluid Mech., Vol. 132, p119.

84. Smith, M.K. and Davis, S.H., 1983b, Instabilities of Dynamics Thermocapillary Liquid Layers. Part 2: Surface-wave Instabilities", J. Fluid Mech., Vol. 132, p145.

85. Smith, M.K., 1986, "Instability Mechanism in Dynamic Thermocapillary Liquid Layers", Phys. Fluids, Vol. 29, p3182.

86. Strani, M. and Piva, R., 1982, "Surface Tension Driven Flows in Micro-Gravity Conditions", International Journal for Numerical Methods in Fluids, Vol. 2, p367.

87. Strani, M, Piva, R. and Graziania, G., 19^3, "Thermocapillary Convection in a Rectangular Cavity: Asymptotic Theory and Numerical Simulation", J. Fluid Mech., Vol. 130, p347.

88. Thompson, J.F., Warsi, Z.U. and Mastin, C.W., 1985, "Numerical Grid Generation: Foundations and Applications", North-Holland, Elsevier, New York.

89. Val'tsiferov, Yu.V., Ryazantsev, Yu.S. and Shevtsova, V.M., 1990, "Investigation of Thermocapillary and Thermogravitational Convection in a Fluid with Local Heating", Fluid Dynamics, Vol. 24, No. 9, p842.

90. Villers, D and Platten, J.K., 1990, "Influence of Interfacial Tension Gradients on Thermal Convection in Two Superposed Immiscible Liquid Layers", Applied Scientific Research, Vol. 47, No. 2, p177.

91. Vybornov, S.I. and Sanochkin, Yu. V., 1985, "Thermocapillary Cell in a Layer of a Heavy Fluid Heated From Above", Fluid Dynamics, Vol. 20, p153.

92. Walter, H.U., 1987, Fluid Sciences and Materials Science in Space, Springer Verlag, Berlin.

93. Wang, C.H., Sen, Mihir and Vasseur, P., 1991, "Analytical Investigation of Benard-Marangoni Convection Heat Transfer in a Shallow Cavity Filled with Two Immiscible Fluids", Applied Scientific Research, Vol. 48, p35.

94. Winters, K.H., Plesser, Th. and Cliffe, K.A., 1988, "The Onset of Convection in a Finite Container Due to Surface Tension and Buoyancy", Physica, Vol. 29D, p387.

95. Yang, H., 1991, "Boundary Condition Methods in the Numerical Solution of the Navier-Stokes Equations with the Application to Free Surface Problems", Ph. D. Thesis, The University of Western Ontario, London, Ontario.

96. Yang, H.Q and Yang K.T., 1990, "Benard-Marangoni Instability in a Two-Layer System with Uniform Heat Flux", J. Thermophysics, Vol. 4, No.1, p73.

97. Yih, C.S., 1968, "Fluid Motion Induced by Surface Tension Variation", Phys. Fluids, Vol. 11, p477.

98. Yih, C.S., 1969, "Three-Dimensional Motion of a Liquid Film Induced by Surface Tension Variation or Gravity", Phys. Fluids, Vol. 12, p1982.

99. Zebib, A., Homsy, G. M. and Meiburg, E., 1985, "High Marangoni Number Convection in a Square Cavity", Phys. Fluids, Vol. 28, p3467.